

1 2 3 4 5 6 7 8 9 10 11 12 13 14 15 16 17 18 19 20 21 22 23 24 25 26 27 28 29 30 31 32

②

EXPERIMENTAL AND THEORETICAL INVESTIGATION OF INNOVATIVE BROADBAND MICROWAVE DEVICES

SAIC FINAL REPORT No. 91/1135

Submitted to:

Vacuum Electronics Branch, Code 6840
Electronics Science and Technology Division
Naval Research Laboratory
Washington, D.C. 20375

Submitted by:

**Plasma Physics Division
Science Applications International Corp.
1710 Goodridge Drive
McLean, VA 22102
(703) 734-5840**

DTIC
ELECTE
JUN 17 1991

Prepared under:

Contract No. N00014-88-C-2173

DISTRIBUTION STATEMENT A
Approved for public release;
Distribution Unlimited

May 1991

DEFENSE TECHNICAL INFORMATION CENTER

9100514

91 5 24 039

CONTENTS

General Discussion	1
References	14
Appendix I: Review of Two-Stream Amplifier Performance	16
Appendix II: Nonlinear Analysis of the Cerenkov Maser	25
Appendix III: Nonlinear Analysis of High-Power Cerenkov Masers	36
Appendix IV: A Millimeter and Submillimeter Wavelength Free-Electron Laser	41
Appendix V: High-Efficiency Operation of Free-Electron Laser Amplifiers	50
Appendix VI: The Ku-Band Ubitron Experiment at the Naval Research Laboratory	56
Appendix VII: Fundamental-Mode Ubitron Amplifier Performance of the NRL Ubitron	64
Appendix VIII: Improved Amplifier Performance of the NRL Ubitron	71
Appendix IX: Multimode Nonlinear Analysis of Free-Electron Laser Amplifiers in Three-Dimensions	81
Appendix X: Nonlinear Theory of Slow-Wave Ubitrons/Free-Electron Lasers	92
Appendix XI: Harmonic Content in a Planar Wiggler Based Free-Electron Laser Amplifier	105
Appendix XII: Nonlinear Theory and Design of a Harmonic Ubitron/Free-Electron Laser	113
Appendix XIII: Another Technical Memorandum	121
Appendix XIV: Linear Theory of a Field-Emitter-Array Distributed Amplifier	136
Appendix XV: Electromagnetic Properties of a Field Emission Distributed Amplifier	150
Appendix XVI: Field Emission Triodes	157

Dist. A per telecon Mr. N. Vanderplaats
NRL/Code 6840

6/13/91 CG



Accession For	
NTIS	CRAGI
DTIC	TAD
Unannounced	
Justification	
By	
Distribution	
Availability	
Dist	Availability
A-1	

GENERAL DISCUSSION

This final report is submitted to the Vacuum Electronics Branch, Electronics Science and Technology Division at the Naval Research Laboratory in order to summarize the research conducted by SAIC under Contract No. N00014-88-C-2173. The general scope of the work performed under this contract was quite broad and included both theoretical and experimental work related to the general problem of microwave and millimeter wave sources. The principal concepts which were of interest at the outset of the contract were the Two-Stream-Amplifier and the Cerenkov Maser. However, general theory and simulation of the Ubitron/Free-Electron Laser was also performed along with specific theoretical support for the Ubitron development program in the Vacuum Electronics Branch. In addition, a great deal of interest developed in the application of Field-Emission Arrays to RF source technology, and the experimental phase of the program shifted to encompass testing, design, and evaluation of several different approaches of this technology. The remainder of this report is devoted to a specific discussion of each phase of the program.

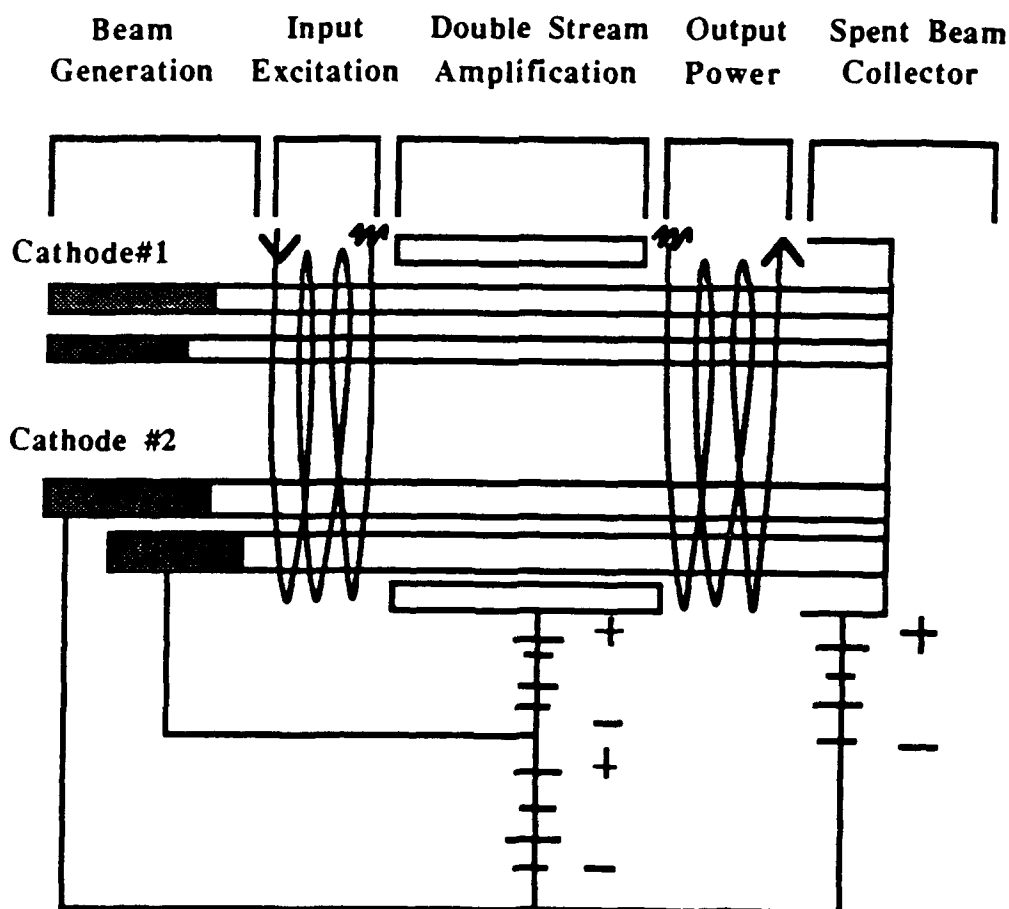


Fig. 1 Schematic illustration of a Two-Stream-Amplifier.

The Two-Stream Amplifier (TSA) concept originated with Pierce and Hebenstreit¹ and Haeff² who proposed the application of the electron-electron two-stream instability as a coherent source of microwaves. The fundamental configuration involved the propagation of two concentric, annular electron beams at different propagating through a waveguide. A schematic illustration of a TSA is shown in Fig. 1, which shows (1) the multiple cathodes necessary for the production of two concentric beams at different voltages, (2) the input and output coupling regions, (3) the drift space/interaction region between the input and output couplers, and (4) the collector. The research conducted on the TSA under this program included several different aspects. Due to the long hiatus between the initial work on this concept and the present program, the initial study was devoted to a detailed investigation of the prior research including the analysis of the original laboratory notebooks detailing the work by Haeff at the Naval Research Laboratory. Analysis of these notebooks showed that Haeff and his coworkers had difficulty in achieving high efficiencies by this approach. The subsequent research conducted under this contract included a detailed analysis of the linear dispersion equation in three-dimensions for this device and the associated gain, as well as a one-dimensional particle-in-cell simulation to determine the behavior of the nonlinear saturation with the relevant beam parameters. The research was summarized in a paper published in the IEEE Transactions on Electron Devices³ and which is reproduced in Appendix I.

The general conclusion reached regarding the TSA is that it is an inherently high gain but low efficiency device. It presents no unambiguous advantages over conventional devices such as the helix TWT. The TSA is also a broad band device; however, the bandwidth of the configuration chosen ultimately depends upon the intrinsic bandwidth of the output stage - which is typically chosen to be a helix. Thus, there seems to be no advantage to be gained by the TSA over the helix TWT in regard to bandwidth as well. Although the high gain in the TSA confers the advantage of being relatively less sensitive to beam thermal effects, the crucial limitation in this regard occurs due to the thermal spread of the bunched electron beams. This thermal spread was found in simulation to be comparable to the voltage separation between the beams, which is relatively large. As a consequence, the interaction will ultimately produce a bunched beam with a large velocity spread which will seriously degrade the performance of the output coupler. Hence, our final conclusion was that the TSA offers no marked advantages over that of conventional TWT technology.

The Cerenkov Maser has been demonstrated over a broad spectral range and operates by means of an interaction between an energetic electron beam and a subluminescent (or slow) electromagnetic wave. Wave-particle resonance occurs when the wave phase and particle velocities are in synchronism. While Orotrons and Backward Wave Oscillators succeed in slowing the electromagnetic wave to subluminescent velocities by means of a grating or a ripple imposed onto the waveguide walls, the Cerenkov Maser achieves this effect by means of a dielectric liner. Cerenkov Masers have been built and operated at 100 kW power levels at 1 mm wavelengths⁴⁻⁷, at 200 MW power levels at 8 cm wavelengths,⁷ as well as wavelengths as short as in the far-infrared at 100 μm .⁸

An exciting recent experiment on the Cerenkov Maser was conducted at General Dynamics⁹ which employed an intense relativistic electron beam [788 keV and 3.1 kA] produced by a cold "knife-edge" cathode which resulted in an annular beam with a mean radius of approximately 1.15 cm and a thickness of 2 mm. After correction for the space-charge depression, therefore, the beam energy is of the order of 736 keV. No diagnostic measurement of the beam quality (i.e., thermal energy spread) was made. The dielectric-lined waveguide employed Stycast ($\epsilon = 10$) and had a radius $R_g = 1.74$ cm and $R_d = 1.47$ cm. The dielectric had a 3.3 cm taper at both ends to suppress oscillation, and a uniform central region which was 23.9 cm in length. Beam transport was accomplished with a 15

kG solenoidal magnetic field. The amplifier was driven by a 200 kW magnetron which was tunable over the band from 8.4–9.6 GHz. The mode conversion process from the TE_{10} rectangular mode of the magnetron to the TM_{01} mode of the dielectric-lined waveguide was accomplished at an expected efficiency of 50% at a frequency of 8.6 GHz for a total injected power of approximately 100 kW. Note that at these frequencies it is only the TM_{01} mode which can interact with the beam. A total gain of 34.5 dB [1.44 dB/cm over the uniform dielectric] was observed at a power level of approximately 280 MW [for an efficiency of 11.5%], with an uncertainty of approximately 3 dB.

The research that was conducted under the present contract in regard to the Cerenkov Maser dealt with the development of a nonlinear slow-time-scale analysis and simulation of the device in a cylindrical geometry. The analysis and simulation code developed under this contract was described in a publication in the *Physics of Fluids*¹⁰ [see Appendix II]. The analysis dealt with the interaction of an electron beam with the TM_{0n} modes of a dielectric-lined cylindrical waveguide, and included both multi-mode effects and the effects of a beam thermal spread on the interaction. The simulation code developed was benchmarked against experiments conducted at Dartmouth College,⁶ and good agreement was found between the experimental observations and the results of the simulation.

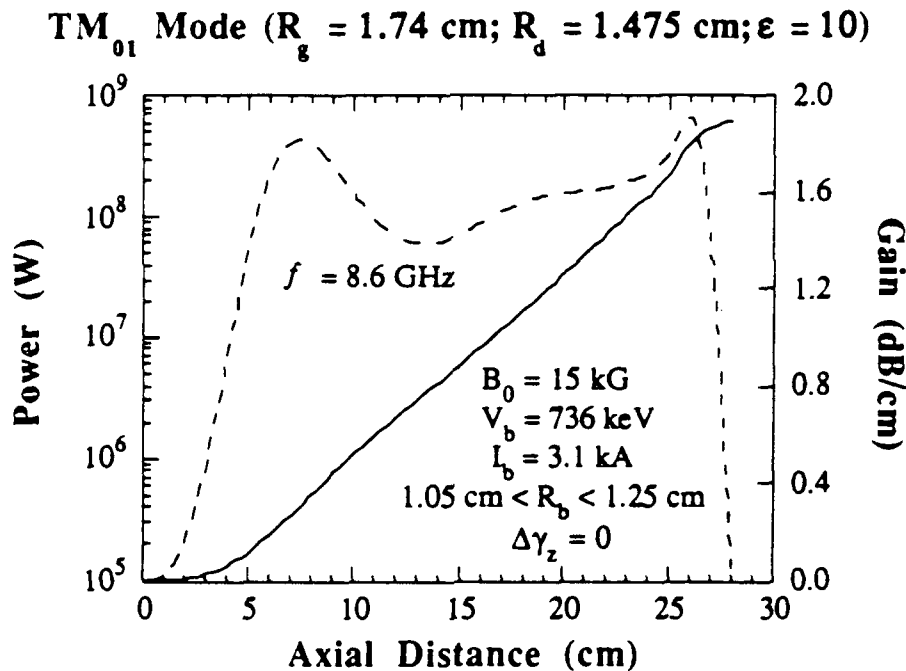


Fig. 2 Graph of the evolution of the power (solid line) and gain (dashed line) with axial distance.

The simulation was also benchmarked against the aforementioned high-power experiment conducted at General Dynamics,¹¹ and good agreement was found between the simulation and this experiment as well [see Appendix III]. The simulation shows that the power has not saturated over the 23.9 cm length of the uniform dielectric. As a result, the power predicted in simulation over this length shows a substantial sensitivity to the specific

choice of any parameter which will modify the linear gain. In particular, the simulation exhibits a large sensitivity to the choice of the thickness of the dielectric than to any of the electron beam parameters. For example, given the choice of $R_d = 1.47$ cm, the simulation predicts a power level of approximately 60 MW over the 23.9 cm length of the uniform dielectric. However, there is an uncertainty in the thickness of the dielectric which is of the order of ± 0.005 cm, and arises due to the fabrication of the liner. In this regard, Stycast (which is a cold-pressed ceramic) must be machined to fit within the waveguide.⁹ If we choose a value of $R_d = 1.475$ cm corresponding to a thinner dielectric, then the power found in simulation over this length rises to approximately 131 MW, which is within the uncertainty in the experimental measurement of the power. This sensitivity to the parameters is largely confined to the linear gain and results from a variation in the dielectric effect of the liner which modifies the tuning of the resonance within the gain band. The saturated power is not substantially altered by variations in R_d over this range, and we find that the saturated power rises from approximately 600 MW to 620 MW as the inner radius of the dielectric changes from 1.47 cm to 1.475 cm. Since the larger figure for R_d is in better agreement with the observations and is within the range of experimental uncertainty, we shall use this value henceforth in the numerical analysis of the experiment.

TM₀₁ Mode ($R_g = 1.74$ cm; $R_d = 1.475$ cm; $\epsilon = 10$)

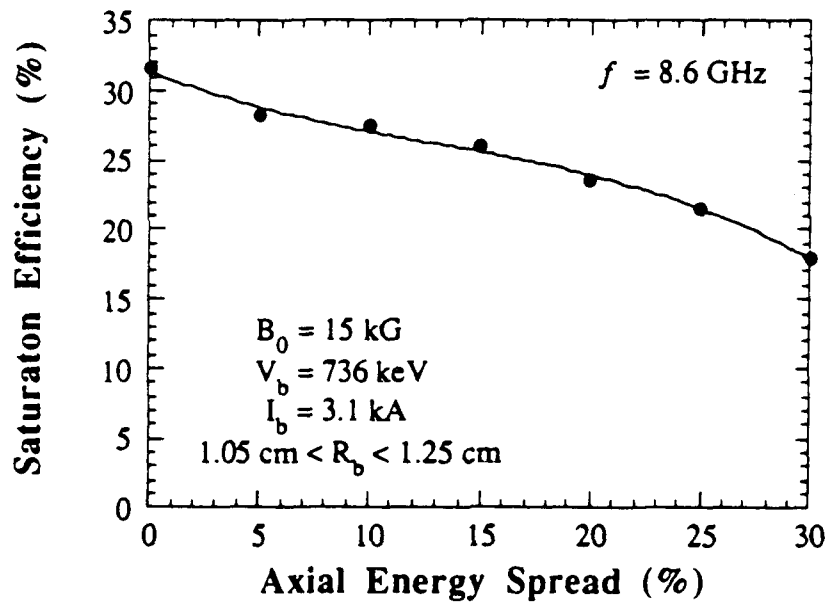


Fig. 3 Graph of the variation of the saturation efficiency versus axial energy spread.

The gain band is found in simulation to cover the range of approximately 7.8–8.8 GHz, and the efficiency at saturation for an ideal beam [i.e., $\Delta\gamma_z = 0$] increases from 16.4% at 7.8 GHz to approximately 30.3% at 8.8 GHz. A graph of the evolution of the power and gain versus axial distance is shown in Fig. 2 for an ideal beam at a frequency of 8.6 GHz. Observe that the power saturates after a length of approximately 28 cm at a level of 620 MW for an efficiency of 31.6%. The average gain over this interaction is in the neighborhood of 1.4 - 1.6 dB/cm which is also in reasonable agreement with the

observations. It should be remarked that the fluctuation evident in the gain is related to the launching loss of the signal, which introduces a fluctuation in the response of the beam to the wave. In most systems this fluctuation is observed to decay away leaving a relatively constant growth rate. However, the growth rate is so large in the present example that these fluctuations are unable to completely decay prior to the saturation of the signal. These fluctuations are also manifested in the evolution of the power, but are not visible when plotted on a logarithmic scale. As mentioned previously, the power level reached after 23.9 cm is approximately 131 MW, which is consistent with the observations given the experimental uncertainty. It is evident that the experiment was too short to reach saturation.

The effect of beam thermal spread is shown in Fig. 3 in which the efficiency is plotted as a function of the energy spread at 8.6 GHz. It is clear from the figure that the interaction is remarkably insensitive to the beam thermal spread, and the saturation efficiency is not significantly degraded by energy spreads as high as 20-25%. In order to explain such a high tolerance for energy spreads, it should be noted that the thermal regime occurs at progressively higher energy spreads as the growth rate increases for any interaction mechanism whether Cerenkov Maser, Free-Electron Laser, or Cyclotron Maser. Since this mechanism relies on the Cerenkov resonance in which $\omega - kv_b = 0$, thermal effects become important when $\Delta v_b/v_b = \text{Im } k/\text{Re } k$. In this case, the growth rate due to the intense beam is extremely high with $\text{Im } k = 0.18 \text{ cm}^{-1}$. Since $\text{Re } k = 2.35 \text{ cm}^{-1}$, this gives $\Delta v_b/v_b \approx 7.5\%$ which corresponds to an axial energy spread of $\Delta\gamma/\gamma_0 \approx 24\%$.

In view of the power levels found both in the laboratory and in simulation, the simplicity of the configuration, and the relative insensitivity to beam thermal effects in the case of intense relativistic electron beams, the Cerenkov Maser is an attractive competitor for Gyrotrons, Free-Electron Lasers, and Relativistic Klystrons for a wide variety of applications. In particular, the potentiality of producing single mode powers in excess of 700 MW at frequencies in the neighborhood of 9 GHz compares favorably with recent results obtained with Relativistic Klystrons;^{12,13} however, unlike the Relativistic Klystron, the Cerenkov Maser is easily scalable to higher frequencies. Indeed, it is anticipated that the level of performance demonstrated herein at 8.6 GHz can be achieved at frequencies as high as 35 GHz as well. It should be remarked that Cerenkov Masers based upon dielectric liners can exhibit both dielectric and mechanical breakdown at high power levels, and that these effects may have operated to limit the power and/or pulse length in the experiment at General Dynamics. However, this configuration represents only one approach to the interaction, and other slow wave structures may be used to overcome these difficulties. In general, this device falls into the category of relativistic intense-beam Traveling Wave Tubes (TWT's), and similar levels of performance have been obtained using a rippled wall slow-wave structure in both Backward Wave Oscillators¹⁴ and TWT amplifiers.¹⁵

The research conducted into the Ubitron/Free-Electron Laser encompassed both general issues and specific support for the experimental Ubitron development program. The theoretical program conducted by SAIC under contract to and in collaboration with researchers at the Naval Research Laboratory includes the development of nonlinear slow-time-scale formulations of the Ubitron in two principal configurations. The first nonlinear analysis and simulation code was developed to treat the case of a relativistic electron beam propagating through a cylindrical waveguide in the presence of a helically symmetric wiggler and an axial guide magnetic field.¹⁶⁻²¹ In the second configuration, the electron beam propagates through a rectangular waveguide in the presence of a planar wiggler field.²²⁻²⁴ We shall divide the discussion of the Ubitron/Free-Electron Laser research into two groups based upon these two configurations.

The basic analysis and code development for the helical wiggler configurations [code named ARACHNE] had been developed under prior contracts, and the work

conducted on this configuration under the present contract was primarily, but not exclusively, devoted to the use of the codes to interpret and optimize experiments. The first experimental comparison which we shall discuss involves an invitation from D. Kirkpatrick and G. Bekefi from the Massachusetts Institute of Technology to use the code as a benchmark for their Free-Electron Laser experiment. This experiment employed an electron beam with energies and currents up to 2.3 MeV and 1 kA in conjunction with a helical wiggler field and a cylindrical waveguide. Comparison between the simulation code and the experimental observations of the output spectrum of the Free-Electron Laser were quite good. A comparison between the ARACHNE code and the spectral measurements from the Free-Electron Laser are shown in Fig. 4 in which the solid line represents the spectrum obtained from the simulation, while the dots represent measurements. As shown in the figure, the comparison between theory and experiment for the center and width of the spectrum are in excellent agreement. This work resulted in a joint publication in the *Physics of Fluids*²⁵ [see Appendix IV].

TE₁₁ and TM₁₁ Modes ($R_g = 0.8$ cm)

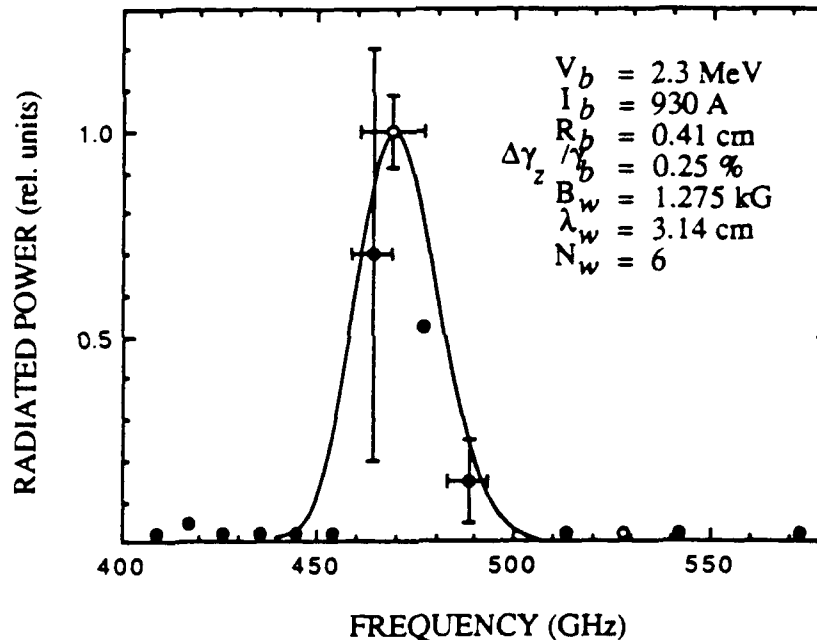


Fig. 4 Comparison between the ARACHNE code and the M.I.T. experiment.

Another application of the ARACHNE simulation was to the study of a high efficiency negative-mass operating regime identified in a preceding paper.¹⁶ This regime exists for a helical wiggler/axial guide field configuration in the strong guide field limit in which $\Omega_0 > \gamma k_w v_b$, where Ω_0 denotes the cyclotron frequency corresponding to the axial guide field, γ is the relativistic factor corresponding to the beam energy, k_w is the wiggler wavenumber, and v_b is the bulk streaming velocity of the beam. In this regime, the electrons can be accelerated as they lose energy to the wave [the energy for this acceleration as well as the wave amplification comes from the transverse motion of the electrons]; hence, the nomenclature of *negative-mass*. The characteristics of this regime can be ultra-high efficiency, and a total efficiency approaching 50% of the electron beam energy was found for an example discussed in ref. 16. The nature of the electron dynamics associated

with this negative-mass regime indicate that it is accessible only at relatively high voltages, and the example discussed in ref. 16 was for a 1 MeV electron beam. In order to determine the low voltage extension of this regime, we studied the variation of the interaction efficiency as a function of beam voltage using the ARACHNE code. This work was published in the IEEE Transactions on Plasma Science²⁰ [see Appendix V]. The ultimate conclusion of this study was that the high-efficiency negative-mass regime appears to be accessible down to voltages in the range of 400-500 keV; but that operation at lower voltages is likely to be impractical.

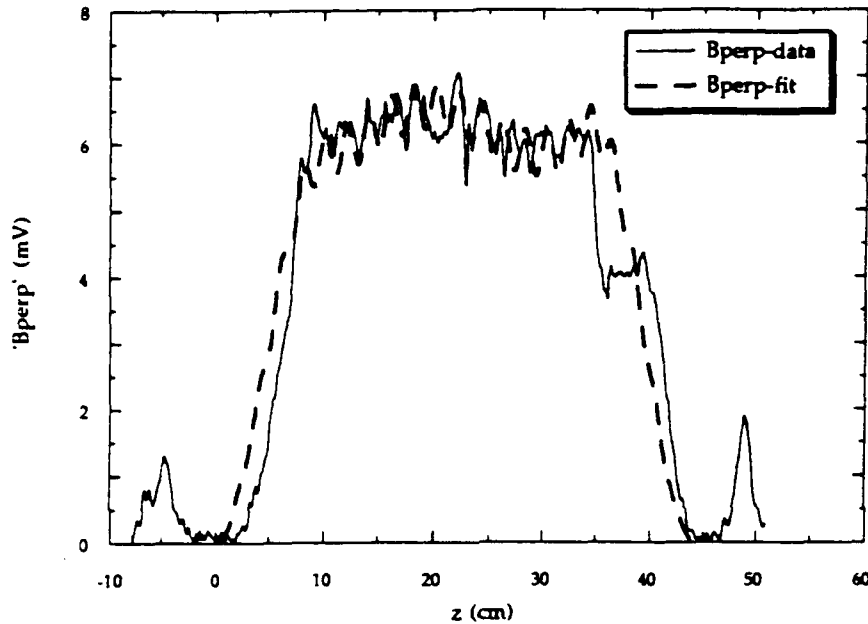


Fig. 5 Comparison between the measured wiggler field and the three-wiggler model incorporated into ARACHNE.

The final application of the ARACHNE code under the present contract was to the ongoing support of the NRL Ubitron experiment²⁶⁻²⁸ [see Appendices VI-VII]. This experiment utilizes an electron beam of up to 250 keV and 100 A in conjunction with a helical wiggler/axial guide magnetic field. The principal limiting factor in the theoretical description of the experiment was in the description of the wiggler field. The reason for this stems from the initial design specification of a CW bifilar helix which was wound on an aluminum form. Unfortunately, there was insufficient cooling capacity to run the wiggler in a CW mode, and it was run in a pulsed mode instead. This caused difficulties due to the magnetic permeability of the aluminum which resulted in field distortions. In order to model the realistic field, we resorted to an empirical fit to the measured field which employed a model field based upon the superposition of three different [i.e., in period and amplitude] ideal wiggler fields [see ref.28]. A comparison of the measured field and the three-wiggler model which was incorporated into ARACHNE is shown in Fig. 5 [see Appendix VII]. The use of this field model was found to result in reasonable agreement between ARACHNE and the experimentally measured gain. A plot of the gain as a function

of frequency is shown in Fig. 6 as determined in the experiment (dots) and by means of ARACHNE. It is clear that good agreement is found between the simulation and the experiment, and that this three-wiggler model is an adequate representation of the actual wiggler field.

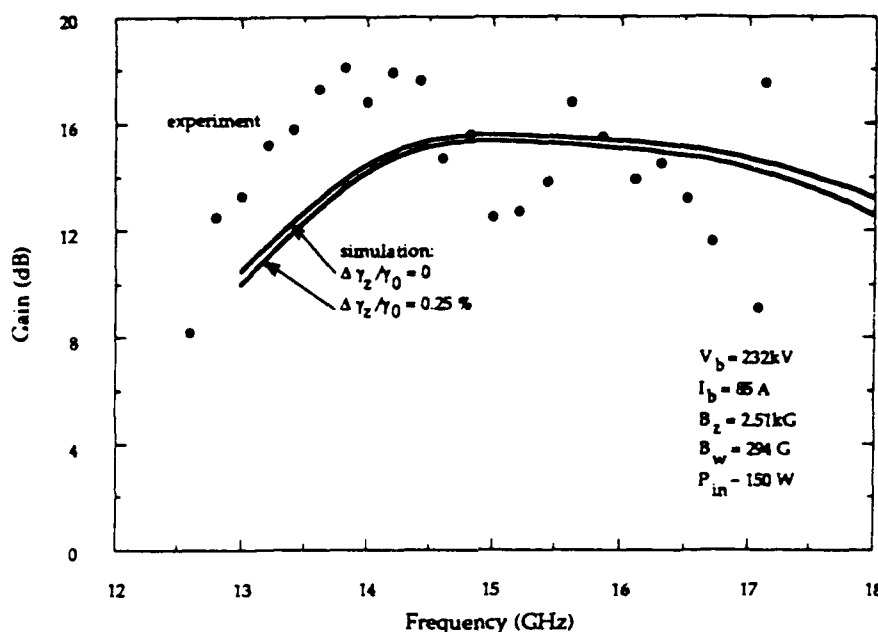


Fig. 6 Comparison of the gain as a function of frequency between the experiment and the ARACHNE code utilizing the three-wiggler model.

The analysis and simulation of the planar wiggler/rectangular waveguide configuration began under a prior contract. The initial work under the current contract dealt with the extension of the initial analysis²² to the inclusion of multiple modes in the treatment²⁴ [see Appendix IX]. This analysis was benchmarked against the Free-Electron Laser experiments at Lawrence Livermore National Laboratory, and good agreement was found between the simulation code and the experiment.^{29,30}

Research into a combination of the concepts of the fast-wave Ubitron and the slow-wave Cerenkov has also been performed under the present contract. This consisted of a slow-time-scale analysis of a slow-wave Ubitron in which a geometry consisting of a dielectric-lined rectangular waveguide was assumed in conjunction with a planar wiggler field. A schematic illustration of this geometry is shown in Fig. 7. The fundamental purpose of such a configuration is to reduce the voltage requirement imposed by the Free-Electron Laser resonance condition to achieve high frequency operation. Thus, we intend to slow down the wave rather than accelerate the electrons. The geometry of this configuration places the dielectric material along the long face of the waveguide which is parallel to the wiggler-induced transverse oscillation; hence, we can minimize the possibility of electrons striking the dielectric. The standard TE and TM modes of a rectangular waveguide do not exist for the dielectric-lined waveguide; instead, we find LSE and LSM modes which

essentially transverse electric and magnetic modes with respect to the y -axis shown in the figure. The development of the nonlinear analysis and simulation will be published in Nuclear Instruments and Methods in Physics Research³¹ [see Appendix X], and the results indicate that this method of reducing the voltage requirement for operation at a given frequency is indeed feasible.

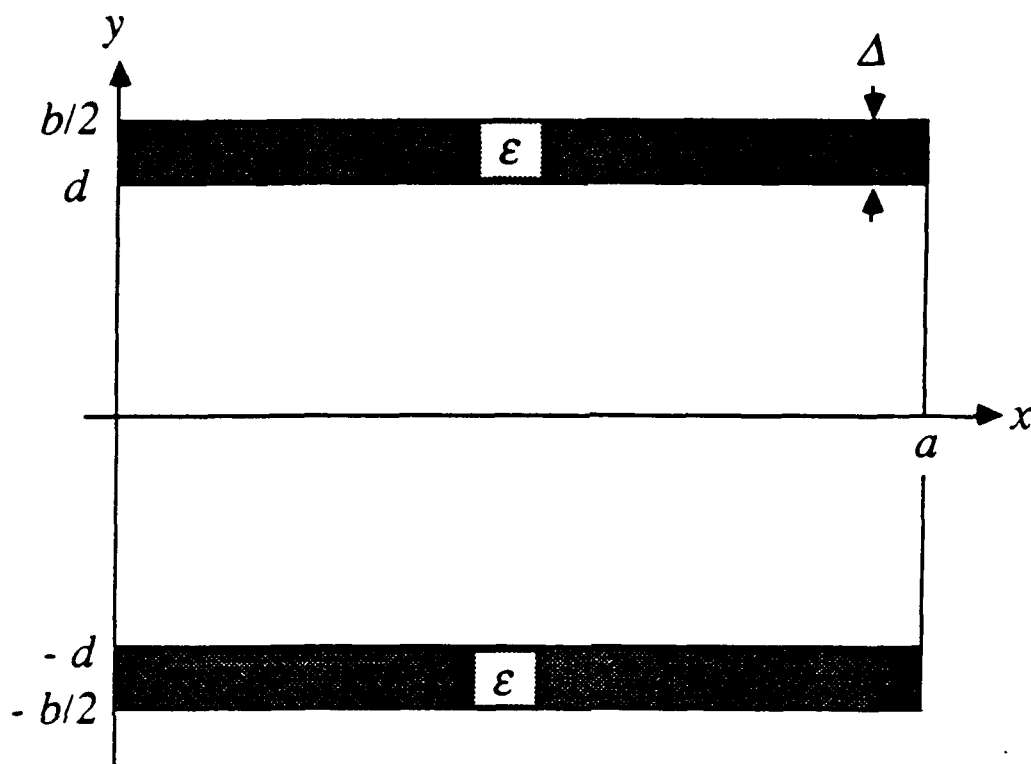


Fig. 7 Schematic illustration of the dielectric-lined rectangular waveguide used in the slow-wave Ubitron analysis.

The remainder of the work on Ubitrons/Free-Electron Lasers was concerned with harmonic emission in planar wiggler configurations^{32,33} [see Appendices XI and XII]. This work was directed toward the harmonic experiment conducted in the Vacuum Electronics Branch by Hans Bluem. The analysis and simulation in this case employed the multimode slow-time scale simulation code (WIGGLIN) described previously,²⁴ and no further modifications were required in order to treat the harmonic interaction. The work described in Appendix XI dealt with general aspects of harmonic excitation in a three-dimensional planar wiggler field, and included the standard odd harmonic emission known to exist for planar wigglers. In addition, however, it was found that betatron oscillations due to the wiggler inhomogeneities can couple to emission at the even harmonics, and this issue was discussed in depth in that paper. The paper in Appendix XII dealt with more pragmatic issues in the design of the experimental apparatus, and the expected performance for both uniform and tapered wiggler configurations. At the present time, this experiment has been completed with good results. This final work in support of the experiment, however, was conducted on another contract.

Recognition for this work has come in the form of invited talks at several scientific conferences. These include invited papers dealing with the Ubitron/Free-Electron Laser program at the Naval Research Laboratory which were presented at both the *10th International Free-Electron Laser Conference* [Jerusalem, Israel, 29 August - 2 September 1988] and the International Congress on Optical Science and Engineering [Paris, France 24-28 April 1989]. In addition, an invited paper dealing with the comparison of fast and slow wave devices was presented at the 15th International Conference on Infrared and Millimeter Waves [Orlando, Florida, 10-14 December 1990].

We now turn to the program of research into the application of field-emission arrays (FEAs) to RF source technology. This program included three specific aspects of the use of FEA applications which include both theory and experiment. The first part of the program involved a study of the FEA distributed amplifier. Under this part of the program, an analytic theory of the linear gain of a distributed amplifier was developed, and a computer code written to evaluate the gain. In addition, a cold test of the circuit was conducted. The second part of the program involved a study of the application of Spindt cathodes to the production of RF sources. In this regard, numerous sample cathodes have been obtained and tested. In particular, a life-test of three samples has continued since 31 January 1990. In addition, Spindt cathodes have been used to construct FE Triodes, and a great deal of effort has been devoted to determining such characteristics of the cathodes as: transconductance, capacitance, and the I-V properties of the cathodes. Successful operation of four such triodes has been accomplished [three structures were inadvertently burned out], and properties such as the gain versus frequency and output resistance of the circuits have been measured. Finally, the computer code TOUCHSTONE has been used to model the circuits. The third aspect of the program has been the testing of samples provided by the Nano-Processing Facility (NPF) of the Naval Research Laboratory for field emission properties. Thus far, no field emission has been found from any of the NPF samples.

The lure of the field emission array is that the vacuum microelectronics technology provides a means to fabricate micron size devices which might be useful for the production of dense arrays of field emitters. The potentially high current density capability of these field emitters holds promise for production of small vacuum electronic devices which can compete with solid state technology. The field emission array is probably the most promising and definitely the most explored tool of this technology. It is a type of electron source that can be used as a cathode in vacuum tubes, or can be the basis of a new generation of on-chip integrable microelectronic devices. A comprehensive account of this technology can be found in the report of Shoulders.³⁴ The concepts described therein have become practical in recent years due to the advancement in microelectronic processing technology. A description of the current state of the art of solid state devices was prepared under this contract and distributed throughout the Vacuum Electronics Branch in October 1989 [see Appendix XIII], in order to provide a point of comparison for the vacuum electronics technology.

The utilization of solid-state microfabrication techniques results in a low cost per unit of these devices. The elimination of short-lifetime thermionic emission cathodes provides a second major advantage. Thus, this technology may satisfy the need for low power, compact, temperature insensitive, and radiation hard amplifiers for operation at higher frequencies with wider bandwidth that are currently available with both vacuum and solid-state devices.

A continuously distributed amplifier uses two electrically coupled transmission lines with matched phase velocities. A detailed description of its linear theory can be found in ref. 35 [see Appendix XIV], and Fig. 8 shows the basic configuration of this device. In order to test the concept, we performed some cold tests of such structures to verify the

possibility of matching the phase velocities in the two lines with dielectric loading. A correlation of these experimental results with a full wave analysis-based theory has been established³⁶ [see Appendix XV]. A small signal theory of a field-emission array based continuously distributed amplifier consisting of two microstriplike transmission lines has been developed to calculate the premodulation in the input circuit and the gain in the output end. The beam wave coupling is treated by a first order perturbation analysis, and the circuit parameters were derived to determine the parametric range for operation of this device for a fairly high frequency range. It was shown that the height of the circuit should lie in the range of 80-120 μm . The loss due to the finite conductivity of the metal walls and the stripline in the circuit is very high if the height is less than 80 μm , whereas the electronic gain is low if the height exceeds 120 μm . The dependence of electronic gain on the relative dielectric constant were also determined. It was recognized that the heat dissipation at the anode circuit is a major problem for this kind of device. This analysis was done for a frequency range above 20 GHz, but it is recognized now that a similar analysis for a lower frequency range is necessary for getting a complete picture of the potential¹ of a continuously distributed amplifier based on field emitters.

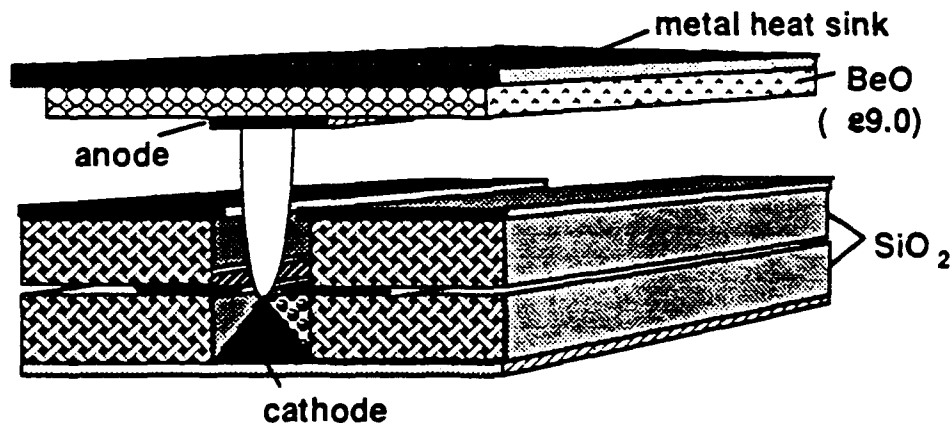


Fig. 8 Schematic Representation of an FE based Continuously Distributed Amplifier.

Our research objectives for the last contract period in regard to the FE triode were to: (1) develop a simulation procedure to calculate the static and dynamic characteristics of a FE triode and obtain design parameters for optimum gain, bandwidth and efficiency by increased transconductance and lowered capacitances, (2) assemble an FE triode and perform experiments to evaluate its characteristics such as transconductance, interelectrode capacitances, parasitic elements, and their effects on gain, bandwidth etc, (3) compare experiments with simulation results, (4) develop a circuit model to explain the experimental observations in order to predict the future performance of FE based devices.

We have been collaborating with SRI International and have successfully assembled a triode based on Spindt cathodes. We have also assembled a life-test configuration with three 10,000 cone based Spindt cathodes/triodes, which have been operating successfully with about 5 mA current (each) for more than 16 months. Fig. 9 shows the basic configuration of Field Emitter based triode. We have tested several Spindt cathodes in this assembly, and results include: (1) I-V characteristics, (2) determination of transconductance, (3) output resistance, (4) gain vs frequency measurements, (5)

theoretical circuit modelling, (6) determination of parasitic elements and their importance on the RF performance of the device and, (7) the requirements of the level of vacuum. Fig. 10 shows the circuit diagram for the above mentioned tests. The I-V characteristics show very flat nature implying high output resistance. The data from several different samples were in good agreement with the Fowler-Nordheim curve, and from these curves the transconductance values were calculated. Using these transconductance values and the measured capacitances, a circuit model using TOUCHSTONE was developed. The results from TOUCHSTONE were compared with the experimental data points for gain vs frequency. As shown in ref. 37 [see Appendix XVI], the agreement between experiment and theory was extremely good. It was concluded that high output resistance along with high output capacitances are responsible for an early roll-off of the gain with frequency. Measures to reduce these parameters are under study. Although the high input capacitance is responsible for the frequency limitation of the device, in our situation the input circuit did not control the performance of the amplifier.

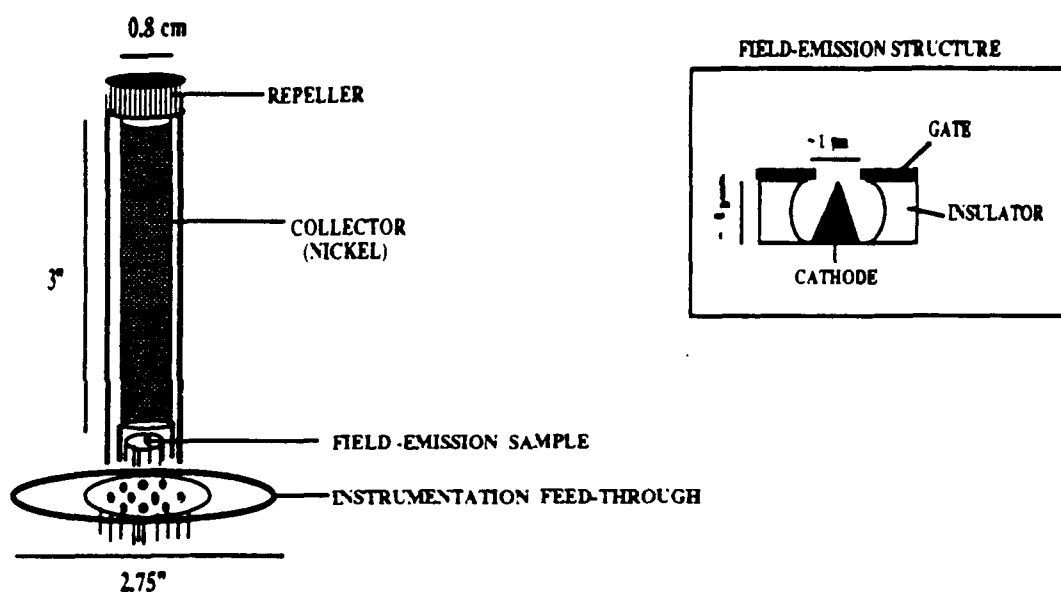


Fig. 9 Basic Configuration of FE based Triode

The above-mentioned experimental results were also compared with a particle simulation.³⁸ The parameters used for these simulations are as follows: cathode height = 1 mm, gate thickness = 4000 Å, half cone angle = 15°, and the tip radius was variable. These parameters were primarily determined by using Scanning Electron Micrographs of the Spindt cathodes taken at the NPF. The agreement between theory and experiment is again quite good for a tip radius of about 250 Å.

In addition to using SRI samples for triode assembly, we have tried to use semiconductor, and metal-coated semiconductor field emitters in both tip and wedge shapes made by the NRL MPF. Unfortunately, none of them gave any results (emission) mostly because of their large tip radius and nonuniform and large gate diameter.

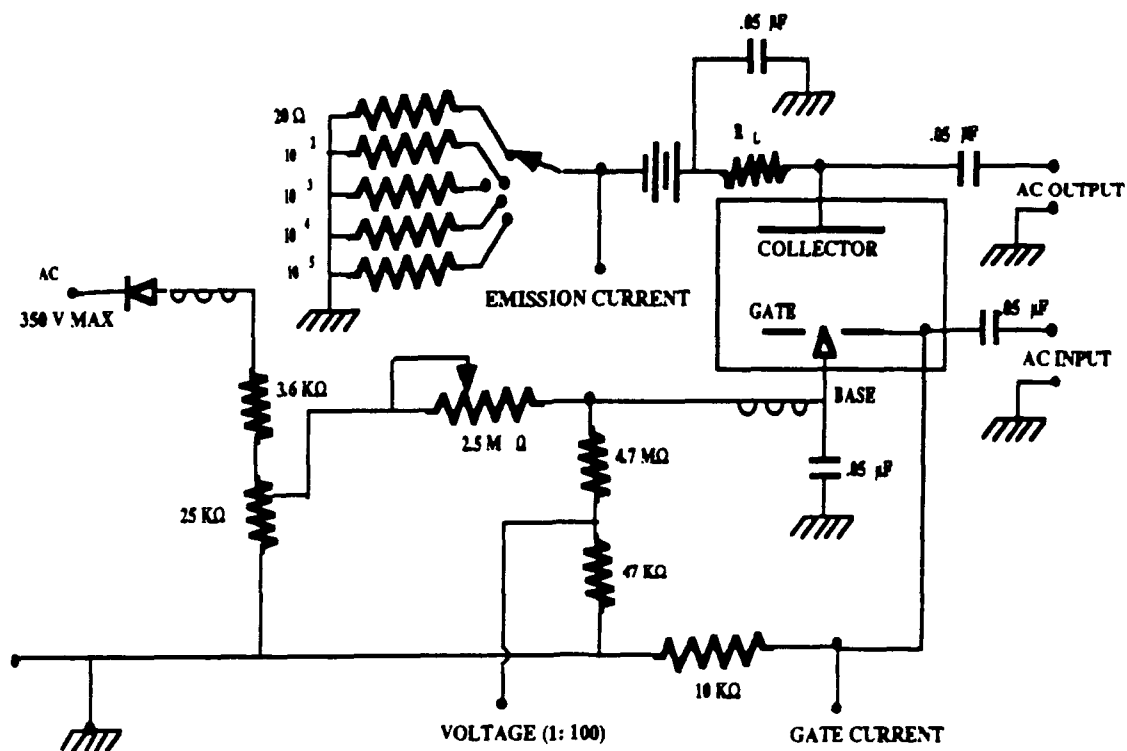


Fig. 10 Schematic of the Circuit Diagram

REFERENCES

- ¹J.R. Pierce and W.B. Hebenstreit, *Bell Syst. Tech. J.* **28**, 33 (1948).
- ²A.V. Haeff, *Proc. IRE* **37**, 4 (1949).
- ³P.M. Phillips, E.G. Zaidman, H.P. Freund, A.K. Ganguly, and N.R. Vanderplaats, *IEEE Trans. Electron Dev.* **37**, 870 (1990).
- ⁴K.L. Felch, K.O. Busby, R. Layman, and J.E. Walsh, *Appl. Phys. Lett.* **38**, 601 (1981).
- ⁵S. Von Laven, J. Branscum, J. Golub, R. Layman, and J.E. Walsh, *Appl. Phys. Lett.* **41**, 408 (1982).
- ⁶E.P. Garate, R. Cook, P. Heim, R. Layman, and J.E. Walsh, *J. Appl. Phys.* **58**, 627 (1985).
- ⁷W. Main, R. Cherry, and E.P. Garate, *Appl. Phys. Lett.* **55**, 1498 (1989).
- ⁸J.E. Walsh, C.H. Shaughnessy, R. Layman, G. Dattoli, G.P. Gallerano, and A. Renieri, *Nucl. Instrum. Meth. A* **272**, 132 (1988).
- ⁹W. Main, E.P. Garate, R. Cherry, and J. Weatherall, *Phys. Fluids* (submitted for publication).
- ¹⁰H.P. Freund and A.K. Ganguly, *Phys. Fluids B* **2**, 2506 (1990).
- ¹¹H.P. Freund, *Phys. Rev. Lett.* **65**, 2993 (1990).
- ¹²M.A. Allen et al., SLAC Publication Nos. 4801 and 5070 (1989).
- ¹³M. Friedman, J.A. Krall, Y.Y. Lau, and V. Serlin, *Rev. Sci. Instrum.* **61**, 171 (1990).
- ¹⁴D. Shiffler, J.A. Nation, and G. Kerslick, *IEEE Trans. Plasma Sci.* **18**, 546 (1990).
- ¹⁵Y. Carmel, K. Minami, R.A. Kehs, W.W. Destler, V.L. Granatstein, D. Abe, and W.L. Lou, *Phys. Rev. Lett.* **62**, 2389 (1989).
- ¹⁶A.K. Ganguly and H.P. Freund, *Phys. Rev. A* **32**, 2275 (1985).
- ¹⁷H.P. Freund and A.K. Ganguly, *Phys. Rev. A* **33**, 1060 (1986).
- ¹⁸H.P. Freund and A.K. Ganguly, *Phys. Rev. A* **34**, 1242 (1986).
- ¹⁹H.P. Freund and A.K. Ganguly, *J. Quantum Electron.* **QE-23**, 1657 (1987).
- ²⁰A.K. Ganguly and H.P. Freund, *IEEE Trans. Plasma Sci.* **16**, 167 (1988).
- ²¹A.K. Ganguly and H.P. Freund, *Phys. Fluids* **31**, 387 (1988).

- ²²H.P. Freund, H. Bluem, and C.L. Chang, *Phys. Rev. A* **36**, 2182 (1987).
- ²³H.P. Freund, C.L. Chang, and H. Bluem, *Phys. Rev. A* **36**, 3218 (1987).
- ²⁴H.P. Freund, *Phys. Rev. A* **37**, 3371 (1988).
- ²⁵D.A. Kirkpatrick, G. Bekefi, A.C. DiRienzo, H.P. Freund, and A.K. Ganguly, *Phys. Fluids* **B1**, 1511 (1989).
- ²⁶D.E. Pershing, R.H. Jackson, H.P. Freund, and H. Bluem, *Nucl. Instrum. Meth.* **A285**, 56 (1989).
- ²⁷D.E. Pershing, R.H. Jackson, H. Bluem, and H.P. Freund, *Nucl. Instrum. Meth.* **A296**, 199 (1990).
- ²⁸D.E. Pershing, R.H. Jackson, H. Bluem, and H.P. Freund, *Nucl. Instrum. Meth.* (to appear in 1991).
- ²⁹T.J. Orzechowski, B.R. Anderson, W.M. Fawley, D. Prosnitz, E.T. Scharlemann, S.M. Yarema, D.B. Hopkins, A.C. Paul, A.M. Sessler, and J.S. Wurtele, *Phys. Rev. Lett.* **54**, 889 (1985).
- ³⁰T.J. Orzechowski, B.R. Anderson, J.C. Clark, W.M. Fawley, A.C. Paul, D. Prosnitz, E.T. Scharlemann, S.M. Yarema, D.B. Hopkins, A.M. Sessler, and J.S. Wurtele, *Phys. Rev. Lett.* **57**, 2172 (1986).
- ³¹H.P. Freund, *Nucl. Instrum. Meth.* (to appear in 1991).
- ³²H. Bluem, H.P. Freund, and C.L. Chang, *Nucl. Instrum. Meth.* **A272**, 579 (1988).
- ³³H.P. Freund, H. Bluem, and R.H. Jackson, *Nucl. Instrum. Meth.* **A285**, 169 (1989).
- ³⁴K.R. Shoulders, in *Advances in Computers* (Academic Press, New York, 1961), vol. 2, p. 135.
- ³⁵A.K. Ganguly, P.M. Phillips, and H.F. Gray, *J. Appl. Phys.* **67**, 7098 (1990).
- ³⁶P.M. Phillips, S.T. Smith, and H.F. Gray, *Inst. Phys. Conf. Ser.* **99**, 211 (1989).
- ³⁷R.E. Neidert R. E., P.M. Phillips, S.T. Smith, and C.A. Spindt, *IEEE Trans Electron Dev.*, **38**, 661 (1991).
- ³⁸E.G. Zaidman, Private Communications.

APPENDIX I

Review of Two-Stream Amplifier Performance

by

P.M. Phillips, E.G. Zaidman, H.P. Freund, A.K. Ganguly, and N.R.
Vanderplaats

Review of Two-Stream Amplifier Performance

PUROBI M. PHILLIPS, ERNEST G. ZAIDMAN, HENRY P. FREUND, ACHINTYA K. GANGULY, AND NORMAN R. VANDERPLAATS, MEMBER, IEEE

Abstract—The basic concept of the two-stream instability and its application in building a microwave/millimeter-wave amplifier are reviewed from the perspective of the general usage of high-frequency devices. A historical review of the relevant literature is presented with additional discussion of unpublished laboratory notebooks from the Naval Research Laboratory. A summary of the theoretical background and its extension to the bounded three-dimensional case is given along with results from one-dimensional nonlinear particle simulation which is compared to nonlinear theory. The advantages, limitations, and shortcomings of a two-stream amplifier are discussed in comparison to other currently available devices that work in the same range of parameters.

1. INTRODUCTION AND HISTORICAL REVIEW

IN the past several years microwave/millimeter-wave technology has advanced significantly due to new requirements for sensors and communications links. Microwave systems are better than optical and infrared systems for penetration of smokes, fog, dust, and similar adverse environments. The advancement includes sources which provide high output power at higher frequencies and usually offer higher lifetimes and reliability. Applications of these systems cover wide areas, for example, communications, radar, radiometry, radio astronomy, spectroscopy, medical research, and plasma diagnostics.

We have reviewed the two-stream amplifier (TSA) as a candidate for a compact high-power/short-wavelength source that requires relatively low beam energies. The TSA is based upon the electron-electron two-stream instability. For a strong interaction the two beams must be in close proximity to each other. This instability is known to be characterized both by an extremely high growth rate and an exceptionally broad bandwidth. For these reasons, interest in the TSA is longstanding. The project was considered by several groups during the period 1949–1959. In 1949, Pierce and Hebenstreit [1] developed a one-dimensional linear theory for a TSA and presented some normalized design curves. Their conceptual device is shown in Fig. 1, and it consisted of an input coupler (to inject a signal), a drift region for the electrostatic interaction, and an output coupler to convert the electrostatic

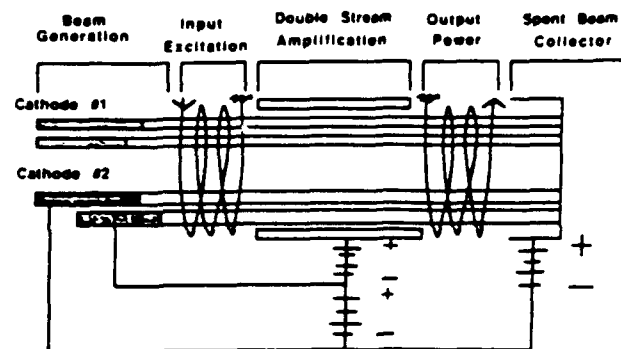


Fig. 1 Two-stream amplifier.

energy into electromagnetic energy for extraction. The theory shows a very promising device with high gain and broad bandwidth that depends mainly on a velocity separation parameter $b = 2(u_1 - u_2)/(u_1 + u_2)$ where u_1 and u_2 are the dc velocities of the two beams. Pierce [2] also discussed the effects of separation between the two beams on the gain, and considered the gap coupling for the input and output. He introduced a coupling parameter S which varied from 0 (coincident beams) to 1 (uncoupled/infinately remote beams). Some normalized design curves were given for various values of S .

Nergaard [3] presented a one-dimensional mathematical model of a two-beam tube. For a tube of 30 cm in length his model showed a gain of 120 dB at 3 GHz with a bandwidth of 0.9 GHz. Substitution of parametric numbers in his model shows that for realizable current densities ($\leq 100 \text{ A}/(\text{cm})^2$) the ratio of two beam voltages cannot be greater than 2. Since in a two-stream interaction the slower beam gains energy at the expense of the faster one, the maximum available output energy is at most this energy difference and this limits the efficiency of a TSA.

At Bell Laboratories, Hollenberg [4] performed an experiment using a helix as an input cavity, and tried both helix and gap output. He operated at 200 MHz and reported a gain of the order of 29 dB with a bandwidth of about 43 percent. The beam voltages were 54 V and 33 V. The current in each beam was 1.1 mA. Maximum output power was 0.3 mW. For a gap output the maximum power obtained was 0.1 mW.

Haefl *et al.* [5] performed an experiment at NRL with a 3-GHz frequency and a total current of 15 mA using a helix as output coupler. He obtained a total gain of 46 dB. His publication shows details of the electron gun assembly and other experimental arrangements. Recently a con-

Manuscript received February 28, 1989; revised September 18, 1989. The review of this paper was arranged by Associate Editor R. True.

P. M. Phillips and H. P. Freund are with Science Applications International Corporation, McLean, VA 22102.

E. G. Zaidman, A. K. Ganguly, and N. R. Vanderplaats are with Vacuum Electronics Branch, Electronics Science and Technology Division, Naval Research Laboratory, Washington, DC 20375.

IEEE Log Number 8931935.

siderable amount of data from these experiments has been recovered from old laboratory books at NRL (dated 1949–1951). These experiments were performed by Haeff [6] *et al.* The unpublished work includes a considerable amount of experimental data and device designs. A series of experiments were performed using coupled cavities as output and input coupling devices. The aim was to generate higher output power at the expense of the bandwidth. The length of the drift tube was varied from 6 to $13\frac{1}{2}$ in. The resonator voltage (V_{tr}) was changed from 800 V to 3.5 kV keeping I_{k1} and I_{k2} fixed. The gain varied from 15 to 24 dB and the results are shown in Fig. 2. In order to increase the gain a new tube with a lower transit time was constructed. They also tried to operate the tube as a self-excited oscillator and found 1.802 W of output power with $(V_1 - V_2) = 335$ V. The voltage of resonator 1 was 2 kV and the currents were 100 and 150 mA. Fig. 3 demonstrates the effect of velocity separation on the gain and the presence of an optimum value of this parameter. The best result was obtained using a tuning stub at the output. For a frequency of 3 GHz, collector current ($I_{k1} + I_{k2}$) of 160 mA, beam voltages 1.12 and 1.59 kV, the output power was 6.3 W and the corresponding efficiency was 2.5 percent.

In 1958, Bemashevskii *et al.* [7] published the result of an experiment that was carried out in the Institute of Radio Engineering and Electronics of the Academy of Sciences of the U.S.S.R. In their electron gun, a portion of the electrons of the faster stream was used to heat the cathode supplying the slower stream. It produced an intermixed beam and provided stable operation. Fig. 4, taken from [7], shows that for strong interaction (large K) the two beams have to be very well mixed. Although the design details were not given, they used tapered helices of different lengths as input and output devices. The maximum gain was 46 dB at 3 GHz with voltages 1.55 and 1.1 kV and current density $153 \text{ mA}/(\text{cm})^2$, which gives an efficiency of 4.72 percent.

The basic small-signal theory and the intended experimental parameters are discussed in Section II. In Section III, the results of a one-dimensional particle simulation are presented. Section IV contains the detailed conclusions.

II. LINEAR THEORY

The small-signal theory for a TSA with two mixed beams but no outer conducting wall has been presented many times in the past [1]–[3], [5] but a complete numerical solution for a three-dimensional case with a surrounding conducting wall has, to our knowledge, never been done. A cylindrical waveguide of radius a with the dominant TM_{01} mode is considered (Fig. 5). The copropagating electron beams are assumed to be well mixed with radius b and the direction of propagation is denoted by \hat{z} . Since it is customary to isolate the RF by terminators at the input and output boundaries, the interaction region is considered separately.

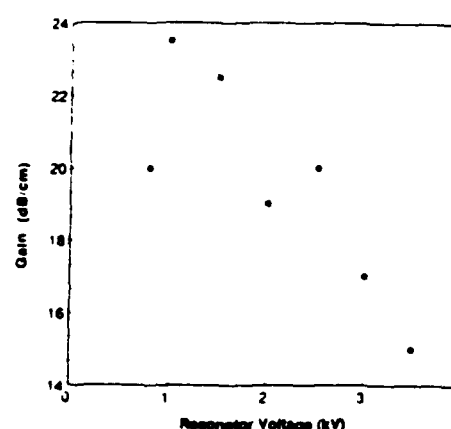


Fig. 2. Variation of gain with the resonator voltage. (Data taken from [14].)

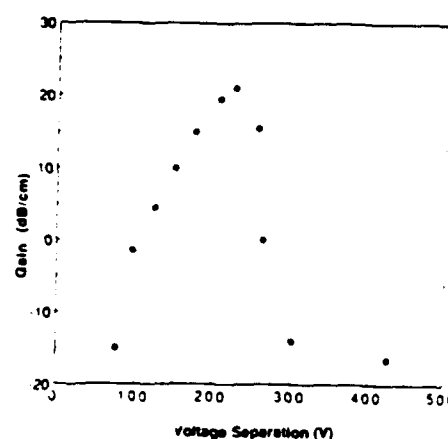


Fig. 3. Effect of voltage separation on the gain. $V_1 = 975$ V, $V_2 = 800$ V, $I_1 = 90$ mA, $I_2 = 60$ mA. (Data taken from [15].)

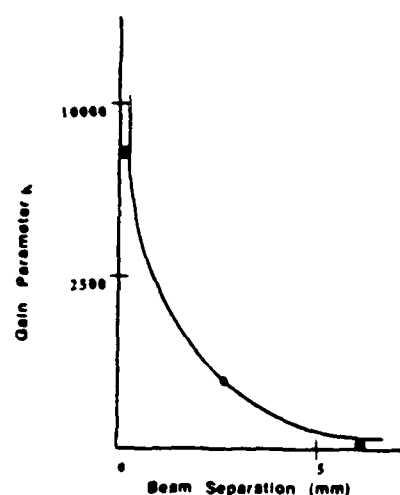


Fig. 4. Effect of beam separation on the gain. Experimental points and the theoretical curve are shown (taken from [7]).

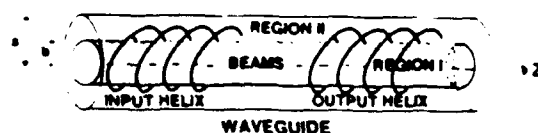


Fig. 5. Basic configuration

In region I ($0 \leq r \leq b$) the fields can be written as (in S.I. units):

$$E_{zI} = A I_0(\Gamma r) e^{i(\omega t - \beta z)}$$

$$E_{rI} = \frac{i\beta\Gamma}{\alpha^2} A I_1(\Gamma r) e^{i(\omega t - \beta z)}$$

$$H_{\theta I} = \frac{i\omega\epsilon_0}{\alpha^2} \Gamma A I_1(\Gamma r) e^{i(\omega t - \beta z)}$$

where I_0 and I_1 are the modified Bessel functions, $\Gamma^2 = (\beta^2 - k^2)L = \alpha^2 L$, and $k = \omega/c$. For the two-beam case chosen [1]

$$L = 1 - \frac{W_1^2 B_1^2}{\gamma_1^{(0)2} (B_1 - Z)^2} - \frac{W_2^2 B_2^2}{\gamma_2^{(0)2} (B_2 - Z)^2}$$

with

$$W_j = \frac{\omega_{pj}}{\omega}$$

$$B_j = \frac{\beta_j}{\beta_{0b}}$$

$$\beta_{0b} = \frac{1}{2} (\beta_{1b} + \beta_{2b})$$

$$Z = \frac{\beta}{\beta_{0b}}$$

where ω_{pj} is the plasma frequency of the j th beam ($j = 1, 2$). $\beta_{jb} = (\omega/u_j)$ is the propagation constant of the j th beam and u_j is the dc velocity of the j th beam. The zero-order relativistic factor is denoted by

$$\gamma_j^{(0)} = \frac{1}{\sqrt{1 - (u_j/c)^2}}$$

In region II ($b < r \leq a$) the electromagnetic fields are:

$$E_{zII} = [C I_0(\alpha r) + D K_0(\alpha r)] e^{i(\omega t - \beta z)}$$

$$E_{rII} = \frac{i\beta}{\alpha} [C I_1(\alpha r) - D K_1(\alpha r)] e^{i(\omega t - \beta z)}$$

$$H_{\theta II} = \frac{i\omega\epsilon_0}{\alpha} [C I_1(\alpha r) - D K_1(\alpha r)] e^{i(\omega t - \beta z)}$$

The three independent boundary conditions are

$$E_{zII} = 0 \quad \text{at } r = a$$

$$E_{zI} = E_{zII} \quad \text{at } r = b$$

$$H_{\theta I} = H_{\theta II} \quad \text{at } r = b.$$

Using these boundary conditions the dispersion relation for the system is

$$\begin{aligned} & \sqrt{L} I_1(\Gamma b) \left[K_0(\alpha b) - I_0(\alpha b) \frac{K_0(\alpha a)}{I_0(\alpha a)} \right] \\ & + I_0(\Gamma b) \left[K_1(\alpha b) + I_1(\alpha b) \frac{K_0(\alpha a)}{I_0(\alpha a)} \right] = 0. \end{aligned}$$

Note that as $a \rightarrow \infty$, $I_0(\alpha a) \rightarrow \infty$, and $K_0(\alpha a) \rightarrow 0$, the dispersion relation reduces to the well known one:

$$\sqrt{L} I_1(\Gamma b) K_0(\alpha b) + K_1(\alpha b) I_0(\Gamma b) = 0.$$

Since the normalized design curves for the unbounded case can be found in [1] and [2] we will present more quantitative graphs with some practically realizable parameters. Based on the information found from the past works [3], we have chosen the following parameters to study:

$$V_1 = 18 \text{ kV}$$

$$V_2 = 10 \text{ kV}$$

$$J_1 = J_2 = 80 \text{ A/(cm)}^2.$$

Fig. 6 shows gain in decibels per centimeter as a function of frequency for this limiting (i.e., one-dimensional) case as well as for various values of b . Curves (a), (b), (c), and (d) correspond to $b = 0.025, 0.035, 0.05$, and 0.075 in, respectively, and represent four practical values for the parameter b . Curve (e) represents the one-dimensional case. In order to have 80 A/(cm)^2 current densities, the required currents are 1, 2, 4, and 9 A, respectively. The bandwidth as well as gain decrease rapidly as the beam radius decreases. In Fig. 7 we see the effect of the outer conductor on the gain for a constant ratio of the conductor to the beam radii ($a/b = 4$) for various values of the beam radius keeping the current density at 80 A/(cm)^2 . The effect of the conducting wall becomes prominent only when the beam radius is small. It can be shown that even for a small beam radius, the effect of the wall becomes small as the ratio (a/b) increases (i.e., as the outer conductor becomes remote). Fig. 8 shows the effect of the voltage ratio V_1/V_2 upon gain. For $V_1 = 18 \text{ kV}$, the voltage ratio was varied from 1.8 to 1.3 for $b = 0.025$ in. The difference in gain becomes prominent as we go toward higher frequencies. Thus, the voltage ratio for an experiment should be chosen depending on the operating frequency. Fig. 9 supports the fact that for the same voltage ratio, the gain and bandwidth increase with decrease in the value of the higher voltage. Although Figs. 8 and 9 show increase in gain and bandwidth with decrease in V_1/V_2 , this trend does not continue for long. As V_1/V_2 approaches unity, the gain drops off rapidly and Fig. 10 shows this along with the fact that for every frequency there is an optimum value of the voltage ratio V_1/V_2 at which the gain is maximum.

III. NONLINEAR ANALYSIS

It is well known that the linear theory of two stream instability offers high gain and broad bandwidth. Pierce's theory shows that the distance between the beams has to be very small (i.e., they have to be intermixed) for a strong interaction, and this has been supported by the Russian experiment [7]. This requirement becomes more severe as the frequency increases from the microwave to the millimeter-wave regime. However, linear theory does not give any quantitative information about the saturation

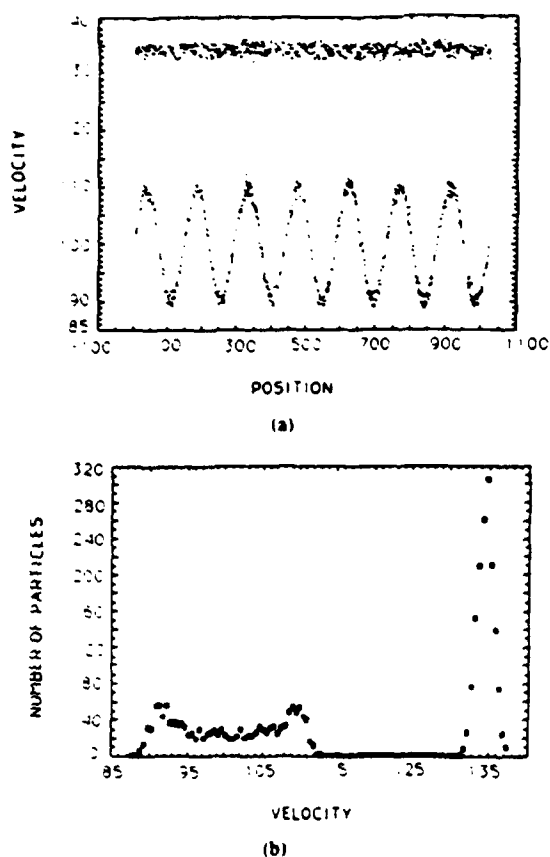


Fig. 11. At time = 0, both beams have the same thermal spread and the slower beam has the RF imposed. (a) Velocity-position phase space. (b) Velocity distribution function.

saturates quickly and although it produces a bunched beam, the quality of bunching is not very good in the sense that a large phase space area is filled. Fig. 15 shows that at the driving frequency (10 GHz), the ratio of ac to dc current modulation is about 55 percent. This corresponds with the result obtained by Filimonov [8], [9]. Another result for this parameter was obtained earlier by Rowe [12]. He used a simplified theory of the interaction based upon the analysis of space charge waves in a klystron (Beck [13]) and obtained an estimate of 88 percent for the maximum value of this ratio. The efficiency in klystron-like devices is related to the ratio of ac to dc electron velocity, and quite high efficiencies are found when this ratio approaches 60 percent. Considering only the ratio of ac to dc current modulation one would naively expect high efficiencies in TSA as well; however, the experimentally found efficiencies were always less than 5 percent.

In order to explain the low observed efficiencies we take note that the TSA operates as a prebuncher for the output helix stage. Thus, the device is essentially a helix TWT with enhanced bunching due to the two-stream interaction. There is an optimum point at which the output helix should be located relative to the bunching caused by the TSA section. If the helix begins at a point further downstream, the interaction should be degraded because the beam will overbunch and thermalize due to the continuation of the nonlinear phase of the two-stream interac-

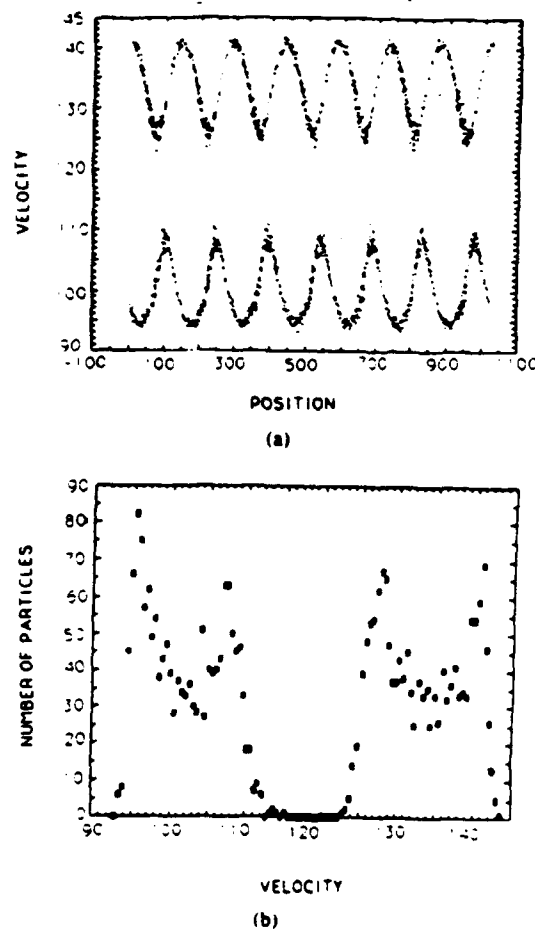
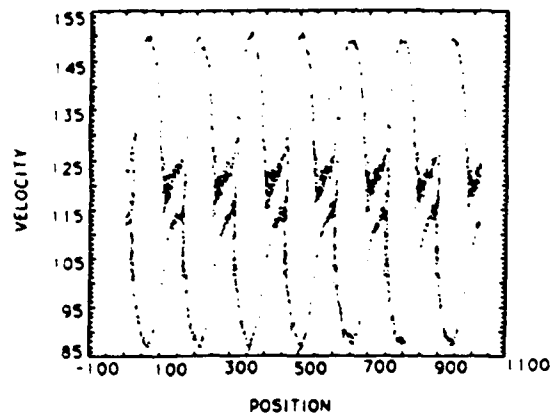


Fig. 12. At time = $3\omega_p^{-1}$ the growth of the wave in the fast beam is shown. (a) Velocity-position phase space. (b) Velocity distribution function.

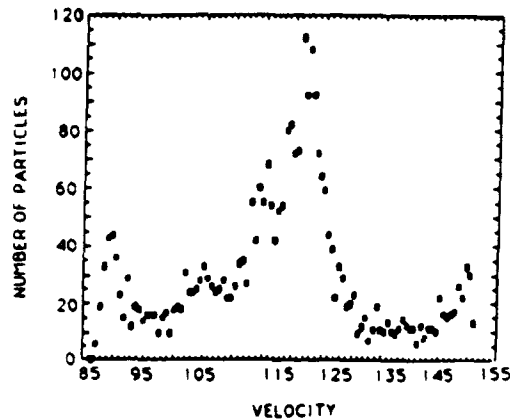
tion. In the event that the helix begins at a point prior to the optimum location, one must consider the TWT in the presence of two electron streams. In this case, Rowe's nonlinear theory of a TWT with two cold beams shows that for Pierce's gain parameter C of approximately 0.1 (which is a practical maximum), the maximum output efficiency is about 5 percent with warm beams degrading the performance still further. The thermal effect is potentially disastrous even when the output stage is optimally located. In order to estimate the maximum thermal spread Δv that can be tolerated, we observe that if $k\Delta v > |\omega - kv|$ then the assumption of a cold beam can no longer be made. This implies that the ratio of the velocity spread to the bulk velocity of the beams must be less than the ratio of the gain to the wavenumber for a cold beam. For a TWT the ratio of $\text{Im}(k)$ to $\text{Re}(k)$ is

$$\frac{\text{Im}(k)}{\text{Re}(k)} = \frac{\sqrt{3}C}{2 + C}$$

Therefore, when $C = 0.1$, the maximum thermal spread that can be tolerated for a cold beam is $\Delta v/v = 8.2$ percent. For the particular case studied, the aggregate of the two beams at the saturation point for the two-stream interaction indicates that $\Delta v/v$ is a substantial fraction of

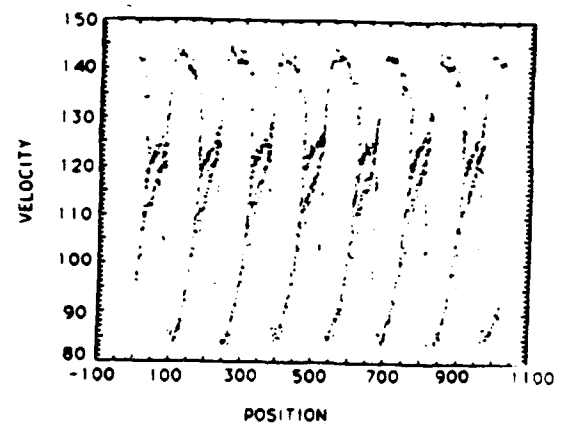


(a)

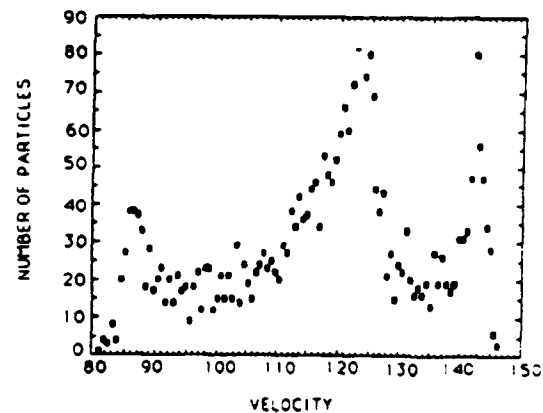


(b)

Fig. 13. At time $= 6\omega_p^{-1}$ the nonlinear beam-beam coupling and the thermalization of the distribution is illustrated. (a) Velocity-position phase space. (b) Velocity distribution function.



(a)



(b)

Fig. 14. At time $= 9\omega_p^{-1}$ the continued nonlinear development of the system and the degradation in harmonic and thermal content of the system is shown. (a) Velocity-position phase space. (b) Velocity distribution function.

the initial velocity separation between the beams and was approximately 20 percent. Thus it can be concluded that a major difficulty in the design and operation of the TSA is thermal degradation of the beam. This is exacerbated by the fact that the TSA has a broad-band character and a wide spectrum of waves is excited which will lead to an even more rapid thermalization of the beam.

IV. SUMMARY AND DISCUSSIONS

Since the TSA is inherently a high gain device, the length of the overall device can be expected to be shorter than that of a helix TWTA. However, the output efficiency will be sensitive to the precise length also. Too long an interaction region will overbunch the beams, while too short an interaction region will underbunch the beams in comparison to a helix output stage.

The TSA is also a broad-band device. However, the bandwidth of the configuration ultimately chosen would involve a helix output stage which limits the bandwidth of the overall device to that defined by the helix. Thus there seems to be no advantage to be gained in bandwidth by going to a TSA instead of a helix TWTA. The choice of a cavity coupler as an output stage might result in a higher output efficiency than a helix, but it would be lim-

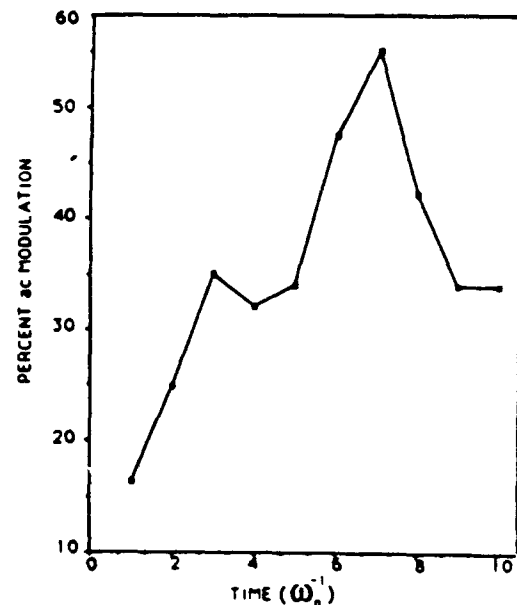


Fig. 15. The percent ac modulation at the driving frequency (10 GHz) peaks near 55 percent when competing modes have grown to significance.

ited to an application which involves a narrow bandwidth. In addition, the bandwidth will also be sensitive to the length of the TSA region, since the required optimum length will vary with the frequency.

Although the high gain of the TSA concept confers the advantage of being relatively less sensitive to thermal effects, the crucial limitation occurs due to the thermal spread of the bunched electron beams. This thermal spread is found to be comparable to the velocity difference between the two beams, which is a large number in itself. Thus, although the TSA interaction can tolerate a relatively large thermal spread, it will produce a bunched beam of relatively large thermal spread as well, which will seriously degrade the efficiency of the output stage.

Most importantly, the TSA imposes a severe constraint on the electron gun design. The generation of two well-mixed high-current-density cold beams is not a routine operation at this time.

An additional problem is that the helix output stage is separated from the TSA interaction region by a terminator which cuts off the electromagnetic modes from this region. However, the TSA interaction is electrostatic in nature, and will not terminate at the boundary to the helix output stage. Thus, the two-stream interaction will continue simultaneously with the interaction of the bunched beams and the helix. This can be expected to result in a further increase in the thermal spread of the beams and a degradation of the efficiency.

Backward wave oscillation is a common problem associated with TWT's. This problem is also expected in a TSA since the output stage is a TWT. If the length of the output device is small enough, this problem will not arise. As discussed before, the output device should be introduced to the beam prior to the saturation point of the two-stream interaction, and the beam that enters into the output device is not very tightly bunched. Even if we neglect the thermal spread completely, it seems clear that the output device must be long enough to support a traveling-wave interaction to get reasonably good output power and efficiency. Thus, the TSA does not necessarily eliminate the problem of backward wave oscillations.

The general conclusions that can be reached concerning the TSA are that it is an inherently high gain but low efficiency device. In addition, the TSA appears to present no unambiguous advantages over such competitive microwave sources such as the helix TWTA.

ACKNOWLEDGMENT

The authors gratefully acknowledge many helpful discussions with former NRL researcher H. Arnett, and also their colleagues, Dr. S. Y. Park and R. Kyser.

REFERENCES

- [1] J. R. Pierce and W. B. Hebenstreit, "A new type of high frequency amplifier," *Bell Syst. Tech. J.*, vol. 28, pp. 33-51, Jan. 1948.
- [2] J. R. Pierce, "Double-stream amplifiers," *Proc. IRE*, vol. 37, pp. 980-985, Sept. 1949.
- [3] L. S. Nergaard, "Analysis of a simple model of a growing-wave tube," *RCR Rev.*, vol. 9, pp. 585-601, Dec. 1948.
- [4] A. V. Hollenberg, "Experimental observation of amplification by interaction between two electron streams," *Bell Syst. Tech. J.*, vol. 28, pp. 52-58, Jan. 1949.
- [5] A. V. Haeff, "The electron-wave tube—A novel method for generation and amplification of microwave energy," *Proc. IRE*, vol. 37, pp. 4-10, Jan. 1949.
- [6] A. V. Haeff, unpublished works, 1949-1951.
- [7] G. A. Bernashevskii, P. S. Voronov, T. I. Izumova, and Z. S. Chernov, "The experimental investigation of double-beam electron-wave systems," *Radiotekh. Elektron.*, vol. 4, pp. 165-172, Sept. 1949.
- [8] G. F. Filimonov, "The nonlinear theory of the two-beam electron tubes. Part I. Deduction and investigation of equations," *Radiotekh. Elektron.*, vol. 4, no. 3, pp. 197-209, 1959.
- [9] G. F. Filimonov, "Nonlinear theory of double-beam electron tubes. Part II. Results of the calculations," *Radiotekh. Elektron.*, vol. 4, no. 5, pp. 141-153, 1959.
- [10] C. K. Birdsall, Ph.D. dissertation, Stanford Univ., Stanford, CA, Stanford Electron. Res. Lab. Rep. 36, June 1951.
- [11] C. K. Birdsall and A. B. Langdon, *Plasma Physics via Computer Simulation*. New York: McGraw-Hill, 1985.
- [12] J. E. Rowe, *Nonlinear Electron-Wave Interaction Phenomena*. New York: Academic, 1965.
- [13] A. H. W. Beck, *Space-Charge Waves*. New York: Pergamon, 1958.
- [14] Laboratory book, Naval Res. Lab., Washington, DC, 1950.
- [15] Laboratory book, Naval Res. Lab., Washington, DC, 1949.



Purobi M. Phillips was born in India on April 19, 1961. She received the B.Sc. degree in physics from Presidency College, Calcutta, India, in 1983, and the A.M. and Ph.D. degrees in physics from Dartmouth College in 1985 and 1987, respectively.

Since 1987 she has been a Research Scientist with Science Applications International Corporation's Plasma Physics division where she is assigned to work in the Electronics Science and Technology Division of the Naval Research Laboratory. Her current research area is vacuum microelectronics.



Ernest G. Zaidman was born in Tampa, FL, on November 15, 1954. He received the B.S. and M.A. degrees in physics from the University of South Florida in 1975 and 1979, respectively, and the Ph.D. degree in physics from the University of Texas at Austin in 1986.

He has been employed as a Research Scientist in the development of mapping and data interpolation software at Zycore, Inc., from 1980 to 1982. He is currently at the Naval Research Laboratory. His current field of interest is the development and application of computer simulation codes for the study of microwave devices.



Henry P. Freund was born in New York, NY, on May 23, 1949. He received the B.S. degree in physics from Rensselaer Polytechnic Institute, Troy, NY, in 1971, and the Ph.D. degree in physics from the University of Maryland, College Park, in 1976.

After graduation he spent a year as a Research Fellow at the Institute for Physical Sciences and Technology, the University of Maryland, and two years as a National Research Council-Naval Research Laboratory Postdoctoral Research Associ-

ate. His current research is devoted primarily to free-electron lasers at the Naval Research Laboratory. At present, he is with the Plasma Physics Division, Science Applications International Corporation, McLean, VA.

tion by interaction of relativistic electron beam and electromagnetic radiation in devices such as the gyrotron and ubitron/FEL.

•

Achintya K. Ganguly received the Ph.D. degree in physics from New York University, New York, NY, in 1965.

At New York University (1965-1972), he worked on the theory of light scattering from quasi-particles in solids. From 1967 to 1972, he was a staff member at GTE Laboratories and worked on electron-phonon interaction in solids and surface acoustic wave propagation in piezoelectric materials. He joined the Naval Research Laboratory in 1972 as a Research Physicist. At NRL, he worked on magnetostatic and magnetoelastic surface wave propagation and cyclotron resonance in a 2-D electron gas system. At present, he is working on problems related to high-power microwave genera-



Norman R. Vanderplaats (S'59-M'60) was born in Modesto, CA, on January 24, 1937. He received the B.S.E.E. degree from the University of California, Berkeley, in 1959 and the M.S.E.E. degree from Stanford University in 1964.

He was employed at Varian Associates from 1959 to 1967 and at Watkins-Johnson Company from 1967 to 1982, engaged in the development of various types of high-power microwave tubes. Since 1972 he has been employed at the Naval Research Laboratory, where he currently heads the

Slow-Wave Section in the Vacuum Electronics Branch. His research interests have remained focused primarily on high-power microwave and millimeter-wave sources.

APPENDIX II

Nonlinear Analysis of the Cerenkov Maser

by

H.P. Freund and A.K. Ganguly

The vacuum mode influences the choice of the coefficients in Eqs. (1)–(4), where J_n and Y_n represent the regular Bessel and Neumann functions, I_n denotes the modified Bessel function of the first kind, and

$$\begin{aligned} a_n &= (\pi/2)\kappa'_n R_d \left[(\kappa'_n/\epsilon\kappa_n) I_1(\kappa_n R_d) Y_0(\kappa'_n R_d) \right. \\ &\quad \left. - I_0(\kappa_n R_d) Y_1(\kappa'_n R_d) \right], \\ b_n &= -(\pi/2)\kappa'_n R_d \left[(\kappa'_n/\epsilon\kappa_n) I_1(\kappa_n R_d) J_0(\kappa'_n R_d) \right. \\ &\quad \left. - I_0(\kappa_n R_d) J_1(\kappa'_n R_d) \right]. \end{aligned} \quad (6)$$

Both κ_n and κ'_n are analogs of the cutoff wave numbers and are defined by

$$\omega^2/c^2 = k_n^2 - \kappa_n^2 \quad (7)$$

in the vacuum and

$$\epsilon(\omega^2/c^2) = k_n^2 + \kappa_n'^2 \quad (8)$$

in the dielectric. It should be remarked that the choice of k_n denotes the vacuum value, which, under the present assumptions, is the initial condition for the wave number. The vacuum dispersion equation¹⁻⁵ for this configuration is

$$\begin{aligned} &\frac{I_1(\kappa_n R_d)}{I_0(\kappa_n R_d)} - \frac{\epsilon\kappa_n}{\kappa'_n} \\ &\times \frac{Y_0(\kappa'_n R_d) J_1(\kappa_n R_d) - J_0(\kappa'_n R_d) Y_1(\kappa_n R_d)}{Y_0(\kappa'_n R_d) J_0(\kappa_n R_d) - J_0(\kappa'_n R_d) Y_0(\kappa_n R_d)} = 0, \end{aligned} \quad (9)$$

which, in combination with Eqs. (7) and (8), relates ω and k_n . Equivalently, one can assume that Eqs. (7), (8), and (9) constitute a set of three equations that permit solution of any three of the quartet $(\omega, k_n, \kappa_n, \kappa'_n)$ in terms of the fourth. Typical dispersion curves for (ω, k_n) are shown in Fig. 2. In contrast with the cutoff wave numbers in simple cylindrical waveguides, the solutions for κ_n and κ'_n are not constants but vary with frequency and wave number. This is illustrated in Fig. 3 in which we plot κ_n^2 vs k_n for the parameters used in Fig. 2. Observe that $\kappa_n^2 < 0$ when the wave is supraluminous; however, the wave-particle interaction is not permitted in

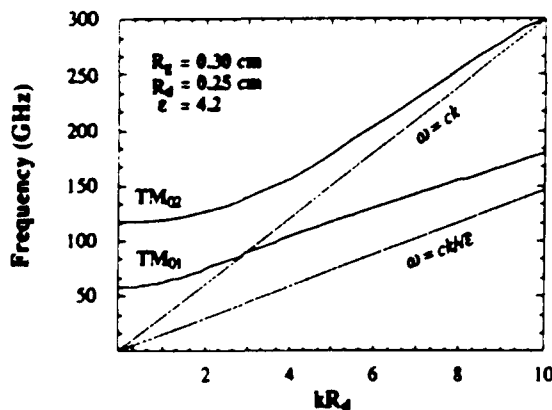


FIG. 2 Plot of the dispersion curves for the TM_{01} and TM_{02} modes in a boron-nitride lined waveguide.

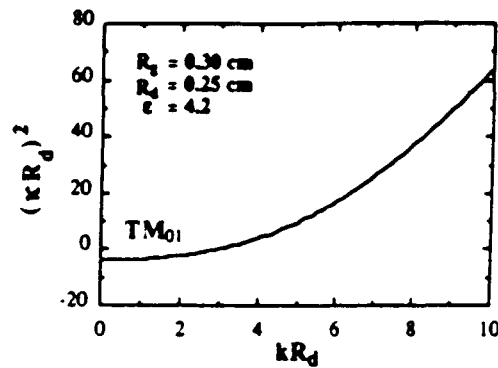


FIG. 3 Plot of the square of the cutoff wave number in vacuum.

this regime. As a consequence, we shall confine ourselves to consideration of the subluminal regime for which $\kappa_n^2 > 0$.

As mentioned previously, the amplitudes and wave numbers of the TM_{0n} modes are assumed to be slowly varying functions of z . In contrast, the cutoff wave numbers (κ_n, κ'_n) are characteristic of the transverse mode structure in the vacuum, and are assumed to be constant over the course of the interaction. Shifts in the transverse mode structure of the *total electromagnetic field* are described by variations in the relative values of the various mode amplitudes under consideration. The microscopic source current that drives the interaction can be written as the following sum over individual particle trajectories:

$$\begin{aligned} \delta \mathbf{J}(\mathbf{x}, t) &= -en_b \frac{L}{N_T} \sum_{i=1}^{N_T} \mathbf{v}_i(z, x_D, y_D, t_D, \mathbf{p}_0) \\ &\times \frac{\delta[t - \tau_i(z, x_D, y_D, t_D, \mathbf{p}_0)]}{|v_z(z, x_D, y_D, t_D, \mathbf{p}_0)|}, \end{aligned} \quad (10)$$

where L is the length of the interaction region, N_T is the total number of electrons, n_b is the average electron density, $\mathbf{v}_i(z, x_D, y_D, t_D, \mathbf{p}_0)$ is the velocity of the i th electron at position z , which entered the interaction region (i.e., crossed the $z = 0$ plane) at time t_D , transverse position (x_D, y_D) , and momentum \mathbf{p}_0 and

$$\tau_i(z, x_D, y_D, t_D, \mathbf{p}_0) = t_D + \int_0^z \frac{dz'}{|v_z(z'; x_D, y_D, t_D, \mathbf{p}_0)|}. \quad (11)$$

The system is assumed to be quasistatic in the sense that particles that enter the interaction region at times t_0 separated by integral multiples of a wave period will execute identical trajectories. This follows from our treatment of the system as a steady-state amplifier. As a result, $\mathbf{v}_i(z, x_D, y_D, t_D + 2\pi N/\omega) = \mathbf{v}_i(z, x_D, y_D, t_D)$ for integer N . The discrete sum over particles can be replaced by an integral over initial conditions, and we may rewrite (10) in the form

$$\begin{aligned} \delta J(\mathbf{x}, t) = & -en_b \iint d\mathbf{p}_0 v_{x0} F_0(\mathbf{p}_0) \\ & \times \int_{A_b} dx_0 dy_0 \sigma_1(x_0 y_0) \int_{-T/2}^{T/2} dt_0 \sigma_1(t_0) \\ & \times \nabla(z, x_0 y_0, t_0, \mathbf{p}_0) \delta[\mathbf{x}_1 - \mathbf{x}_1(z, x_0 y_0, t_0, \mathbf{p}_0)] \\ & \times \frac{\delta[t - \tau(z, x_0 y_0, t_0, \mathbf{p}_0)]}{|v_z(z, x_0 y_0, t_0, \mathbf{p}_0)|}, \end{aligned} \quad (12)$$

where v_{x0} is the initial axial velocity, \mathbf{p}_0 is the initial momentum, A_b is the cross-sectional area of the waveguide, $T = L/v_{x0}$, and σ_1 , σ_1 , and F_0 describe the distribution of the initial conditions subject to the normalizations

$$\iint_{A_b} dx_0 dy_0 \sigma_1(x_0 y_0) = A_b, \quad (13)$$

$$\int_{-T/2}^{T/2} dt_0 \sigma_1(t_0) = T, \quad (14)$$

where A_b is the cross-sectional area of the beam, and

$$\iint d\mathbf{p}_0 F_0(\mathbf{p}_0) = 1. \quad (15)$$

The dynamical equations that govern the evolution of the slowly varying amplitude and phase are derived in the Appendix under the assumption that terms in the second-order derivatives of the amplitude and phase (i.e., observe that the wave number varies as the first derivative of the phase; hence terms in the derivative of k_n are neglected). We find that the dispersion of the mode in the presence of the electron beam is described by

$$\begin{aligned} \left(1 - \frac{\kappa_n^2}{k_n^2}\right) \left(\frac{\omega^2}{c^2} - k_n^2 + \kappa_n^2\right) \delta a_{0n} \\ = 2 \frac{\omega_b^2}{c^2} \frac{1}{A_n} \left\langle I_1(\kappa_n r) \frac{v_z}{|v_z|} \cos \alpha_n - \frac{\kappa_n}{k_n} I_0(\kappa_n r) \sin \alpha_n \right\rangle, \end{aligned} \quad (16)$$

where $\omega_b^2 \equiv 4\pi n_b e^2/m_e$ is the square of the beam plasma frequency and $\delta a_{0n} \equiv e\delta A_{0n}/m_e c$. Equation (16) describes an algebraic equation for the evolution of the wave number in terms of the dielectric effect of the beam. It is trivially satisfied in the limit in which the beam vanishes (i.e., $\omega_b = 0$) since $\omega^2/c^2 = k_n^2 - \kappa_n^2$ for each mode. The description of the amplification (or damping) of each mode is equivalent to a calculation of $\mathbf{J} \cdot \delta \mathbf{E}_{0n}$ for each mode and is given by

$$\begin{aligned} 2k_n \left(1 - \frac{\kappa_n^2}{k_n^2}\right) \frac{d}{dz} \delta a_{0n} = & -2 \frac{\omega_b^2}{c^2} \frac{1}{A_n} \left\langle I_1(\kappa_n r) \frac{v_z}{|v_z|} \sin \alpha_n \right. \\ & \left. + \frac{\kappa_n}{k_n} I_0(\kappa_n r) \cos \alpha_n \right\rangle, \end{aligned} \quad (17)$$

where

$$\begin{aligned} A_n \equiv & \frac{\epsilon - 1}{\epsilon} \left(I_1^2(\kappa_n R_d) - \frac{\epsilon k_n^2}{\kappa_n^2} I_0^2(\kappa_n R_d) \right. \\ & \left. + \frac{2}{\kappa_n R_d} \frac{\epsilon \omega^2}{c^2 \kappa_n^2} I_0(\kappa_n R_d) I_1(\kappa_n R_d) \right) \\ & + \frac{R_d^2}{R_d^2} \frac{\kappa_n^2}{\kappa_n^2} [a_n J_1(\kappa_n R_d) + b_n Y_1(\kappa_n R_d)]^2. \end{aligned} \quad (18)$$

It is clear from Eq. (17) that the derivative of the amplitude is zero when $\omega_b = 0$. Thus there is no amplification of the modes in the absence of the beam, and Eqs. (16) and (17) are reduced to the description of the propagation of the "bare" TM_{0n} modes.

The averaging operator in Eqs. (16) and (17) is defined over the initial conditions of the beam, and includes the effect of an initial momentum spread by means of the distribution function

$$\begin{aligned} F_0(\mathbf{p}_0) = & A \exp[-(\rho_{x0} - p_0)^2/\Delta p_x^2] \\ & \times \delta(\rho_0^2 - p_{x0}^2 - p_{y0}^2) H(p_{x0}), \end{aligned} \quad (19)$$

where p_0 and Δp_x describe the initial bulk momentum and momentum spread, $H(x)$ is the Heaviside function, and the normalization constant is

$$A \equiv \left[\pi \int_0^\infty dp_{x0} \exp\left(-\frac{(\rho_{x0} - p_0)^2}{\Delta p_x^2}\right) \right]^{-1}. \quad (20)$$

Observe that this distribution describes a beam that is monoenergetic but with a pitch-angle spread that is equivalent to an axial energy spread of

$$\Delta \gamma_x / \gamma_0 = 1 - 1/\sqrt{1 + 2(\gamma_0^2 - 1)(\Delta p_x/p_0)}. \quad (21)$$

where $\gamma_0 \equiv (1 + p_0^2/m_e^2 c^2)^{1/2}$. As a result, the averaging operator takes the form

$$\begin{aligned} \langle (\dots) \rangle \equiv & \frac{A}{2\pi R_d^2} \int_0^{2\pi} d\varphi_0 \int_0^\infty dp_{x0} \beta_{x0} \\ & \times \exp\left(-\frac{(\rho_{x0} - p_0)^2}{\Delta p_x^2}\right) \\ & \times \int_0^{2\pi} d\psi_0 \sigma_1(\psi_0) \int_0^{R_d} dr_0 r_0 \sigma_1(r_0) (\dots), \end{aligned} \quad (22)$$

where $\psi_0 (\equiv -\omega t_0)$ is the initial phase, $\varphi_0 \equiv \tan^{-1}(p_{y0}/p_{x0})$, $\beta_{x0} \equiv v_{x0}/c$, and $\sigma_1(\psi_0)$ and $\sigma_1(r_0)$ describe the initial beam distributions in phase and cross section. It should be remarked that (1) there is no average over the initial azimuthal distribution of the beam since the configuration has been assumed to be azimuthally symmetric, and (2) the radial variation is taken over the vacuum only (i.e., $r < R_d$) since electrons that intercept the dielectric are lost to the interaction.

It should be remarked that the average over the initial phase corresponds to inclusion of only a single *beamlet* of electrons that enter the interaction region within one wave period. The reason for this is illustrated by the behavior of the particle trajectories in a steady-state amplifier. In the absence of the electromagnetic field, all particles with the

same initial conditions execute identical trajectories. The presence of the electromagnetic field disrupts this, but imposes a periodicity upon the orbits based upon the entry time. Specifically, all other initial conditions being identical, particles that enter the interaction region with entry times separated by a wave period will also execute identical trajectories. Thus one need only describe the interaction of a single *beamlet*. This slow-time-scale formulation has been extensively applied to the analysis of gyrotrons and free-electron lasers and is amply described in the literature,¹⁵⁻²² and the implications of the quasistatic assumption are rigorously proved by Sprangle *et al.*¹⁵

The assumption of single frequency wave propagation and the subsequent average of Maxwell's equations over the wave period excludes harmonics of the fundamental interaction frequency from the treatment. However, harmonic interactions will, in general, occur because the source current will also oscillate at the harmonics of the injected signal. The harmonics can be included in a self-consistent manner for the case in which the wave is far from cutoff and the harmonics are commensurate with the frequency of the injected signal. However, the harmonic interaction must grow from noise on the beam, and we choose to ignore them in the present analysis under the assumption that the drive power of the injected signal overwhelms the harmonics. It is important to observe, however, that the harmonic interaction is implicitly included for the case in which the injected signal itself is at a harmonic.

While electrons that intercept the dielectric liner cease to be important to the interaction, the determination of the time-averaged Poynting flux for the TM modes requires the inclusion of the fields in the dielectric liner. Integrating over the entire cross section of the waveguide (i.e., $0 < r < R_g$), we find that the time-averaged power carried by the TM_{0n} mode is

$$P_{0n} = \left(\frac{m_e^2 c^5}{8e^2} \right) \frac{\omega k_n}{c} A_n \delta a_{0n}^2 R_d^2 \left(1 - \frac{\kappa_n^2}{k_n^2} \right). \quad (23)$$

The phase variation of the modes can be analyzed by the inclusion of an equation to integrate the phase relative to the phase of a wave *in vacuo* as follows:

$$\frac{d}{dz} \Phi_n(z) = k_n(z) - \sqrt{\frac{\omega^2}{c^2} + \kappa_n^2}. \quad (24)$$

Since the departure of $k_n(z)$ from the vacuum wave number describes the effect of the interaction, $\Phi_n(z)$ represents a measure of the dielectric effect of the beam.

Each mode will interact resonantly with the electron beam, and will be coupled through the collective response of the electrons to the bulk electromagnetic field. Therefore, in order to complete the formulation, the electron orbit equations must be specified as well. Since we are interested in amplifier configurations, we integrate in z and write the Lorentz force equations in the form

$$v_z \frac{d}{dz} \mathbf{p} = -e\delta\mathbf{E} - \frac{e}{c} \mathbf{v} \times (B_0 \hat{\mathbf{e}}_z + \delta\mathbf{B}), \quad (25)$$

where an axial guide magnetic field is included to provide for the confinement of the beam, and the electromagnetic field is given in Eqs. (1)–(4).

III. NUMERICAL ANALYSIS

The set of coupled nonlinear differential equations described in Sec. II is solved numerically for an amplifier configuration in which a single wave of frequency ω is launched into the interaction region in synchronism with the electron beam at $z = 0$. The algorithm employed is a fourth-order Runge-Kutta-Gill technique, and the particle averages in Eqs. (16) and (17) are performed by means of an n th-order Gaussian quadrature technique in each of the initial coordinates and momenta ($r_0, \psi_0, p_{z0}, \phi_0$). Note that the order of the Gaussian quadrature used to resolve each of these degrees of freedom need not be identical, and that the total number of electrons is given by the product of the orders of the Gaussian quadratures. The initial state was chosen to model the injection of an axisymmetric electron beam with a uniform cross section (i.e., a flat-topped beam), and the radial profile can be either solid or annular. Within the context of this beam geometry, the plasma frequency is related to the total beam I_b current by means of the relation

$$\omega_p^2 = (4e/\gamma_0^3 m_e v_{z0}) [I_b / (R_{\max}^2 - R_{\min}^2)], \quad (26)$$

where R_{\max} and R_{\min} denote the maximum and minimum radii of the electron at the start of the interaction. The explicit neglect of the beam space-charge modes from the formulation is valid as long as (1) $\omega_p \ll \omega$, and (2) the exponentiation time is much less than the period of the beam-plasma wave. These conditions are satisfied for the specific cases under consideration.

The first case that we consider is that of the propagation of an electron beam with an energy of 150 keV, a current of 8 A, and an initial radius of 0.24 cm through a boron nitride lined waveguide ($\epsilon = 4.2$) with $R_g = 0.3$ cm and $R_d = 0.25$ cm. The dispersion curves for the TM_{01} and TM_{02} modes in this system are shown in Fig. 2. The resonant frequencies for the wave-particle interaction are given by the intersections of the dispersion curves and the resonance line $\omega = kv_z$, which for the parameters of interest occur at frequencies in the range of 101–105 GHz in the TM_{01} mode. As is evident in the figure, the TM_{02} mode (as well as all higher-order modes) are cut off at these frequencies and do not interact with the beam. As a result, this system can be treated using only the TM_{01} mode in the analysis. This system has been described in an experiment by Garate *et al.*,⁴ and a detailed comparison will be given after the description of the theoretical results.

Typical results showing the amplification of a resonant wave are shown in Fig. 4, in which the evolution of the TM_{01} mode is illustrated as a function of axial position. This figure represents the launching of a 10 W signal at a frequency of 104 GHz in the case of the idealized limit of a beam with a vanishing energy spread. As seen in the figure, the growth of the wave is approximately exponential, and saturation occurs at a power of 26 kW. The detailed variation of the normalized growth rate $\Gamma_{01} R_d$ (where Γ_{0n} denotes the logarithmic derivative of δa_{0n}) with axial position is shown in Fig. 5. The growth of the signal is not purely exponential as the growth rate varies somewhat in z with fluctuations in the response of the beam to the wave, but an average growth rate of the order $\Gamma_{01} R_d \approx 0.08$ is observed.

TM₀₁ Mode ($R_1 = 0.3$ cm; $R_2 = 0.25$ cm; $\epsilon = 4.2$)

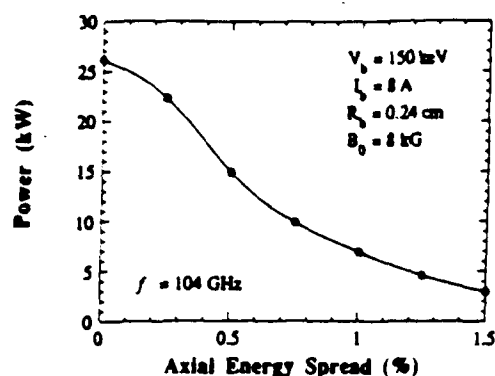


FIG. 8. Variation in the maximum output power as a function of beam energy spread corresponding to the frequency of maximum gain.

unstable gain band in the limit of a vanishing axial energy spread is chosen to be the reference point. This corresponds to a resonant energy of 150 keV and frequency of 102.4 GHz. At this frequency and beam energy, a 10 W input signal is found to reach saturation at $z/R_2 = 72$ and yield a power level of 19.2 kW and a relative phase of 211° . The phase stability of the device can be evaluated by allowing the beam energy to vary while holding all other parameters to be fixed and to observe the effect of these variations on the relative phase at a fixed point. Choosing this point to be the saturation point at 150 keV, we show the results of variations in beam voltage over the range of 140–160 keV in Fig. 11. As seen in the figure, the relative phase decreases with increasing beam energies between 142.5 and 160 keV at the rate of about $45^\circ/\text{keV}$. For purposes of comparison, this is of the order of the variation calculated for free-electron lasers operating in the millimeter/submillimeter regime.²⁵

As previously mentioned, a Cerenkov maser oscillator experiment has been conducted along these lines by Garate *et al.*⁴ that mirrors this system configuration and detailed parameters. Specifically, the experiment employed a boron-

TM₀₁ Mode ($R_1 = 0.3$ cm; $R_2 = 0.25$ cm; $\epsilon = 4.2$)

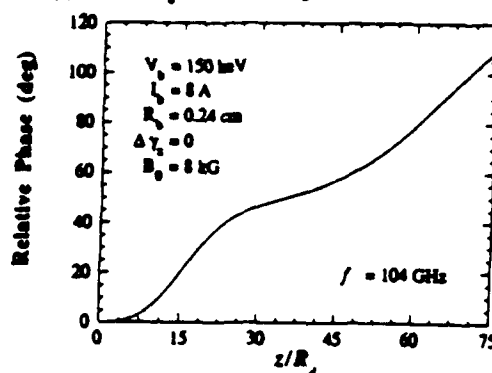


FIG. 10. Evolution of the relative phase versus axial position for an idealized beam with vanishing axial energy spread at the frequency corresponding to the peak saturation efficiency.

nitride-lined cylindrical waveguide and an electron beam with energies of as much as 300 keV and currents up to approximately 10 A over a pulse time of as much as 2 μsec . Further, it was found that an axial guide field was necessary to confine and propagate the beam, and an axial guide field of up to 8 kG was possible in the experiment. It should be remarked that the experimental results were insensitive to the magnitude of the axial guide field over the range of 2.5–8 kG, subject to the requirement of beam confinement, and that this same insensitivity to the magnetic field has been observed in the simulation. The comparison of the results of this oscillator experiment with the amplifier simulation described herein must be made under the assumption that, as a result of the short pulse time of the beam, the oscillator produced a narrow linewidth in the vicinity of the frequency of maximum gain. As such, we compare the output power at saturation found in simulation at the frequency of maximum growth rate with that seen in the experiment.

The first experimental case we consider corresponds to the parameters described previously, specifically, that of a 150 keV/8 A electron beam propagating through a boron-

TM₀₁ Mode ($R_1 = 0.3$ cm; $R_2 = 0.25$ cm; $\epsilon = 4.2$)

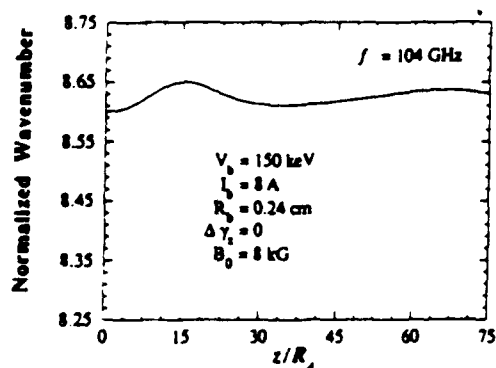


FIG. 9. Evolution of the wave number versus axial position for an idealized beam with vanishing axial energy spread at the frequency corresponding to the peak saturation efficiency.

TM₀₁ Mode ($R_1 = 0.3$ cm; $R_2 = 0.25$ cm; $\epsilon = 4.2$)

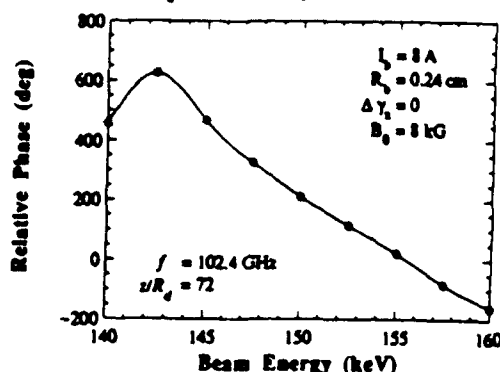


FIG. 11. Variation in the relative phase as a function of beam energy at $z/R_2 = 65$, which corresponds to saturation of the signal for a 150 keV beam.

nitride ($\epsilon = 4.2$) lined cylindrical waveguide ($R_s = 0.3$ cm and $R_d = 0.25$ cm). An output power of approximately 8 kW was observed in the experiment at frequencies above 98 GHz. It should be remarked that no more precise information is available on the frequency characteristics of the output since a 98 GHz high pass filter was used. Under the assumption that the radiation occurs in a narrow band about the frequency of peak gain (i.e., 104 GHz), then the predicted variation in the output power with $\Delta\gamma_s/\gamma_0$, as shown in Fig. 8, is consistent with the interpretation that the beam energy spread was of the order of 1.0–1.5%. No more precise association is possible because of uncertainties in the power measurement of up to several decibels.

A second experimental observation⁴ deals with the case of an electron beam energy and current of 180 keV and 10 A, respectively, and the boron-nitride-lined waveguide was of the dimensions $R_s = 0.24$ cm and $R_d = 0.29$ cm. An 80 GHz high pass filter was used in this case since the resonant frequency for a 180 keV beam in this waveguide occurs at about 93 GHz, and the observed output signal from the device was of the order of 20 kW. The peak frequency of peak gain found in simulation of this case was shifted somewhat from the vacuum resonance, and occurred at 95.6 GHz. The decrease in the output power as a function of axial energy spread calculated in simulation is shown in Fig. 12, which is consistent with the conclusion that $\Delta\gamma_s/\gamma_0 \approx 1.5\% - 2.0\%$. This energy spread is in reasonable agreement with that found with the 150 keV/8 A electron beam case, and no closer agreement is to be expected in view of the uncertainties previously mentioned in the power measurements.

IV. SUMMARY AND DISCUSSION

In this paper, a fully three-dimensional nonlinear analysis of the Cerenkov maser has been developed for a configuration in which an energetic electron beam propagates through a dielectric-lined cylindrical waveguide. The analysis has been performed subject to the assumption of azi-

muthal symmetry and includes a multimode analysis of the TM_{0n} modes of the vacuum waveguide. The overlap of the electron beam and the transverse structure of the modal superposition is included in a self-consistent manner, which implicitly includes the filling factor in the formulation. The electron trajectories are integrated using the Lorentz force equations with no *a priori* restrictions or approximations. In contrast, the analysis of an amplifier configuration permits the restriction to a single wave frequency, which allows Maxwell's equations to be averaged over a wave period. This eliminates the fast-time-scale phenomena from the formulation, and results in a major improvement in computational efficiency in relation to particle-in-cell techniques.

Numerical simulations were conducted for parameters corresponding to Cerenkov maser experiments conducted at Dartmouth College,⁴ which dealt with electron energies of 150 and 180 keV, currents of 8–10 A, and frequencies in the vicinity of 100 GHz in the TM_{01} mode. Note that the parameters used in this series of experiments and simulations ensure that a resonant wave-particle interaction is possible only with this mode. Although we have restricted the discussion to comparison with experiments, further results of the simulation indicate that output powers in the neighborhood of 90–110 kW should be possible for similar beams with higher currents (but still practical) and extremely low axial energy spreads. The output power was found, both in experiment and theory, to be relatively insensitive to the magnitude of the axial guide field as long as the field was strong enough to confine the electron beam. In addition, the output power was found to decrease rapidly with increasing energy spread to the point where the efficiency falls by roughly an order of magnitude for axial energy spreads of only a few percent. This sensitivity to the energy spread is consistent to within experimental uncertainties with the observed powers, which were found to be of the order of 8 kW (at 150 keV) and 20 kW (at 180 keV). Although the energy spread associated with the experiment was unknown, we take this as tentative confirmation that the actual energy spread in the experiment was in this range, which is consistent with the type of beams produced by the barium-oxide coated dispenser cathodes used in the experiment.

In view of the power levels found to be obtainable in simulation and the simplicity of the configuration, the Cerenkov maser is an attractive competitor for gyrotrons, free-electron lasers, and relativistic klystrons for a wide variety of applications. In particular the potentiality of producing single mode powers in excess of 100 kW at a frequency in the neighborhood of 100 GHz compares favorably with the most recent results obtained with advanced gyrotrons, which require operation in extremely high-order cavity modes and suffer from associated mode control problems. Recent studies on an S-band Cerenkov maser oscillator by Main *et al.*²⁶ produced approximately 200 MW at a frequency of 3.8 GHz. Furthermore, while free-electron lasers that operate in the far-infrared wavelengths have been constructed, they require relatively high energy beams and complex accelerators for their operation. The Cerenkov maser, in contrast, has the potentiality for operation in this spectral range with much lower energy electron beams.

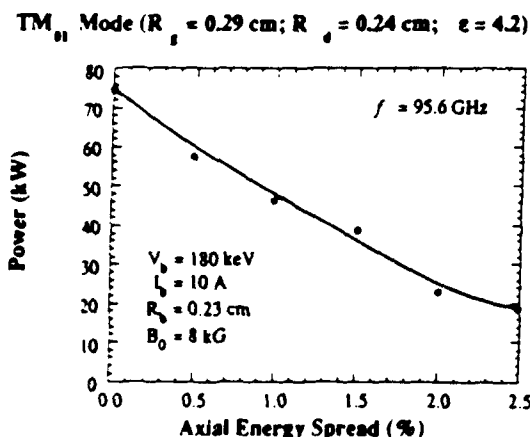


FIG. 12 Variation in the maximum output power as a function of beam energy spread corresponding to the frequency of maximum gain for a 180 keV beam

ACKNOWLEDGMENTS

The author would like to thank Dr. J. Walsh for stimulating and helpful discussions.

This work was supported by the Office of Naval Research and the Office of Naval Technology.

APPENDIX: THE DYNAMICAL EQUATIONS

The dynamical equations [Eqs. (16) and (17)] are obtained by substitution of the magnetic field from Eqs. (2) and (4) and the source current (12) into Maxwell's equations,

$$\left(\nabla^2 - \frac{\epsilon}{c^2} \frac{\partial^2}{\partial t^2}\right) \delta \mathbf{B} = -\frac{4\pi}{c} \nabla \times \delta \mathbf{J}. \quad (\text{A1})$$

We implicitly assume that the scalar potential associated with beam space-charge waves is negligible. This is valid as long as (1) the beam plasma frequency is much less than the resonant frequencies of interest, and (2) the exponentiation time of the instability is much shorter than the period of the beam-plasma waves.

Substitution of the magnetic field from Eqs. (2) and (4) into (A1) yields

$$\sum_{n=1}^{\infty} k_n \left(1 - \frac{\kappa_n^2}{k_n^2}\right) I_1(\kappa_n r) \left[\left(\frac{\omega^2}{c^2} - k_n^2 + \kappa_n^2 \right) \delta A_{0n} \sin \alpha_n + 2k_n \frac{d}{dz} \delta A_{0n} \cos \alpha_n \right] = \frac{4\pi}{c} \left(\frac{\partial}{\partial z} \delta J_r - \frac{\partial}{\partial r} \delta J_z \right), \quad (\text{A2})$$

within the vacuum for $0 < r < R_d$, and

$$\sum_{n=1}^{\infty} k_n \left(1 - \frac{\kappa_n^2}{k_n^2}\right) \frac{\epsilon \kappa_n}{\kappa_n'} [a_n J_1(\kappa_n' r) + b_n Y_1(\kappa_n' r)] \times \left[\left(\frac{\omega^2}{c^2} - k_n^2 + \kappa_n^2 \right) \delta A_{0n} \sin \alpha_n + 2k_n \frac{d}{dz} \delta A_{0n} \cos \alpha_n \right] = 0, \quad (\text{A3})$$

in the dielectric for $R_d < r < R_s$, where we have neglected second-order derivatives of the amplitude and phase, and made use of the identities $\omega^2/c^2 - k_n^2 + \kappa_n^2 = \epsilon \omega^2/c^2 - k_n^2 - \kappa_n'^2$ and $1 + \kappa_n'^2/k_n^2 = \epsilon(1 - \kappa_n^2/k_n^2)$. In addition, we have assumed that electrons are lost to the interaction after impact to the dielectric.

The radial variation of the magnetic field satisfies the orthogonality condition

$$\begin{aligned} \frac{1}{2} A_n R_d^2 \delta_{n,m} &\equiv \int_0^{R_d} dr r I_1(\kappa_n r) I_1(\kappa_m r) \\ &+ \epsilon \frac{\kappa_n \kappa_m}{\kappa_n' \kappa_m'} \int_{R_d}^{R_s} dr r [a_n J_1(\kappa_n' r) \\ &+ b_n Y_1(\kappa_n' r)] [a_m J_1(\kappa_m' r) \\ &+ b_m Y_1(\kappa_m' r)], \end{aligned} \quad (\text{A4})$$

and hence we obtain

$$\begin{aligned} &k_n \left(1 - \frac{\kappa_n^2}{k_n^2}\right) \left[\left(\frac{\omega^2}{c^2} - k_n^2 + \kappa_n^2 \right) \delta A_{0n} \sin \alpha_n + 2k_n \frac{d}{dz} \delta A_{0n} \cos \alpha_n \right] \\ &= \frac{8\pi}{c R_d^2 A_n} \int_0^{R_d} dr r I_1(\kappa_n r) \left(\frac{\partial}{\partial z} \delta J_r - \frac{\partial}{\partial r} \delta J_z \right). \end{aligned} \quad (\text{A5})$$

If we multiply (A5) by $\cos \alpha_m$ and $\sin \alpha_m$ and then average these equations over a wave period, we obtain

$$\begin{aligned} &\left(1 - \frac{\kappa_n^2}{k_n^2}\right) \left(\frac{\omega^2}{c^2} - k_n^2 + \kappa_n^2 \right) \delta A_{0n} \\ &= \frac{8\omega}{c R_d^2 A_n} \int_0^{2\pi/\omega} dt \int_0^{R_d} dr r \left(\frac{1}{k_n} I_1(\kappa_n r) \frac{\partial}{\partial z} \delta J_r + \frac{\kappa_n}{k_n} I_0(\kappa_n r) \delta J_z \right) \sin \alpha_n, \end{aligned} \quad (\text{A6})$$

and

$$\begin{aligned} &2k_n \left(1 - \frac{\kappa_n^2}{k_n^2}\right) \frac{d}{dz} \delta A_{0n} \\ &= \frac{8\omega}{c R_d^2 A_n} \int_0^{2\pi/\omega} dt \int_0^{R_d} dr r \left(\frac{1}{k_n} I_1(\kappa_n r) \frac{\partial}{\partial z} \delta J_r + \frac{\kappa_n}{k_n} I_0(\kappa_n r) \delta J_z \right) \cos \alpha_n, \end{aligned} \quad (\text{A7})$$

where we have integrated by parts over the radial integral.

The source current has the functional dependence $\delta \mathbf{J} = \delta J_0(z) \mathbf{f}(\alpha_n)$ because it depends upon the response of the electron beam to the electromagnetic wave, where $\delta J_0(z)$ describes slow variations in the current as a result of the growth or damping of the wave and $\mathbf{f}(\alpha_n)$ describes the rapid sinusoidal variation. As a consequence,

$$\frac{1}{k_n} \frac{\partial}{\partial z} \delta \mathbf{J} \approx -\frac{1}{\omega} \frac{\partial}{\partial t} \delta \mathbf{J}, \quad (\text{A8})$$

which is correct to within terms of order $d(\delta A_{0n})/dz$. Neglecting the effect of these terms on the source integrals, we substitute (A8) for $\delta \mathbf{J}$, into (A6) and (A7) and integrate by parts over the time integral to obtain

$$\begin{aligned} &\left(1 - \frac{\kappa_n^2}{k_n^2}\right) \left(\frac{\omega^2}{c^2} - k_n^2 + \kappa_n^2 \right) \delta A_{0n} \\ &= -\frac{8\omega}{c R_d^2 A_n} \int_0^{2\pi/\omega} dt \int_0^{R_d} dr r \left(I_1(\kappa_n r) \delta J_r \cos \alpha_n - \frac{\kappa_n}{k_n} I_0(\kappa_n r) \delta J_z \sin \alpha_n \right) \end{aligned} \quad (\text{A9})$$

and

$$\begin{aligned} &2k_n \left(1 - \frac{\kappa_n^2}{k_n^2}\right) \frac{d}{dz} \delta A_{0n} \\ &= \frac{8\omega}{c R_d^2 A_n} \int_0^{2\pi/\omega} dt \int_0^{R_d} dr r \left(I_1(\kappa_n r) \delta J_r \sin \alpha_n + \frac{\kappa_n}{k_n} I_0(\kappa_n r) \delta J_z \cos \alpha_n \right). \end{aligned} \quad (\text{A10})$$

The dynamical equations [Eqs. (16) and (17)] are obtained by substitution of the source current in Eq. (12) into (A9) and (A10).

- ¹ K. L. Felch, K. O. Busby, R. Layman, and J. E. Walsh, *Appl. Phys. Lett.* **38**, 601 (1981).
- ² S. Von Laven, J. Branscum, J. Golub, R. Layman, and J. E. Walsh, *Appl. Phys. Lett.* **41**, 408 (1982).
- ³ E. P. Garate, S. Moustizis, J. M. Buzzi, C. Rouille, H. Lamain, J. E. Walsh, and B. Johnson, *Appl. Phys. Lett.* **48**, 1326 (1986).
- ⁴ E. P. Garate, R. Cook, P. Heim, R. Layman, and J. E. Walsh, *J. Appl. Phys.* **58**, 627 (1985).
- ⁵ J. E. Walsh, C. H. Shaughnessy, R. Layman, G. Dattoli, G. P. Gallerano, and A. Renieri, *Nucl. Instrum. Meth. Res. A* **272**, 132 (1988).
- ⁶ C. K. Birdsall and J. R. Whinnery, *J. Appl. Phys.* **24**, 314 (1953).
- ⁷ W. B. Case, R. D. Kaplan, J. E. Golub, and J. E. Walsh, *J. Appl. Phys.* **55**, 2651 (1984).
- ⁸ J. E. Walsh, B. Johnson, G. Dattoli, and A. Renieri, *Phys. Rev. Lett.* **53**, 779 (1984).
- ⁹ E. P. Garate and J. E. Walsh, *IEEE Trans. Plasma Sci.* **PS-13**, 524 (1985).
- ¹⁰ B. Johnson and J. E. Walsh, *Phys. Rev. A* **33**, 3199 (1986).
- ¹¹ E. P. Garate, C. H. Shaughnessy, and J. E. Walsh, *IEEE J. Quantum Electron.* **QE-23**, 1627 (1987).
- ¹² G. Mishra and V. K. Tripathi, *IEEE Trans. Plasma Sci.* **PS-17**, 12 (1989).
- ¹³ J. E. Walsh, in *Advances in Electronics and Electron Devices* (Academic, New York, 1982), Vol. 58, pp. 271-310.
- ¹⁴ D. S. Lemons and L. E. Thode, *Phys. Rev. Lett.* **56**, 2684 (1986).
- ¹⁵ P. Sprangle, C. M. Tang, and W. M. Manheimer, *Phys. Rev. A* **21**, 302 (1980).
- ¹⁶ H. P. Freund, *Phys. Rev. A* **27**, 1977 (1983).
- ¹⁷ A. K. Ganguly and H. P. Freund, *Phys. Rev. A* **32**, 2275 (1985).
- ¹⁸ P. Sprangle, C. M. Tang, and P. Serafini, *Appl. Phys. Lett.* **49**, 1154 (1986).
- ¹⁹ P. Sprangle, A. Ting, and C. M. Tang, *Phys. Rev. Lett.* **59**, 202 (1987); *Phys. Rev. A* **36**, 2772 (1987).
- ²⁰ H. P. Freund, *Phys. Rev. A* **37**, 3371 (1988).
- ²¹ A. W. Fliflet, M. E. Read, K. R. Chu, and R. Seeley, *Int. J. Electron.* **53**, 505 (1982).
- ²² A. K. Ganguly, S. Ahn, and S. Y. Park, *Int. J. Electron.* **65**, 597 (1988).
- ²³ A. K. Ganguly, H. P. Freund, and S. Ahn, *Phys. Rev. A* **36**, 2199 (1987).
- ²⁴ R. F. Harrington, *Times-Harmonic Electromagnetic Fields* (McGraw-Hill, New York, 1961), Chap. 5.
- ²⁵ H. P. Freund and A. K. Ganguly, *IEEE J. Quantum Electron.* **QE-23**, 1657 (1987).
- ²⁶ W. Main, R. Cherry, and E. P. Garate, *Appl. Phys. Lett.* **55**, 1498 (1989).

APPENDIX III

Nonlinear Analysis of High-Power Cerenkov Masers

by

H.P. Freund

Nonlinear Analysis of High-Power Cherenkov Masers

H. P. Freund^(a)

Naval Research Laboratory, Washington, D.C. 20375

(Received 6 July 1990; revised manuscript received 4 September 1990)

A nonlinear simulation of the Cherenkov maser amplifier is presented for a configuration in which an electron beam propagates through a dielectric-lined cylindrical waveguide. The parameters used correspond to an experiment at General Dynamics which measured a total efficiency of 11.5% at 8.6 GHz. The simulation is in agreement with this but indicates that the system was too short to reach saturation and that an efficiency of 30% would have been possible for a longer system, and the performance is not significantly degraded by thermal spreads up to 20%.

PACS numbers: 42.52.+x, 52.25.Sw, 52.75.Ms, 85.10.Jz

The Cherenkov maser has been demonstrated over a broad spectral range and operates by means of an interaction between an energetic electron beam and a subluminal (or slow) electromagnetic wave. Wave-particle resonance occurs when the wave phase and particle velocities are in synchronism. While oortrons and backward-wave oscillators succeed in slowing the electromagnetic wave to subluminal velocities by means of a grating or a ripple imposed on the waveguide walls, the Cherenkov maser achieves this effect by means of a dielectric liner. Cherenkov masers have been built and operated at 100-kW power levels at 1-mm wavelengths,¹⁻³ at 200-MW power levels at 8-cm wavelengths,⁴ as well as at wavelengths as short as in the far infrared at 100 μm .⁵

In the present work, we describe a comparison between a nonlinear formulation of the Cherenkov maser amplifier⁶ and an experiment conducted at General Dynamics.⁷ This experiment achieved a total output power of 280 MW at a frequency of 8.6 GHz, and provides the motivation for the present use of the nonlinear model to investigate the feasibility of a high-power Cherenkov maser amplifier. The nonlinear theory is in substantial agreement with the experimental measurements for the quoted beam and waveguide parameters. However, the theory indicates that the experiment was too short to reach saturation, and that a total output power in the neighborhood of 800 MW could have been achieved with a longer system. The response of the system to the beam thermal spread is also remarkable in that the gain and saturation efficiency are not substantially degraded by energy spreads as high as 20%.

The configuration employed in the nonlinear formulation is that of an electron beam propagating through a cylindrical, dielectric-lined waveguide. We use R_i and R_d to denote the inner radii of the waveguide and dielectric liner (with a dielectric constant of ϵ), respectively. The boundary conditions imposed on the electromagnetic field are satisfied by expanding the field in terms of the normal modes of the vacuum waveguide. The beam interacts with the parallel component of the electric field

and couples primarily with the TM modes. We make the further assumption of azimuthal symmetry, and represent the field as an expansion of the TM_{0n} modes of the vacuum waveguide,⁸ for which

$$\delta E(x, t) = - \sum_{n=1}^{\infty} \frac{\omega}{c} \delta A_{0n} \left[Z_{1n}(r) \hat{e}_r \sin a_n + \frac{\kappa_n}{k_n} Z_{0n}(r) \hat{e}_z \cos a_n \right], \quad (1)$$

$$\delta B(x, t) = - \sum_{n=1}^{\infty} k_n \left[1 - \frac{\kappa_n^2}{k_n^2} \right] \delta A_{0n} Z_{1n}(r) \hat{e}_\theta \sin a_n, \quad (2)$$

where δA_{0n} measures the amplitude and has the dimensions of a vector potential, ω and k_n denote the frequency and wave number, and

$$a_n \equiv \int_0^z dz' k_n(z') - \omega t \quad (3)$$

is the phase of the TM_{0n} mode. Both the amplitude and the wave number are assumed to be slowly varying functions of z in the sense that both vary slowly with respect to the wavelengths of interest. The radial dependence of these eigenmodes is given by ($l=0, 1$)

$$Z_{ln}(r) = \begin{cases} I_l(\kappa_n r), & 0 \leq r \leq R_d, \\ a_n J_l(\kappa'_n r) + b_n Y_l(\kappa'_n r), & R_d < r \leq R_i, \end{cases} \quad (4)$$

where J_n and Y_n represent the regular Bessel and Neumann functions, I_n denotes the modified Bessel function of the first kind, and

$$a_n \equiv \frac{\pi}{2} \kappa'_n R_d \left[\frac{\kappa'_n}{\epsilon \kappa_n} I_1(\kappa_n R_d) Y_0(\kappa'_n R_d) - I_0(\kappa_n R_d) Y_1(\kappa'_n R_d) \right], \quad (5)$$

$$b_n \equiv - \frac{\pi}{2} \kappa'_n R_d \left[\frac{\kappa'_n}{\epsilon \kappa_n} I_1(\kappa_n R_d) J_0(\kappa'_n R_d) - I_0(\kappa_n R_d) J_1(\kappa'_n R_d) \right].$$

Both κ_n and κ'_n are analogs of the cutoff wave numbers and are defined by

$$\omega^2/c^2 = k_n^2 - \kappa_n^2 \quad (6)$$

in the vacuum, and

$$\epsilon\omega^2/c^2 = k_n^2 + \kappa_n'^2 \quad (7)$$

in the dielectric. It should be remarked that the choice of k_n in Eqs. (6) and (7) denotes the vacuum value which, under the present assumptions, is the initial condition for the wave number. The vacuum dispersion equation¹⁻⁵ for this configuration is

$$\frac{I_1(\kappa_n R_d)}{I_0(\kappa_n R_d)} - \frac{\epsilon \kappa_n}{\kappa_n'} \frac{Y_0(\kappa_n' R_g) J_1(\kappa_n' R_d) - J_0(\kappa_n' R_g) Y_1(\kappa_n' R_d)}{Y_0(\kappa_n' R_g) J_0(\kappa_n' R_d) - J_0(\kappa_n' R_g) Y_0(\kappa_n' R_d)} = 0, \quad (8)$$

which, in combination with Eqs. (5) and (6), relates ω and k_n .

The dynamical equations which govern the evolution of the slowly varying amplitude and phase have been derived by Freund and Ganguly.⁶ The dispersion of each mode in the presence of the electron beam is described by

$$\left(1 - \frac{\kappa_n^2}{k_n^2}\right) \left[\frac{\omega^2}{c^2} - k_n^2 + \kappa_n^2\right] \delta a_{0n} = \frac{2\omega_b^2}{A_n c^2} \left\langle I_1(\kappa_n r) \frac{v_r}{|v_z|} \cos a_n - \frac{\kappa_n}{k_n} I_0(\kappa_n r) \sin a_n \right\rangle, \quad (9)$$

where $\omega_b^2 \equiv 4\pi n_b e^2/m_e$ is the square of the beam-plasma frequency and $\delta a_{0n} \equiv e\delta A_{0n}/m_e c$. The amplification (or damping) of each mode is given by

$$2k_n \left(1 - \frac{\kappa_n^2}{k_n^2}\right) \frac{d}{dz} \delta a_{0n} = -\frac{2\omega_b^2}{A_n c^2} \left\langle I_1(\kappa_n r) \frac{v_r}{|v_z|} \sin a_n + \frac{\kappa_n}{k_n} I_0(\kappa_n r) \cos a_n \right\rangle, \quad (10)$$

where

$$A_n \equiv \frac{\epsilon - 1}{\epsilon} \left[I_1^2(\kappa_n R_d) - \frac{\epsilon \kappa_n^2}{\kappa_n'^2} I_0^2(\kappa_n R_d) + \frac{2}{\kappa_n R_d} \frac{\epsilon \omega^2}{c^2 \kappa_n'^2} I_0(\kappa_n R_d) I_1(\kappa_n R_d) \right] + \epsilon \frac{R_g^2}{R_d^2} \frac{\kappa_n^2}{\kappa_n'^2} [a_n J_1(\kappa_n' R_g) + b_n Y_1(\kappa_n' R_g)]^2. \quad (11)$$

It is clear from Eq. (10) that the derivative of the amplitude is zero when $\omega_b = 0$, and there is no amplification of the modes in the absence of the beam. The neglect of beam space-charge modes from the formulation is valid as long as (1) $\omega_b \ll \omega$, and (2) the exponentiation time is much less than the period of the beam-plasma wave.

The averaging operator is defined over the initial conditions of the beam, and includes the effect of an initial momentum spread by means of the distribution function

$$F_0(p_0) = A \exp[-(p_{z0} - p_0)^2/\Delta p_z^2] \delta(p_\theta^2 - p_{z0}^2 - p_\perp^2) H(p_{z0}), \quad (12)$$

where p_0 and Δp_z describe the initial bulk momentum and momentum spread, $H(x)$ is the Heaviside function, and the normalization constant is

$$A \equiv \left[\pi \int_0^\infty dp_{z0} \exp[-(p_{z0} - p_0)^2/\Delta p_z^2] \right]^{-1}. \quad (13)$$

Observe that this distribution describes a beam which is monoenergetic but with a pitch-angle spread which is equivalent to an axial energy spread of

$$\Delta \gamma_z/\gamma_0 = 1 - [1 + 2(\gamma_0^2 - 1)\Delta p_z/p_0]^{-1/2}, \quad (14)$$

where $\gamma_0 \equiv (1 + p_0^2/m_e^2 c^2)^{1/2}$. As a result, the averaging operator takes the form

$$\langle (\dots) \rangle \equiv \frac{A}{2\pi R_d^2} \int_0^{2\pi} d\varphi_0 \int_0^\infty dp_{z0} \beta_{z0} \exp\left[-\frac{(p_{z0} - p_0)^2}{\Delta p_z^2}\right] \int_0^{2\pi} d\psi_0 \sigma_1(\psi_0) \int_0^{R_d} dr_0 r_0 \sigma_\perp(r_0) (\dots), \quad (15)$$

where $\psi_0 \equiv -\omega t_0$ is the initial phase, $\varphi_0 \equiv \tan^{-1}(p_y/p_x)$, $\beta_{z0} \equiv v_{z0}/c$, and $\sigma_1(\psi_0)$ and $\sigma_\perp(r_0)$ describe the initial beam distributions in phase and cross section.

In order to complete the formulation, the electron-orbit equations must be specified as well. Since we are interested in amplifier configurations, we integrate the complete Lorentz-force equations in z using an axial guide magnetic field to provide for the confinement of the beam, and the electromagnetic field given in Eqs. (1) and (2).

This formulation is used to investigate a recent amplifier experiment conducted at General Dynamics⁷ which employed an intense relativistic electron beam (788 keV and 3.1 kA) produced by a cold "knife-edge" cathode which

resulted in an annular beam with a mean radius of approximately 1.15 cm and a thickness of 2 mm. After correction for the space-charge depression, therefore, the beam energy is of the order of 736 keV. No diagnostic measurement of the beam quality (i.e., thermal energy spread) was made. The dielectric-lined waveguide employed Stycast ($\epsilon=10$) and had radii $R_g=1.74$ cm and $R_d=1.47$ cm. The dielectric had a 3.3-cm taper at both ends to suppress oscillation, and a uniform central region which was 23.9 cm in length. Beam transport was accomplished with a 15-kG solenoidal magnetic field. The amplifier was driven by a 200-kW magnetron which was tunable over the band from 8.4 to 9.6 GHz. The mode conversion process from the TE_{10} rectangular mode of the magnetron to the TM_{01} mode of the dielectric-lined waveguide was accomplished at an expected efficiency of 50% at a frequency of 8.6 GHz for a total injected power of approximately 100 kW. Note that at these frequencies it is only the TM_{01} mode which can interact with the beam. A total gain of 34.5 dB (1.44 dB/cm over the uniform dielectric) was observed at a power level of approximately 280 MW (for an efficiency of 11.5%), with an uncertainty of approximately 3 dB.

Simulation of this experimental configuration is in reasonable agreement with the observations, and shows that the power has not saturated over the 23.9-cm length of the uniform dielectric. As a result, the power predicted in simulation over this length shows a substantial sensitivity to the specific choice of any parameter which will modify the linear gain. In particular, the simulation exhibits a larger sensitivity to the choice of the thickness of the dielectric than to any of the electron-beam parameters. For example, given the choice of $R_d=1.47$ cm, the simulation predicts a power level of approximately 60 MW over the 23.9-cm length of the uniform dielectric. However, there is an uncertainty in the thickness of the dielectric which is of the order of ± 0.005 cm, and arises due to the fabrication of the liner. In this regard, Stycast (which is a cold-pressed ceramic) must be machined to fit within the waveguide.⁹ If we choose a value of $R_d=1.475$ cm corresponding to a thinner dielectric, then the power found in simulation over this length rises to approximately 131 MW, which is within the uncertainty in the experimental measurement of the power. This sensitivity to the parameters is largely confined to the linear gain and results from a variation in the dielectric effect of the liner which modifies the tuning of the resonance within the gain band. The saturated power is not substantially altered by variations in R_d over this range, and we find that the saturated power rises from approximately 600 to 620 MW as the inner radius of the dielectric changes from 1.47 to 1.475 cm. Since the larger figure for R_d is in better agreement with the observations and is within the range of experimental uncertainty, we shall use this value henceforth in the numerical analysis of the experiment.

The gain band is found in simulation to cover the

range of approximately 7.8–8.8 GHz, and the efficiency at saturation for an ideal beam (i.e., $\Delta\gamma_z=0$) increases from 16.4% at 7.8 GHz to approximately 30.3% at 8.8 GHz. A graph of the evolution of the power and gain versus axial distance is shown in Fig. 1 for an ideal beam at a frequency of 8.6 GHz. Observe that the power saturates after a length of approximately 28 cm at a level of 620 MW for an efficiency of 31.6%. The average gain over this interaction is in the neighborhood of 1.4–1.6 dB/cm which is also in reasonable agreement with the observations. It should be remarked that the fluctuation evident in the gain is related to the launching loss of the signal, which introduces a fluctuation in the response of the beam to the wave. In most systems this fluctuation is observed to decay away leaving a relatively constant growth rate. However, the growth rate is so large in the present example that these fluctuations are unable to completely decay prior to the saturation of the signal. These fluctuations are also manifested in the evolution of the power, but are not visible when plotted on a logarithmic scale. As mentioned previously, the power level reached after 23.9 cm is approximately 131 MW, which is consistent with the observations given the experimental uncertainty. It is evident that the experiment was too short to reach saturation.

The effect of beam thermal spread is shown in Fig. 2 in which the efficiency is plotted as a function of the energy spread at 8.6 GHz. It is clear from the figure that the interaction is remarkably insensitive to the beam thermal spread, and the saturation efficiency is not significantly degraded by energy spreads as high as (20–25)%. In order to explain such a high tolerance for energy spreads, it should be noted that the thermal regime occurs at progressively higher energy spreads as the growth rate increases for any interaction mechanism, whether Cherenkov maser, free-electron laser, or cyclotron maser. Since this mechanism relies on the Cherenkov resonance in which $\omega - kv_b \approx 0$, thermal effects be-

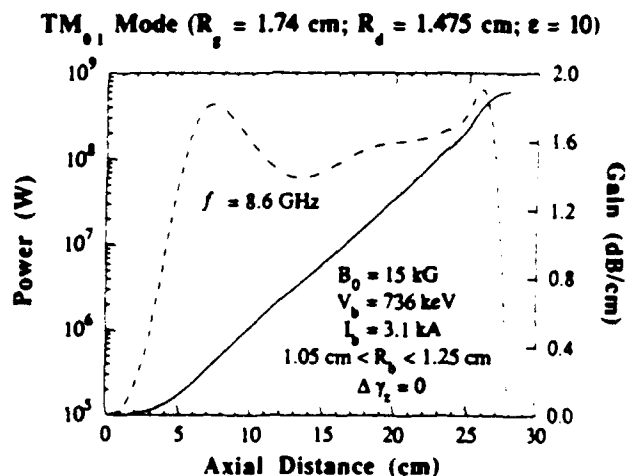


FIG. 1. Graph of the evolution of the power (solid line) and gain (dashed line) with axial distance.

TM₀₁ Mode ($R_s = 1.74$ cm; $R_d = 1.475$ cm; $\epsilon = 10$)

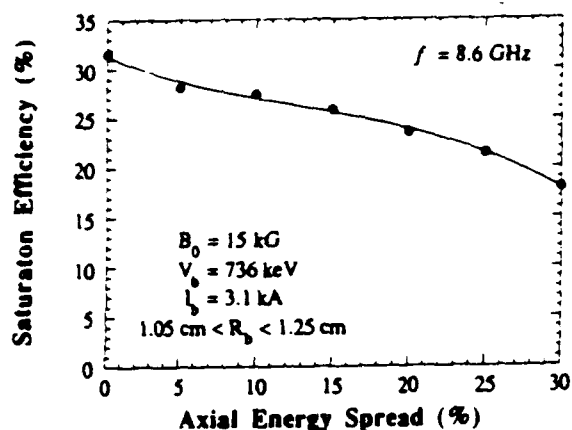


FIG. 2. Graph of the variation of the saturation efficiency vs axial energy spread.

come important when $\Delta v_b/v_b \approx \text{Im}k/\text{Re}k$. In this case, the growth rate due to the intense beam is extremely high with $\text{Im}k \approx 0.18 \text{ cm}^{-1}$. Since $\text{Re}k \approx 2.35 \text{ cm}^{-1}$, this gives $\Delta v_b/v_b \approx 7.5\%$ which [using Eq. (14)] corresponds to an axial energy spread of $\Delta\gamma/\gamma_0 \approx 24\%$.

In view of the power levels found both in the laboratory and in simulation, the simplicity of the configuration, and the relative insensitivity to beam thermal effects in the case of intense relativistic electron beams, the Cherenkov maser is an attractive competitor for gyrotrons, free-electron lasers, and relativistic klystrons for a wide variety of applications. In particular, the potentiality of producing single-mode powers in excess of 700 MW at frequencies in the neighborhood of 9 GHz compares favorably with recent results obtained with relativistic klystrons;^{10,11} however, unlike the relativistic klystron, the Cherenkov maser is easily scalable to higher frequencies. Indeed, it is anticipated that the level of performance demonstrated herein at 8.6 GHz can be achieved at frequencies as high as 35 GHz as well. It should be remarked that Cherenkov masers based upon dielectric liners can exhibit both dielectric and mechani-

cal breakdown at high power levels, and that these effects may have operated to limit the power and/or pulse length in the experiment at General Dynamics.⁹ However, this configuration represents only one approach to the interaction, and other slow-wave structures may be used to overcome these difficulties. In general, this device falls into the category of relativistic intense-beam traveling-wave tubes (TWTs), and similar levels of performance have been obtained using a rippled-wall slow-wave structure in both backward-wave oscillators¹² and TWT amplifiers.¹³

This work was supported by the Office of Naval Research and the Office of Naval Technology.

(a)Permanent address: Science Applications International Corp., McLean, VA 22102.

¹K. L. Felch, K. O. Busby, R. Layman, and J. E. Walsh, *Appl. Phys. Lett.* **38**, 601 (1981).

²S. Von Laven, J. Branscum, J. Golub, R. Layman, and J. E. Walsh, *Appl. Phys. Lett.* **41**, 408 (1982).

³E. P. Garate, R. Cook, P. Heim, R. Layman, and J. E. Walsh, *J. Appl. Phys.* **58**, 627 (1985).

⁴W. Main, R. Cherry, and E. P. Garate, *Appl. Phys. Lett.* **55**, 1498 (1989).

⁵J. E. Walsh, C. H. Shaughnessy, R. Layman, G. Dattoli, G. P. Gaillerano, and A. Renieri, *Nucl. Instrum. Methods Phys. Res., Sect. A* **272**, 132 (1988).

⁶H. P. Freund and A. K. Ganguly, *Phys. Fluids* (to be published).

⁷W. Main, E. P. Garate, R. Cherry, and J. Weatherall (to be published).

⁸R. F. Harrington, *Time-Harmonic Electromagnetic Fields* (McGraw-Hill, New York, 1961), Chap. 5.

⁹W. Main (private communication).

¹⁰M. A. Allen *et al.*, SLAC Report No. 4801, 1989 (unpublished); SLAC Report No. 5070, 1989 (unpublished).

¹¹M. Friedman, J. A. Krall, Y. Y. Lau, and V. Serlin, *Rev. Sci. Instrum.* **61**, 171 (1990).

¹²D. Shiffer, J. A. Nation, and G. Kerslick, *IEEE Trans. Plasma Sci.* **18**, 546 (1990).

¹³Y. Carmel, K. Minami, R. A. Kehs, W. W. Destler, V. L. Granatstein, D. Abe, and W. L. Lou, *Phys. Rev. Lett.* **62**, 2389 (1989).

APPENDIX IV

A Millimeter and Submillimeter Wavelength Free-Electron Laser

by

D.A. Kirkpatrick, G. Bekefi, A.T. DiRienzo, H.P. Freund, and A.K.
Ganguly

A millimeter and submillimeter wavelength free-electron laser

D. A. Kirkpatrick,^{a)} G. Bekefi, and A. C. DiRienzo

Department of Physics and Research Laboratory of Electronics, Massachusetts Institute of Technology, Cambridge, Massachusetts 02139

H. P. Freund^{a)} and A. K. Ganguly

Naval Research Laboratory, Washington, D.C. 20375-5000

(Received 20 January 1989; accepted 28 March 1989)

Measurements of millimeter and submillimeter wavelength emission ($240 \text{ GHz} < \omega/2\pi < 470 \text{ GHz}$) from a free-electron laser are reported. The laser operates as a superradiant amplifier and without an axial guide magnetic field; focusing and transport of the electron beam through the wiggler interaction region are achieved by means of the bifilar helical wiggler field itself. Approximately 18 MW of rf power has been observed at a frequency of 470 GHz, corresponding to an electronic efficiency of 0.8%. Frequency spectra are measured with a grating spectrometer and show linewidths $\Delta\omega/\omega \sim 2\% - 4\%$. The experimental results are in very good agreement with nonlinear numerical simulations.

I. INTRODUCTION

The free-electron laser (FEL) has long been looked to as a promising source of coherent radiation in wavelength regimes that are otherwise difficult to access. To date, most experiments have been concentrated in the visible-to-infrared wavelength range¹ and in the microwave range.²⁻⁵ Some experiments have operated in the vicinity of 400 μm wavelengths,^{6,7} but observed very low electronic efficiencies ($P_{\text{RAD}}/P_{\text{BEAM}} \sim 3 \times 10^{-3}$). Recent advances in electron guns applicable to FEL experiments⁸ were essential to the operation of the present experiment at high power ($P_{\text{RAD}} \approx 18 \text{ MW}$) and reasonable efficiency ($P_{\text{RAD}}/P_{\text{BEAM}} \sim 0.01$).

A FEL produces coherent radiation by inducing a coherent, periodic, undulation in the trajectory of an electron beam. This undulation is effected by the application of a periodic "wiggler" magnetic field, which bends the electron paths in the plane transverse to the applied field. For the case of a helical wiggler field,

$$\mathbf{B} = B_w (\hat{x} \cos k_w z + \hat{y} \sin k_w z), \quad (1)$$

the electron trajectories are helices of the same periodicity, but $\pi/2$ out of phase with the magnetic field. In Eq. (1), B_w is the amplitude of the wiggler magnetic field, and $k_w = 2\pi/\lambda_w$, where λ_w is the period of the wiggler field. The output frequency of the FEL is given approximately by

$$\omega = (1 + \beta_{\parallel}^2) \gamma_1^2 k_w v_z. \quad (2)$$

Here γ_1 is the relativistic factor $\gamma_1 = (1 - \beta_{\parallel}^2)^{-1/2}$, $\beta_{\parallel} = v_z/c$, v_z is the axial velocity of the electron, and c is the speed of light in vacuum. The factor of γ_1^2 allows for large upshifts in the FEL frequency by variation of the electron beam energy, and is the reason FEL's have been able to operate in frequency ranges spanning many orders of magnitude.

A bifilar helical winding is employed to produce the helical wiggler magnetic field. The nonzero transverse gradi-

ent and nonzero axial component of this field⁹ act to focus the electrons, and no axial guide field is necessary. For a high-quality electron beam, a modest wiggler field amplitude is sufficient to focus and transport kiloamperes of current through the wiggler interaction region. Using the wiggler field to provide focusing and transport simplifies access to the experimental system and entirely removes the requirement for a large power supply or superconducting magnet to provide the focusing and transport fields. The absence of an axial guide field also avoids the possibility of exciting unwanted absolute and convective instabilities of the gyrotron and cyclotron-maser variety.¹⁰

A previous effort to use the wiggler field for focusing¹¹ was able to transport only about 25% of the electron beam. The fraction of the beam current that was caught in the wiggler focusing fields was successfully transported, and the major cause of beam loss was attributed to poor beam quality. In the present experiment, most of the electron beam current is successfully injected and transported the full length (1.5 m) of the wiggler interaction region.

Our FEL is operated as a single-pass superradiant amplifier, where the input signal arises from noise or spontaneous emission. The output radiation is characterized by measurements of the total power, power gain, and frequency spectrum. Data are obtained as functions of the wiggler field strength and the electron beam energy. The FEL output frequency is tuned from 240 to 470 GHz by variation of the electron beam energy. For a 2.3 MeV, 930 A electron beam we measure an output power of 18 MW at an output frequency of 470 GHz. Measurements of power gain for these same parameters show that this output power has not yet reached saturation. Frequency spectra are measured using a grating spectrometer and show linewidths $\Delta\omega/\omega \sim 2\% - 4\%$.

The observations are compared with theoretical analyses of the experimental configuration based on the nonlinear simulation code ARACHNE.¹²⁻¹⁶ The ARACHNE simulation follows the evolution of an arbitrary number of vacuum waveguide modes coupled with an ensemble of electrons. The simulation is fully three dimensional and self-consis-

^{a)} Permanent address: Science Applications International Corporation, McLean, Virginia 22102.

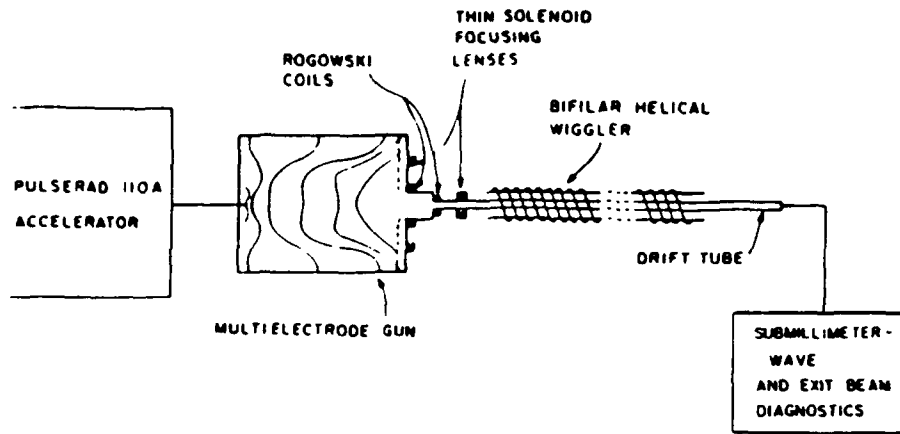


FIG. 1 The schematic layout of this experiment

tently includes the overlap of the electron beam and the radiation field of each mode. Neither self-field nor space-charge effects are included in the simulation, which is valid in the strong-pump Compton regime of the FEL interaction. Simple one-dimensional criteria¹⁷ suggest that these experiments are in the collective, Raman regime where RF space-charge effects cannot be neglected. However, the ARACHNE simulations that neglect space-charge effects are in close agreement with the experimental results. This would suggest that in our parameter regime, three-dimensional effects have reduced the effects of rf space charge and have blurred any distinction between the Compton and Raman regimes of operation.

II. EXPERIMENT

A schematic illustration of the experimental layout is shown in Fig. 1. The Pulserad 110 A accelerator (pulse length $\tau \sim 30$ nsec, $V_0 = 1.4$ MV, $I_0 = 32$ kA, impedance $Z_0 = 43 \Omega$) terminates in the electron gun, which acts as a mismatched load ($Z_{gun} \sim 300 \Omega$) resulting in an accelerator output voltage of ~ 2 MV and an accelerator output current of ~ 7 kA. The electron gun is a five-stage multielectrode field emission electron gun shown in Fig. 2. The electron beam is generated in the gap between the cathode and first anode (A1) by field emission from an emitting surface embedded in the cathode. The aperture in the first anode is

covered with an 80% transmitting molybdenum mesh. The resultant beam is accelerated to the full applied voltage by stages two through five. The aperture in the last anode (A5) is also covered with an 80% transmitting molybdenum mesh. The purpose of the two meshes is to reduce the effects of fringing fields, which induce temperature in the beam.

The cathode plate is a spin-formed aluminum disk with a cylindrical hole in the center, allowing the insertion of a plug of emitting material. The entire surface of the cathode, with the exception of the small emitting area, is anodized to minimize undesired emission. The hard aluminum oxide (anodized) coating has a thickness of 0.05 mm. The voltages on the successive anodes A1-A4 are $(-\frac{1}{4}V_0, -\frac{1}{2}V_0, -\frac{3}{4}V_0, -V_0)$, where V_0 is the full accelerator voltage. For a 2 MV beam, for example, the successive voltages in megavolts from the cathode to the last anode are $(-0.5, -1.0, -1.5, -2.0)$. This division is achieved by means of an axisymmetric, cylindrical copper sulfate voltage divider (see Fig. 2) with which the electrodes are in electrical contact. Typically, the total resistance of this divider equals $\sim 400 \Omega$. The shapes of the electrodes are designed¹⁸ with the view of balancing the self-electric and self-magnetic fields of the beam so as to produce a paraxial electron beam of radius $r \approx 2.5$ cm. Earlier experiments investigated the emittance,⁸ and the temporal evolution of the emittance,¹⁹ as a function of the cathode material and the applied electric field in the cathode-anode gap. The present FEL measurements are conducted using a 2.0 cm diameter reactor graphite cathode at a $K-A$ gap of 1.55 cm. The measured time-integrated normalized emittance for this configuration is $\epsilon_n = 52 \times 10^{-1} (\pi \text{ cm rad})$, for a beam energy of 2.3 MeV and a beam current of 930 A. Typical voltage and current pulse traces are shown in Fig. 3.

The electron beam emerging from the multistage gun is transported and focused into the wiggler by thin solenoid lenses. The configuration of a large diameter coil at the electron gun output, combined with a smaller diameter coil positioned over the wiggler entrance, is shown in Fig. 4. This combination provides us with substantial flexibility in choosing the axial position and radius of the electron beam waist, while at the same time minimizing any increase in electron beam emittance produced by spherical lens aberration. The large diameter coil, which takes the beam emerging

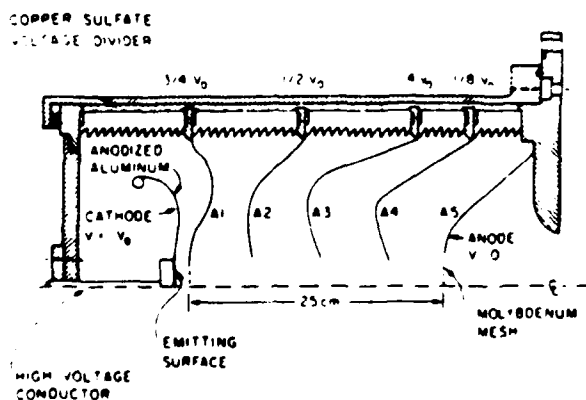


FIG. 2 A cross-sectional view of the multistage electron gun used in these experiments.

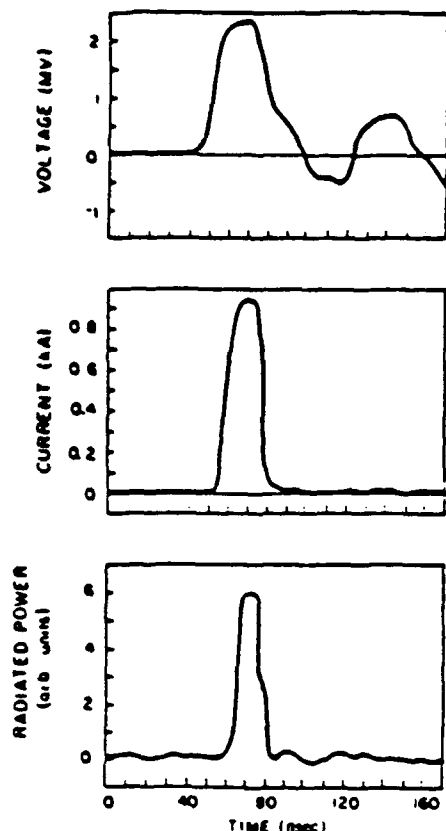


FIG. 3. Typical voltage, beam current, and microwave output waveforms.

from the electron gun and focuses it into the drift tube, has an inner radius of 14.5 cm, an axial thickness of 2.0 cm, a radial thickness of 1.5 cm, and approximately 200 turns of 18 AWG copper wire. Peak axial fields under the center of this

coil are typically 1–2 kG. The second thin coil has an inner radius of 5.0 cm, an axial thickness of 1.0 cm, a radial thickness of 1.6 cm, and approximately 100 turns of 18 AWG copper wire. Peak axial fields under the center of this coil are typically in the range 3–6 kG. In all cases, the magnetic field at the cathode surface due to the external focusing coils is measured to be less than 20 G. This is important because the electron gun is designed to be electrostatically focused. Within the limits imposed by the need to confine and transport the electron beam, the coil parameters are chosen to minimize the induced emittance caused by spherical aberration in the coils.^{20,21}

The electron beam is focused and transported through the wiggler interaction region by the wiggler field itself. The magnetic field of a finite radius-infinite length bifilar helical wiggler magnet is given by⁹

$$B_{\text{w}} = 2B_w \left[\hat{e}_r I_1'(k_w r) \cos(\theta - k_w z) - \hat{e}_\theta \frac{I_1(k_w r)}{k_w r} \times \sin(\theta - k_w z) + \hat{e}_z I_1(k_w r) \sin(\theta - k_w z) \right], \quad (3)$$

where I_1 is the modified Bessel function and k_w is the wave-number associated with the wiggler period, r is the radius of the electron orbit, and higher spatial harmonics have been neglected. Using this field, and in the limit of modest wiggler field amplitude such that $R_b > r_{\text{wig}}$, where R_b is the electron beam radius and r_{wig} is the radial amplitude of the wiggler induced oscillations, it is possible to derive the space-charge dominated and emittance dominated equilibrium radii,

$$R_w = (c/\tilde{\Omega}_w)(2I/17\gamma\beta)^{1/2}, \quad (4)$$

$$R_e = (\epsilon_e c/\tilde{\Omega}_w)^{1/2}, \quad (5)$$

where

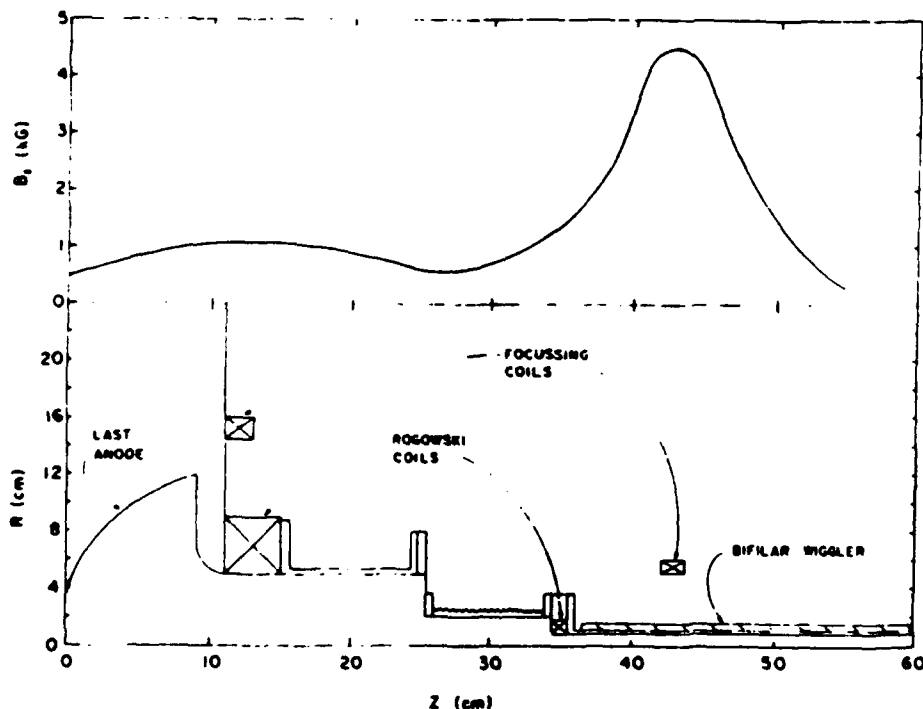


FIG. 4. The axial magnetic field profile of the thin solenoid focusing coils used to inject the electron beam into the wiggler magnet (top), and the corresponding cross section of the beam transport line showing the coil positions, the placements of the Rogowski coils, and the position of the bifilar wiggler windings (bottom).

$$\tilde{\Omega}_w = (eB_w/mc) [2I_1(k_w R_b)/k_w R_b]. \quad (6)$$

In these equations, I is the beam current in kiloamperes and ϵ_n is the normalized emittance given by $\epsilon_n = \gamma\beta x\delta\theta_x$, where γ is the relativistic energy factor, and x and $\delta\theta_x = (\delta v_x)/v$, are the semiminor and semimajor axis of an elliptical contour in phase space that encloses 90% of the beam electrons. These radii are derived within the framework of the beam envelope equation²² and are valid for a uniform density cross-section electron beam. Deviations from this density profile result in larger equilibrium radii.²³

The wiggler magnet is a bifilar helical winding with a period of 3.14 cm and a radius of 1.28 cm. The helices are wound with #12 AWG copper wire into a machined linen phenolic tube. This phenolic tube slides over a stainless steel drift tube (i.d. = 0.8 cm, wall thickness = 0.15 cm). The six-period entrance taper to the wiggler magnetic field is achieved by gradually tapping off the current in the windings with pairs of resistive ring terminations placed every half-period of the wiggler winding.²⁴ The resistive terminations are made from nichrome wire flashed with a very fine copper coating. This copper coating is necessary to insure good electrical contact between the resistive termination and the copper wiggler winding. This method of tapering the wiggler field results in a very smooth entrance.

The focusing properties of the bifilar helical wiggler are demonstrated by measuring the transmitted current as a function of axial position within the wiggler interaction region. The electron beam current is measured at any axial position inside the drift tube by a small, moveable current probe. This probe consists of a POCO graphite current collector, carbon based (low inductance) shunt resistors, and a 0.25 in. diam, 50 Ω rigid coaxial cable. The current probe is fitted with a collector of a radius larger than the estimated electron beam radius. A series of discharges is taken for a given set of accelerator parameters, focusing fields, and wiggler field strength, while varying the axial position of the probe. A set of such measurements is shown in Fig. 5. In these measurements the on-axis wiggler field is $B_w = 1275$ G. As can be seen, all of the electron beam current is focused

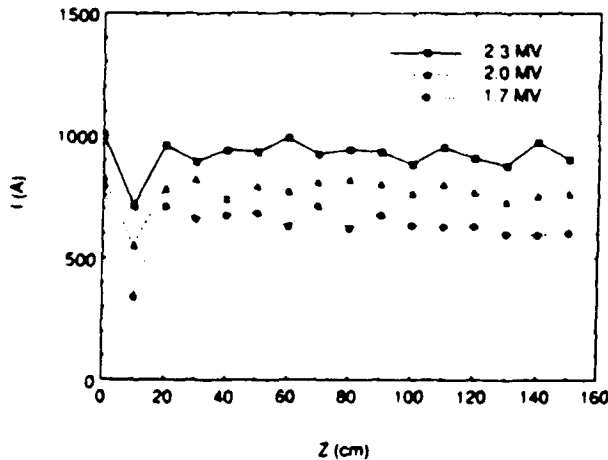


FIG. 5 The transmitted electron beam current as a function of distance in the wiggler interaction region, measured for different electron beam parameters. In all cases, $B_w = 1275$ G

into the wiggler region and remains confined. There is a <20% loss of current between the electron gun exit and the drift tube entrance. This represents that portion of the beam that was initially scattered by the last molybdenum mesh in the electron gun and thus acquired too much perpendicular temperature to be focused by the magnetic lenses. The polished graphite collectors used on the probe to measure the transmitted current also serve as witness plates. The beam-induced shadows on the witness plate show that a uniform, solid beam, with a 3–4 mm radius is obtained at all axial positions.

The various contributions to the spread in parallel momentum of the electron beam can be estimated once the beam radius inside the wiggler region is known. Given the electron beam emittance ϵ_n , if we assume a Gaussian spread in perpendicular velocity, then the σ of that distribution is given by

$$\sigma/c = \Delta\beta_\perp = \epsilon_n/1.96\gamma. \quad (7)$$

The corresponding spread in parallel velocity is given by

$$\Delta\beta_\parallel = \beta_\parallel - [\beta_\parallel^2 - (\Delta\beta_\perp)^2]^{1/2} \quad (8)$$

and the spread in axial energy $\Delta\gamma_\parallel/\gamma_\parallel$ is given by

$$\Delta\gamma_\parallel/\gamma_\parallel = \gamma_\parallel^2 \beta_\parallel \Delta\beta_\parallel. \quad (9)$$

Because either a positive or negative $\Delta\beta_\perp$ results in a decrease in β_\parallel , the two sides of the perpendicular distribution map into the same values of the parallel distribution, and the result arrived at in Eq. (9) is not a half-width at $1/e$ spread in γ_\parallel , but the full width at $1/e$ spread.

A range for this value can be computed from the measured emittance ϵ_n of the electron beam before it enters the focusing coils, and this measured emittance plus the upper limit to the emittance induced by the focusing coils themselves, ϵ_n^{ind} . For our focusing coil parameters, $\epsilon_n^{\text{ind}} < 0.02$ (π cm rad).^{20,21} Using our measured value $\epsilon_n = 0.052$ (π cm rad), $r_b = 0.4$ cm, we obtain

$$0.22\% < \Delta\gamma_\parallel/\gamma_\parallel < 0.40\%. \quad (10)$$

The spread in total energy due to the self-electric potential drop across the beam is given by

$$\Delta\gamma/\gamma = \omega_p^2 r_b^2 / 4c^2 < 0.2\% \quad (11)$$

for $I < 950$ A, $r_b \sim 0.4$ cm. There is a further source of axial energy spread generated by the transverse variation in the magnitude of the wiggler magnetic field,

$$\Delta\gamma_\parallel/\gamma_\parallel = [a_w/(1 + a_w^2)] \Delta a_w, \quad (12)$$

where $a_w = \tilde{\Omega}_w / ck_w$ is the normalized wiggler amplitude. Taking $a_w = 0.37$, $\Delta a_w = 0.05 \times a_w$ (approximate for $k_w r = 0.5$, the weighted "middle" of the beam), one finds $(\Delta\gamma_\parallel/\gamma_\parallel) = 0.6\%$. Adding these contributions as independent, and assuming the space-charge energy spread appears as an axial energy spread, yields an overall $(\Delta\gamma_\parallel/\gamma_\parallel) = 0.6\% - 0.8\%$.

The output radiation intensity is measured with a variety of detectors, including Joule calorimeters, pyroelectric detectors, and waveguide mounted whisker diode detectors in WR8(90–140 GHz) and WR3(170–300 GHz) bands. Which detector is employed is dependent on the frequency range being investigated and on the power available for de-

tection. The total output power is obtained by measuring the pulse energy with the calorimeter and dividing this by the measured FWHM of the radiation pulse, as measured by the pyroelectric pulse detector. The frequency range of the microwave radiation incident on the calorimeter is limited to 100 GHz $< f < 900$ GHz by a system of meshes used in reflection. In all cases, the radiated power is measured to be predominantly ($> 90\%$) above 100 GHz in frequency. Frequency spectra are measured using a grating spectrometer designed by Boyd.²⁵

III. THEORETICAL CONSIDERATIONS

Small signal calculation of the radiation frequency and the small signal growth rate of the free electron laser interaction has been covered extensively elsewhere.^{17,26-29} To find the radiation frequency, one notes that the magnetostatic wiggler field with wavenumber k_w couples the negative energy electrostatic wave associated with the electron beam,

$$\omega = \beta_1 c(k + k_w) - p_1 \omega_p / \gamma^{1/2} \gamma_1 \quad (13)$$

to an electromagnetic waveguide mode

$$\omega^2 = c^2 k^2 + \omega_c^2 \quad (14)$$

In these equations, ω and k are the angular frequency and wavenumber, respectively, of the output radiation, $\omega_p^2 = 4\pi N e^2 / m_0$ is the nonrelativistic plasma frequency squared, $\omega_c = \sqrt{\omega_{c0}^2 + (p_2^2 \omega_p^2 / \gamma)}$ is the cutoff frequency of a particular waveguide mode, including effects of the presence of the electron beam, ω_{c0} is the vacuum waveguide cutoff frequency for the waveguide mode in question, p_1 is a numerical factor associated with the finite transverse geometry of the electron beam,³⁰⁻³² and p_2 is a numerical factor approximately equal to the fractional overlap of the electron beam with the electromagnetic energy of the waveguide mode. For these experiments, $p_1 \sim 0.96-0.98$, $p_2 \sim 0.2-0.4$. The free-electron laser interaction occurs in the neighborhood of the intersections of the two dispersion relations, Eqs. (13) and (14). These intersections occur at

$$\omega^\pm = \gamma_1^2 k_w v_1 \left(1 - \frac{p_1 \hat{\omega}_p}{\gamma_1^{1/2} \gamma_1 \beta_1} \right) \left[1 \pm \beta_1 \left[1 - \left(\frac{\hat{\omega}_c}{\gamma_1 \beta_1 (1 - p_1 \hat{\omega}_p / \gamma_1^{1/2} \gamma_1 \beta_1)} \right)^2 \right]^{1/2} \right] \quad (15)$$

where we have abbreviated $\hat{\omega}_p = \omega_p / ck_w$, $\hat{\omega}_c = \omega_c / ck_w$. The $+$ / $-$ roots in Eq. (15) correspond to the Doppler-upshifted/Doppler-downshifted FEL interactions; the present experiment is concerned with the generation of short-wavelength, high-frequency radiation, and it is ω^+ which is of interest.

The complete (linear and nonlinear) simulation code ARACHNE¹²⁻¹⁶ constitutes a fully three-dimensional nonlinear formulation of a FEL amplifier used here in calculating the gain and spectral characteristics of our FEL. It is one of several FEL codes now in existence.³³⁻³⁶ The analysis consists in the solution of a set of coupled nonlinear differential equations that self-consistently describes the evolution of both an ensemble of electrons and the electromagnetic fields. Space-charge fields are neglected in the analysis; therefore, the treatment is applicable to the strong-pump Compton (sometimes called the high-gain) regime of operation. The nonlinear current that mediates the interaction is computed from the microscopic behavior of an ensemble of electrons by means of an average of the electron phases relative to the pondermotive wave formed by the beating of the wiggler and radiation fields. The equations are solved for the case in which the electron beam is injected into the wiggler by means of an adiabatic entry taper in which the wiggler field increases from zero to a constant level. The electron beam, upon injection, is assumed to be monoenergetic but to have a pitch angle spread in transverse velocity. This pitch angle spread is chosen to correspond to the emittance dominated axial energy spread, $\Delta\gamma_1 / \gamma_1$. The finite geometry is included in the treatment by the introduction of the boundary conditions appropriate to the TE and/or TM modes of the vacuum waveguide. As a result, all transverse and finite-geome-

try effects are included in the static wiggler and radiation fields in a self-consistent manner and affect the interaction through betatron oscillations and velocity shear in the electron orbits. ARACHNE was conceived to model a FEL amplifier and treats the case of a single interaction frequency. This permits the field equations to be averaged over a wave period that eliminates the fast time scale phenomena from the formulation and results in a substantial reduction in the computational requirements.

Although the above analysis is restricted to single-frequency propagation, an arbitrary number of propagating TE and TM modes can be included at this frequency. The inclusion of multiple modes is relatively straightforward and involves the calculation of the individual source currents for each mode as well as the integration of the electron orbit equations in the aggregate field. The only caution that must be observed is that each of the included modes must be sufficiently close to resonance with the beam that the pondermotive phase does not vary on the fast time scale. However, this caution is not terribly restrictive in overmoded waveguides, and a similar multimode code WIGGLIN³⁷ based upon a planar wiggler/rectangular waveguide configuration has given good agreement with the results of the 35 GHz ELF amplifier experiment.³⁸

In the one-dimensional case, the FEL interaction occurs in the Raman regime if the parameter $4(\hat{\Omega}_p / \gamma_1^2 \hat{\Omega}_w^2)^{1/2} \gg 1$, where $\hat{\Omega}_p = \hat{\omega}_p / \gamma_1^{1/2}$ is the normalized relativistic plasma frequency, and $\hat{\Omega}_w = (eB_w / m_0 c) \times (1 / \gamma c k_w)$ is the normalized relativistic cyclotron frequency associated with the wiggler field. For the parameters of the present experiment, $4(\hat{\Omega}_p / \gamma_1^2 \hat{\Omega}_w^2)^{1/2} \sim 2-3$ and the inequality is only weakly satisfied. Such a simple criterion cannot be obtained to separate

Raman and Compton regimes in three dimensions. In this case, the regime of FEL operation has to be determined by a comparison of the experiment with the theory including or excluding the collective effects.

IV. RADIATION MEASUREMENTS

The total power, signal gain, and signal spectra are measured as functions of the electron beam energy and the applied wiggler field. The expected FEL frequency and the focusing of the electron beam provided by the thin solenoid lenses are affected by variations in the electron beam energy or the electron beam current. The beam energy and beam current are monitored on each discharge. On any discharge, a variation in the beam energy of greater than $\pm 1\%$, or a variation in the beam current of greater than $\pm 5\%$, from some predetermined "run values" result in that data being discarded. This procedure generally retained data from between 25%–50% of the discharges as "good." All data points shown in subsequent figures represent an average of three to seven good discharges.

The system growth rate is measured for two wiggler fields ($B_w = 1275$ G and $B_w = 1510$ G) by measuring the relative output power as a function of wiggler interaction length for a 2.0 MV, 780 A electron beam. The interaction length is varied by moving a transverse kicker magnet along the length of the wiggler, thereby turning the electron beam into the drift tube wall and terminating the FEL. The data shown in Fig. 6 clearly show the regions of exponential gain and, in the case of the greater wiggler field strength, the region of saturation onset. In the case of the 1275 G measurements, a gain of 56 dB/m is observed with an uncertainty of ± 3 dB/m. A higher gain of 70 dB/m is found for a wiggler field strength of 1510 G with an uncertainty of ± 6 dB/m.

The variation in the gain with the axial energy spread for these two cases has been studied with ARACHNE, and the

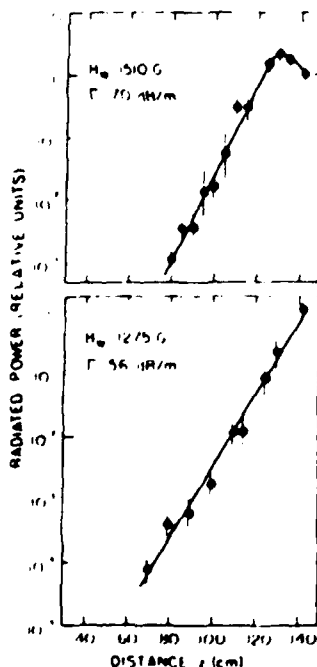


FIG. 6. Observed output power as a function of wiggler length, for two different wiggler pump strengths. (a) $B_w = 1275$ G, (b) $B_w = 1510$ G. The graph clearly shows the characteristic exponential gain, and in the case of the stronger pump field, the saturation of the FEL instability. Here $V = 2.0$ MV, $I = 780$ A.

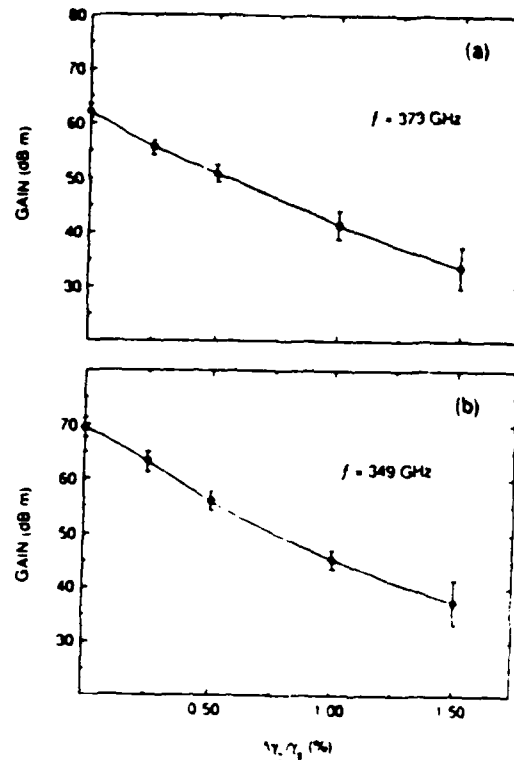


FIG. 7. Calculated gain as a function of axial energy spread due to electron beam emittance, $\Delta\gamma_1/\gamma_1$, for two different wiggler pump strengths. (a) $B_w = 1275$ G, (b) $B_w = 1510$ G. In both cases, $V = 2.0$ MV, $I = 780$ A, $r_w = 0.4$ cm. The frequency for which the gain is calculated is the frequency at peak growth, as noted in each case.

results are shown in Fig. 7. It should be noted that the axial energy spread here refers to that spread due to the electron beam emittance only. The simulation ignores the effects of space charge, but includes self-consistently any axial energy spread induced by the finite transverse gradient of the wiggler field. The maximum gain is obtained with a vanishing axial energy spread, $\Delta\gamma_1/\gamma_1 = 0$. For the case $B_w = 1275$ G, the calculated gain is found to be approximately 62 dB/m for $\Delta\gamma_1/\gamma_1 = 0$, and decreases to 56 dB/m for $\Delta\gamma_1/\gamma_1 = 0.25\%$. Similarly, for $B_w = 1510$ G, the gains calculated for $\Delta\gamma_1/\gamma_1 = 0$ and $\Delta\gamma_1/\gamma_1 = 0.25\%$ are 70 dB/m and 64 dB/m, respectively. When compared with the measured gains of 56 ± 3 dB/m (for $B_w = 1275$ G) and 70 ± 6 dB/m (for $B_w = 1510$ G), these results are consistent with an interpretation of a beam energy spread of less than or of the order of 0.25%. This is also in excellent agreement with the range calculated from the measured emittance given in Eq. (10) of 0.22%–0.40%. The value $\Delta\gamma_1/\gamma_1 = 0.25\%$ is used in all subsequent simulations.

The measured output spectra for beam voltages of 1.7, 2.0, and 2.3 MV are shown in Figs. 8–10, together with the spectra obtained with ARACHNE. These spectra are taken at a constant on-axis wiggler amplitude of 1275 G. In all cases the results of the ARACHNE simulations are in good agreement with the experiment. It is noteworthy that there are no free parameters in the simulations: All of the relevant parameters are given by measured values. The absolute calibration accuracy of the voltage monitor is $\sim 3\%$, and the spec-

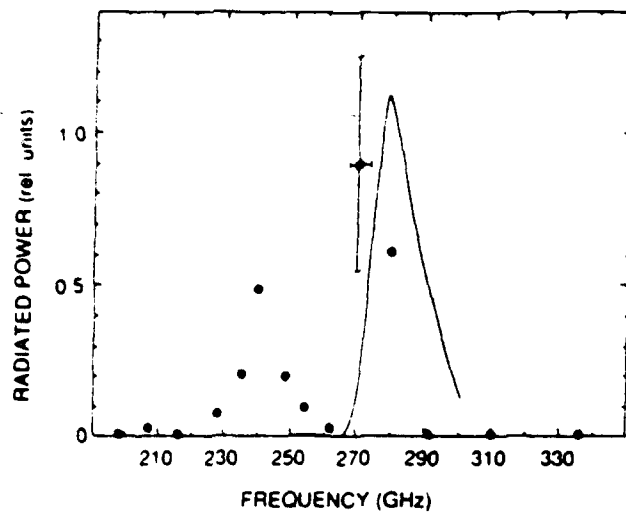


FIG. 8 The measured output spectrum for a 1.7 MV, 630 A electron beam for an on-axis wiggler field strength of 1275 G. The data are taken with a receiver that has a width covering ± 2.5 GHz. The curve is the calculated theoretical output spectrum for a 1.7 MV, 630 A electron beam with the measured electron beam radius $r_e = 0.36$ cm, using the nonlinear ARACHNE code. The measured output power is $P_{out} = 13$ MW.

tral peaks found by ARACHNE are within 2% of the peaks in the measured spectra. The measurement of the output spectrum for the 2.3 MV beam was carried out over an extended frequency range to investigate the presence of any other frequency components. Over the frequency range 110–650 GHz no other frequency components are observed. The dynamic range in observable signal for these measurements is greater than 20 dB.

A lone exception to the agreement between the experiment and the ARACHNE simulations is a lower frequency spectral feature at $f \sim 240$ GHz in the 1.7 MV data shown in Fig. 8, and believed to be emission in the TM_{11} waveguide

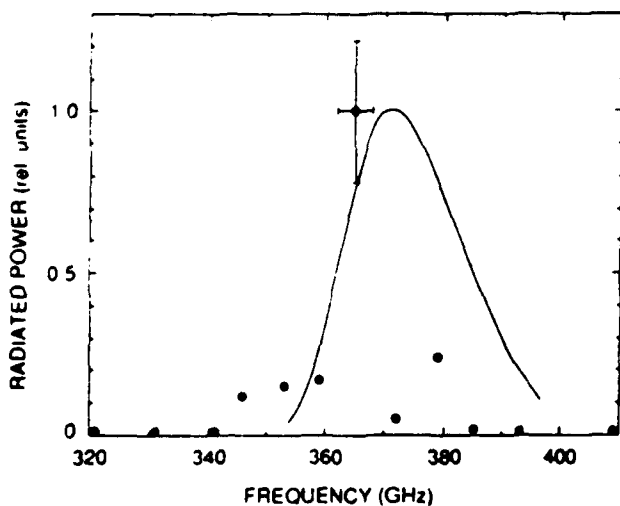


FIG. 9 The measured output spectrum for a 2.0 MV, 780 A electron beam, for an on-axis wiggler field strength of 1275 G. The data are taken with a receiver that has a width covering ± 3 GHz. The curve is the calculated theoretical output spectrum for a 2.0 MV, 780 A electron beam with the measured radius $r_e = 0.40$ cm, using the nonlinear ARACHNE code. The measured output power is $P_{out} = 14$ MW.

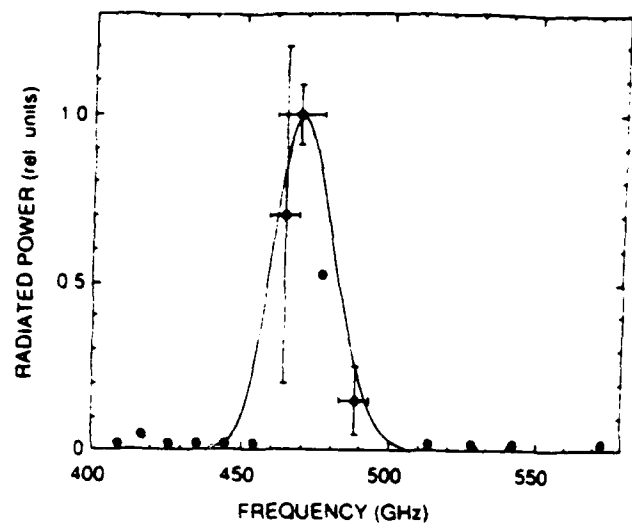


FIG. 10 The measured output spectrum for a 2.3 MV, 930 A electron beam, for an on-axis wiggler field strength of 1275 G. The data are taken with a receiver that has a width covering ± 4 GHz; the peak data point is taken with a receiver that has a width covering ± 8 GHz, which is less sensitive to discharge-to-discharge fluctuations. The relative sensitivities of the two receivers has been factored out of the data. The curve is the calculated theoretical output spectrum for a 2.3 MV, 930 A electron beam with the measured radius $r_e = 0.41$ cm, using the nonlinear ARACHNE code. The measured output is $P_{out} = 18$ MW.

mode where ARACHNE shows no significant radiation. Calculation of the interaction frequency for the TM_{11} waveguide mode using Eq. (15) gives $f = 243$ GHz, in good agreement with the lower frequency spectral feature in the data. In this calculation we have taken $p_1 = 1$, $p_2 = 0.3$, $\hat{\omega}_p = 0.49$, $\gamma = 4.33$, and $\gamma_1 = 4.02$, which is an average value obtained from numerical calculations that include the finite geometries of the wiggler field and the electron beam.¹⁴

V. DISCUSSION

We have described measurements of a free-electron laser operating at millimeter and submillimeter wavelengths. There is no axial magnetic field in this experiment. The focusing and transport of the electron beam through the wiggler interaction region is achieved by means of the bifilar helical wiggler field itself. A multielectrode field emission electron gun is used to generate an electron beam with low beam emittance; the full beam current is successfully injected and transported the full length (1.5 m) of the wiggler interaction region.

The FEL operates with electron beam voltages $V = 1.7$ –2.3 MV, beam currents $I = 630$ –930 A, and generates output frequencies tunable from $f = 240$ –470 GHz. It is important to point out that the radiation frequency depends sensitively on the waveguide mode in which the FEL operates. Our experiments indicate that the electron beam couples predominantly to the lowest TE_{11} mode despite the fact that the overmoded waveguide can support some 50 higher modes. We measure powers $P \sim 13$ –18 MW across the entire range of operation. The laser operates as a single-pass super-radiant amplifier, where the input signal arises either out of noise or from spontaneous emission. Along the length of the wiggler interaction region we measure signal gains of 56 dB/m for an applied wiggler field of $B_w = 1275$ G, and 70

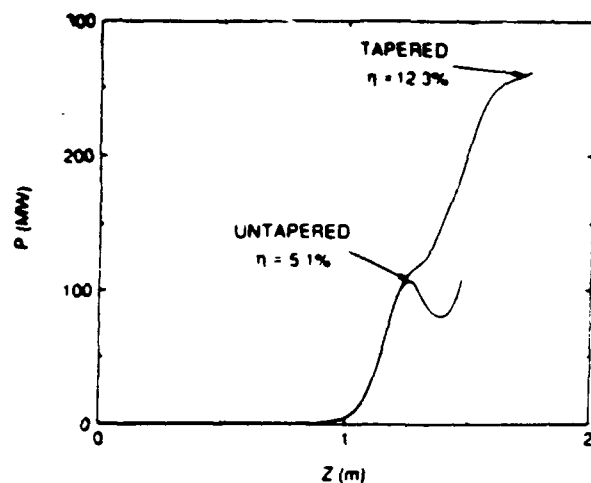


FIG. 11. The output power as a function of wiggler length for a tapered and an untapered wiggler. Here $V = 2.3$ MV, $I = 930$ A, $\lambda_w = 2.2$ cm, $f = 498$ GHz, $\Delta\gamma_1/\gamma_1 = 0.25\%$.

dB/m for $B_w = 1510$ G ($V = 2.0$ MV, $I = 780$ A, $\lambda_w = 3.14$ cm).

One-dimensional criteria would indicate our experiment is only weakly in the Raman regime. Three-dimensional effects, such as the finite geometries of the circular waveguide and the electron beam, may reduce the effective electron beam plasma frequency and push the experimental parameters closer to the transition region between the Raman and Compton regimes. In this case, a distinction of the experiment as being either in the Compton or Raman regime may not be possible nor fruitful.

In general, the measured values are in good agreement with a nonlinear numerical simulation, ARACHNE, which is valid in the strong-pump Compton regime of the FEL. The single exception to this agreement is the lower frequency spectral peak measured in the 1.7 MV electron beam case that is not predicted by the simulation. While all of the other spectral peaks are identified as predominantly TE_{11} waveguide mode interactions, a straightforward calculation of the FEL interaction frequency using the linear dispersion relation [Eq. (15)] from Sec. III, and including nonvanishing beam plasma frequency effects, indicates that the lower frequency spectral peak in Fig. 8 occurs where we might expect an interaction with the TM_{11} waveguide mode ($f = 243$ GHz).

Previous experiments have noted substantial increases in efficiency when the wiggler field amplitude is tapered.^{18,40} An example of the possible effect of tapering the wiggler field amplitude in this experiment is shown in Fig. 11, where the ARACHNE simulation is extended in the axial direction, for both a tapered and an untapered wiggler. The electron beam parameters for the simulation shown in Fig. 11 are identical to those in Fig. 10 used in comparison with our experiments. To optimize the tapering process, the wiggler period and initial wiggler field amplitude have been changed to $\lambda_w = 2.2$ cm and $B_w = 3100$ G, respectively. This results in a maximum possible output power of 263 MW at a frequency of 498 GHz, corresponding to an efficiency of $P_{RAD}/P_{BEAM} = 12.3\%$.

ACKNOWLEDGMENTS

This work was supported by the Air Force Office of Scientific Research, the National Science Foundation, and the Office of Naval Research.

- ¹L. R. Elias, W. M. Fairbank, J. M. J. Madey, H. A. Schwettman, and T. I. Smith, *Phys. Rev. Lett.* **36**, 717 (1976).
- ²M. Phillips, *IRE Trans. Electron. Devices* **ED-7**, 231 (1960).
- ³J. Fajans, G. Bekefi, Y. Z. Yin, and B. Lax, *Phys. Rev. Lett.* **53**, 246 (1984).
- ⁴S. H. Gold, D. L. Hardesty, A. K. Kirkpatrick, L. R. Barnett, and V. L. Granatstein, *Phys. Rev. Lett.* **52**, 1218 (1984).
- ⁵T. J. Orzechowski, B. Anderson, W. M. Fawley, D. Prosnitz, E. T. Scharlemann, S. M. Yarema, D. Hopkins, A. C. Paul, A. M. Sessler, and J. Wurtele, *Phys. Rev. Lett.* **54**, 889 (1985).
- ⁶V. L. Granatstein, S. P. Schlesinger, M. Herndon, and R. K. Parker, *Appl. Phys. Lett.* **30**, 384 (1977).
- ⁷D. B. McDermott, T. C. Marshall, S. P. Schlesinger, R. K. Parker, and V. L. Granatstein, *Phys. Rev. Lett.* **41**, 1368 (1978).
- ⁸D. A. Kirkpatrick, R. E. Shefer, and G. Bekefi, *J. Appl. Phys.* **57**, 5011 (1985).
- ⁹P. Diament, *Phys. Rev. A* **23**, 2537 (1981).
- ¹⁰P. Sprangle and A. T. Drobot, *IEEE Trans. Microwave Theory Technol.* **MTT-25**, 528 (1977).
- ¹¹J. A. Pasour, R. F. Lucey, and C. Kapetanakis, *Phys. Rev. Lett.* **53**, 1728 (1984).
- ¹²A. K. Ganguly and H. P. Freund, *Phys. Rev. A* **32**, 2275 (1985).
- ¹³H. P. Freund and A. K. Ganguly, *Phys. Rev. A* **33**, 1060 (1986).
- ¹⁴H. P. Freund and A. K. Ganguly, *Phys. Rev. A* **34**, 1242 (1986).
- ¹⁵A. K. Ganguly and H. P. Freund, *IEEE Trans. Plasma Sci.* **16**, 167 (1988).
- ¹⁶H. P. Freund and A. K. Ganguly, *J. Quantum Electron.* **QE-23**, 1657 (1987).
- ¹⁷P. Sprangle, R. A. Smith, and V. L. Granatstein, in *Infrared and Millimeter Waves*, edited by K. J. Button (Academic, New York, 1979), Vol. 1.
- ¹⁸W. Dommaschk (private communication).
- ¹⁹G. Bekefi, F. Hartemann, and D. A. Kirkpatrick, *J. Appl. Phys.* **62**, 1564 (1987).
- ²⁰C. Fert and P. Durandau, *Focussing of Charged Particles* (Academic, New York, 1967), Chap. 2.3, Vol. 1.
- ²¹P. Grivet, *Electron Optics* (Pergamon, Oxford, England, 1965), Chap. 7.
- ²²V. K. Neil (private communication).
- ²³T. P. Wangler, K. R. Crandall, R. S. Mills, and M. Reiser, *IEEE Trans. Nucl. Sci.* **NS-32**, 2196 (1985).
- ²⁴J. Fajans, *J. Appl. Phys.* **55**, 43 (1984).
- ²⁵J. Fisher, D. A. Bryd, and A. Cavallo, *Rev. Sci. Instrum.* **54**, 1085 (1983).
- ²⁶N. M. Kroll and W. A. McMullin, *Phys. Rev. A* **17**, 300 (1978).
- ²⁷L. Friedland, *Phys. Fluids* **23**, 2376 (1980).
- ²⁸H. P. Freund and A. K. Ganguly, *Phys. Rev. A* **28**, 1438 (1983).
- ²⁹H. S. Uhm and R. C. Davidson, *Phys. Fluids* **26**, 288 (1983).
- ³⁰G. M. Branch and T. G. Miharn, *IRE Trans. Electron. Devices* **ED-2**, 3 (1955).
- ³¹R. E. Tritman, *Longitudinal Space Charge Waves* (Chapman and Hall, London, 1966).
- ³²A. Gover and P. Sprangle, *IEEE J. Quantum Electron.* **QP-17**, 1146 (1981).
- ³³W. M. Fawley, D. Prosnitz, and E. T. Scharlemann, *Phys. Rev. A* **30**, 2472 (1984).
- ³⁴J. Wurtele, E. T. Scharlemann, and A. Sessler, *Nucl. Instrum. Methods* **A250**, 176 (1986).
- ³⁵S. K. Dutt, A. Friedman, A. Gover, and C. Pellegrini, *Nucl. Instrum. Methods* **A272**, 564 (1988).
- ³⁶J. A. Byers and R. H. Cohen, *Nucl. Instrum. Methods* **A272**, 595 (1988).
- ³⁷H. P. Freund, *Phys. Rev. A* **37**, 3371 (1988).
- ³⁸T. J. Orzechowski, B. Anderson, J. C. Clark, W. M. Fawley, A. C. Paul, D. Prosnitz, E. T. Scharlemann, S. M. Yarema, D. Hopkins, A. M. Sessler, and J. Wurtele, *Phys. Rev. Lett.* **57**, 2172 (1986).
- ³⁹J. Fajans, D. A. Kirkpatrick, and G. Bekefi, *Phys. Rev. A* **32**, 3448 (1985).
- ⁴⁰H. Boehmer, M. Z. Caponi, J. Edighoffer, S. Fornaca, J. Munch, G. R. Neil, B. Saur, and C. Shih, *Phys. Rev. Lett.* **48**, 141 (1982).

APPENDIX V

High Efficiency Operation of Free-Electron Laser Amplifiers

by

A.K. Ganguly and H.P. Freund

High-Efficiency Operation of Free-Electron-Laser Amplifiers

A. K. GANGULY AND H. P. FREUND

Abstract—A high-efficiency regime is studied for free-electron-laser (FEL) amplifier configurations that employ a helically symmetric wiggler and a uniform axial guide magnetic field. Efficiencies of the order of 50 percent are found to be possible in the presence of axial fields sufficiently strong that the Larmor period is shorter than the wiggler period. This operating regime is accessible for electron beam energies greater than approximately 400 keV.

THE EXISTENCE of an operating regime of extremely high efficiency and broad bandwidth has been identified in simulation recently [1] for free-electron-laser (FEL) amplifier configurations that employ both a helically symmetric wiggler and an axial guide magnetic field. A detailed description of the formulation is given in [1], in which a fully three-dimensional nonlinear analysis of the FEL amplifier is derived for a configuration in which an energetic electron beam is propagating through a loss-free cylindrical waveguide in the presence of the external magnetic fields. To this end, a set of coupled nonlinear differential equations is derived, which self-consistently describes the evolution of both an ensemble of electrons and the electromagnetic fields. Space-charge fields are neglected in the analysis; hence, the treatment is applicable to the high-gain Compton (or strong-pump) regime. This is generally valid as long as the electron beam plasma frequency (ω_b) is sufficiently small that

$$\frac{\omega_b}{\gamma^{3/2}ck_w} \ll \frac{p_w^2/m^2c^2}{(1 + p_w^2/m^2c^2)^{3/2}}$$

where p_w is the transverse wiggler-induced momentum, and $(\gamma - 1)mc^2$ is the kinetic energy of the beam. In the absence of an axial guide magnetic field $|p_w/mc| = \Omega_w/k_w c$, where $\Omega_w = |eB_w/mc|$, B_w is the wiggler amplitude, and $k_w (= 2\pi/\lambda_w)$ is the wiggler wavenumber. However, the presence of the axial guide field enhances the transverse momentum [7]. In particular, $\Omega_w/ck_w = 0.28$ for the parameters shown in Fig. 1, while $p_w/mc = 1.16$. For this case, $\omega_b/\gamma^{3/2}ck_w = 0.05$, and, as a con-

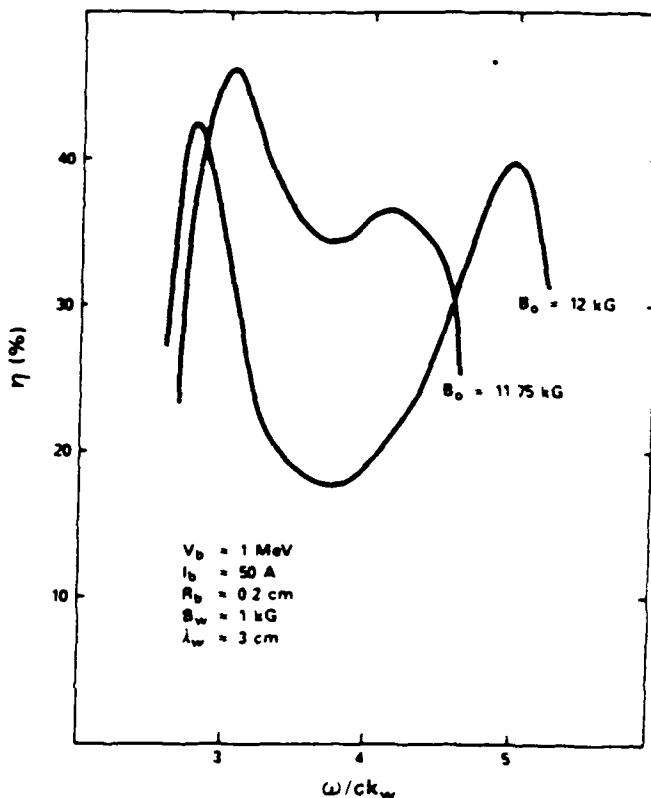


Fig. 1. Graph of the efficiency versus frequency for a 1-MeV beam TE_{11} mode ($R_b = 0.5$ cm, $P_{in} = 1$ kW)

sequence, the space-charge effects are small and the Compton regime approximation is valid. The nonlinear current which mediates the interaction is computed from the microscopic behavior of an ensemble of electrons by means of an average of the electron phases relative to the ponderomotive wave formed by the beating of the radiation and wiggler fields. The finite waveguide geometry is included in the analysis by the introduction of the boundary conditions appropriate for either the transverse electric (TE) or transverse magnetic (TM) modes in a cylindrical waveguide. In addition, since the problem of interest is that of an FEL amplifier, only single-wave-mode propagation is considered, which permits an average over a wave period to be performed that eliminates the fast-time-scale phenomena from the formulation.

A complete derivation of the dynamical equations is given in [1], and we restate the equations here in the interest of clarity. The external magnetostatic fields de-

Manuscript received August 11, 1987; revised October 30, 1987. This work was supported by the Office of Naval Research and the Office of Naval Technology.

A. K. Ganguly is with the Naval Research Laboratory, Washington, DC 20375-5000.

H. P. Freund is with Science Applications International Corp., McLean, VA 22102.

IEEE Log Number 8719467.

scribe the superposition of a uniform axial guide field and a helical wiggler field:

$$\mathbf{B}(x) = B_0 \hat{e}_z + \mathbf{B}_w(x) \quad (1)$$

where

$$\begin{aligned} \mathbf{B}_w(x) = 2B_w(z) [I'_1(\lambda) \hat{e}_r \cos \chi \\ - \frac{1}{\lambda} I_1(\lambda) \hat{e}_\theta \sin \chi + I_1(\lambda) \hat{e}_z \sin \chi] \quad (2) \end{aligned}$$

$B_{0,w}$ describe the amplitudes of the axial guide and wiggler magnetic fields, $\lambda = k_w r$, $\chi = \theta - k_w z$, $k_w (= 2\pi/\lambda_w)$, where λ_w is the wiggler wavelength), and I_n and I'_n represent the modified Bessel function of order n and its derivative. The adiabatic injection of the electron beam is modeled by allowing the wiggler amplitude to increase slowly from zero to a constant value over N_w wiggler periods, and we assume that

$$B_w(z) = \begin{cases} B_w \sin^2(k_w z/4N_w), & 0 \leq z \leq N_w \lambda_w \\ B_w, & z > N_w \lambda_w \end{cases} \quad (3)$$

We restrict the analysis to TE modes and write the vector potential of the radiation field in the form

$$\begin{aligned} \delta \mathbf{A}(x, t) = \sum_{l=0}^{\infty} \delta A_{ln}(z) \left[\frac{l}{k_{ln} r} J_l(k_{ln} r) \hat{e}_r \sin \alpha_l \right. \\ \left. + J'_l(k_{ln} r) \hat{e}_\theta \cos \alpha_l \right] \quad (4) \end{aligned}$$

where for frequency ω and wavenumber $k(z)$,

$$\alpha_l = \int_0^z dz' k(z') + l\theta - \omega t \quad (5)$$

J_l and J'_l are the regular Bessel function of the first kind of order l and its derivative, and k_{ln} describes the vacuum cutoff of the mode. It is implicitly assumed in this formulation that both the mode amplitude $\delta A_{ln}(z)$ and wavenumber are slowly varying functions of axial position.

Substitution of the fields into Maxwell's equations yields the following equations for the amplitude and wavenumber:

$$\begin{aligned} \frac{d^2}{dz^2} \delta a_{ln} + \left(\frac{\omega^2}{c^2} - k^2 - k_{ln}^2 \right) \delta a_{ln} \\ = \frac{\omega_b^2}{c^2} \beta_{z0} H_{ln} \left\langle \frac{v_1 T_l^{(+)} + v_2 W_l^{(+)}}{|v_z|} \right\rangle \quad (6) \end{aligned}$$

and

$$\begin{aligned} 2k^{1/2} \frac{d}{dz} (k^{1/2} \delta a_{ln}) \\ = \frac{\omega_b^2}{c^2} \beta_{z0} H_{ln} \left\langle \frac{v_1 W_l^{(+)} - v_2 T_l^{(+)}}{|v_z|} \right\rangle \quad (7) \end{aligned}$$

where $\delta a_{ln} = e \delta A_{ln} / mc^2$, ω_b is the bulk plasma frequency of the beam, $\beta_{z0} = v_{z0}/c$ (v_{z0} is the initial axial velocity of the beam), and (v_1, v_2) are the components of

the transverse velocity relative to the basis vectors $\hat{e}_1 = \hat{e}_r \cos k_w z + \hat{e}_\theta \sin k_w z$ and $\hat{e}_2 = -\hat{e}_r \sin k_w z + \hat{e}_\theta \cos k_w z$. In addition, H_{ln} , $T_l^{(\pm)}$, and $W_l^{(\pm)}$ are polarization dependent functions defined as

$$H_{ln} = \frac{(x'_{ln})^2}{[(x'_{ln})^2 - l^2] J_l^2(x'_{ln})} \quad (8)$$

and

$$\begin{aligned} T_l^{(\pm)} &= F_l^{(\pm)} \sin \psi_l + G_l^{(\pm)} \cos \psi_l \\ W_l^{(\pm)} &= F_l^{(\pm)} \cos \psi_l - G_l^{(\pm)} \sin \psi_l \quad (9) \end{aligned}$$

where

$$\psi_l = \psi_0 + \int_0^z dz' \left(k + lk_w - \frac{\omega}{v_z} \right) \quad (10)$$

is the ponderomotive phase, and

$$\begin{aligned} F_l^{(\pm)} &= J_{l-1}(k_{ln} r) \cos[(l-1)\chi] \\ &\quad \pm J_{l+1}(k_{ln} r) \cos[(l+1)\chi] \\ G_l^{(\pm)} &= J_{l-1}(k_{ln} r) \sin[(l-1)\chi] \\ &\quad \pm J_{l+1}(k_{ln} r) \sin[(l+1)\chi]. \quad (11) \end{aligned}$$

Finally, the average operator $\langle (\dots) \rangle$ is defined over an ensemble of the initial conditions (i.e., at $z = 0$) of the beam as

$$\begin{aligned} \langle (\dots) \rangle &= \frac{1}{2\pi^2 R_b^2} \int_{-\pi}^{\pi} d\psi_0 \sigma_1(\psi_0) \\ &\quad \cdot \int \int_{A_t} d\theta_0 dr_0 r_0 \sigma_\perp(r_0, \theta_0) (\dots) \quad (12) \end{aligned}$$

where $\sigma_1(\psi_0)$ and $\sigma_\perp(r_0, \theta_0)$ describe the initial distribution of the beam in phase and cross section. For simplicity, we choose a continuous beam (i.e., $\sigma_1(\psi_0) = 1$ for $-\pi \leq \psi_0 \leq \pi$) with a uniform cross section ($\sigma_\perp(r_0, \theta_0) = 1$ for $r_0 \leq R_b$).

In order to complete the formulation, the electron orbit equations must be specified in the presence of the static and fluctuating fields. Since we describe an amplifier configuration, we choose to integrate in z and write the Lorentz force equations in the form

$$v_z \frac{d}{dz} \mathbf{p} = -e \delta \mathbf{E}_{ln} - \frac{e}{c} \mathbf{v} \times (\mathbf{B}_0 + \mathbf{B}_w + \delta \mathbf{B}_{ln}) \quad (13)$$

where

$$\begin{aligned} \delta \mathbf{E}_{ln} &= -\frac{1}{c} \frac{\partial}{\partial t} \delta \mathbf{A}_{ln} \\ \delta \mathbf{B}_{ln} &= \nabla \times \delta \mathbf{A}_{ln}. \quad (14) \end{aligned}$$

In addition, we also integrate

$$v_z \frac{d}{dz} x = v_1 \cos k_w z - v_2 \sin k_w z \quad (15)$$

$$v_z \frac{d}{dz} v = v_1 \sin k_w z + v_2 \cos k_w z \quad (16)$$

and

$$\frac{d}{dz} \psi = k + ik_w - \frac{\omega}{v_z} \quad (17)$$

As a result, there are $6N$ particle equations (N is the total number of electrons in the analysis) that must be integrated simultaneously with the field equations.

The particular case of interest is the strong guide-field regime in which the electron Larmor period is shorter than the wiggler period (i.e., $\Omega_0 > \gamma k_w v_z$, where $\Omega_0 \equiv |eB_0/mc|$, B_0 is the magnitude of the axial field, and v_z is the axial electron velocity). It has been well established that operation near the magnetic resonance at $\Omega_0 = \gamma k_w v_z$ results in enhancements in the transverse wiggler velocity, the linear gain, and the nonlinear saturation efficiency [2], [3]. In the present paper, we are concerned with a regime of extremely high intrinsic efficiency found to occur for strong guide fields near the resonance $\Omega_0 \geq \gamma k_w v_z$. The specific case is shown in Fig. 1, in which we plot the efficiency (η) versus frequency for a 35-GHz amplifier operating in the TE₁₁ mode and which involves the propagation of a beam with 1-MeV energy, 50-A current, and 0.2-cm initial radius through a drift tube of radius $R_d = 0.5$ cm. The magnetic fields are given by $B_0 = 11.75$ kG, $B_w = 1.0$ kG, and $\lambda_w = 3.0$ cm. As is evident from the figure, a maximum efficiency $\eta = 47$ percent is found in the vicinity of 35 GHz with a bandwidth of approximately 57 percent. It should be noted that a recent experiment [4] has demonstrated operation of a 35-GHz FEL amplifier with an efficiency of 35 percent by means of a linearly polarized wiggler field with a tapered amplitude. The effect of the tapered wiggler is to accelerate the beam and maintain the wave-particle resonance (i.e., $\omega = (k + k_w)v_z$) over an extended interaction length, thereby enhancing the efficiency [5], [6]. In contrast, the configuration described herein requires no tapering of the external magnetic fields.

The physical explanation for the high efficiency associated with the strong guide-field regime is rooted in the magnetic resonance at $\Omega_0 = \gamma k_w v_z$. Since the transverse velocity and the ponderomotive potential are resonantly enhanced by the axial guide field, both the interaction strength (i.e., growth rate) and bandwidth are also greater. In particular, the enhanced bandwidth implies that an electron can yield a relatively larger fraction of its energy to the wave (in comparison with the weak guide-field regime) before the wave-particle resonance is broken. The effect of the guide field, therefore, is to increase the amount of energy which can be extracted from the beam. It should be remarked, however, that the enhanced growth rates found near resonance lead to shorter overall interaction lengths. This efficiency enhancement occurs both above ($\Omega_0 \geq \gamma k_w v_z$) and below ($\Omega_0 \leq \gamma k_w v_z$) the resonance; however, the effect is more pronounced in the strong guide-field regime above the resonance. The rea-

son for this is that the resonant effect itself makes injection of the electron beam into the wiggler difficult, and there is a point of diminishing returns as the resonance is approached beyond which the efficiency begins to decrease [3]. Thus, a practical experiment cannot be operated arbitrarily close to the resonance. However, it is found that the resonance can be more closely approached in the strong guide-field regime, and this is the fundamental source for the high efficiencies found.

The principal issue we address in this paper is the extension of this high-efficiency regime to lower beam energies. In so doing, we observe that the high-efficiency example shown in Fig. 1 occurs when the beam resonance line falls slightly below the vacuum waveguide dispersion curve ($\omega^2 = c^2 k^2 + \omega_{co}^2$, where ω_{co} denotes the cutoff frequency of the mode). This occurs when

$$\omega_{co} \geq \gamma_z k_w v_z \quad (18)$$

where $\gamma_z \equiv (1 - v_z^2/c^2)^{-1/2}$, and no intersection between these lines is found. The interaction is possible because the dielectric effect of the beam results in a shift in the waveguide mode dispersion curve. It should be remarked that the highest operating efficiencies are found in this "below-grazing" regime for a wide variety of microwave devices. Thus, in extending this regime to lower beam energies, we shall vary the parameters of the system in such a way as to maintain this "below-grazing" condition (18).

The first example we consider is that of an 800-keV electron beam, shown in Fig. 2. For this case of a lower energy, the magnetic resonance condition requires that the axial field also be reduced, and we choose $B_0 = 10.5$ kG. In addition, the cutoff frequency must be decreased in order for the interaction to remain slightly "below-grazing," and we choose $R_d = 0.54$ cm, 0.55 cm, and 0.56 cm. The maximum efficiency for this case is of the order of 40 percent, which is somewhat reduced relative to the 1-MeV beam example shown in Fig. 1. However, it should be noted that the magnetic resonance becomes "sharper" as the beam energy is reduced, in the sense that the linear gain and nonlinear efficiency change more rapidly with variations in the operational parameters. Hence, it may be possible to optimize the 800-keV example to achieve efficiencies approaching 50 percent over a narrow range of operating parameters.

Indeed, the sensitivity of the interaction to fluctuations in the operational parameters in the vicinity of the magnetic resonance for beam energies ≤ 400 keV represents a critical practical limitation of this concept to low-voltage applications. However, for beam energies greater than about 400 keV, this resonant interaction appears to be a realizable approach to high-efficiency FEL amplifiers without the necessity of tapered wiggler fields. Examples of the spectrum of the efficiency versus frequency are shown in Figs. 3 and 4 for beam energies of 600 and 400 keV, respectively. Observe that the bandwidth $\Delta\omega/\omega > 50$ percent for all examples shown, and it appears to be relatively insensitive to the voltage over this range.

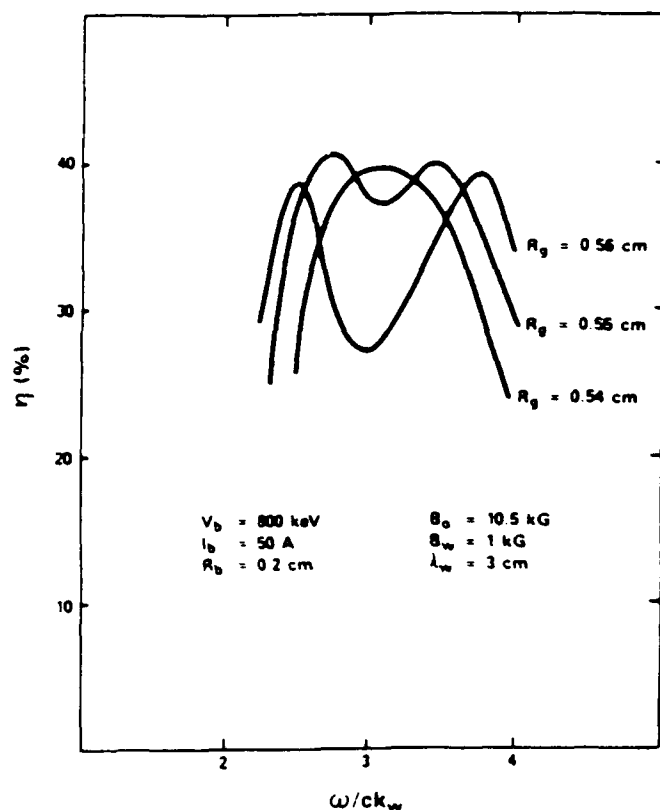


Fig. 2. Graph of the efficiency versus frequency for an 800-keV beam, TE₁₁ mode ($P_{in} = 1$ kW).

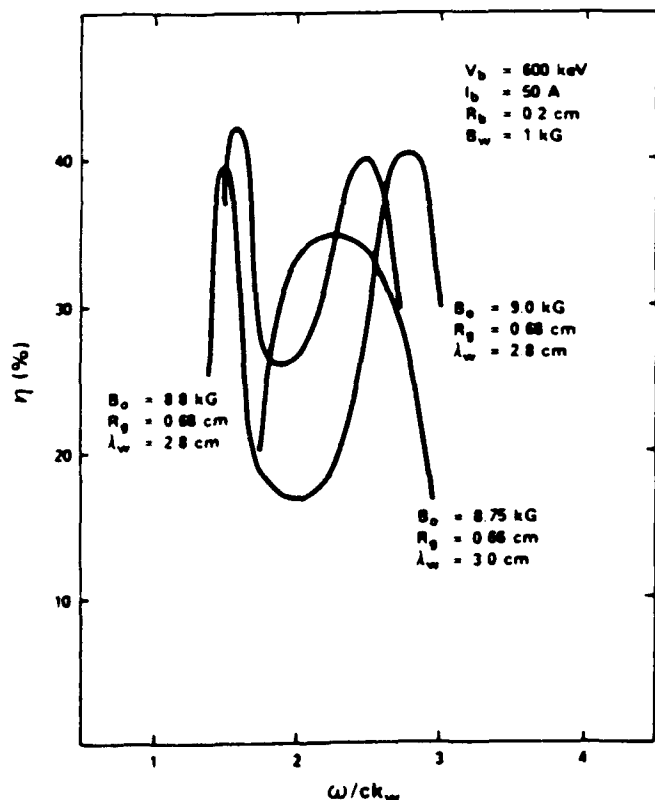


Fig. 3. Graph of the efficiency versus frequency for a 600-keV beam, TE₁₁ mode ($P_{in} = 1$ kW).

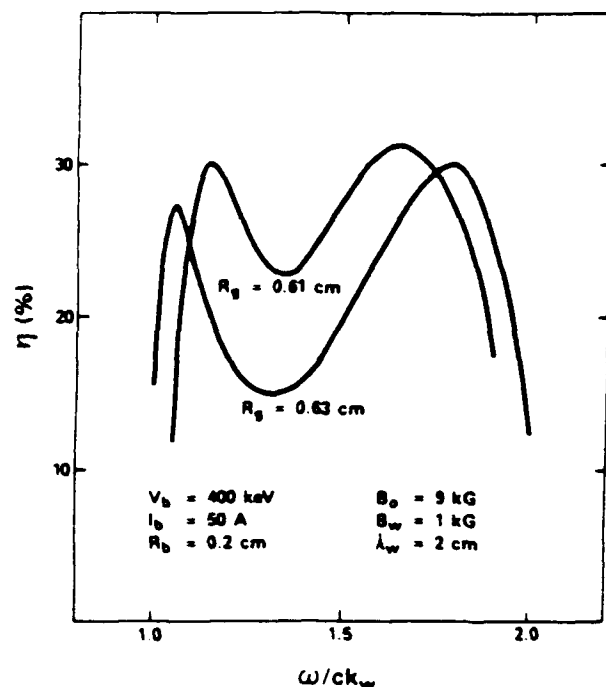


Fig. 4. Graph of the efficiency versus frequency for a 400-keV beam, TE₁₁ mode ($P_{in} = 1$ kW).

Finally, an important consideration in the design of FEL's is the effect of electron beam quality on the interaction. The results shown in Figs. 1–4 were obtained under the assumption of a monoenergetic, zero-emittance [8] electron beam, and the saturation mechanism is that of electron trapping in the ponderomotive potential formed by the beating of the wiggler and radiation fields. This type of saturation mechanism is extremely sensitive to the axial energy spreads of the electron beam, and even relatively small energy spreads (i.e., $\Delta\gamma_z/\gamma_0 \sim 1$ percent) often result in substantial decreases in the efficiency. However, recent simulation results [9] indicate that the axial magnetic field acts to reduce the sensitivity of the interaction to the beam thermal spread due to a resonant enhancement in the ponderomotive potential. As a result, the extremely high efficiencies found in this strong axial field resonant regime occur in conjunction with an increased tolerance for beam thermal effects. The sensitivity of the interaction to the axial energy spread in this regime is illustrated in Fig. 5 in which we plot the normalized efficiency η/η_0 versus the axial energy spread for the 1-MeV and 400-keV cases, where η_0 refers to the efficiency obtained in the limit of $\Delta\gamma_z = 0$. The 1-MeV results correspond to the $B_0 = 11.75$ kG curve shown in Fig. 1 for $\omega/ck_w = 3.0$, and indicate that the efficiency declines by an order of magnitude as the axial energy increases to $\Delta\gamma_z/\gamma_0 = 5$ –6 percent. As discussed in [9], this represents a relatively slow decline of efficiency with axial energy spread. In contrast, the 400-keV results (corresponding to the curve in Fig. 4 for which $R_g = 0.63$ cm and $\omega/ck_w = 1.7$) show *even less* sensitivity to the axial energy spread. The reason for this decrease in sensitivity

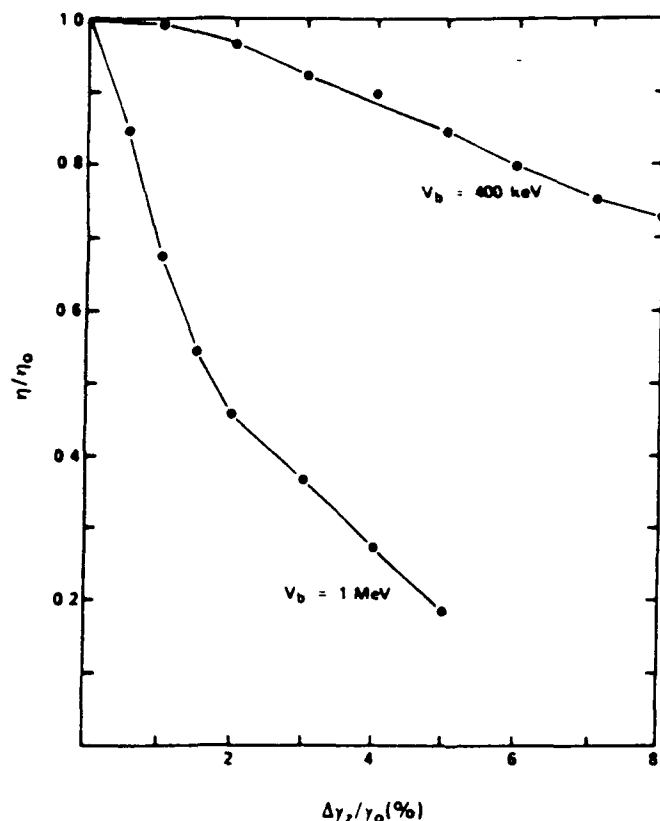


Fig. 5. Graph of the normalized efficiency versus $\Delta\gamma/\gamma_0$ for $V_b = 1$ MeV and $V_b = 400$ keV.

to $\Delta\gamma$ is that the lower energy example corresponds to operation much closer to the resonance at $\Omega_0 \sim \gamma k_u v_z$. It should be noted, however, that while operation close to the resonance is beneficial from the standpoint of easing the requirements on beam energy spread, the *ultimate* price paid is the increased sensitivity to fluctuations in the operating parameters.

Finally, we address the question of the accessibility of this regime to higher frequency operation. The two constraints on this high-efficiency regime appear to be that $\Omega_0 \gtrsim \gamma k_u v_z$, and that there be a near-grazing intersection between the fundamental TE_{11} mode dispersion curve and the beam resonance line (i.e., $\omega_{11} \sim \gamma k_u v_z$). If we note that the operating frequency for near-grazing intersections scales as $\omega \sim \gamma k_u v_z$, then we must require that B_0 (kG) $\gtrsim 0.36 f$ (GHz)/ γ and R_x (cm) $\leq 8.8/f$ (GHz). As a result, higher operating frequencies require progressively higher axial fields and smaller waveguides. As an exam-

ple, consider operation at 600 GHz, which is thought to be necessary for the cyclotron resonance heating of controlled thermonuclear plasmas. If a 1-MeV beam is to be employed, then the axial field must exceed 72 kG and the waveguide radius must be of the order of 0.15 mm, which are difficult targets to attain. Of these two requirements, the axial field is the least restrictive since 1) superconducting solenoids can achieve such fields, and 2) higher energy beams would lower the field requirement. The constraint on the waveguide radius, however, is independent of the beam energy. Indeed, the necessity of such a narrow waveguide imposes practical limitations due to difficulties in both the production of such thin electron beams and the propagation of high-radiation power densities through the waveguide. In contrast, if an operating frequency of 140 GHz is desired, then the requirements become $B_0 \gtrsim 16.8$ kG (for $V_b = 1$ MeV) and $R_x \leq 0.63$ mm. Thus, we conclude that 600 GHz is an impractically high operating frequency for this regime, and expectations of scaling the frequency to the vicinity of 140 GHz also appear to be difficult.

ACKNOWLEDGMENT

The authors would like to thank Dr. R. K. Parker, Dr. R. H. Jackson, and Dr. D. E. Pershing.

REFERENCES

- [1] A. K. Ganguly and H. P. Freund, "Nonlinear analysis of free-electron laser amplifiers in three dimensions," *Phys. Rev. A*, vol. 32, pp. 2275-2286, 1985.
- [2] L. Friedland and J. L. Hirshfield, "Free-electron laser with a strong axial magnetic field," *Phys. Rev. Lett.*, vol. 44, pp. 1456-1460, 1980.
- [3] H. P. Freund, "Nonlinear analysis of free-electron laser amplifiers with axial guide fields," *Phys. Rev. A*, vol. 27, pp. 1977-1988, 1983.
- [4] T. J. Orzechowski *et al.*, "High efficiency extraction of microwave radiation from a tapered wiggler free-electron laser," *Phys. Rev. Lett.*, vol. 57, pp. 2172-2175, 1986.
- [5] P. Sprangle, C. M. Tang, and W. Manheimer, "Nonlinear formulation and efficiency enhancement of free-electron lasers," *Phys. Rev. Lett.*, vol. 43, pp. 1932-1936, 1979.
- [6] N. M. Kroll, P. L. Morton, and M. N. Rosenbluth, in *Physics of Quantum Electronics: Free-Electron Generators of Coherent Radiation*, vol. 7, S. F. Jacobs, H. S. Pilloff, M. Sargent, M. O. Scully, and R. Spitzer, Eds. Reading, MA: Addison-Wesley, 1980, chs 4 and 5, p. 89.
- [7] P. Diament, "Electron orbits and stability in realizable and unrealizable wigglers of free-electron lasers," *Phys. Rev. A*, vol. 23, pp. 2537-2552, 1981.
- [8] J. D. Lawson, *The Physics of Charged Particle Beams*. Oxford, England: Oxford Univ. Press, 1977, ch. 4.
- [9] H. P. Freund and A. K. Ganguly, "Effect of beam quality on the free-electron laser," *Phys. Rev. A*, vol. 34, pp. 1242-1246, 1986.

APPENDIX VI

The Ku-Band Ubitron Experiment at the Naval Research Laboratory

by

D.E. Pershing, R.H. Jackson, H.P. Freund, and H. Bluem

THE K_u-BAND UBITRON EXPERIMENT AT THE NAVAL RESEARCH LABORATORYD.E. PERSHING ^{*}, R.H. JACKSON, H.P. FREUND ^{*} and H. BLUEM [†]*Electronics Science and Technology Division, Naval Research Laboratory, Washington, DC 20375, USA*

Operation of a ubitron/FEL amplifier with a helical wiggler/axial guide field configuration in the frequency band from approximately 13 to 18 GHz is reported. The experiment employs a 190-250 keV electron beam with currents up to 37 A, and has been operated using the fundamental wiggler harmonic interaction with the TE₁₁ circular waveguide mode. The wiggler is a bifilar helix with a 2.54 cm period and a total length of 50 cm, and is capable of achieving an amplitude of 575 G or more in pulsed mode. The wiggler is flared both on entry and exit in order to obtain smooth transitions in the beam trajectory with 12 periods of uniform amplitude. Small signal gains as high as 17-19 dB have been observed, corresponding to a gain per free-space wavelength approaching 1.25 dB/λ. The experimental results are in reasonable agreement with nonlinear simulation of the interaction in the Raman regime.

1. Introduction

The Naval Research Laboratory has instituted a program to investigate the ubitron/FEL interaction [1-3] as the basis for a new class of high-power, broadband micro- and millimeter-wave amplifiers. Attractive features of the ubitron include high power (due to the fast-wave nature of the interaction), high gain, relatively broad instantaneous bandwidth, high-frequency operation, and compatibility with space-charge-limited, laminar-flow electron gun configurations. The NRL program consists of both theoretical and experimental efforts to explore ubitron performance and identify critical technology issues. Close coupling between theory and experiment is designed to permit a detailed comparison and validation of the theory and resulting design codes. The program will also address areas such as gain and efficiency enhancement techniques, harmonic operation and alternate interaction geometries.

The present experiment has been designed to ameliorate technological constraints where possible and to provide a test bed for scaling to more interesting parameter ranges. In order to facilitate comparison with theory, the interaction occurs between a solid, uniform-density cylindrical beam propagating in a transverse helical magnetic field and a circularly polarized TE₁₁ cylindrical waveguide mode. An axial magnetic field

provides beam focusing and transport, and, in addition, permits gyroresonant enhancement of the wiggler field and efficiency enhancement by axial field tapering. The performance goals for the amplifier are a 30 dB large signal gain (2-3 dB/λ), a saturated instantaneous bandwidth greater than or of the order of 20%, and an efficiency greater than 15% (without enhancement techniques). These values are considered sufficient to demonstrate the potential of the ubitron as a practical alternative for high-power, high-frequency rf generation.

2. K_u-band ubitron amplifier

A schematic representation of the present experimental configuration is shown in fig. 1 and consists of a modified SLAC klystron electron gun, an injected-current monitor, a modified turnstile rf input coupler, a double tapered bifilar helix wiggler and solenoid magnets, a transmitted-current monitor, rf output monitors and a water calorimeter/load. Details of component designs and performance have been reported elsewhere [4,5]. Operation in the K_u-band as a single-stage amplifier was chosen because of equipment and diagnostic availability, and reduced constraints on beam quality and fabrication tolerances.

Three modifications have recently been made to the experiment to correct problems and improve performance. The iron pole piece at the front of the solenoid was modified to alter the field profile in the electron gun. Electron trajectory calculations using the revised magnetic field profile indicate that the axial velocity spread of the beam as it exits the input coupler falls within the range $0.26\% \geq \Delta v/v_1 \geq 0.023\%$, depending

^{*} Permanent address: Mission Research Corporation, Newington, VA 22122, USA.

[†] Permanent address: Science Applications International Corporation, McLean, VA 22102, USA.

[‡] Permanent address: Electrical Engineering Department, University of Maryland, College Park, MD 20742, USA.

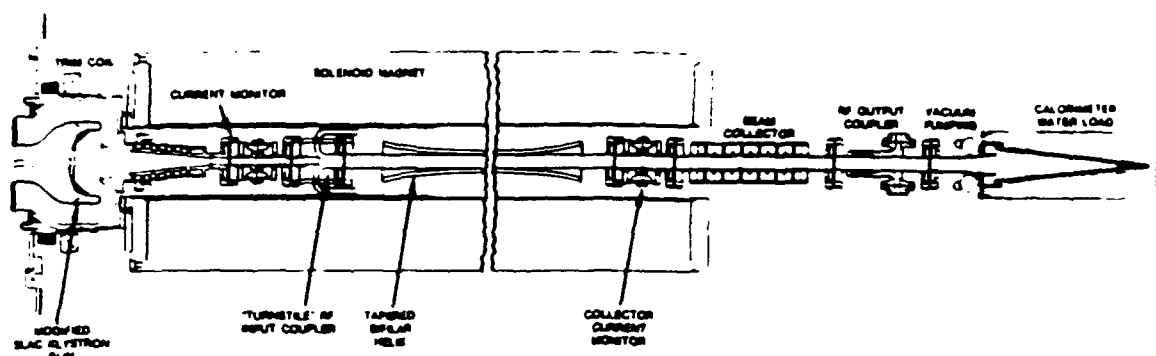


Fig. 1. A schematic illustration of the ubitron experiment.

on the trim coil setting. Comparison of measured macroscopic beam quantities, such as total diode current and transmitted current, shows good agreement with code calculations. Hence, although the quality of the extracted beam has not been directly measured, this agreement suggests that the beam quality has indeed been improved. However, as discussed in more detail below, results from a nonlinear simulation of the interaction indicate that the assumption of a 1% velocity spread is a better match to the experiment.

The wiggler has been rewound to repair damage resulting from a coolant flow failure. To prevent poisoning of the oxide-coated cathode, the new windings were wrapped while the tube was still under vacuum, precluding use of the original wire and winding technique. Although the present wiggler differs in several minor

geometrical respects from the old one (round instead of rectangular wire, new end pieces, etc.), a reduction in the number of turns has resulted in a significantly reduced wiggler strength [G/A]. This has necessitated a shift from dc to pulsed-wiggler operation. Since the winding form and shell are aluminum, possible magnetic diffusion effects resulting from pulsed operation introduce some uncertainty in the performance of the wiggler. However, both pulsed and dc measurements on a replica of the winding form have shown very good agreement with the calculated wiggler strength.

Finally, an adapter was attached to one of the four output monitor ports to change the circular-to-rectangular guide coupling from broad wall to narrow wall. This eliminates coupling to TM modes and, in conjunction with the other ports of the monitor, provides a means of

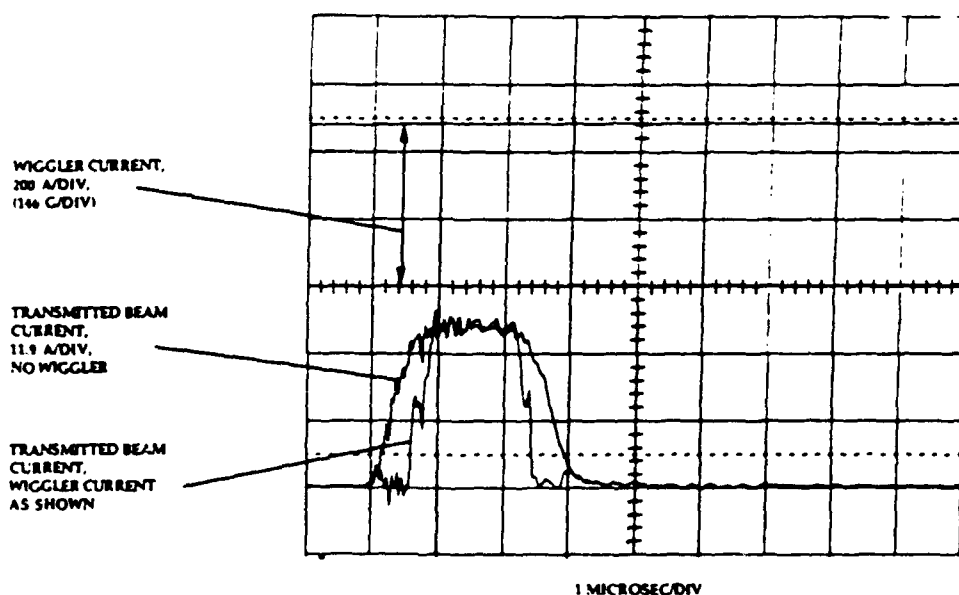


Fig. 2. Typical data showing the wiggler current and transmitted beam current for a run with a beam voltage of 215 kV, a current of 32 A, a wiggler amplitude of 378 G, and an axial field of 2.24 kG.

II. HIGH GAIN EXPERIMENTS

Table 1
The original design and current ubitron experimental parameters

	Present	Design
Voltage [kV]	190–250	250
Current [A]	0–37	30/100
Beam radius [cm]	0.4	0.4
Pulse length [μ s]	1	1
Repetition rate [Hz]	3–30	1–100
Wiggler:		
Period [cm]	2.54	2.54
Entrance [periods]	5	5
Uniform [periods]	12	12
Exit [periods]	3	3
Field [G]	575	500
Solenoid [kG]	1.8–2.8	1–3.2
Frequency [GHz]	13.5–17.4	12.4–18

discriminating between TE and TM modes at the same frequency.

The present and design operating parameters for the experiment are given in table 1. The modulator voltage and repetition rate are tunable over a wide range, but the pulse width is fixed. Beam current is tunable from a few to approximately 30 A by adjustment of a trim coil located over the cathode. The wiggler has adiabatic entrance and exit profiles and is driven by a pulsed current supply at the modulator repetition rate. The solenoid is operated dc with a flat field profile for all results reported here. The frequency range of the experiment is presently limited by the rf driver amplifier on

the low side and rf input coupler falloff on the high side.

3. Experimental results and analysis

Figs. 2 and 3 show typical experimental data. The traces in fig. 2 show the transmitted beam current (with and without the wiggler field) and the pulsed operation of the wiggler. Note that the wiggler current is flat during the beam current pulse. These traces show that the electrons are on Group II orbits at the beginning of the voltage pulse. As the voltage rises, the electrons move toward and through gyroresonance, and then onto Group I orbits during the voltage flat top, passing again through gyroresonance during the fall of the voltage pulse. These effects are demonstrated by the reduction in transmitted current on the rise and fall of the voltage pulse. Note that the current is constant during the voltage flat top.

Modulator voltage and rf output monitor traces are shown in fig. 3. Two traces are shown for the rf, the transmitted rf-driver signal without the wiggler (lower) and an amplified signal with the wiggler turned on. The width of the rf-driver pulse and the overlap with the voltage pulse can be adjusted as desired. Although the portion of the rf-driver pulse before the voltage flat top could be used to determine the gain, this does not account for several factors such as beam loading of the input coupler. Hence, the gain is determined from the output power measured with the wiggler turned off and

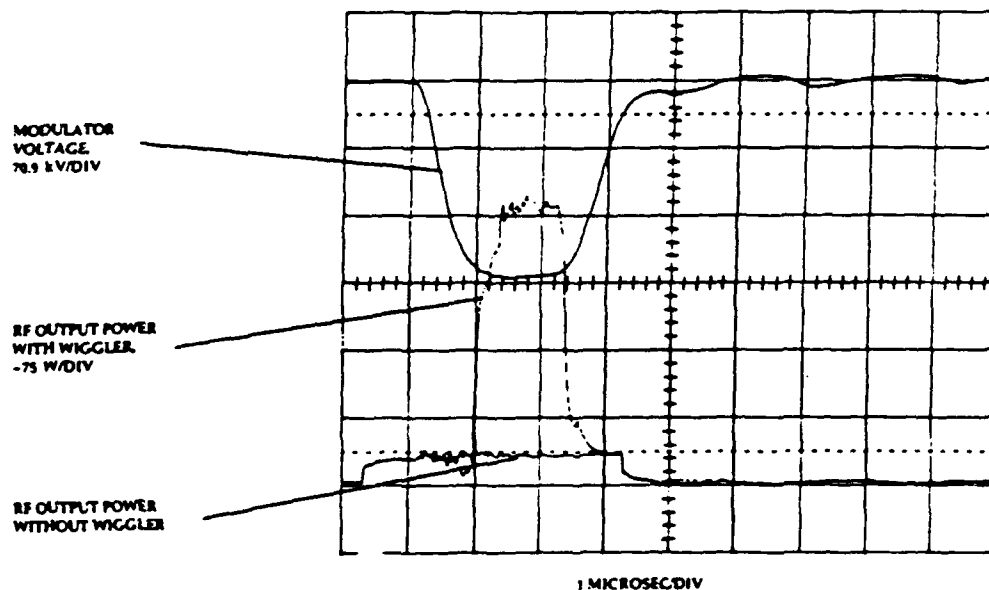


Fig. 3. Typical data showing the modulator voltage and rf output signal for a run with a beam voltage of 215 kV, a current of 32 A, a wiggler amplitude of 378 G, and an axial field of 2.24 kG.

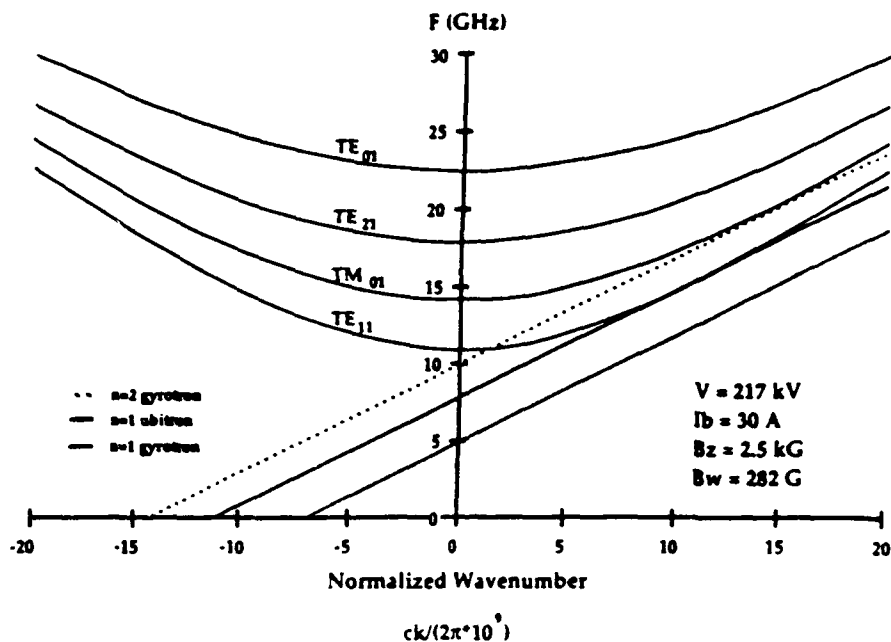


Fig. 4. Uncoupled dispersion curves for the waveguide modes and the beam resonance lines for the fundamental ubitron and the fundamental and harmonic gyrotron interactions for a beam voltage of 217 kV and a wiggler amplitude of 378 G.

with the wiggler turned on, all other factors being held constant. Both a digital oscilloscope and a peak power meter are used for these measurements. Other factors monitored on each pulse are diode current, injected

current, transmitted current, wiggler current and calorimeter temperature.

RF performance has been measured as a function of input signal polarization, rf-drive power, wiggler field,

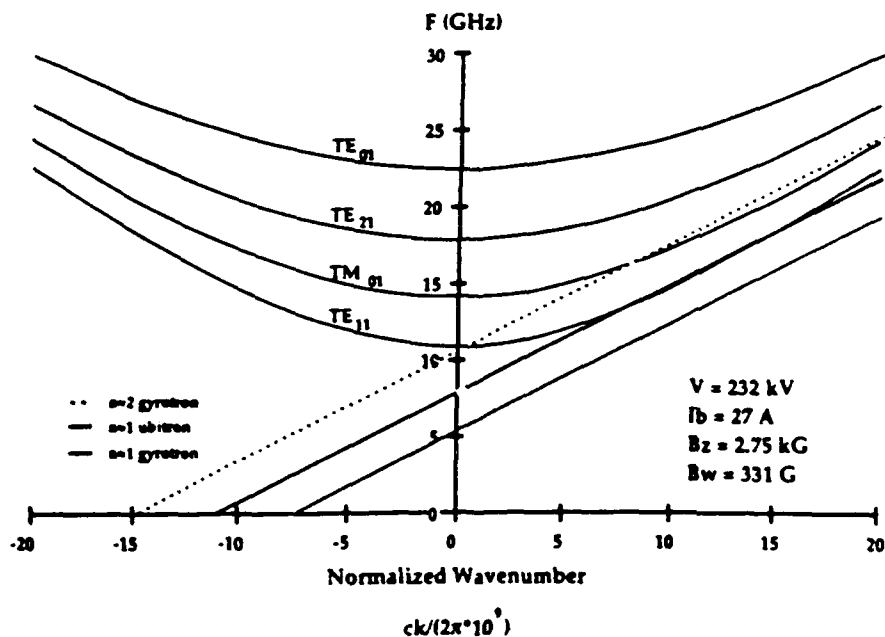


Fig. 5. Uncoupled dispersion curves for the waveguide modes and the beam resonance lines for the fundamental ubitron and the fundamental and harmonic gyrotron interactions for a beam voltage of 232 kV and a wiggler amplitude of 331 G.

II. HIGH GAIN EXPERIMENTS

injected current and frequency. One of the unique features of this experiment is a flexible input coupling scheme providing the ability to launch left- or right-circularly polarized waves, linearly polarized waves, as well as selected waveguide modes. The rf results presented below are in the small-signal-gain regime with output power directly proportional to input power using left-circular polarization. There is no evidence of saturation and an estimated gain of 30 dB is required for saturation with the available rf-drive power. As predicted by theory, very little or no gain was observed using right-circular polarization. Theory also indicates that the combination of a helical wiggler field and a circularly polarized wave will yield the highest gain for a given input power and wiggler velocity.

In order to achieve high gain, efficiency and bandwidth simultaneously, operating parameters have been chosen to produce a grazing intersection of the wiggler-shifted negative-energy space-charge wave with the TE_{11} circular-waveguide mode. Uncoupled dispersion curves of the ubitron and the first two gyrotron harmonics for two parameter sets are shown in figs. 4 and 5. Note that a broad intersection is achieved for the ubitron line and that possible gyrotron interactions are well separated and would be identifiable by both frequency and mode. Grazing intersection results in slightly different characteristics than those usually associated with FELs. Voltage tuning is negligible while the instantaneous bandwidth becomes very large. Lowering the voltage or increasing the wiggler field beyond a certain point results in narrowing and then decoupling of the gain profile, while raising the voltage eventually results in a double-peak profile with decoupling in the center of the band (see following results). However, operation near grazing intersection should have a beneficial effect on issues such as phase sensitivity to voltage and wiggler variations.

The experimental observations are compared with a fully three-dimensional nonlinear analysis and simulation of the ubitron/FEL [6-9] for this configuration. In this analysis, a set of coupled nonlinear differential equations is solved which describes the evolution of the trajectories of an ensemble of electrons as well as the electromagnetic fields. The nonlinear current which mediates the interaction is computed from the microscopic behavior of the electron ensemble by means of an average of the electron phases relative to the ponderomotive potential formed by the beating of the wiggler and rf fields. No wiggler average is performed over the electron trajectories; rather, the orbits are integrated in three dimensions using the Lorentz-force equations. As a result, it is possible to model the injection of the electron beam into the wiggler field, and the initial conditions on the beam are specified prior to the entry of the beam into the interaction region. It is important to remark, in this regard, that such quantities

as the energy spread within the interaction region derive from both the initial energy spread (derived from the gun and beam transport system) and the wiggler gradient. The electromagnetic fields are represented in the form of a superposition of the vacuum-waveguide modes, and an arbitrary number of both TE and/or TM modes may be included in general, although only the TE_{11} mode is important in the present experiment. The rf space-charge fields are approximated by the Gould-Trivelpiece modes of a fully filled waveguide [10]. Although such a representation does not precisely correspond to the experimental configuration, it constitutes a reasonable approximation in the case of a grazing-incidence interaction [9].

Comparisons between the simulation results and the measured gain indicate that an initial axial velocity spread in the neighborhood of 1% is required in the simulation for quantitative agreement with measurements. The initial velocity spread used in the simulation describes the condition of the beam prior to the entry into the wiggler. Subsequent increases in the velocity spread due to transverse wiggler gradients are included self-consistently in the simulation. As mentioned earlier, the electron trajectory code used to design the electron gun and transport system predicts velocity spreads on the order of 0.26% or less. There is, therefore, a discrepancy between the axial velocity spread predicted by the trajectory code and that used in the ubitron/FEL simulation. Although the source(s) of this discrepancy is not completely understood, one possible contributor is wiggler end effects not modelled in the code. This is an area of important ongoing study. The nonlinear simulation has, however, shown good agreement with previous experiments in different parameter regimes [9,11].

A comparison of the gains as found in theory and experiment is shown in figs. 6 and 7, as functions of the frequency for the parameter sets of figs. 4 and 5. Fig. 6 illustrates the gain curves found (1) in the experiment, (2) in simulation with collective Raman effects disabled, and (3) in simulation with complete collective effects. In practice, the collective effects may be disabled by removal of the space-charge waves from the formulation. It is evident from the figure that the gain found by means of the collective Raman theory is in good agreement with the experiment. We reiterate that an initial axial velocity spread of 1% has been assumed and that, in general, the Raman theory has been found to be in close agreement with the measured gain under the assumption of a 1% velocity spread for all parameters studied (see also fig. 7). Comparison of the Compton and Raman simulations shows the importance of collective effects to the experiment since the collective effect results in a decrease in the gain by a factor of more than 2. It should be noted, however, that the shape of the experimental spectrum is suggestive of a double-peaked spectrum, which is in closer agreement with the Comp-

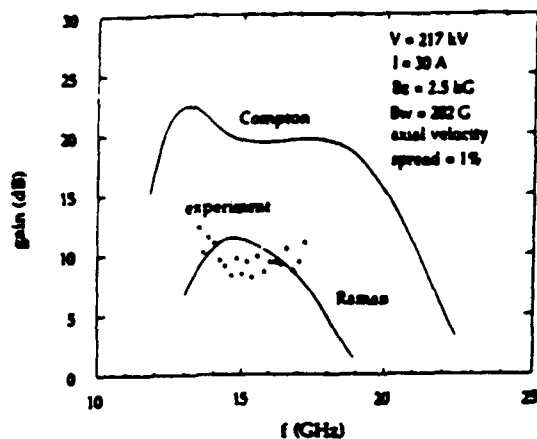


Fig. 6. Comparison between the experimentally observed gain and the gain found in both collective Raman- and Compton-regime simulations for a beam voltage of 217 kV and wiggler amplitude of 282 G.

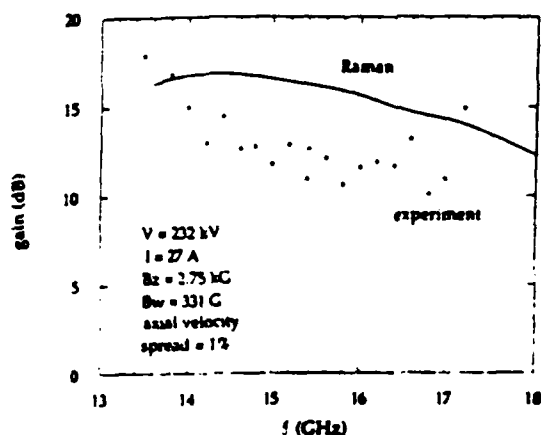


Fig. 7. Comparison between the experimentally observed gain and that found in simulation for a beam voltage of 232 kV and a wiggler amplitude of 331 G.

ion simulation. In order to account for this, we point out that the experiment operates in a regime in which the two intersection points between the waveguide dispersion curve and the beam resonance line are sufficiently close that the two resonant peaks have merged into a single broad gain band. Small changes in any of the parameters can have a marked effect upon the detailed shape of the spectrum. For example, a small change in the beam voltage or wiggler amplitude which results in an increase in the axial beam velocity would shift the intersection points far enough apart to give a double-peaked spectrum in simulation. A small drop in the beam current would have a similar effect. As such, it is difficult to model the detailed spectral shape.

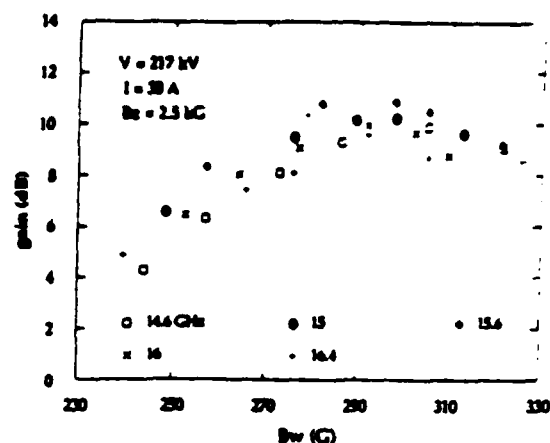


Fig. 8. Graph showing the variation in the gain with wiggler amplitude at frequencies of 14.6, 15, 15.6, and 16.4 GHz.

All gain measurements are presently limited in bandwidth by the output of the rf driver which drops off at 13.5 GHz and by the performance of the rf input coupler which falls off around 17 GHz. The measured values typically show a double-peak profile over the 13.5–17.4 GHz band ($\geq 25\%$ bandwidth), although a fairly flat gain profile has been measured with parameters selected for barely grazing intersection. To date, the peak gain measured is approximately 19 dB at 17 GHz. For a different parameter set, a peak gain of 17 dB was measured at 13.5 GHz. Assuming that the gain occurs mainly over the 12 uniform periods in the wiggler, this translates into approximately 1.25 dB per free-space wavelength. This value, achieved at less than optimum operational parameters, is an improvement over the 0.5–0.7 dB per free-space wavelength achieved in Phillips' and other more recent experiments [1–3].

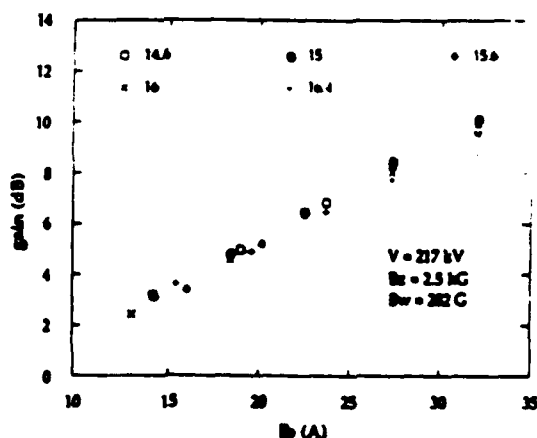


Fig. 9. Graph showing the variation in the gain with beam current at frequencies of 14.6, 15, 15.6, and 16.4 GHz.

II. HIGH GAIN EXPERIMENTS

Measurements of the dependence of the gain on wiggler field and beam current have also been made. In the collective mode of operation, the gain is proportional to α , the ratio of v_z/v_{ph} , which is directly proportional to the wiggler field. This relationship is approximate, due to gyroresonance effects and the increase in wiggler field off-axis. Measurements of gain versus wiggler field (fig. 8) show this type of linear behavior for low field strengths, but then the gain rolls over and begins to drop with increasing wiggler field as the ubitron line decouples from the waveguide mode. Also, in the collective or Raman mode, gain is proportional to the fourth root of the injected current. The measured gain versus beam current (fig. 9) appears to be consistent with this dependence, but the range of currents tested is not sufficient to discriminate between a $I^{1/4}$ (Raman) or $I^{1/3}$ (strong-pump) dependence.

4. Conclusions

Amplifier operation of the NRL ubitron experiment has been achieved with a peak gain of 19 dB and an instantaneous bandwidth exceeding 25%. The measured peak gain per wavelength is 1.25 dB/ λ at 13.5 GHz. The interaction has been identified by frequency, waveguide mode and amplification characteristics to be a fundamental wiggler harmonic ubitron/FEL interaction with the TE_{11} waveguide mode. Reasonable agreement has been obtained between measurements and theory concerning gain, bandwidth and general performance characteristics. In particular, higher values of gain per free-space wavelength have been achieved due to the combination of helical wiggler and circularly polarized waveguide mode. The gain per free-space wavelength is an important parameter to optimize for future ubitron applications.

Immediate plans include improvements in the small-signal calculations to correct the handling of space-charge and nonlinear calculations for both pre-

sent and design experimental parameters. Additional measurements such as calorimetric efficiency, enhancement by axial field tapering and phase sensitivity are also planned.

Acknowledgements

The authors would like to acknowledge useful discussions with Drs. A.K. Ganguly and R.K. Parker. This work was supported by the Office of Naval Technology and the Office of Naval Research.

References

- [1] R.M. Phillips, IRE Trans. Electron Devices ED-7 (1960) 231.
- [2] R.M. Phillips, Proc. 4th Int. Congress on Microwave Tubes, Scheveningen, 1962 (Centrex Publ. Co., Eindhoven, 1962) p. 371.
- [3] C.E. Enderby and R.M. Phillips, IEEE Proc. 53 (1965) 1648.
- [4] R.H. Jackson and D.E. Pershing, Technical Digest Int. Electron Devices Meeting (IEEE Press, New York, 1986) p. 342.
- [5] R.H. Jackson, D.E. Pershing and F. Wood, Nucl. Instrum. Meth. A259 (1987) 99.
- [6] A.K. Ganguly and H.P. Freund, Phys. Rev. A28 (1983) 2275.
- [7] H.P. Freund and A.K. Ganguly, Phys. Rev. A33 (1986) 1060.
- [8] H.P. Freund and A.K. Ganguly, Phys. Rev. A34 (1986) 1242.
- [9] A.K. Ganguly and H.P. Freund, Phys. Fluids 31 (1988) 387.
- [10] N.A. Krall and A.W. Trivelpiece, Principles of Plasma Physics (McGraw-Hill, New York, 1973) p. 202.
- [11] D.A. Kirkpatrick, G. Bekefi, A.C. DiRienzo, H.P. Freund, and A.K. Ganguly, Phys. Fluids, submitted for publication.

APPENDIX VII

Fundamental Mode Amplifier Performance of the NRL Ubitron

by

D.E. Pershing, R.H. Jackson, H. Bluem, and H.P. Freund

FUNDAMENTAL-MODE AMPLIFIER PERFORMANCE OF THE NRL UBITRON

D.E. PERSHING^{*}, R.H. JACKSON, H. BLUEM[†] and H.P. FREUND[‡]

Naval Research Laboratory, Washington, DC 20375, USA

An experimental and theoretical research program to study the ubitron-FEL interaction is in progress at the Naval Research Laboratory, including both fundamental and harmonic modes of operation. Operation of a ubitron-FEL amplifier using the fundamental wiggler harmonic interaction with the TE_{11} circular-waveguide mode is reported here. The experiment employs a 190-250 keV electron beam with currents up to 37 A, using a helical wiggler/axial guide-field configuration. Small-signal gains as high as 17-19 dB have been observed in the 13-18 GHz frequency band, corresponding to a gain per free-space wavelength approaching 1.5 dB/ λ . These results were obtained using a modified SLAC klystron gun. Improved performance is expected using a higher-current (100 A), higher-quality electron gun currently being installed. The theoretical program includes a nonlinear analysis of the rf and electron beam interaction while propagating through a cylindrical waveguide with a helical-wiggler field and an axial guide field. The analysis includes beam injection into the wiggler, wiggler inhomogeneities, efficiency enhancement by means of tapered wigglers, beam thermal effects and harmonic interactions. The experimental results presented in this paper are in reasonable agreement with the nonlinear simulation of the interaction in the Raman regime.

1. Experimental configuration

The Naval Research Laboratory has instituted a program to investigate the ubitron-FEL interaction [1-3] as the basis for a new class of high-power, broadband micro- and millimeter-wave amplifiers. Experimentally, this program includes the design, construction and operation of a K_u band amplifier. Performance goals for the NRL ubitron amplifier are: 30 dB large-signal gain (2-3 dB/ λ), saturated instantaneous bandwidth greater than 20% and efficiency greater than 15%.

The present experimental configuration (fig. 1) consists of an advanced gun [4], injected-current monitor, modified turnstile rf input coupler, double-tapered bifilar helix wiggler and solenoid magnets, transmitted-current monitor, rf output monitors and a water calorimeter/load. Details of component designs and performance have been reported elsewhere [5,6]. Since the advanced gun has only recently been installed, the results reported here were obtained using a modified SLAC klystron gun. However, preliminary performance measurements of the ubitron using the advanced gun operated at 190 kV are consistent with previous measurements, with the exception of higher beam current. The entire emitted current, approximately 70 A, was transported through the tube without transmission loss.

The modulator voltage is tuned over the range of 190 to 250 kV, but the pulse width is fixed at 1 μ s. Beam current is tunable from a few to approximately 37 A by adjustment of a trim coil located over the cathode. The solenoid is operated dc with a flat field profile at 2-3 kG for all results reported here. The beam modulator, rf modulator and wiggler pulser are all repetitively pulsed at 6-60 Hz.

The wiggler has adiabatic entrance and exit profiles when driven dc. However, to achieve sufficient transverse field with a repaired and modified wiggler, the wiggler is driven by a pulsed-current supply at the modulator repetition rate. Measurements of the modified wiggler field profile could only be made after the ubitron amplifier data were obtained, since repairs were made while the tube was still under vacuum. The measured transverse field profile of the wiggler, operated both pulsed and dc, is shown in fig. 2. Two effects are observed. First, adiabaticity deteriorates during pulsed operation, resulting from magnetic diffusion effects due to the aluminum winding form. Also, the effective wiggler period is slightly larger. Secondly, the perpendicular field in the "uniform" region is not constant. The large aperiodic variations of the perpendicular field in this region are difficult to model theoretically, and are partially responsible for the differences between experiment and theory described below.

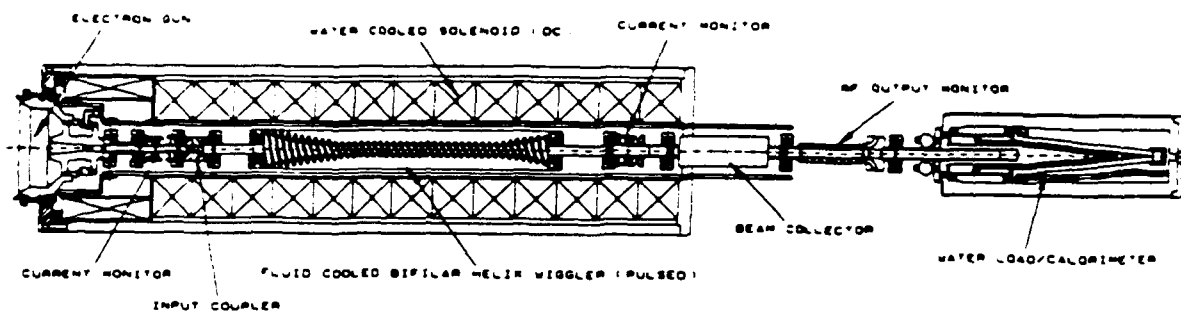
2. Experimental results and analysis

Rf performance has been measured as a function of input signal polarization, rf-drive power, wiggler field,

^{*} Mission Research Corporation, Newington, VA 22122, USA.

[†] Laboratory for Plasma Research, University of Maryland, College Park, MD 20742, USA.

[‡] Science Applications International Corporation, McLean, VA 22102, USA.

Fig. 1. NRL K_u -band ubitron amplifier: experimental configuration.

injected current and frequency. The rf results presented below are in the small-signal gain regime with output power directly proportional to input power using left-circular polarization. Gain is determined from the output power measured with the wiggler turned off and with the wiggler turned on, all other factors being held constant. Output power is linearly dependent on input power, with no evidence of saturation at present. As predicted by theory, very little or no gain was observed using right-circular polarization.

A set of typical waveforms obtained for a particular parameter set, overlaid to show their temporal relationship, is shown in fig. 3. Notice the fraction of beam lost

to the wall during the Group II-Group I orbit transitions on the rise and fall of the voltage pulse.

All gain measurements are presently limited in bandwidth by components external to the interaction region; the high-power rf driver below 13.5 GHz and the rf input coupler above 17 GHz. The measured values typically show a double-peak profile over the 13.5-17.4 GHz band ($\geq 25\%$ bandwidth), although a fairly flat gain profile has been measured with parameters selected for barely grazing intersection. To date, the maximum measured gain is approximately 19 dB at 17 GHz. For a different parameter set, a maximum gain of 17 dB was measured at 13.5 GHz. Assuming that gain occurs

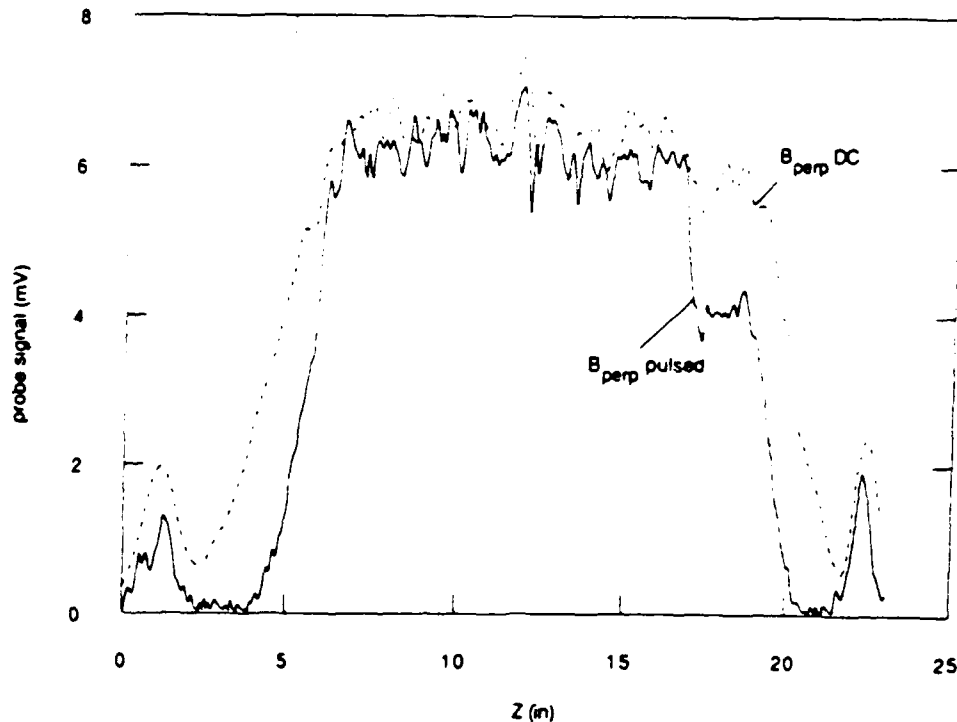


Fig. 2. Wiggler on-axis transverse field profile.

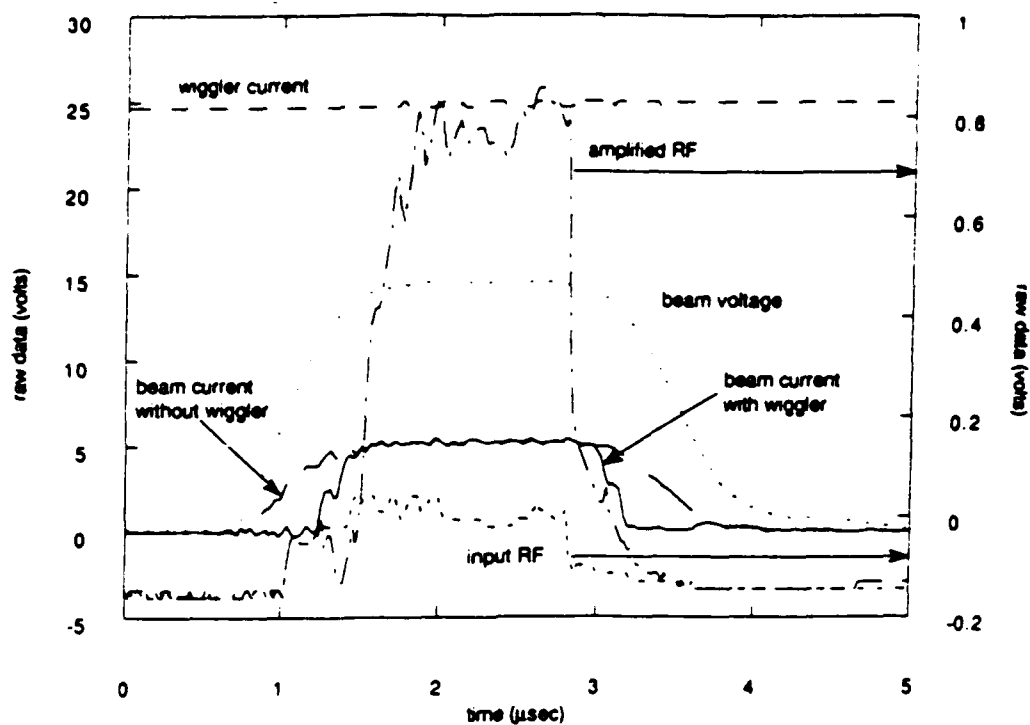


Fig. 3. Typical waveforms showing temporal relationship: $V_b = 200$ kV, $I_b = 30$ A, $B_w = 325$ G, $f = 15.03$ GHz, $P_{in} = 160$ W, $P_{out} = 2.3$ kW.

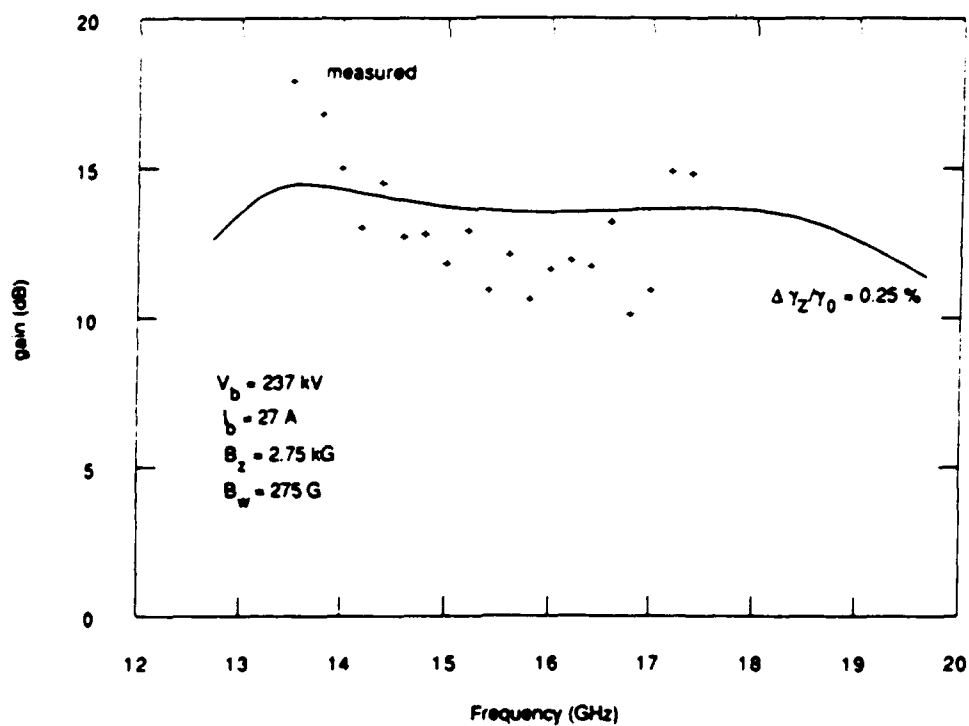


Fig. 4. Comparison between theory and experiment: gain vs frequency.

1. EXISTING EXPERIMENTS

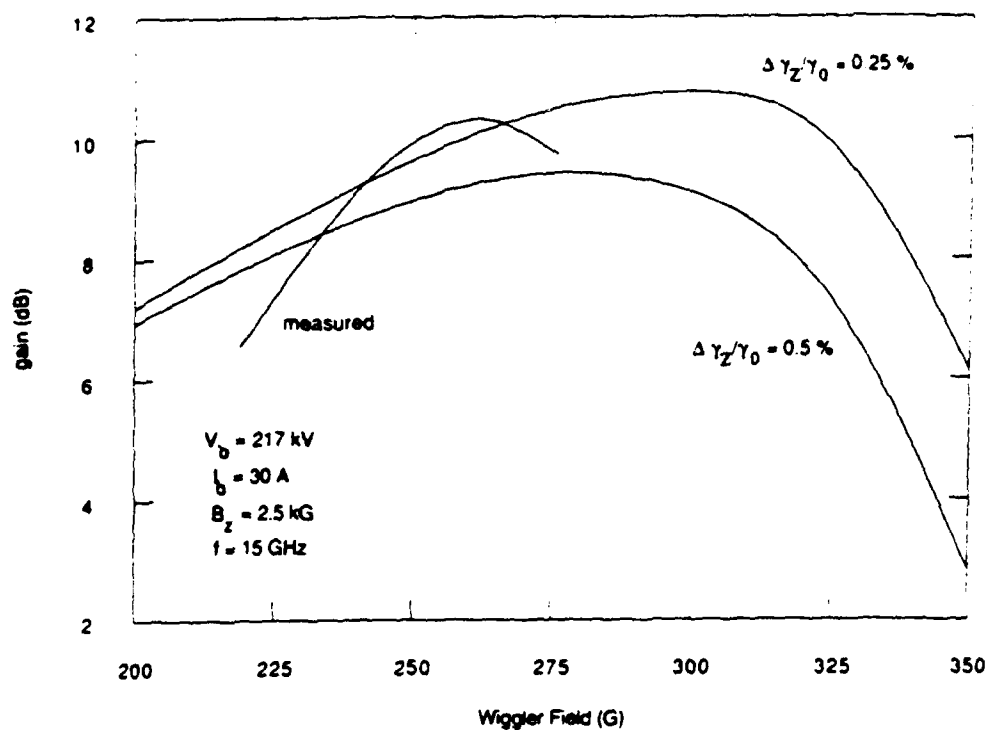


Fig. 5. Comparison between theory and experiment: gain vs wiggler field.

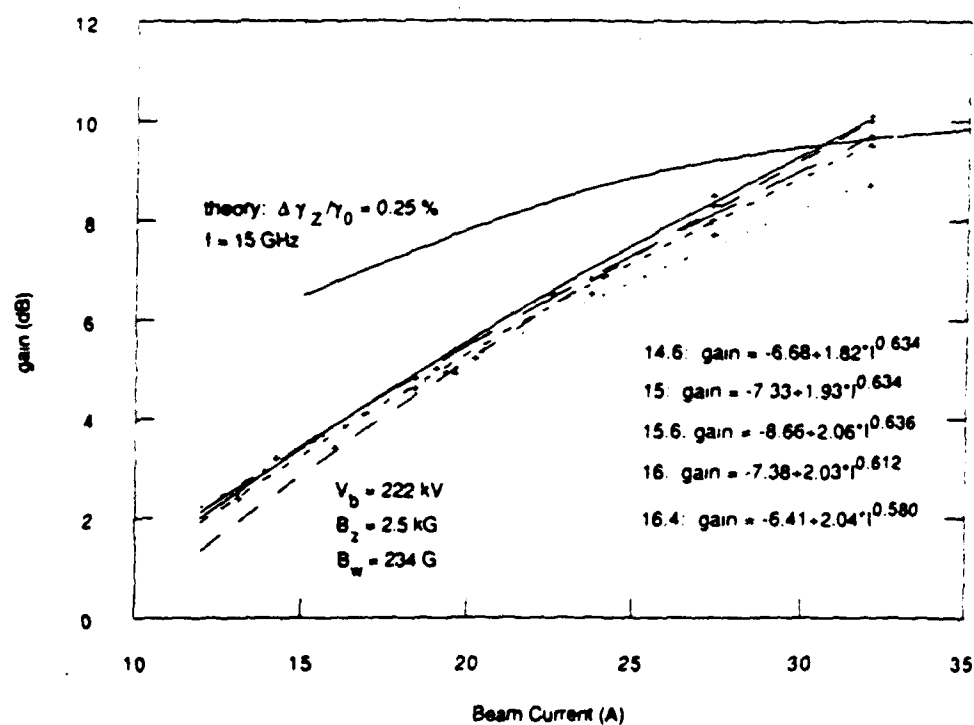


Fig. 6. Comparison between theory and experiment: gain vs beam current.

mainly over the measured 10 uniform periods in the wiggler, this translates into approximately 1.5 dB per free-space wavelength. This value, achieved at less than optimum operational parameters, is an improvement over the 0.5–0.7 dB per free-space wavelength achieved in Phillips' [1–3] and other more recent experiments.

Although a portion of the experimental results have been previously presented, theoretical performance has been recalculated in light of the measured wiggler field profile. Comparisons between the simulation results and experiment are complicated by the shape of the measured wiggler profile. The present theoretical formulation requires adiabatic magnetic-field changes; a condition not well satisfied by the present wiggler. For simulation purposes, the measured wiggler field profile is approximated by reducing the effective entry taper from 5 to 4 periods, decreasing the "uniform" region from 12 to 10 periods with constant amplitude and increasing the exit taper from 3 to 5 periods.

The experimental observations are compared with a fully three-dimensional nonlinear analysis and simulation of the ubitron/FEL [7–10] for this configuration. Injection of the electron beam into the wiggler field is modelled using beam initial conditions specified prior to the entry of the beam into the interaction region. The energy spread within the interaction region results from both the initial energy spread (derived from the gun and beam transport system) and the wiggler gradient, and is computed self-consistently. An initial axial velocity spread of $\sim 0.25\%$ is required in the simulation for quantitative agreement with measurements. This is consistent with velocity spreads calculated by the electron trajectory code used to design the electron gun and transport system.

A comparison of the gain as found in theory and experiment is shown in figs. 4, 5 and 6 as a function of frequency, wiggler field, and beam current, respectively. Experimental parameters are as listed. It should be noted that the shape of the experimental spectrum is more sharply peaked than the simulation spectrum. At least two factors could be responsible for the observed differences. First, small changes in any of the parameters can have a marked effect upon the detailed shape of the spectrum. For example, a small change in the beam voltage or wiggler amplitude which results in an increase in the axial beam velocity would shift the intersection points far enough apart to give a more sharply peaked spectrum in simulation. A small drop in the beam current would have a similar effect. As such, it is difficult to model the detailed spectral shape. Secondly, differences between the actual wiggler field profile and the approximated profile for simulation could be sufficient to preclude exact agreement. Modifications to the simulation code are currently in progress to permit modelling wiggler fields such as shown in fig. 2. Modifi-

cations to the wiggler design are also in progress that will result in a much flatter uniform region.

Gain, as a function of wiggler field, is shown in fig. 5 for a second parameter set. Also shown is the calculated dependence of gain on wiggler field for two values of velocity spread. Although the calculated profiles are considerably broader than the experimental measurement, the field at peak gain is only 8–15% greater than the experimental value.

The measured gain versus beam current (fig. 6) generally follows an $I^{0.6}$ dependence, which is closer to an $I^{1/3}$ (1D, strong-pump) than an $I^{1/4}$ (Raman) dependence. Experimental measurements for frequencies from 14.6 to 16.4 GHz are shown, as well as the simulation result for 15 GHz. However, more data is needed before a definitive current dependence statement can be made.

3. Conclusions

Amplifier operation of the NRL ubitron experiment has been achieved with a peak gain of 19 dB and an instantaneous bandwidth exceeding 25%. The measured peak gain per wavelength is 1.5 dB/ λ at 13.5 GHz. The interaction has been identified by frequency, waveguide mode and amplification characteristics to be a fundamental wiggler harmonic ubitron–FEL interaction with the TE_{11} waveguide mode. High values of gain per free-space wavelength have been achieved due to the combination of helical wiggler and circularly polarized waveguide mode. In spite of a rather poor wiggler field profile, reasonable agreement has been obtained between measurements and theory concerning gain, bandwidth and general performance characteristics. This indicates that ubitron performance is relatively insensitive to wiggler field aberrations for configurations resulting in high gain per free-space wavelength.

Immediate plans include extended performance measurements using the advanced gun, improvements in the small-signal calculations involving space charge and realistic wiggler magnetic fields, as well as nonlinear calculations for both present and design experimental parameters. Additional measurements such as calorimetric efficiency, enhancement by axial field tapering and phase sensitivity are also planned.

Acknowledgements

The authors would like to acknowledge useful discussion with Drs. A.K. Ganguly and R.K. Parker. This work was supported by the Office of Naval Technology and the Office of Naval Research.

References

- [1] R.M. Phillips, IRE Trans. Electron Dev. ED-7 (1960) 231.
- [2] R.M. Phillips, Proc. 4th Int. Congress on Microwave Tubes, Scheveningen, The Netherlands, 1962 (Centrex Publ. Co., Eindhoven, The Netherlands, 1962) p. 371.
- [3] C.E. Enderby and R.M. Phillips, IEEE Proc. 53 (1965) 1648.
- [4] G. Merdman, G. Miram, R. Jackson, R. Parker and D. Pershing, Technical Digest Int. Electron Devices Meeting, Washington, DC, 1985 (IEEE Press, New York, 1985) p. 188.
- [5] R.H. Jackson and D.E. Pershing, Technical Digest Int. Electron Devices Meeting, Los Angeles, CA, 1986 (IEEE Press, New York, 1986) p. 342.
- [6] R.H. Jackson, D.E. Pershing and F. Wood, Nucl. Instr. and Meth. A259 (1987) 99.
- [7] A.K. Ganguly and H.P. Freund, Phys. Rev. A28 (1983) 2275.
- [8] H.P. Freund and A.K. Ganguly, Phys. Rev. A33 (1986) 1060.
- [9] H.P. Freund and A.K. Ganguly, Phys. Rev. A34 (1986) 1242.
- [10] A.K. Ganguly and H.P. Freund, Phys. Fluids 31 (1988) 387.

APPENDIX VIII

Improved Amplifier Performance of the NRL Ubitron

by

D.E. Pershing, R.H. Jackson, H. Bluem, and H.P. Freund

IMPROVED AMPLIFIER PERFORMANCE OF THE NRL UBITRON

D.E. Pershing,* R. H. Jackson, H. Bluem,** and H.P. Freund†
Vacuum Electronics Branch
Electronics Science and Technology Division
Naval Research Laboratory, Washington, D.C. 20375

ABSTRACT

Improved amplifier performance of the NRL Ku-band ubitron is reported following several experimental modifications. The major modification is the substitution of a higher current (100A), higher quality electron gun for the original modified SLAC klystron gun (250 kV, 37A). The experimental configuration is otherwise unchanged: a solid, uniform density electron beam propagating through a helical wiggler/axial guide field configuration, interacting with a copropagating circularly polarized TE_{11} RF wave. With these changes, small signal gains of 23 dB have been observed in the 12.6 - 17.5 GHz frequency range. Good agreement between measured and calculated gain in the Raman regime has been obtained using a three-wiggler model in the 3-D nonlinear FEL code ARACHNE.

*Permanent Address: Mission Research Corporation, 8560 Cinderbed Rd., Suite 700, Newington, VA 22122.

**Permanent Address: Laboratory for Plasma Research, University of Maryland, College Park, Maryland 20742.

†Permanent Address: Science Applications International Corp., McLean, Virginia 22102.

INTRODUCTION

The Vacuum Electronics Branch of the Naval Research Laboratory has an ongoing program to evaluate the potential of the ubitron/FEL interaction as a high-gain, high-power, broad bandwidth micro- or millimeter wave source. Moderate gain operation of the NRL ubitron has been previously reported using a modified SLAC klystron gun [1,2]. An improvement in the gain has been observed following the installation of a higher current, higher quality electron gun [3]. The maximum gain for a uniform axial field is 20 dB, and substantial gain has been measured over the 12.6 to 17.4 GHz frequency range. Gain is found to be limited by the onset of a high-power oscillation. The oscillation can reach high power levels (≈ 700 kW) and is dependent on the wiggler field. Power is also dependent on the axial field profile and trim coil current. In addition, it exhibits oscillation thresholds dependent upon both beam voltage and wiggle-velocity. Both amplifier and oscillator experimental measurements are compared with a fully three-dimensional nonlinear simulation of this configuration using the code ARACHNE [4-7].

EXPERIMENTAL CONFIGURATION

The present amplifier configuration is shown in Fig. 1. The electron gun is on the left. All current emitted from the gun is magnetically focused and injected into the interaction region; no beam scraping is used. A solenoidal field, generated by 14 individual coils, is used for beam confinement and transport. Following the direction of beam propagation, the major components are: resistive injected-current monitor, modified 4-port turnstile junction input coupler, double taper, fluid cooled bifilar helix (repetitively pulsed), resistive transmitted current monitor, beam collector, 4-port output coupler, and combination water load/calorimeter. The input coupler generally launches a LHCP TE_{11} fundamental mode wave into the interaction region, although it can also launch a linearly

polarized wave if desired. The output coupler employs both broadwall and narrow wall ports for TE/TM mode selection purposes. Essentially all of the injected and amplified RF power is absorbed in the water load/calorimeter. The parameter range over which the ubitron has been operated is: $190 < V_b < 250$ kV, $65 < I_b < 94$ A, $1.8 < B_z < 2.9$ kG, $B_w < 575$ G, and $12.6 < f < 17.4$ GHz. The wiggler field has a 2.54 cm period with effectively 10 periods in the uniform region and 4 and 5 periods in the entrance and exit tapers, respectively. The device is typically repetitively pulsed in the 3 - 6 Hz range.

EXPERIMENTAL RESULTS AND COMPARISON WITH THEORY

Ubitron amplifier performance has been measured as a function of several independent variables: RF frequency, wiggler field, beam voltage, and axial field. Most measurements are in the small signal regime; saturation was not reached. The major performance results discussed below are gain vs. frequency and wiggler field.

The RHCP wiggler field is generated by a multiple turn bifilar helix electromagnet with radially tapered entrance and exit sections which was wound on an aluminum form in anticipation of DC operation. However, due to cooling problems, the wiggler is operated in a repetitively pulsed mode to achieve high field strengths. As shown in Fig. 2, the resulting transverse field profile was measured only on-axis. Due principally to magnetic diffusion effects, the field profile departs considerably from the ideal profile, which would consist of a smooth adiabatic increase in transverse field followed by a constant transverse field region and then an adiabatically decreasing field.

In addition to the reduced performance that could be expected from this wiggler profile, comparison between experiment and theory is complicated due to the difficulty in modelling this field. Since only the on-axis transverse field profile was measured, insufficient data were obtained to directly incorporate the measured profile into the

simulation. For simulation purposes, therefore, the wiggler field is approximated as the superposition of the fields of three ideal bifilar helices of different amplitude and period. The fit is also shown in Fig. 2, and comes reasonably close to replicating the fine structure in the uniform field region.

The small signal gain is shown in Fig. 3 for the following parameters: $V_b = 232\text{kV}$, $I_b = 85\text{A}$, $B_z = 2.51\text{kG}$, $B_w = 294\text{G}$, and $P_{in} = 150\text{W}$. The solid line represents simulation results in the Raman regime from the code ARACHNE for axial energy spreads of 0 and 0.25%. For this set of parameters, velocity spread has little effect on gain. The simulation results are in good agreement with the measured average gain, but are less accurate concerning the detailed profile. Contributing factors to this discrepancy are the wiggler field model, detailed beam characteristics not included in the code, and treatment of AC space charge in the code.

The saturation behavior has not been measured due to an RF oscillation that limited the maximum gain to approximately 20 dB. This value was measured at 14.8 and 16.6 GHz for different combinations of V_b , B_z , and B_w . Insufficient RF drive power was available to achieve saturation at this level of gain. The maximum power measured in the amplifier mode was 200 - 300 kW using a uniform B_z field. However, approximately 23 dB of gain has been measured using a nonuniform B_z field. Bandwidth in the small signal regime exceeds 25%, and the calculated peak gain/wavelength is approximately $1.6\text{ dB}/\lambda$.

To further characterize ubitron performance, the gain dependence on wiggler field was measured and calculated for a second set of parameters and is shown in Fig. 4. In this case, the simulation and measurements are in good agreement for the wiggler field required to generate maximum gain. However, the values of that maximum gain differ significantly. Discrepancies between experiment and theory are due to the same factors listed above.

HIGH POWER OSCILLATION

In attempting to increase amplifier gain by increasing the wiggler field, an oscillation was observed that limited maximum gain, and which reached power levels of approximately 700 kW [corresponding to an efficiency of 3%] at a frequency of approximately 17.4 GHz. Severe beam disruption also occurred at high power levels. Identification of the oscillation mechanism remains elusive at this time. Experimental evidence points to either a fundamental ubitron oscillation with the TE_{11} mode, or a second harmonic ubitron interaction with the TE_{21} mode. This ambiguity results from inadequate diagnostics to discriminate between TE modes. The principal characteristics of the oscillation are:

- 1) The oscillation requires the wiggler field, and is not strongly dependent on the axial field; hence it is not a cyclotron maser. The oscillation would have to switch between the 2nd, 3rd and 4th gyrotron harmonics to maintain either a TE_{21} , or a TE_{11} intersection near 18 GHz for the parameters at which oscillation was observed.
- 2) Oscillation power is dependent on the axial field profile, wiggler field amplitude, and on gun trim coil current. Measurements of oscillator power dependence on wiggler field is shown in Fig. 5 for two axial field profiles. The compression B_z profile has the effect of slightly reducing the beam diameter in the wiggler region. The maximum power in this case is considerably reduced from the maximum power measured with a uniform B_z , for nominal values of trim current, although the oscillation will start at a lower wiggler field. Measurements of oscillator power vs. trim coil current for both field profiles show a strong linear reduction in oscillator power with increasing trim current.
- 3) High output power is possible. However, at high power levels, considerable pulse-to-pulse amplitude fluctuations were observed, not correlated to macroscopic parameter variations. Both output coupler/diode detector and calorimetric power measurements were made.

4) The oscillation frequency is near the TE_{21} mode cutoff which, typically, differs from the amplifier frequency. A wavemeter was used for this measurement. The oscillation does not appear to be a typical feedback oscillation at the driven frequency, but grows from noise on the beam at 17.4 GHz. Examination of uncoupled dispersion curves for both TE_{11} and TE_{21} combinations show possible intersections near 17.4 GHz.

5) An oscillation threshold exists at an on-axis velocity ratio, independent of the axial field over the range of 1.9 to 2.9 kG. The wiggler field required to initiate the oscillation was measured for a variety of beam voltages and axial field values and/or profiles. Although the initiation wiggler field spans the range of 250 to 300 G, the on-axis v_{\perp}/v_{\parallel} is found to be approximately 0.13, computed in each case for an ideal wiggler field and a uniform axial field of the measured values.

6) No oscillation occurs for beam voltages below approximately 200 kV - independent of the wiggler field magnitude. At this voltage, the second harmonic TE_{21} interaction occurs at a frequency of 18.7 GHz which is considerably higher than observed. However, there is no TE_{11} mode intersection at all at this voltage.

7) Output coupler characteristics eliminate the possibility of a TM interaction.

The amplifier code ARACHNE [including the three-wiggler model], was employed to model the interaction. In order to obtain a second harmonic ubitron interaction with the TE_{21} mode the waveguide radius was increased from 0.815 cm to 0.844 cm in order to lower the cutoff frequency below the measured 17.4 GHz oscillation frequency. Simulation results are presented in Fig. 5, showing the computed oscillator power (saturated amplifier power) as a function of wiggler field for a uniform 2.76 kG axial field. The shape of the curve is in reasonable agreement with measured data, lending credence to the hypothesis that this is a second harmonic interaction with the TE_{21} mode. The maximum computed oscillator power [intracavity] is approximately 1.5 MW, also in reasonable agreement with the estimated maximum oscillator output power of 700 kW. Calculations of the saturated amplifier power for the TE_{11} mode using ARACHNE [with the nominal waveguide radius

of 0.815 cm] are on the order of 4-5 MW. This is considerably higher than the measured value.

Factors favoring the TE_{11} interpretation are: 1) the measured frequency is consistent with a TE_{11} intersection for the nominal waveguide radius, 2) the voltage threshold is consistent with no TE_{11} intersection for those parameters, and 3) no mode conversion is required for the free propagation of the signal. Arguments against the TE_{11} interpretation are less well founded on explicit observations: 1) measurements of component return loss using linear polarization do not show large reflections at 17.4 GHz, reflectivity is actually higher near 17.8 GHz, 2) the reason for the power sensitivity to trim coil current is not clear, and 3) the measured power level appears to be considerably lower than predicted by simulation.

The primary factors leading to a TE_{21} interpretation of the observed oscillation characteristics are: 1) The reflectivity is high near cutoff which facilitates oscillation, 2) the dispersion curve intersection frequency is fairly constant, not highly dependent on external parameters, 3) operation near cutoff is also consistent with pulse-to-pulse power fluctuations and power sensitivity to trim current, and 4) the observed power is consistent with the expected saturation level based on simulations. The primary factors against a TE_{21} interpretation are related. While it is possible that the dispersion curve is altered in such a manner to reduce the cutoff frequency from the vacuum value of 17.8 to 17.4 GHz in the interaction region, TE_{21} propagation beyond the beam collector is not possible without mode conversion, since 17.4 GHz is below the vacuum waveguide cutoff.

SUMMARY

Amplifier performance of the NRL ubitron has improved following the installation of a higher current, higher quality electron gun. A gain of 20 dB has been measured, corresponding to a peak gain/wavelength of 1.6 dB/ λ . The maximum output power is 200-

300 kW. 3-D nonlinear simulations of the ubitron configuration, including a three wiggler model, are in reasonable agreement with measured data. Small signal bandwidth has been measured to exceed 25%. However, saturation has not been achieved due to gain limitations caused by the onset of a high power oscillation. The oscillation can be fairly powerful; approx. 700 kW has been measured. The oscillation mechanism has not been conclusively identified at this time. A major component redesign is currently under way in order to improve the wiggler and to enhance the diagnostics available for distinguishing between TE modes.

ACKNOWLEDGEMENTS

This work was supported by the Office of Naval Research and the Office of Naval Technology.

REFERENCES

- [1] R. H. Jackson, D. E. Pershing, and F. Wood, Nucl. Instr. and Meth. **A259** (1987) 99.
- [2] D. E. Pershing, R. H. Jackson, H. P. Freund, and H. Bluem, Nucl. Instr. and Meth. **A285** (1989) 56.
- [3] G. Merdinian, G. Miram, R. Jackson, R. Parker, and D. Pershing, Technical Digest Int. Electron Devices Meeting, 1985, Washington, D. C. (IEEE Press, New York, 1985) p. 188.
- [4] A.K. Ganguly and H.P. Freund, Phys. Rev. A **32** (1985) 2275.
- [5] H.P. Freund and A.K. Ganguly, Phys. Rev. A **33** (1986) 1060.
- [6] H.P. Freund and A.K. Ganguly, Phys. Rev. A **34** (1986) 1242.
- [7] A.K. Ganguly and H.P. Freund, Phys. Fluids **31** (1988) 387.

FIGURE CAPTIONS

Fig. 1 Schematic illustration of the NRL ubitron.

Fig. 2 Comparison of the measured transverse on-axis wiggler field and the three-wiggler model used in simulation.

Fig. 3 Small signal gain of the amplifier in the TE_{11} mode.

Fig. 4 Dependence of the TE_{11} small-signal gain upon the wiggler field.

Fig. 5 Dependence of the oscillation power on wiggler field for two axial field profiles, and comparison with the TE_{21} mode second harmonic oscillation calculation.

APPENDIX IX

Multimode Nonlinear Analysis of Free-Electron Laser Amplifiers in Three-Dimensions

by

H.P. Freund

Multimode nonlinear analysis of free-electron laser amplifiers in three dimensions

H. P. Freund

Science Applications International Corporation, McLean, Virginia 22102

(Received 7 October 1987)

The nonlinear evolution of a free-electron laser (FEL) amplifier is investigated for a configuration in which an electron beam propagates through an overmoded rectangular waveguide in the presence of a planar wiggler with parabolically tapered pole pieces. The analysis is fully three dimensional and describes the evolution of an arbitrary number of resonant TE and/or TM modes of the rectangular guide as well as the trajectories of an ensemble of electrons. Numerical simulations are conducted for parameters consistent with the 35-GHz amplifier experiment performed by Orzechowski and co-workers [Phys. Rev. Lett. **54**, 889 (1985); **57**, 2172 (1986)], in which the TE_{01} , TE_{21} , and TM_{21} modes were observed. The theory is found to be in good agreement with the experiment. Surprisingly, comparison with a single-mode analysis shows that the enhancement of the efficiency of the TE_{01} mode obtained by means of a tapered wiggler is significantly greater (as well as being in substantial agreement with the experiment) when the TE_{21} and TM_{21} modes are included in the simulation.

I. INTRODUCTION

The free-electron laser (FEL) has been shown to be a high-power radiation source over a broad spectrum extending from microwave¹⁻¹³ through optical¹⁴⁻²¹ wavelengths. For operation at relatively low beam energies (typically below about 500 keV) and long wavelengths, the device is termed a Ubitron¹ and the interaction occurs in the vicinity of the lowest-order waveguide cutoff. As a consequence, the system can be designed in such a way that the beam is resonant only with the lowest-order waveguide mode, and a single-mode analysis is sufficient to describe many aspects of the interaction. However, at higher energies and shorter wavelengths, the interaction is overmoded in the sense that the electron beam can be resonant with several (perhaps many) modes, and the competition and interaction between the modes has important consequences for the interaction.

The motivation for the present work is to develop a multimode nonlinear theory and simulation code for a Ubitron FEL amplifier which employs a planar wiggler. This general configuration has been extensively studied in the linear regime.²²⁻²⁷ The present nonlinear analysis is based on previously described single-mode nonlinear analyses of a helical-wiggler-axial-guide-field²⁸⁻³¹ and planar-wiggler³² configurations. The development of a multimode analysis represents a straightforward generalization of the single-mode theories, and involves the calculation of $J \cdot E$ for each mode as well as the integration of electron trajectories in the aggregate field composed of the sum of all the resonant modes. The particular configuration considered in the present work is that of a planar-wiggler geometry in which the electron beam propagates through a rectangular waveguide, although multimode analyses can also be developed for optical Gaussian resonator modes.³³⁻³⁵ The detailed wiggler model we employ includes the effect of parabolically shaped pole pieces in order to provide for electron focus-

ing in the plane of the bulk wiggler motion,^{1,36} and we model the injection of the electron beam into the wiggler by allowing the wiggler amplitude to increase adiabatically from zero to a constant level. In addition, we consider the effect of a tapered wiggler amplitude on efficiency enhancement in overmoded systems. As in the case of the single-mode analysis,³² the overlap between the electron beam and the transverse-mode structure of either TE or TM modes is included in a self-consistent way, and no arbitrary "filling factor" is necessary. Although the problem of interest is that of an overmoded FEL amplifier which requires a multimode treatment, only single-frequency propagation need be considered. As a result, Maxwell's equations may be averaged over a wave period which results in the elimination of the fast-time-scale phenomena from the formulation.

The organization of the paper is as follows. The general formulation is described in Sec. II, and allows for the inclusion of an arbitrary number of modes of TE and/or TM polarization, subject to the restriction that all are propagating modes at the same frequency. A direct application of the multimode analysis is to the description of a recent experiment by Orzechowski and co-workers,^{9,13} in which the TE_{01} , TE_{21} , and TM_{21} modes of a rectangular waveguide were observed. Numerical examples appropriate to this experiment are discussed in Sec. III, and good agreement with the experiment is found. A summary and discussion is given in Sec. IV.

II. GENERAL FORMULATION

The configuration we employ is that of an electron beam propagating through an overmoded rectangular waveguide in the presence of a planar-wiggler field generated by a magnet array with parabolically tapered pole pieces.^{1,36} As a result, the wiggler field is assumed to be of the form

$$B_w(x) = B_w \left\{ \cos k_w z \left[\sinh \left[\frac{k_w x}{\sqrt{2}} \right] \sinh \left[\frac{k_w y}{\sqrt{2}} \right] \hat{e}_x + \cosh \left[\frac{k_w x}{\sqrt{2}} \right] \cosh \left[\frac{k_w y}{\sqrt{2}} \right] \hat{e}_y \right] - \sqrt{2} \cosh \left[\frac{k_w x}{\sqrt{2}} \right] \sinh \left[\frac{k_w y}{\sqrt{2}} \right] \sin(k_w z) \hat{e}_z \right\}, \quad (1)$$

where B_w denotes the wiggler amplitude and k_w ($\equiv 2\pi/\lambda_w$) is the wiggler wave number. The injection of the beam into the wiggler is modeled by an adiabatic increase in the wiggler amplitude over N_w periods. In addition, since the enhancement of the efficiency by means of a tapered wiggler is also studied, the wiggler amplitude will be tapered downward starting at some point z_0 downstream from the entry region in a linear fashion. For this purpose we choose

$$B_w(z) = \begin{cases} B_w \sin^2(k_w z / 4N_w), & 0 \leq z \leq N_w \lambda_w \\ B_w, & N_w \lambda_w < z \leq z_0 \\ B_w [1 + \epsilon_w k_w (z - z_0)], & z > z_0 \end{cases} \quad (2)$$

where

$$\epsilon_w \equiv \frac{1}{k_w} \frac{d}{dz} \ln B_w \quad (3)$$

describes the slope of the taper. Since the fringing fields associated with the tapered wiggler amplitude are neglected, this representation requires the slopes of the taper to be small (i.e., N_w must be large and $|\epsilon_w| \ll 1$).

The boundary conditions at the waveguide wall may be satisfied by expanding the vector potential in terms of the orthogonal basis functions of the vacuum waveguide. Thus we write the vector potential of the radiation in the form

$$\delta A(x, t) = \sum_{l, n=0}^{\infty} \delta A_{ln}(z) e_{ln}^{(1)}(x, y) \cos \alpha \quad (4)$$

for the TE modes and

$$\delta A(x, t) = \sum_{l, n=1}^{\infty} \delta A_{ln}(z) \left[e_{ln}^{(2)}(x, y) \cos \alpha + \frac{k_{ln}}{k} \sin \left[\frac{l\pi X}{a} \right] \times \sin \left[\frac{n\pi Y}{b} \right] \sin \alpha \hat{e}_z \right] \quad (5)$$

for the TM modes, where, for frequency ω and wave number $k(z)$,

$$\alpha \equiv \int_0^z dz' k(z') - \omega t. \quad (6)$$

In addition, \sum' indicates that l and n are not both zero, and

$$\frac{d^2}{dz^2} \delta a_{ln} + \left[1 + \frac{k_{ln}^2}{k^2} \right] \left[\frac{\omega^2}{c^2} - k^2 - k_{ln}^2 \right] \delta a_{ln} = 8 \frac{\omega_b^2}{c^2} \left\langle \frac{\cos \alpha}{|v_z|} e_{ln}^{(2)} \cdot v + \frac{v_z}{|v_z|} \frac{k_{ln}}{k} \sin \left[\frac{l\pi X}{a} \right] \sin \left[\frac{n\pi Y}{b} \right] \sin \alpha \right\rangle \quad (12)$$

and

$$2 \left[k + \frac{k_{ln}^2}{k} \right]^{1/2} \frac{d}{dz} \left[\left[k + \frac{k_{ln}^2}{k} \right]^{1/2} \delta a_{ln} \right] = -8 \frac{\omega_b^2}{c^2} \left\langle \frac{\sin \alpha}{|v_z|} e_{ln}^{(1)} \cdot v - \frac{v_z}{|v_z|} \frac{k_{ln}}{k} \sin \left[\frac{l\pi X}{a} \right] \sin \left[\frac{n\pi Y}{b} \right] \cos \alpha \right\rangle, \quad (13)$$

$$e_{ln}^{(1)}(x, y) \equiv \frac{n\pi}{k_{ln} b} \cos \left[\frac{l\pi X}{a} \right] \sin \left[\frac{n\pi Y}{b} \right] \hat{e}_x - \frac{l\pi}{k_{ln} a} \sin \left[\frac{l\pi X}{a} \right] \cos \left[\frac{n\pi Y}{b} \right] \hat{e}_y, \quad (7)$$

$$e_{ln}^{(2)}(x, y) \equiv \frac{l\pi}{k_{ln} a} \cos \left[\frac{l\pi X}{a} \right] \sin \left[\frac{n\pi Y}{b} \right] \hat{e}_x + \frac{n\pi}{k_{ln} b} \sin \left[\frac{l\pi X}{a} \right] \cos \left[\frac{n\pi Y}{b} \right] \hat{e}_y, \quad (8)$$

are the polarization vectors. In this representation, the waveguide is assumed to be centered at the origin and bounded by $-a/2 \leq x \leq a/2$ and $-b/2 \leq y \leq b/2$. As a consequence, $X \equiv x + a/2$, $Y \equiv y + b/2$, and

$$k_{ln} \equiv \pi \left[\frac{l^2}{a^2} + \frac{n^2}{b^2} \right]^{1/2} \quad (9)$$

denotes the cutoff wave vector. It is implicitly assumed that both $\delta A_{ln}(z)$ and $k(z)$ vary slowly over a wave period.

The multimode treatment includes an arbitrary number of propagating modes of TE and/or TM polarization. The detailed equations which describe the evolution of the amplitudes and wave numbers of these modes are identical to those derived in the single-mode analysis,³² and we merely restate the results here. The equations which govern the evolution of the TE_{ln} mode are

$$\frac{d^2}{dz^2} \delta a_{ln} + \left[\frac{\omega^2}{c^2} - k^2 - k_{ln}^2 \right] \delta a_{ln} = 8 \frac{\omega_b^2}{c^2} F_{ln} \left\langle \frac{\cos \alpha}{|v_z|} e_{ln}^{(1)} \cdot v \right\rangle \quad (10)$$

and

$$2k^{1/2} \frac{d}{dz} (k^{1/2} \delta a_{ln}) = -8 \frac{\omega_b^2}{c^2} F_{ln} \left\langle \frac{\sin \alpha}{|v_z|} e_{ln}^{(2)} \cdot v \right\rangle, \quad (11)$$

where $\delta a_{ln} \equiv e \delta A_{ln} / mc^2$, $\omega_b^2 \equiv 4\pi n_b e^2 / m$ (where n_b is the bulk density of the beam), v is the instantaneous electron velocity, and $F_{ln} \equiv \frac{1}{2}$ when either $l=0$ or $n=0$, and unity otherwise. For the TM_{ln} mode we obtain a similar result,

where we note that there is no nontrivial TM-mode solution when $l = 0$ and $n = 0$.

Equations (10)–(13) are equivalent to a calculation of $J \cdot \delta E_n$ for each mode. The averaging operator $\langle (\dots) \rangle$ is defined over the initial conditions of the beam, and includes the effect of an initial momentum spread by means of the distribution function

$$F_0(p_0) = A \exp[-(p_{x0} - p_0)^2 / \Delta p_x^2] \delta(p_0^2 - p_{x0}^2 - p_{y0}^2) H(p_{x0}), \quad (14)$$

where p_0 and Δp_x describe the initial bulk momentum and momentum spread, $H(x)$ is the Heaviside function, and the normalization constant is

$$A \equiv \left[\pi \int_0^{p_0} dp_{x0} \exp[-(p_{x0} - p_0)^2 / \Delta p_x^2] \right]^{-1}. \quad (15)$$

Observe that this distribution is *monoenergetic*, but contains a pitch-angle spread which describes an axial energy spread given approximately by

$$\frac{\Delta \gamma_z}{\gamma_0} \approx 1 - \left[1 + 2(\gamma_0^2 - 1) \frac{\Delta p_x}{p_0} \right]^{-1/2}, \quad (16)$$

where $\gamma_0 \equiv (1 + p_0^2 / m^2 c^2)^{1/2}$. As a result, the averaging operator takes the form

$$\langle (\dots) \rangle \equiv \frac{A}{2\pi ab} \int_0^{2\pi} d\phi_0 \int_0^{p_0} dp_{x0} \beta_{x0} \exp[-(p_{x0} - p_0)^2 / \Delta p_x^2] \int_{-\pi}^{\pi} d\psi_0 \sigma_1(\psi_0) \int_{-a/2}^{a/2} dx_0 \int_{-b/2}^{b/2} dy_0 \sigma_1(x_0, y_0) (\dots), \quad (17)$$

where $\psi_0 (\equiv -\omega t_0)$ is the initial ponderomotive phase, $\phi_0 \equiv \tan^{-1}(p_{y0}/p_{x0})$, $\beta_{x0} \equiv v_{x0}/c$, and $\sigma_1(\psi_0)$ and $\sigma_1(x_0, y_0)$ describe the initial-beam distributions in phase and in the cross section.

The phase variation of each mode can be analyzed by the addition of an equation to integrate the relative phase:

$$\Phi(z) \equiv \int_0^z dz' [k(z') - k_0], \quad (18)$$

where $k_0 \equiv (\omega^2/c^2 - k_n^2)^{1/2}$, is the wave number of the vacuum guide. Since the departure of $k(z)$ from the vacuum wave number describes the effect of the wave-particle interaction, $\Phi(z)$ represents a measure of the dielectric effect of the FEL interaction. Thus we integrate the additional equation

$$\frac{d}{dz} \Phi = k - k_0, \quad (19)$$

for each TE and TM mode.

Each mode will interact resonantly with the electrons and be coupled through the electron motion in the combined wiggler and bulk radiation fields. Thus in order to complete the formulation, the electron orbit equations must also be specified. Since we describe an amplifier model, we choose to integrate in z , and write the Lorentz force equations in the form

$$v_z \frac{d}{dz} \mathbf{p} = -e \delta \mathbf{E} - \frac{e}{c} \mathbf{v} \times (\mathbf{B}_w + \delta \mathbf{B}), \quad (20)$$

where \mathbf{B}_w is given by Eq. (1) and the radiation fields are given by

$$\delta \mathbf{E} = -\frac{1}{c} \frac{\partial}{\partial t} \sum_{\text{all modes}} \delta \mathbf{A}_n \quad (21)$$

and

$$\delta \mathbf{B} = \nabla \times \sum_{\text{all modes}} \delta \mathbf{A}_n. \quad (22)$$

Finally the electron coordinates obey the equations

$$v_z \frac{d}{dz} x = v_x, \quad (23)$$

$$v_z \frac{d}{dz} y = v_y, \quad (24)$$

and

$$\frac{d}{dz} \psi = k + k_w - \frac{\omega}{v_z}, \quad (25)$$

which describe the evolution of ponderomotive phase

$$\psi = \psi_0 + \int_0^z dz' \left[k + k_w - \frac{\omega}{v_z} \right]. \quad (26)$$

III. NUMERICAL ANALYSIS

The dynamical equations for the particles and fields described in Sec. II are now solved for an overmoded amplifier configuration in which several modes may be in resonance with the beam at a fixed frequency ω . The numerical problem involves the solution of a set of $6N_T + 4N_M$ ordinary differential equations (where N_T is the number of particles and N_M is the number of modes) as an initial-value problem. Observe that equations for the amplitude, growth rate, wave number, and phase are integrated for each mode. The integration is accomplished by means of a fourth-order Runge-Kutta-Gill technique, and the particle average described in Eq. (17) is performed by N th-order Gaussian quadrature in each of the initial variables. The initial conditions on the fields are chosen to model the injection of an arbitrary power level of each mode, and the initial wave numbers correspond to the vacuum state [i.e., $k(z=0) = k_0$]. Further, the initial value of the relative phase of each mode is zero, and both the wiggler field and growth rate are initially zero. The initial state of the electron beam is chosen to model the injection of a continuous, axisymmetric electron beam with a uniform cross section so that $\sigma_1 = 1$ for $-\pi \leq \psi_0 \leq \pi$ and $\sigma_1 = 1$ for $r_0 \leq R_b$. A more

detailed description of the procedure is to be found in Refs. 22 and 26.

The particular example we consider is that of a 35-GHz amplifier employing an electron beam with an energy of 3.5 MeV, a current of 850 A, and an initial radius of 1.0 cm propagating through a waveguide characterized by $a = 9.8$ cm and $b = 2.9$ cm. Wave-particle resonance is obtained in the vicinity of 35-GHz for a wiggler field of 3.72-kG amplitude and a 9.8-cm period, and beam injection is accomplished over an entry with a length of five wiggler periods. For this choice of parameters three wave modes are resonant; specifically, the TE_{01} , TE_{21} , and TM_{21} modes. The multimode results described herein will be compared with a previous single-mode treatment. In addition, the parameters correspond with an experiment conducted by Orzechowski and co-workers,^{9,13} and a comparison of the simulation with the experiment will be given in Sec. IV.

The detailed evolution of the total wave power as a function of axial position is shown in Fig. 1 for an axial energy spread of $\Delta\gamma_z/\gamma_0 = 1.5\%$ on the beam and the injection of a signal at $\omega/ck_w = 11.3$ (34.6 GHz) composed of the TE_{01} mode at 50 kW, the TE_{21} mode at 500 W, and the TM_{21} mode at 100 W. As shown in the figure, saturation of the total signal occurs at $k_w z = 96$ (1.5 m) at a power level of 201 MW for a total efficiency of $\eta \approx 6.87\%$. It is also evident that although the TE_{01} mode was the overwhelming dominant mode upon injection, it comprises only about 60% of the signal at saturation. The remaining power is composed primarily of the TE_{21} mode (at 37% of the signal) with only a relatively small contribution of the TM_{21} mode. As discussed in

Ref. 32, the reason for this is that at this frequency the growth rate of the TE_{21} mode exceeds that of the TE_{01} mode, and compensates for the lower initial power level. Due to the polarization of the TM_{21} mode, the growth rate and efficiency are smaller than for the TE modes, and the TM_{21} mode never accounts for more than about 7 MW. The rapid oscillation shown in the figure has a period of approximately $\lambda_w/2$ and occurs because the evolution of $J \cdot E$ for a planar wiggler exhibits both a slow variation corresponding to the ponderomotive phase and a rapid oscillation at $\lambda_w/2$.³² Observe that the single-mode analysis showed a saturated power of 162 MW for the TE_{01} mode, 126 MW for the TE_{21} mode, and 25 MW for the TM_{21} mode. Thus while the total power of the signal in the multimode analysis somewhat exceeds that shown in the single-mode cases (for the TE modes), the power levels of the individual modes are lower.

The phase variation of each of these modes is shown in Fig. 2 as a function of axial position, where the arrow denotes the point at which the total power saturates. Of these modes, the TE_{01} mode qualitatively behaves in the same way as in the single-mode case. Specifically, the bulk phase at this frequency (apart from the rapid oscillation at $\lambda_w/2$) increases monotonically with axial position through, and beyond, the saturation point. In contrast, the relative phases of both the TE_{21} and TM_{21} modes are decidedly not monotonic and exhibit a decrease with axial position starting at a point somewhat beyond saturation. This is a multimode effect since the relative phases of the TE_{21} and TM_{21} modes also exhibit a monotonic increase with axial position at this frequency in the single-mode analysis. Finally, we observe that the curves of rel-

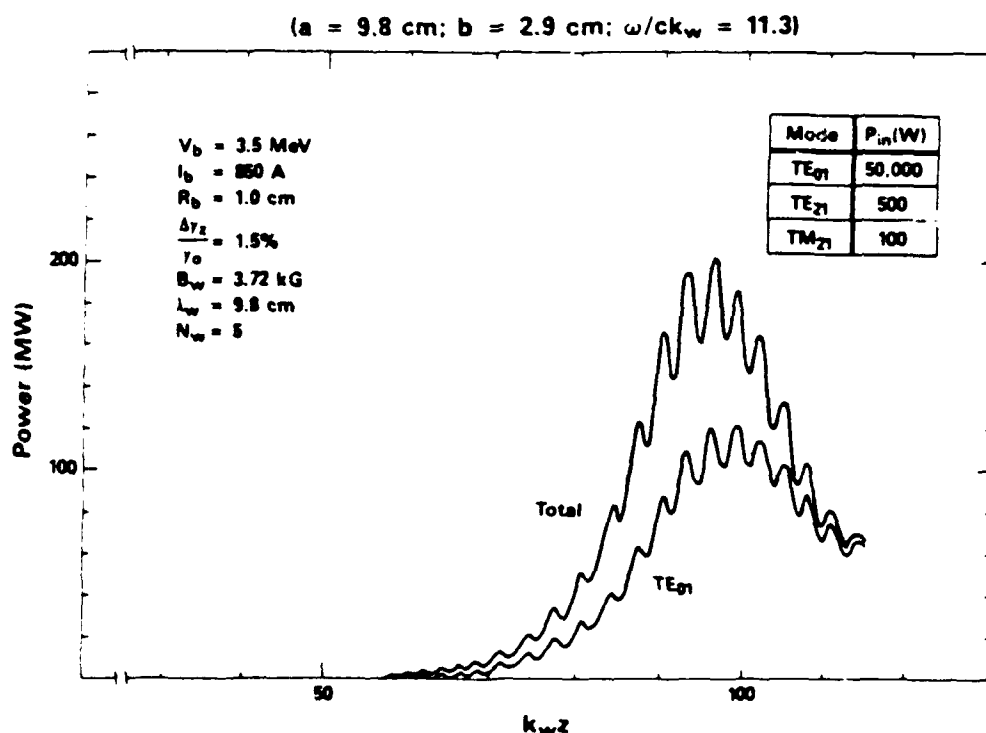


FIG. 1. Evolution of the wave power (both total and TE_{01} model) with axial position.

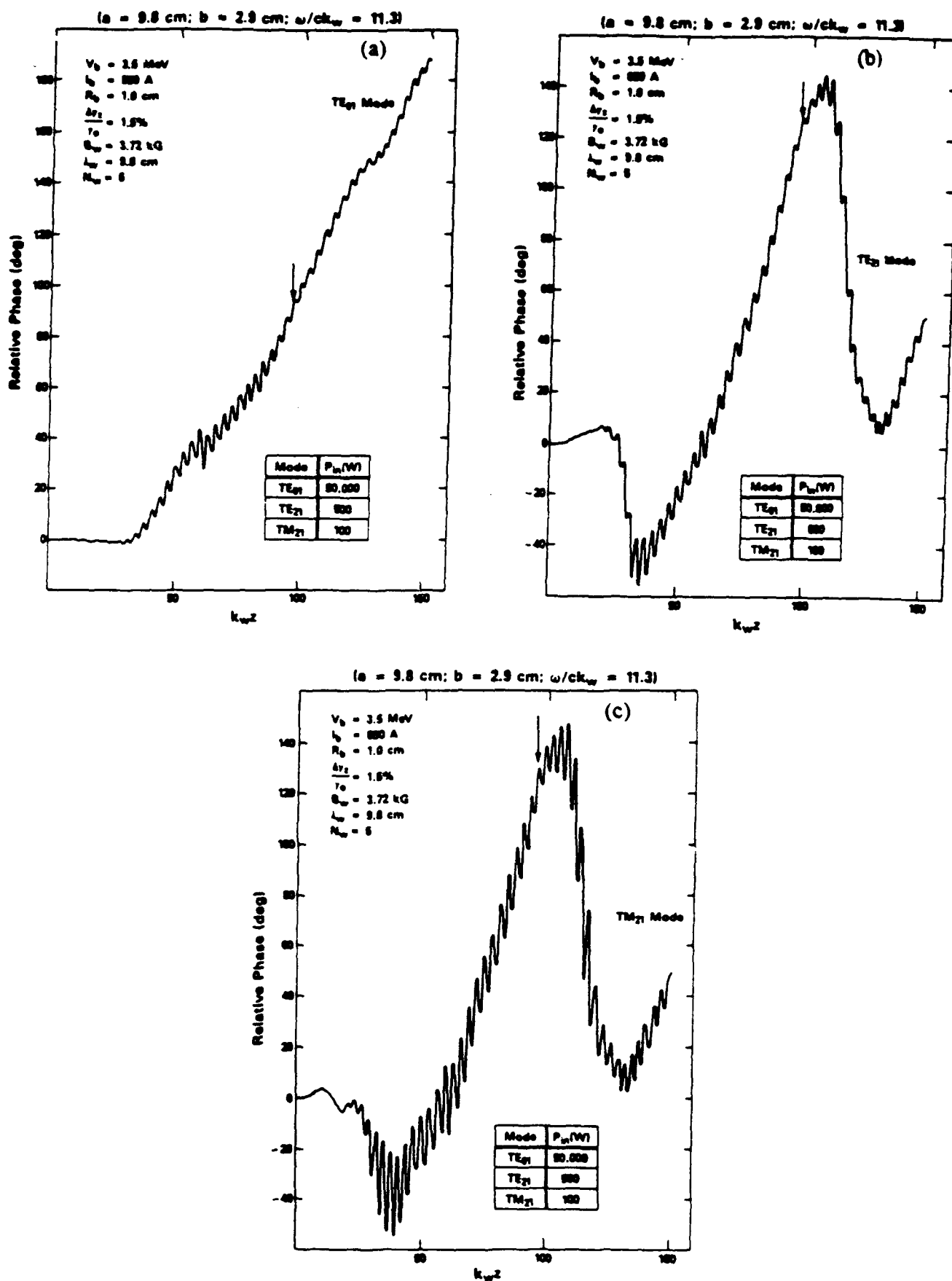


FIG. 2. Plots of the evolution of the relative phase vs axial position for (a) the TE₀₁ mode, (b) the TE₂₁ mode, and (c) the TM₂₁ mode.

active phase for the TE_{21} and TM_{21} modes are almost identical. The reason for this is that the dispersion curves for the TE_{1n} and TM_{1n} modes are degenerate in a rectangular waveguide.

The effect of an initial momentum spread on the saturation efficiency of the total signal and the TE_{01} and TE_{21} mode components is shown in Fig. 3. The TM_{21} mode is excluded from the figure because it composes such a small fraction of the signal. As shown in the figure, the saturation efficiency is relatively insensitive to the axial energy spread over the range $\Delta\gamma_z/\gamma_0 \leq 2.5\%$, and decreases from $\eta \approx 8.6\%$ at $\Delta\gamma_z/\gamma_0 = 0$ to $\eta \approx 5.9\%$ at $\Delta\gamma_z/\gamma_0 = 2.5\%$. The reason for this is that the coupling coefficient (and, hence, the growth rate) depends upon the product of the wiggler amplitude and period. Since this product is large for the present choice of parameters, the growth rate is large and the interaction can accept a relatively large axial energy spread without suffering a severe degradation.

The saturation efficiency is known to scale as the cube root of the beam current at the frequency of peak growth from the idealized one-dimensional theory of the high-gain Compton (i.e., the strong-pump) regime, and this type of scaling law was also found from the three-dimensional single-mode simulation of this configuration. The scaling of the total power as a function of beam current for the multimode analysis is shown in Fig. 4 for $\Delta\gamma_z = 0$ and $\Delta\gamma_z/\gamma_0 = 1\%$, and the efficiency is found to scale approximately as $\eta \sim I_b^{1/3}$.

Turning to the question of the enhancement of the efficiency by means of a tapered wiggler, we plot the evolution of the power with axial position in Fig. 5 for pa-

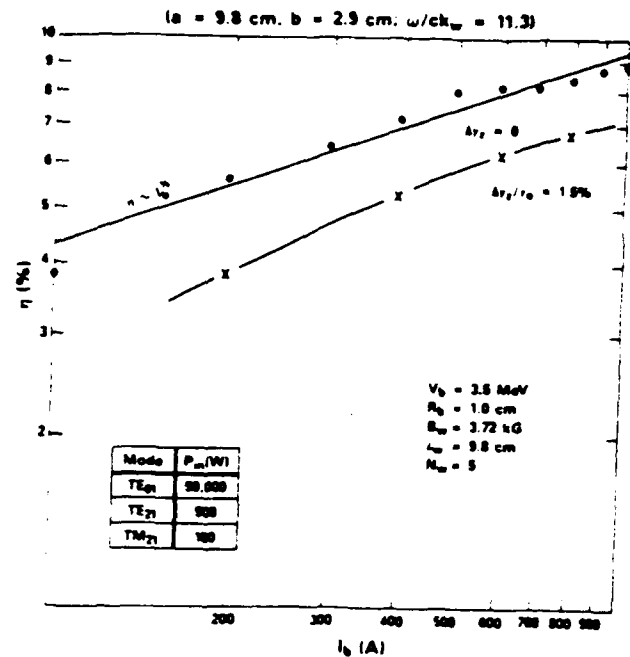


FIG. 4. Graph showing the scaling of the efficiency of the total signal with beam current for $\Delta\gamma_z/\gamma_0 = 0$ and 1% .

rameters corresponding to those shown in Fig. 1. The optimal start-taper point for this case is $k_w z_0 = 86$, and we choose a slope of $\epsilon_w = -0.007$, which was also studied for the single-mode analysis. The central conclusion to be drawn from the figure is that it is possible to selectively enhance the TE_{01} mode. The uniform wiggler interac-

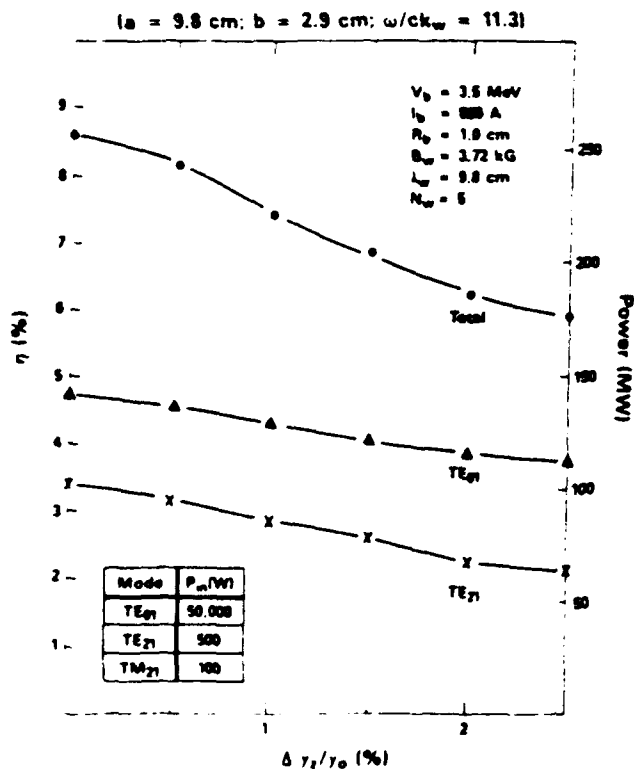


FIG. 3. Variations of the saturation efficiencies of the total signal and the TE modes vs axial energy spread.

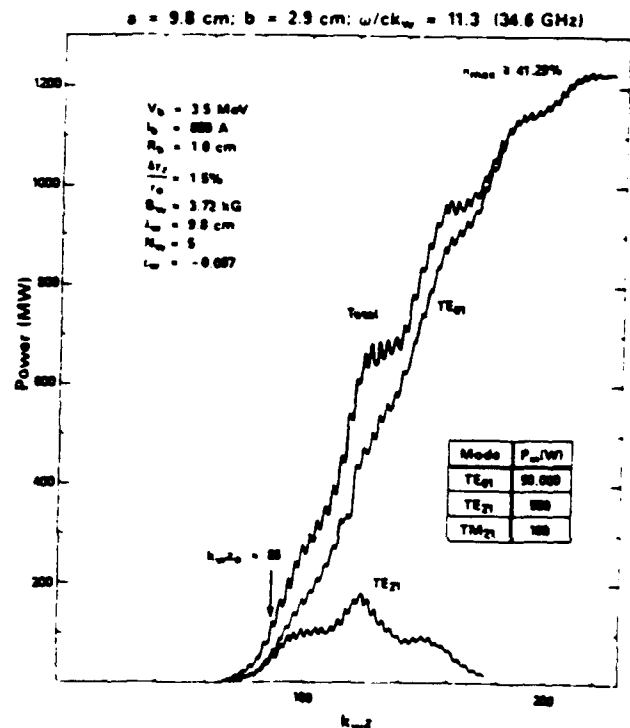


FIG. 5. Plot showing the evolution of the total signal and the TE modes for a tapered wiggler interaction characterized by $\epsilon_w = -0.007$ and $k_w z_0 = 86$.

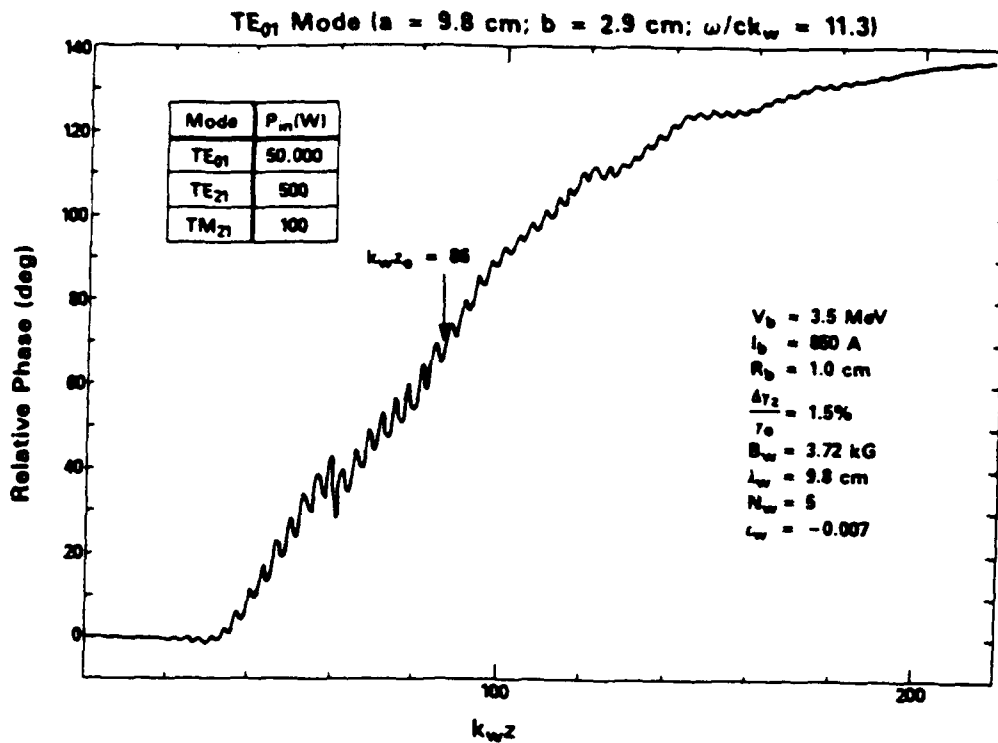


FIG. 6. Graph of the evolution of the relative phase of the TE₀₁ mode during the course of the tapered wiggler interaction.

tion for this example yields a total efficiency of 6.8%, of which the TE₀₁ mode comprises only 60% of the signal. By contrast, careful choice of both the start-taper point and the slope of the taper shows that the efficiency can be enhanced to $\eta_{\max} \approx 41.29\%$ (if the wiggler field is tapered to zero) with 99% of the power in the TE₀₁ mode. Both the TE₂₁ and TM₂₁ (not shown in the figure) modes ultimately decay to extremely low intensities. One surprising result of the present multimode analysis is that the maximum efficiency to be obtained by tapered wiggler fields is enhanced relative to the single-mode analysis. By comparison, the single-mode analysis for these parameters yields a maximum efficiency of $\eta_{\max} \approx 34\%$, which is substantially lower than the 41.29% found in the multimode simulation. The phase variation of the TE₀₁ mode for this example is shown in Fig. 6, and exhibits the same qualitative variation as in the single-mode analysis. Another characteristic of the tapered wiggler interaction observed in the single-mode treatment is that the overall efficiency appears to be relatively insensitive to the axial energy spread. As shown in Fig. 7, in which we plot the maximum obtainable efficiency versus $\Delta\gamma_z/\gamma_0$, this is also found to be the case in the multimode analysis. As shown in the figure, the maximum efficiency decreases from 43.6% at $\gamma_z = 0$ to as much as 39.4% at $\Delta\gamma_z/\gamma_0 = 2\%$. This is a much lower proportional sensitivity to the axial energy spread than is illustrated in Fig. 3 for the uniform wiggler case.

Finally, we address the question of the sensitivity of the tapered wiggler interaction to fluctuations in the bulk energy of the beam. The reason for concern with this is-

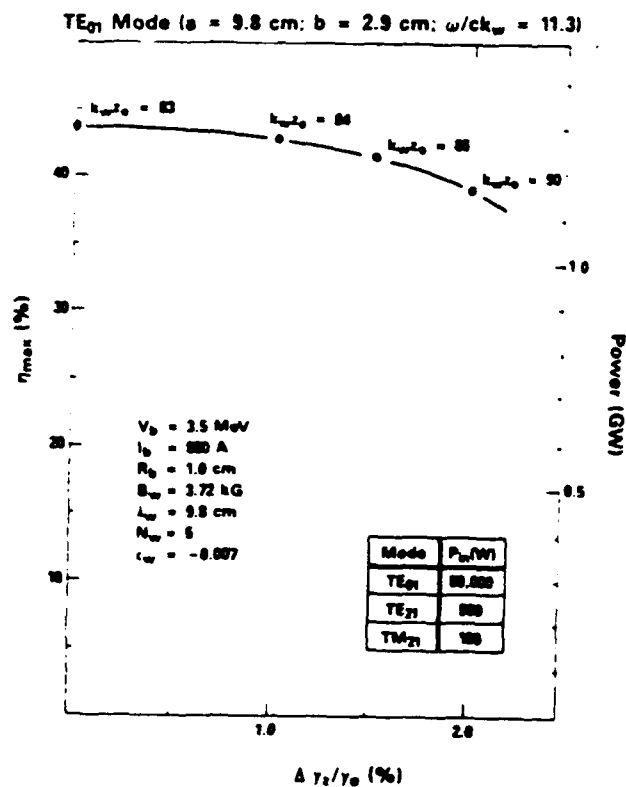


FIG. 7. Illustration of the effect of an axial energy spread on the tapered wiggler interaction. Observe that each point corresponds to the optimal start-taper point of the associated $\Delta\gamma_z$.

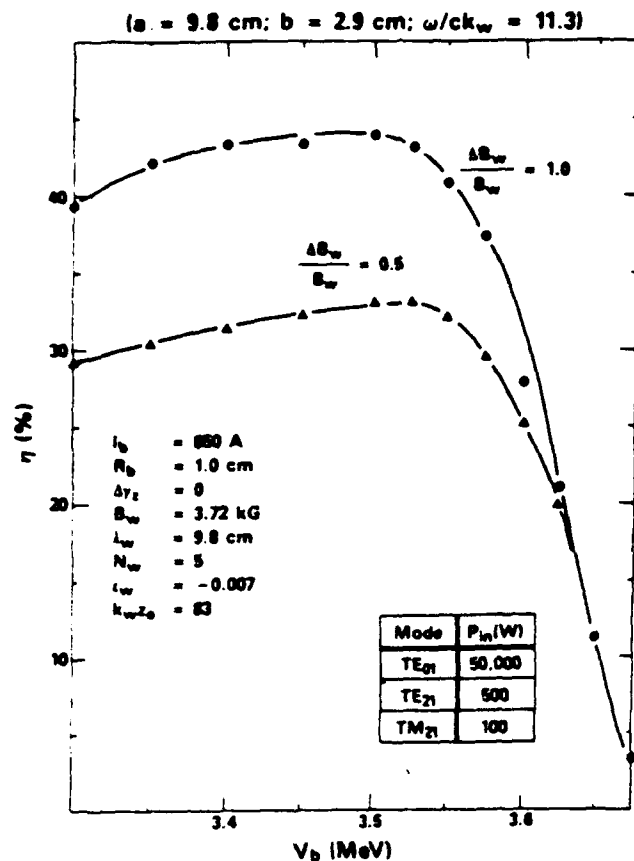


FIG. 8. Variation in the efficiency of the tapered wiggler interaction with fluctuations in the bulk energy of the beam.

sue is that the tapered wiggler interaction is known to be sensitive to the start-taper point. In particular, the taper should begin at a point shortly prior to saturation (for the untapered wiggler), corresponding to the trapping of the bulk of the beam in the ponderomotive potential. Changes or fluctuations in the beam energy at a fixed frequency are equivalent to the variation of the frequency at fixed energy, and result in shifts in the growth rate and saturation point. For this reason it might be expected that the tapered wiggler interaction is sensitive to fluctuations in the bulk energy of the beam. In order to address this question, the variation in the efficiency has been studied as a function of beam energy, and the results are shown in Fig. 8. For convenience, this figure has been generated for the limiting case of zero axial energy spread for which the optimal start-taper point is $k_w z_0 = 83$ at a beam energy of 3.5 MeV. Hence, choosing $\epsilon_w = -0.007$ and the aforementioned start-taper point, Fig. 8 describes the variation in the efficiency with beam energy when (1) the wiggler is tapered to zero ($\Delta B_w/B_w = 1$) and (2) when the wiggler is tapered to half its ambient level ($\Delta B_w/B_w = 0.5$). As shown in the figure, there is a sharp decline in the efficiency above, approximately, 3.55 MeV. In contrast, there is a more gradual decrease in the efficiency for energies down to 3.3 MeV, below which the resonant interaction at $\omega/ck_w = 11.3$ is lost. As a result, the tapered wiggler interaction will tolerate a bulk energy

fluctuation of the order of 8.6% without severe degradation in performance for these parameters.

IV. SUMMARY AND DISCUSSION

In this paper a multimode analysis and simulation of FEL amplifiers in three dimensions has been given for a configuration in which a relativistic electron beam propagates through an overmoded rectangular waveguide in the presence of a planar wiggler generated by means of an array of magnets with tapered pole pieces. The multimode analysis is accomplished by expansion of the radiation field in terms of the vacuum waveguide modes, and an arbitrary number of propagating TE and/or TM modes is included in the analysis. Although multiple modes are included in the analysis, the problem of interest is that of an amplifier and single-frequency propagation. As a result, the field equations are averaged over a wave period in order to eliminate the fast-time-scale phenomena. However, no average of the orbit equations was performed, and the electron dynamics were treated by means of the fully three-dimensional Lorentz force equations. As a result, the effects of the adiabatic injection process, bulk wiggler motion, Betatron oscillations, velocity shear, beam focusing due to the wiggler gradients, and phase trapping of the beam in the ponderomotive potential formed by the beating of the wiggler and radiation fields are all included in a self-consistent manner.

The numerical example describes a 35-GHz amplifier which employs a 3.5-MeV-850-A electron beam with a 1.0-cm initial radius propagating through a rectangular waveguide with dimensions $a = 9.8$ cm and $b = 2.9$ cm in the presence of a wiggler field with a 3.72-kG amplitude and 9.8 cm period. Three distinct wave modes are found to be resonant; specifically, the TE₀₁, TE₂₁, and TM₂₁ modes. The simulation is carried out under the assumption that the injected signal consists primarily of the TE₀₁ mode at a 50 kW power level, the TE₂₁ mode at 500 W, and the TM₂₁ mode at 100 W. Results indicate that although the TE₂₁ mode was at a relatively low initial power level, it comprises upwards of 37% of the saturated signal. The coupling between the beam and the TM₂₁ mode was weaker than for the TE modes, and never accounted for more than a few percent of the total signal. Comparison with a previous single-mode analysis³² indicates that the efficiency of the total signal is somewhat higher than that found for single modes in the case of a uniform wiggler. A more dramatic difference between the multimode and single-mode treatments is found for a tapered wiggler interaction. In this case, it is found that the selective enhancement of the TE₀₁ mode is possible and, indeed, has been experimentally observed.¹³ However, the power levels to be obtained in the TE₀₁ mode through the multimode tapered wiggler interaction were found to be *substantially* higher than found in the single-mode simulation. This constitutes an important question for future study.

The configuration and parameters described in this paper nominally correspond to the experiment performed by Orzechowski and co-workers.^{6,13} The principal

differences between the analytical configuration and the experiment are that in the experiment (1) the beam was injected into the wiggler through an entry taper region one-wiggler-period long and (2) a quadrupole field was used to provide additional electron focusing instead of parabolically tapered pole pieces. Since the fringing fields associated with the wiggler field in the entry taper region are not included in the analytical model, it would be invalid to apply the analysis for $N_w=1$. However, the choice of $N_w=5$ is made as a compromise and gives good agreement with experiment, subject to the additional assumption of an axial energy spread of $\Delta\gamma_z/\gamma_0=1.5\%$. This is within an upper bound of 2% on the axial energy spread established by means of an electron spectrometer measurement.³⁷ The experimental measurement for a uniform wiggler interaction resulted in a saturated power level of 180 MW over a length of 1.3 m. As shown by Fig. 1, the simulation gives a peak power of 204 MW, which, if we average over the fast $\lambda_w/2$ oscillation, is reduced to 185 MW. Given the experimental uncertainties in high-power measurements, the latter figure is more relevant for comparison and is in substantial agreement with the experiment. The saturation length found from simulation (that is, the length of the uniform wiggler region plus one wiggler period to account for the entry taper region) is 1.1 m, which is also in good agreement with the experiment. Note that rapid oscillation in the power and relative phase at a period of $\lambda_w/2$ is likely to introduce a 10–20% uncertainty in the measurement of

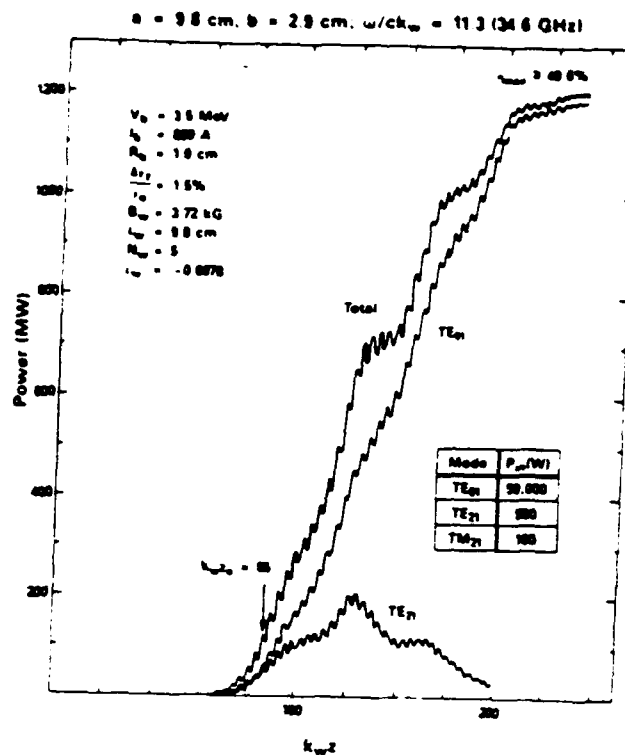


FIG. 9. Plot of the evolution of the total signal and the TE modes for a tapered wiggler characterized by $\epsilon_w = -0.0078$ and $k_w z_0 = 86$.

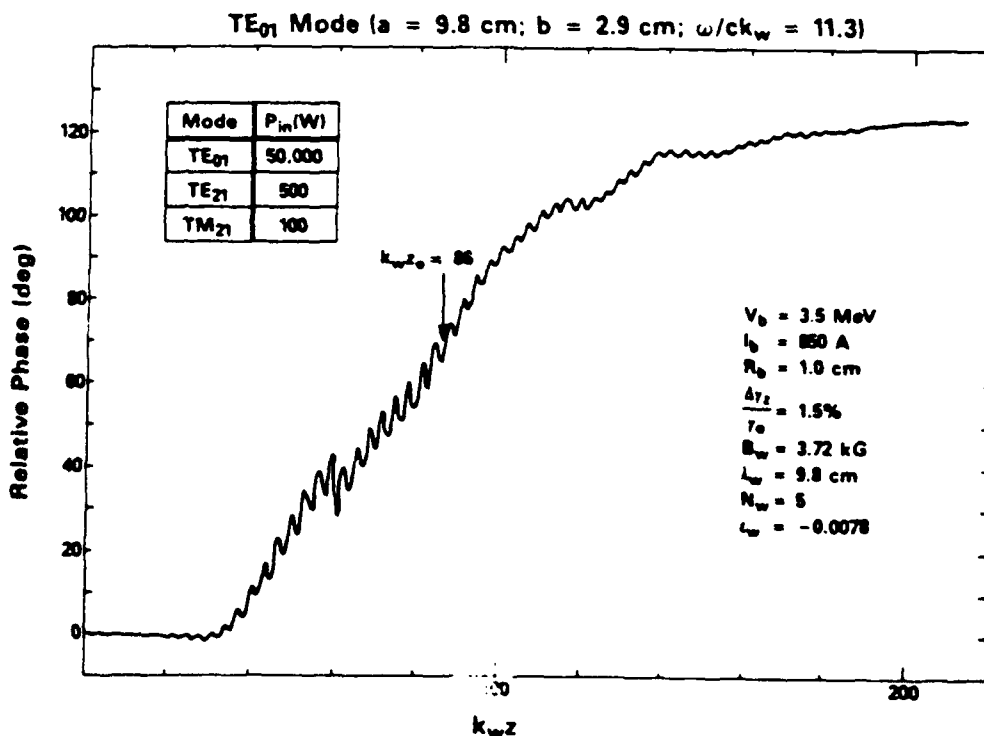


FIG. 10. Graph of the evolution of the relative phase for a tapered wiggler interaction characterized by $\epsilon_w = -0.0078$ and $k_w z_0 = 86$.

these quantities. A comparison can also be made with the tapered wiggler experiment¹³ in which the wiggler field was decreased by 55% ($\Delta B_w/B_w=0.55$) over a length of 1.1 m (i.e., $\epsilon_w=-0.0078$) and the efficiency was found to increase to 34% for a total power of 1 GW. The evolution of the total signal power, and that of the TE modes, is shown in Fig. 9 for parameters consistent with the tapered wiggler experiment (the optimal start-taper point found in simulation was $k_w z_0=86$). As shown in the figure, the maximum efficiency obtained by tapering the wiggler field to zero is approximately 40.6%, of which more than 95% of the power is contained in the TE₀₁ mode. However, over a length of only 1.1 m beyond the start-taper point (i.e., $k_w z-k_w z_0=70.5$) the efficiency is 34%, of which approximately 90% of the power is in the TE₀₁ mode. The evolution of the relative phase for this case is shown in Fig. 10, in which the rela-

tive phase saturates at a value in the neighborhood of 120° downstream from the start-taper point. This is in good agreement with reported measurements of the evolution of the relative phase in the tapered wiggler experiment.³⁸ Thus within the uncertainties imposed by the choices of N_w and $\Delta\gamma_z$, the nonlinear analysis is found to be in good agreement with the experimental measurements for both uniform and tapered wiggler interactions.

ACKNOWLEDGMENTS

This research was supported by the U. S. Office of Naval Research and the U. S. Office of Naval Technology. The author would like to thank Dr. A. K. Ganguly, Dr. R. K. Parker, and Dr. R. H. Jackson for helpful discussions.

- ¹R. M. Phillips, IRE Trans. Electron. Devices 7, 231 (1960).
- ²V. L. Granatstein, S. P. Schlesinger, M. Herndon, R. K. Parker, and J. A. Pasour, Appl. Phys. Lett. 30, 384 (1977).
- ³D. B. McDermott, T. C. Marshall, S. P. Schlesinger, R. K. Parker, and V. L. Granatstein, Phys. Rev. Lett. 41, 1368 (1978).
- ⁴R. K. Parker, R. H. Jackson, S. H. Gold, H. P. Freund, V. L. Granatstein, P. C. Efthimion, M. Herndon, and A. K. Kinkead, Phys. Rev. Lett. 48, 238 (1982).
- ⁵J. Fajans, G. Bekefi, Y. Z. Yin, and B. Lax, Phys. Rev. Lett. 53, 246 (1984).
- ⁶J. A. Pasour, R. F. Lucey, and C. W. Roberson, Proc. Soc. Photo-Opt. Instrum. Eng. 453, 328 (1984).
- ⁷J. A. Pasour, R. F. Lucey, and C. A. Kapetanakis, Phys. Rev. Lett. 53, 1728 (1984).
- ⁸S. H. Gold, D. L. Hardesty, A. K. Kinkead, L. R. Barnett, and V. L. Granatstein, Phys. Rev. Lett. 52, 1218 (1984).
- ⁹T. J. Orzechowski, B. Anderson, W. M. Fawley, D. Prosnitz, E. T. Scharlemann, S. Yarema, D. Hopkins, A. C. Paul, A. M. Sessler, and J. Wurtele, Phys. Rev. Lett. 54, 889 (1985).
- ¹⁰J. Fajans, G. Bekefi, Y. Z. Yin, and B. Lax, Phys. Fluids 28, 1995 (1985).
- ¹¹J. Masud, T. C. Marshall, S. P. Schlesinger, and F. G. Yee, Phys. Rev. Lett. 56, 1567 (1986).
- ¹²J. Fajans, J. Wurtele, G. Bekefi, D. S. Knowles, and K. Xu, Phys. Rev. Lett. 57, 579 (1986).
- ¹³T. J. Orzechowski, B. Anderson, J. C. Clark, W. M. Fawley, A. C. Paul, D. Prosnitz, E. T. Scharlemann, S. Yarema, D. B. Hopkins, A. M. Sessler, and J. Wurtele, Phys. Rev. Lett. 57, 2172 (1986).
- ¹⁴L. R. Elias, W. M. Fairbanks, J. M. J. Madey, H. A. Schwettman, and T. I. Smith, Phys. Rev. Lett. 36, 717 (1976).
- ¹⁵D. A. G. Deacon, L. R. Elias, J. M. J. Madey, G. J. Ramian, H. A. Schwettman, and T. I. Smith, Phys. Rev. Lett. 38, 892 (1977).
- ¹⁶R. W. Warren, B. E. Newnam, J. G. Winston, W. E. Stein, L. M. Young, and C. A. Brau, IEEE J. Quantum Electron. QE-19, 391 (1983).
- ¹⁷M. Billandon, P. Ellaume, J. M. Ortega, C. Bazin, M. Bergher, M. Velghe, Y. Petroff, D. A. G. Deacon, K. E. Robinson, and J. M. J. Madey, Phys. Rev. Lett. 51, 1652 (1983).
- ¹⁸J. M. Slater, J. L. Adamski, D. C. Quimby, T. L. Churchill, L. Y. Nelson, and R. E. Center, IEEE J. Quantum Electron. QE-19, 374 (1983).
- ¹⁹J. A. Edighoffer, G. R. Neil, C. E. Hess, T. I. Smith, S. W. Fornaca, and H. A. Schwettman, Phys. Rev. Lett. 52, 344 (1984).
- ²⁰B. E. Newnam, R. W. Warren, R. L. Sheffield, W. E. Stein, M. T. Lynch, J. S. Faser, J. C. Goldstein, J. E. Solid, T. A. Swann, J. M. Watson, and C. A. Brau, IEEE J. Quantum Electron. QE-21, 867 (1985).
- ²¹C. R. Pidgeon, S. D. Smith, W. J. Firth, D. A. Jorosynski, D. M. Tratt, J. S. Mackay, M. F. Kimmitt, J. M. Reid, M. G. Kelliher, M. W. Poole, G. Saxon, R. P. Walker, W. A. Gillespie, and P. F. Martin, IEEE J. Quantum Electron. QE-21, 1083 (1985).
- ²²Y. Z. Yin and G. Bekefi, J. Appl. Phys. 55, 33 (1983).
- ²³T. Shiozawa and H. Nakano, IEEE J. Quantum Electron. QE-21, 931 (1985).
- ²⁴R. C. Davidson and J. Wurtele, IEEE Trans. Plasma Sci. PS-13, 464 (1985).
- ²⁵E. Jerby and A. Gover, Nucl. Instrum. Method A 250, 192 (1986).
- ²⁶R. C. Davidson, Phys. Fluids 29, 267 (1986).
- ²⁷B. W. J. McNeil and W. J. Firth, Nucl. Instrum. Meth. A 259, 240 (1987).
- ²⁸A. K. Ganguly and H. P. Freund, Phys. Rev. A 32, 2275 (1985).
- ²⁹H. P. Freund and A. K. Ganguly, Phys. Rev. A 33, 1060 (1986).
- ³⁰H. P. Freund and A. K. Ganguly, Phys. Rev. A 34, 1242 (1986).
- ³¹H. P. Freund and A. K. Ganguly, IEEE J. Quantum Electron. QE-23, 1657, (1987).
- ³²H. P. Freund, H. Bluem, and C.-L. Chang, Phys. Rev. A 36, 2182 (1987).
- ³³C. M. Tang and P. Sprangle, IEEE J. Quantum Electron. QE-21, 970 (1985).
- ³⁴P. Sprangle, A. Ting, and C. M. Tang, Phys. Rev. Lett. 59, 202 (1987).
- ³⁵P. Sprangle, A. Ting, and C. M. Tang, Phys. Rev. A 36, 2773 (1987).
- ³⁶E. T. Scharlemann, J. Appl. Phys. 58, 2154 (1985).
- ³⁷T. J. Orzechowski (private communication).
- ³⁸T. J. Orzechowski, E. T. Scharlemann, and D. B. Hopkins, Phys. Rev. A 35, 2184 (1987).

APPENDIX X

Nonlinear Theory of Slow-Wave Ubitrons/Free-Electron Lasers

by

H.P. Freund

NONLINEAR THEORY OF SLOW-WAVE UBITRONS/FREE-ELECTRON LASERS

H.P. Freund[†]
Naval Research Laboratory
Washington, D.C. 20375
(202) 767-0034
FAX: (202) 767-0546

ABSTRACT

A 3-dimensional nonlinear formulation of a slow-wave Ubitron/Free-Electron Laser is presented. The configuration is that of an electron beam propagating through a dielectric-lined rectangular waveguide in the presence of a planar wiggler field. The wiggler field model describes parabolic pole faces for enhanced beam focussing. The electromagnetic field is described in terms of a multi-mode ensemble of the normal modes of the vacuum waveguide. In this case, the dielectric liner is imposed along the y -axis of the guide [which is also the principle orientation of the wiggler], and there are no orthogonal TE or TM modes. Instead, we deal with modes which are transverse electric (LSE) or magnetic (LSM) to the y -axis. Equations are derived which describe the evolution of the amplitude and phase of these modes in terms of the microscopic particle currents. These equations are solved in conjunction with the complete Lorentz force equations for the electron trajectories. The essential purpose of employing a slow-wave structure is to reach shorter wavelengths at relatively low beam energies, and numerical results will be presented to demonstrate the potentialities of this concept.

[†]Permanent Address: Science Applications International Corp., McLean, Virginia 22102, USA.

Ubitrons and Free-Electron Lasers have been constructed with a wide range of waveguide and optical geometries.¹⁻⁸ In the bulk of these cases, the electron beam interacts with a supraluminous wave in which the resonant wavelength scales inversely as the square of the beam energy. In many cases, however, this imposes too high a requirement on the electron beam energy, and methods for reducing the beam energy requirement have been eagerly sought. One technique is to pursue the interaction at harmonics of the resonant frequency. Unfortunately, the harmonic interaction poses difficulties in that (1) some method of suppressing the fundamental interaction must be found, (2) there is some penalty to be paid in terms of reductions in both the gain and efficiency at the harmonics, and (3) the requirements of high beam quality become progressively more severe as the harmonic number increases. In this paper, therefore, an alternate method of reducing the beam energy requirement is studied; specifically, the use of a dielectric liner to slow the phase velocity of the wave. The interaction that results can be either with a supraluminous or a subluminoous wave, but in either case the beam energy required for interaction at a given frequency is reduced.

The configuration employed is that of a single-frequency amplifier in which a relativistic electron beam propagates through a dielectric-lined rectangular waveguide in the presence of a planar wiggler field. The waveguide is characterized as shown in Fig. 1 in which the dimensions of the outer walls are at $x = 0, a$ and $y = \pm b/2$. The dielectric is aligned parallel to the long (i.e., x) axis of the waveguide with a thickness Δ and an inner surface at $y = \pm d$, where $d = b/2 - \Delta$. The wiggler field model is chosen to describe the effect of parabolic pole faces for enhanced focussing^{1,9}, i.e.

$$\begin{aligned} \mathbf{B}_w = B_w(z) \left\{ \cos(k_w z) \left[\hat{\mathbf{e}}_x \sinh\left(\frac{k_w x}{\sqrt{2}}\right) \sinh\left(\frac{k_w y}{\sqrt{2}}\right) + \hat{\mathbf{e}}_y \cosh\left(\frac{k_w x}{\sqrt{2}}\right) \cosh\left(\frac{k_w y}{\sqrt{2}}\right) \right] \right. \\ \left. - \sqrt{2} \hat{\mathbf{e}}_z \sin(k_w z) \cosh\left(\frac{k_w x}{\sqrt{2}}\right) \sinh\left(\frac{k_w y}{\sqrt{2}}\right) \right\}, \quad (1) \end{aligned}$$

where $k_w [\equiv 2\pi/\lambda_w]$, where λ_w denotes the wiggler period] is the wiggler wavenumber, and $B_w(z)$ describes the amplitude. The wiggler amplitude is allowed to vary slowly in z as follows

$$B_w(z) = \begin{cases} B_w \sin^2(k_w z / 4N_w) & ; 0 < z < N_w \lambda_w \\ B_w & ; N_w \lambda_w < z < z_0 \\ B_w [1 + \epsilon_w k_w (z - z_0)] & ; z > z_0 \end{cases}, \quad (2)$$

in order to describe (1) the injection of the beam through an adiabatic entry taper over N_w wiggler periods, and (2) the efficiency enhancement by means a tapered wiggler amplitude [in which ϵ_w describes the slope of the taper]. This wiggler model is both curl and divergence free for a uniform wiggler amplitude, and we implicitly assume that the gradients imposed by the amplitude tapering are small [i.e., $N_w \gg 1$ and $\epsilon_w \ll 1$]. Observe that the orientation of this wiggler model implies that the direction of the transverse wiggler-induced oscillations are aligned parallel to the dielectric liner. This was chosen, along with the enhanced focussing provided by the parabolic pole faces, in order to minimize loss of the beam to the dielectric.

The electromagnetic field is represented by means of an expansion in terms of the vacuum modes [i.e., in the absence of the electron beam] of the waveguide. The standard TE and TM modes of a rectangular waveguide do not exist in the presence of the dielectric liner. Instead, there are normal modes which are either transverse electric (LSE) or Transverse magnetic (LSM) with respect to the y -axis in the present configuration.¹⁰ We focus on the LSE modes since only this polarization presents an electric field component which is aligned with the bulk wiggler-induced transverse velocity. The electric and magnetic fields of these modes can be represented in the form

$$\delta \mathbf{E}(\mathbf{x}, t) = -\frac{\omega}{c} \sum_{l,n} \delta A_{ln} Z_{ln}(y) \left[\hat{\mathbf{e}}_x \cos\left(\frac{l\pi x}{a}\right) \sin \alpha - \frac{l\pi}{k_{ln} a} \hat{\mathbf{e}}_z \sin\left(\frac{l\pi x}{a}\right) \cos \alpha \right], \quad (3)$$

and

$$\delta \mathbf{B}(\mathbf{x}, t) = \sum_{l,n} k_{ln} \delta A_{ln} \left[\frac{l\pi}{ak_{ln}^2} Z'_{ln}(y) \hat{\mathbf{e}}_x \sin\left(\frac{l\pi x}{a}\right) \sin \alpha - \left(1 + \frac{l^2 \pi^2}{a^2 k_{ln}^2}\right) Z_{ln}(y) \hat{\mathbf{e}}_y \cos\left(\frac{l\pi x}{a}\right) \sin \alpha - \frac{1}{k_{ln}} Z'_{ln}(y) \hat{\mathbf{e}}_z \cos\left(\frac{l\pi x}{a}\right) \cos \alpha \right], \quad (4)$$

where we assume that the amplitude δA_{ln} and the wavenumber k_{ln} are slowly-varying functions of z , and the phase is given by

$$\alpha \equiv \int_0^z dz' k_{ln}(z') - \omega t. \quad (5)$$

There are even and odd modes which are differentiated by the dispersion equations and the transverse mode patterns $Z_n(y)$. For the even modes, the dispersion equation is

$$\kappa_{ln} \tan \kappa_{ln} d = \kappa'_{ln} \cot \kappa'_{ln} \Delta, \quad (6)$$

where

$$\frac{\epsilon \omega^2}{c^2} = k_{ln}^2 + \frac{l^2 \pi^2}{a^2} + \kappa_{ln}^2, \quad (7)$$

in the dielectric, and

$$\frac{\omega^2}{c^2} = k_{ln}^2 + \frac{l^2 \pi^2}{a^2} + \kappa_{ln}^2, \quad (8)$$

in the vacuum. The transverse variation for these modes is given by

$$Z_{ln}(y) \equiv \begin{cases} \sin \kappa'_{ln}(b/2 - y) & ; d < y < b/2 \\ \frac{\kappa'_{ln} \cos \kappa'_{ln} \Delta}{\kappa_{ln} \sin \kappa_{ln} d} \cos \kappa_{ln} y & ; -d < y < d \\ \sin \kappa'_{ln}(b/2 + y) & ; -b/2 < y < -d \end{cases}. \quad (9)$$

For the odd modes, we have the dispersion equation

$$\kappa_{ln} \cot \kappa_{ln} d = -\kappa'_{ln} \cot \kappa'_{ln} \Delta, \quad (10)$$

and the transverse mode structure

$$Z_{ln}(y) \equiv \begin{cases} \sin \kappa'_{ln}(b/2 - y) & ; d < y < b/2 \\ -\frac{\kappa'_{ln} \cos \kappa'_{ln} \Delta}{\kappa_{ln} \cos \kappa_{ln} d} \sin \kappa_{ln} y & ; -d < y < d \\ -\sin \kappa'_{ln}(b/2 + y) & ; -b/2 < y < -d \end{cases} \quad (11)$$

The dynamical equations which govern the evolution of the slowly-varying amplitude and wave number are obtained by substitution of the representation of the electric field (3) into Maxwell's equations

$$\left(\nabla^2 - \frac{1}{c^2} \frac{\partial^2}{\partial t^2} \right) \delta \mathbf{E}(\mathbf{x}, t) - \nabla(\nabla \cdot \delta \mathbf{E}(\mathbf{x}, t)) = \frac{4\pi}{c^2} \frac{\partial}{\partial t} \delta \mathbf{J}(\mathbf{x}, t) \quad , \quad (12)$$

where the source current is given by

$$\delta \mathbf{J}(\mathbf{x}, t) = -en_b \iiint d\mathbf{p}_0 v_{z0} F_b(\mathbf{p}_0) \iint_{A_g} dx_0 dy_0 \sigma_{\perp}(x_0, y_0) \int_{-\pi/2}^{\pi/2} dt_0 \sigma_{\parallel}(t_0) \\ \times \mathbf{v}(z; x_0, y_0, t_0, \mathbf{p}_0) \delta[\mathbf{x}_{\perp} - \mathbf{x}_{\perp}(z; x_0, y_0, t_0, \mathbf{p}_0)] \frac{\delta[t - \tau(z; x_0, y_0, t_0, \mathbf{p}_0)]}{|v_z(z; x_0, y_0, t_0, \mathbf{p}_0)|} \quad , \quad (13)$$

where v_{z0} is the initial axial velocity, \mathbf{p}_0 is the initial momentum, A_g is the cross-sectional area of the waveguide, $T = L/v_{z0}$ [where L is the length of the system], and σ_{\parallel} , σ_{\perp} , and F_b describe the distribution of the initial conditions of the beam.

Substitution of the field representation into Maxwell's equation yields

$$\left(1 + \frac{l^2 \pi^2}{a^2 k_{ln}^2} \right) \left(\frac{\omega^2}{c^2} - k_{ln}^2 - \kappa_{ln}^2 \right) \delta a_{ln} = \\ = 8 \frac{\omega_b^2}{c^2} \frac{G_l}{F_{ln}} \left\langle Z_{ln}(y) \left[\frac{v_x}{v_z} \cos \left(\frac{l\pi x}{a} \right) \cos \alpha + \frac{l\pi}{ak_{ln}} \sin \left(\frac{l\pi x}{a} \right) \sin \alpha \right] \right\rangle \quad , \quad (14)$$

and

$$2 \left(k_{ln} + \frac{l^2 \pi^2}{a^2 k_{ln}} \right) \frac{d}{dz} \delta a_{ln} = \\ = -8 \frac{\omega_b^2}{c^2} \frac{G_l}{F_{ln}} \left\langle Z_{ln}(y) \left[\frac{v_x}{v_z} \cos \left(\frac{l\pi x}{a} \right) \sin \alpha - \frac{l\pi}{ak_{ln}} \sin \left(\frac{l\pi x}{a} \right) \cos \alpha \right] \right\rangle \quad , \quad (15)$$

after averaging over a wave period and neglecting second order derivatives of the amplitude and phase, where $\delta a_{ln} \equiv e\delta A_{ln}/m_e c^2$, $\omega_b^2 \equiv 4\pi e^2 n_b/m_e$, n_b denotes the ambient beam density, $G_l = 1/2$ when $l = 0$ and unity otherwise,

$$F_{ln} \equiv \frac{\sin^2 \kappa'_{ln} \Delta}{\cos^2 \kappa_{ln} d} \left(1 + \frac{\sin 2\kappa_{ln} d}{2\kappa_{ln} d} \right) + \frac{\Delta}{d} \left(1 - \frac{\sin 2\kappa'_{ln} \Delta}{2\kappa'_{ln} \Delta} \right), \quad (16)$$

for the even modes, and

$$F_{ln} \equiv \frac{\sin^2 \kappa'_{ln} \Delta}{\sin^2 \kappa_{ln} d} \left(1 - \frac{\sin 2\kappa_{ln} d}{2\kappa_{ln} d} \right) + \frac{\Delta}{d} \left(1 - \frac{\sin 2\kappa'_{ln} \Delta}{2\kappa'_{ln} \Delta} \right), \quad (17)$$

for the odd modes. The averaging operator in Eqs. (14) and (15) is defined over the initial conditions of the beam, and includes the effect of an *initial* momentum spread by means of the distribution function

$$F_b(\mathbf{p}_0) = A \exp \left[- (p_{z0} - p_0)^2 / \Delta p_z^2 \right] \delta(p_0^2 - p_{\perp 0}^2 - p_{z0}^2) H(p_{z0}), \quad (18)$$

where p_0 and Δp_z describe the initial bulk momentum and momentum spread, $H(x)$ is the Heaviside function, and the normalization constant is

$$A \equiv \left[\pi \int_0^{p_0} dp_{z0} \exp \left[- (p_{z0} - p_0)^2 / \Delta p_z^2 \right] \right]^{-1}. \quad (19)$$

Observe that this distribution describes a beam which is monoenergetic but with a pitch-angle spread which is equivalent to an *axial* energy spread of

$$\frac{\Delta \gamma_z}{\gamma_0} = 1 - \frac{1}{\sqrt{1 + 2(\gamma_0^2 - 1) \frac{\Delta p_z}{p_0}}}, \quad (20)$$

where $\gamma_0 \equiv (1 + p_0^2/m_e^2 c^2)^{1/2}$. As a result, the averaging operator takes the form

$$\begin{aligned} \langle \langle \dots \rangle \rangle &\equiv \frac{A}{4\pi A_g} \int_0^{2\pi} d\varphi_0 \int_0^{p_0} dp_{z0} \beta_{z0} \exp \left[- (p_{z0} - p_0)^2 / \Delta p_z^2 \right] \times \\ &\quad \times \int_0^{2\pi} d\psi_0 \sigma_{||}(\psi_0) \iint_{A_\perp} dx_0 dy_0 \sigma_{\perp}(x_0, y_0) (\dots). \end{aligned} \quad (21)$$

In order to complete the formulation, we must specify the orbit equations for the electron ensemble. Since we deal with an amplifier model, we integrate the complete three-dimensional Lorentz force equations in z . No average of these equations over a wiggler period is performed.

The numerical example we consider deals with a waveguide with dimensions $a = 9.8$ cm, $b = 2.9$ cm, and $\Delta = 0.5$ cm, and the dielectric constant is $\epsilon = 4.2$ which corresponds to boron nitride. The wiggler field has a period $\lambda_w = 9.8$ cm and increases to a constant value $B_w = 1$ kG over an entry taper region which is five wiggler periods in length. We assume an ideal (i.e., $\Delta\gamma_z = 0$) solid pencil electron beam with an energy of 1.35 MeV, a current of 1.0 kA, and with a radius of 0.25 cm. This example corresponds to a resonance at a frequency of 5.1 GHz in the LSE_{01} mode which is still in the supraluminous range, but has a phase velocity well below that of the TE_{01} mode in the absence of the dielectric. As shown in Fig. 2, we inject a 50 kW signal in the LSE_{01} mode, which subsequently grows to a peak power level of approximately 324 MW for a saturation efficiency of 24.15%. The oscillation seen in the power occurs with a period of $\lambda_w/2$, and corresponds to the effect of the lower beat wave upon the interaction in planar wiggler configurations.¹¹ No attempt has yet been made to optimize these parameters.

In summary, a nonlinear formulation and simulation code has been developed which is capable of treating the interaction between a relativistic electron beam and a planar wiggler field in the presence of a dielectric-lined rectangular waveguide. Note that a dielectric liner is only one way of slowing the wave, and that alternate techniques include a variety of slow wave structures including gratings and rippled wall geometries. An example showing high gain and efficiency is given for the case of the resonant interaction of the LSE_{01} mode in the supraluminous regime. Although this does not represent a slow wave [which usually denotes a subluminal wave], there is still a substantial advantage to be gained in achieving high frequency operation at relatively lower voltages than would be

possible in the absence of a dielectric. However, future studies will extend this analysis to the subluminal regime. Finally, it should also be remarked that this formulation is capable of treating the Cerenkov Maser interaction for subluminal waves as well by the simple expedient of letting the wiggler field amplitude vanish.

ACKNOWLEDGEMENTS

This work was supported by the Office of Naval Research and the Office of Naval Technology.

REFERENCES

- ¹R.M. Phillips, IRE Trans. Electron Dev. **7**, 231 (1960).
- ²L.R. Elias, W.M. Fairbanks, J.M.J. Madey, H.A. Schwettman, and T.I. Smith, Phys. Rev. Lett. **36**, 717 (1976).
- ³R.K. Parker, R.H. Jackson, S.H. Gold, H.P. Freund, V.L. Granatstein, P.C. Efthimion, M. Herndon, and A.K. Kinkead, Phys. Rev. Lett. **48**, 238 (1982).
- ⁴M. Billandon, P. Ellaume, J.M. Ortega, C. Bazin, M. Bergher, M. Velghe, Y. Petroff, D.A. G. Deacon, K.E. Robinson, and J.M.J. Madey, Phys. Rev. Lett. **51**, 1652 (1983).
- ⁵J. Fajans, G. Bekefi, Y.Z. Yin, and B. Lax, Phys. Rev. Lett. **53**, 246 (1984).
- ⁶B.E. Newnam, R.W. Warren, R.L. Sheffield, W.E. Stein, M.T. Lynch, J.S. Fraser, J.C. Goldstein, J.E. Sollid, T.A. Swann, J.M. Watson, and C.A. Brau, IEEE J. Quantum Electron. **QE-21**, 867 (1985).
- ⁷T.J. Orzechowski, B. Anderson, W.M. Fawley, D. Prosnitz, E.T. Scharlemann, S. Yarema, D. Hopkins, A.C. Paul, A.M. Sessler, and J. Wurtele, Phys. Rev. Lett. **54**, 889 (1985).
- ⁸J. Masud, T.C. Marshall, S.P. Schlesinger, and F.G. Yee, Phys. Rev. Lett. **56**, 1567 (1986).
- ⁹E.T. Scharlemann, J. Appl. Phys. **58**, 2154 (1985).
- ¹⁰R.F. Harrington, *Time-Harmonic Electromagnetic Fields* (McGraw-Hill, New York, 1961), Chap. 4.
- ¹¹H.P. Freund, Phys. Rev. A **37**, 3371 (1988).

FIGURE CAPTIONS

Fig. 1 Schematic illustration of the configuration of the dielectric-lined waveguide.

Fig. 2 Graph of the evolution of the power in the LSE_{01} mode as a function of axial distance.

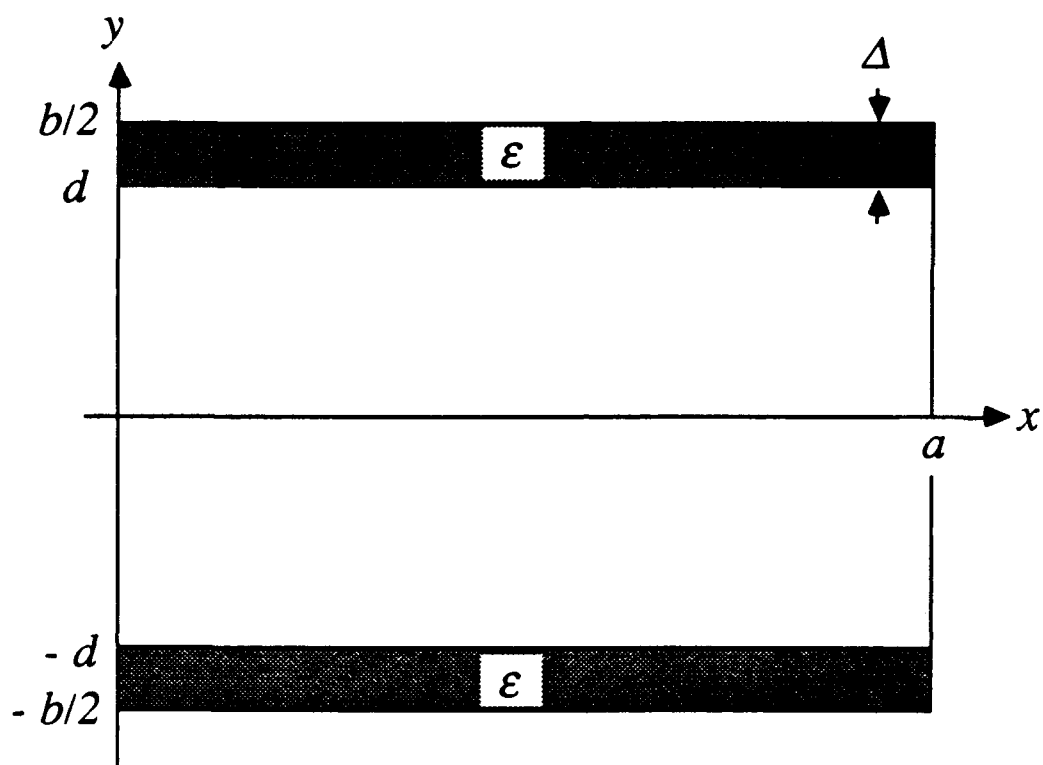


Fig. 1

LSE₀₁ ($a = 9.8$ cm; $b = 2.9$ cm; $\Delta = 0.5$ cm; $\epsilon = 4.2$)

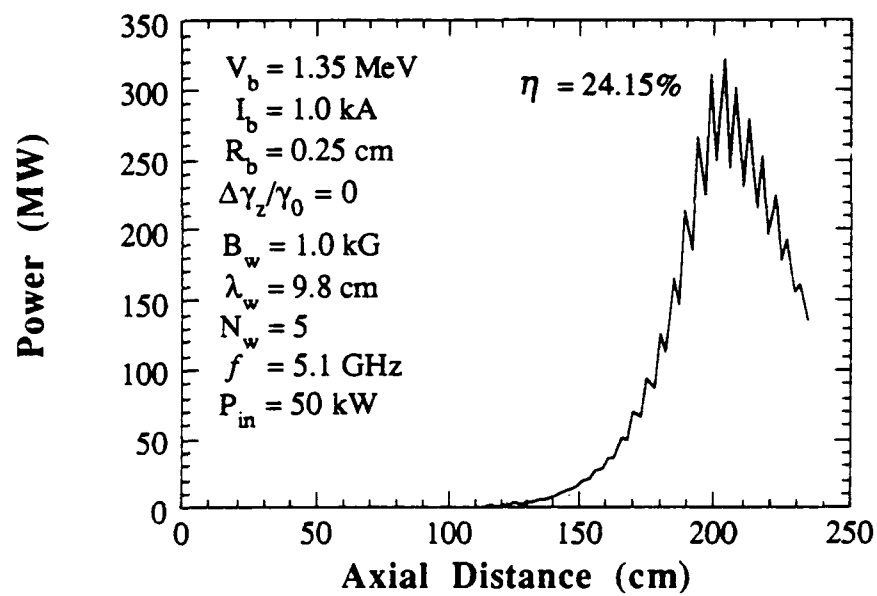


Fig. 2

APPENDIX XI

Harmonic Content in a Planar Wiggler Based Free-Electron Laser Amplifier

by

H. Bluem, H.P. Freund, and C.L. Chang

HARMONIC CONTENT IN A PLANAR WIGGLER BASED FREE ELECTRON LASER AMPLIFIER

H. BLUEM

Electrical Engineering Department, University of Maryland, College Park, MD 20742, USA

H.P. FREUND and C.L. CHANG

Science Applications International Corp., McLean, VA 22102, USA

Amplification at harmonics of the fundamental frequency of the free electron laser (FEL) is studied for a configuration utilizing a planar wiggler with parabolically shaped pole pieces. The analysis employs a fully three-dimensional FEL simulation code, which treats the propagation of the electron beam and radiation through a rectangular waveguide. Substantial power is found at odd harmonics of the fundamental resonance frequency. In addition, the three-dimensional nature of the wiggler field produced by the parabolic pole pieces introduces a low frequency component to the electron motion which results in emission in the vicinity of the even harmonics as well. The physical basis for this is investigated by analytic and numerical solution of the single-particle trajectories. In general, the results indicate that the effect of the wiggler plane focussing can act to enhance the harmonic content of the output spectrum.

1. Introduction

Planar wiggler magnets are being employed in several existing and planned free electron laser (FEL) experiments [1-5]. They have an advantage over helical wigglers in that they are easier to construct and adjust. A property of linearly polarized wigglers is that the current possesses odd harmonics of the fundamental wiggle frequency, giving rise to gain at the odd harmonics of the FEL interaction frequency [$\omega = (k + ik_w)v_z$, l odd]. Another characteristic of a linear wiggler, however, is that it provides no focussing in the wiggle plane. One method to furnish a focussing force in the wiggle plane is by utilizing parabolically shaped pole faces on the wiggler magnet, first employed experimentally by Phillips [6].

A fully three-dimensional, nonlinear code has been developed to study an FEL using this type of wiggler magnet configuration and a rectangular waveguide [7]. Strong growth is found at the odd harmonics. Additionally, due to the three-dimensional nature of the wiggler field produced by the parabolic pole faces, growth is sometimes found at a doublet around the even harmonics. This growth can be substantial for electron beams of larger radius, and must be considered when an FEL is designed with this type of configuration. The source, in the beam current, for this growth is studied by analytic and numeric solution of the single-particle trajectories.

2. Nonlinear analysis

The fully three-dimensional formulation is for an FEL amplifier which consists of an electron beam propagating down a loss-free rectangular waveguide in the presence of a linear wiggler magnetic field. A set of nonlinear differential equations is used which self-consistently describes the evolution of both the electrons and the electromagnetic fields. The magnetic field used is that generated by a linear wiggler with parabolically shaped pole faces, which is of the form [8]

$$B_w(x) = B_w \left\{ \cos(k_w z) \left[\sinh\left(\frac{k_w x}{\sqrt{2}}\right) \sinh\left(\frac{k_w y}{\sqrt{2}}\right) \hat{e}_x + \cosh\left(\frac{k_w x}{\sqrt{2}}\right) \cosh\left(\frac{k_w y}{\sqrt{2}}\right) \hat{e}_y \right] - \sqrt{2} \cosh\left(\frac{k_w x}{\sqrt{2}}\right) \sinh\left(\frac{k_w y}{\sqrt{2}}\right) \sin(k_w z) \hat{e}_z \right\}, \quad (1)$$

where (B_w, k_w) denote the wiggler amplitude and wave number. The injection of the electron beam into the wiggler is modeled by using an adiabatic input taper on the wiggler amplitude over N_w periods which is given by

$$B_w(z) = \begin{cases} B_w \sin^2(k_w z / 4N_w), & 0 \leq z \leq N_w \lambda_w, \\ B_w, & z > N_w \lambda_w. \end{cases} \quad (2)$$

The radiation field is represented by an expansion in terms of the orthogonal basis functions of the TE modes. The details of the derivation are given in ref. [7], only the results are presented here. Substituting the field expansion into Maxwell's equations, we obtain

$$\frac{d^2}{dz^2} \delta a_{mn} + \left[\frac{\omega^2}{c^2} - k^2 - k_{mn}^2 \right] \delta a_{mn} = \frac{\omega_b^2}{c^2} F_{mn} \beta_{z0} \left\langle \frac{\cos \alpha}{|v_z|} e_{mn} \cdot v \right\rangle, \quad (3)$$

and

$$2k^{1/2} \frac{d}{dz} (k^{1/2} \delta a_{mn}) = - \frac{\omega_b^2}{c^2} F_{mn} \beta_{z0} \left\langle \frac{\sin \alpha}{|v_z|} e_{mn} \cdot v \right\rangle, \quad (4)$$

after orthogonalizing in x and y and averaging over a wave period. In eq. (3) and (4) for frequency ω , wave number $k(z)$, and mode numbers m and n ,

$$\alpha \equiv \int_0^z dz' k(z') - \omega t, \quad (5)$$

$$e_{mn}(x, y) \equiv \frac{\pi n}{k_{mn} b} \cos \left[\frac{m\pi X}{a} \right] \sin \left[\frac{n\pi Y}{b} \right] \hat{e}_x - \frac{\pi m}{k_{mn} a} \sin \left[\frac{m\pi X}{a} \right] \cos \left[\frac{n\pi Y}{b} \right] \hat{e}_y, \quad (6)$$

$$k_{mn} \equiv \pi \left[\frac{m^2}{a^2} + \frac{n^2}{b^2} \right]^{1/2}. \quad (7)$$

$\delta a_{mn} \equiv e \delta A_{mn} / mc^2$, δA_{mn} is the amplitude of the vector potential of the TE_{mn} mode. ω_b is the plasma frequency, $\beta_{z0} \equiv v_{z0}/c$ (where v_{z0} is the initial axial beam velocity), v is the instantaneous velocity, and $F_{mn} = 4$ when either $m = 0$ or $n = 0$ and 8 otherwise. The waveguide is assumed to be centered at the origin and is bounded by $-a/2 \leq x \leq a/2$ and $-b/2 \leq y \leq b/2$; and $X \equiv x + a/2$ and $Y \equiv y + b/2$. The averaging operator $\langle (\dots) \rangle$ describes the source current. The average is over the initial conditions and is defined as

$$\langle (\dots) \rangle \equiv \frac{1}{2\pi ab} \int_{-\pi}^{\pi} d\alpha_0 \sigma_{\parallel}(\alpha_0) \int_{-a/2}^{a/2} dx_0 \int_{-b/2}^{b/2} dy_0 \sigma_{\perp}(x_0, y_0) (\dots), \quad (8)$$

where $\alpha_0 (\equiv -\omega t_0)$, and t_0 is the time the electron crosses the $z = 0$ plane) is the initial phase, and $\sigma_{\parallel}(\alpha_0)$ and $\sigma_{\perp}(x_0, y_0)$ describe the electron distributions in initial phase and cross section. For simplicity, the beam is assumed to be uniformly distributed in phase ($\sigma_{\parallel} = 1$) and cross section for an initially cylindrical beam ($\sigma_{\perp} = 1$ for $r_0 \leq R_b$). The effect of an initial thermal spread is also included in the analysis but will not be detailed here. The electron trajectories are followed by means of the Lorentz force equations in the combined wiggler and radiation field. No average of the Lorentz force equations is performed.

In an earlier work [9], we considered a case involving a 3.3 MeV/100 A electron beam with an initial radius of 0.2 cm in a rectangular waveguide of dimensions $a = 10$ cm and $b = 3$ cm. The wiggler had an amplitude of 4.2 kG, a period of 9.8 cm, and an input taper of 10 periods. The radiation was a TE₀₁ mode with an input signal of 6 kW. Ref. [9] presents a complete study of this example. We remark here that the efficiency spectrum contains a peak at the fundamental and well defined peaks at the odd harmonics. No gain was found at any other frequencies.

We now consider the case of a 3.5 MeV/800 A electron beam with an initial radius of 1.0 cm propagating through a waveguide with dimensions $a = 9.8$ cm and $b = 2.9$ cm in the presence of a wiggler

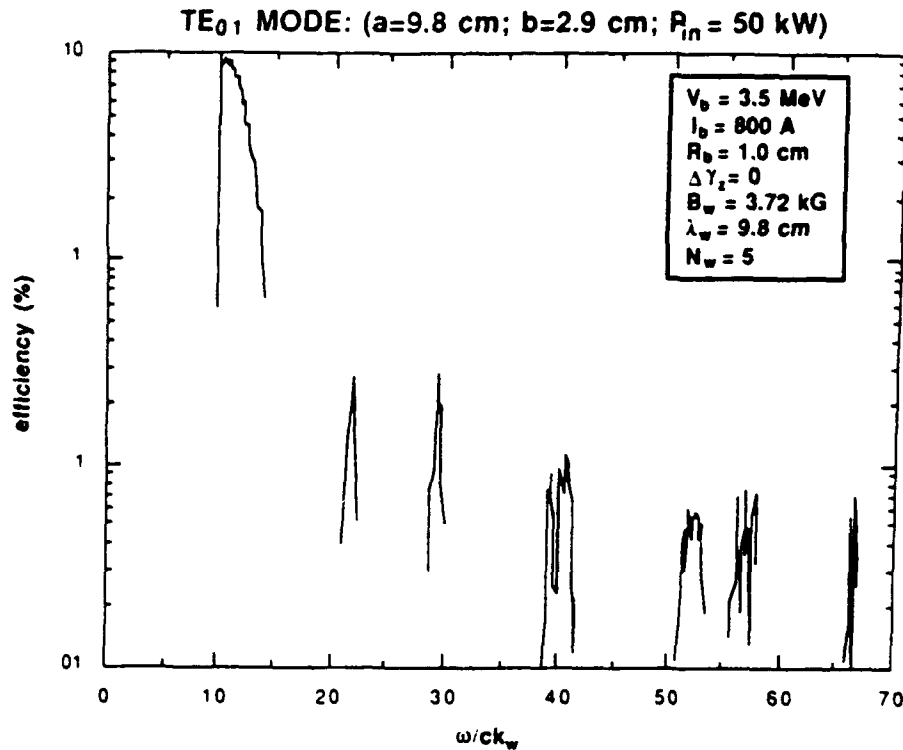


Fig. 1. Plot of the efficiency vs frequency at the fundamental through fifth harmonics. The doublets centered at $\omega/ck_w = 25$ and 55 corresponds to emission near the second and fourth harmonics.

field with a 3.72 kG amplitude, a 9.8 cm period, and an entry taper region of $N_w = 5$. The mode of interest is, again, the TE₀₁ mode but with an input power level of 50 kW. The spectrum of the saturation efficiency which results is shown in fig. 1. As expected, we find emission near the fundamental ($\omega/ck_w \approx 11.3$) and odd harmonics ($\omega/ck_w \approx 40.3, 66.5$). However, in this case we also find emission in the vicinity of the even harmonics, in the form of a doublet. As shown in fig. 1, emission is found in the vicinity of $\omega/ck_w \approx 22.0$ and 29.5 which corresponds to the second harmonic, and at $\omega/ck_w \approx 52.3$ and 56.8 corresponding to the fourth harmonic. The efficiency of the emission at the second harmonic is approximately $\eta \approx 0.27\%$, which exceeds that found at the third harmonic ($\eta \approx 0.11\%$). As discussed previously [9], the efficiency decreases sharply between the fundamental and the nearest harmonic, but falls off slowly with harmonic number thereafter. The source of emission near the even harmonics is the wiggler plane focussing of the parabolic pole pieces. The spatial variation of the field in the wiggler plane induces a slow modified betatron oscillation in the x-component of the velocity which is the source of oscillations in the axial velocity with periods $k_w \pm K_B$ (where K_B denotes the modified betatron wave number). It is this oscillation in the axial velocity which drives the even harmonic emission. It is important to remark that although we have considered a specific wiggler model, such behavior can be expected to occur in any planar wiggler field which exhibits an inhomogeneity in the wiggler plane.

3. Modified betatron oscillations

We now consider the effect of the wiggler plane gradients in driving the modified betatron oscillations, and analytically solve an approximation to the Lorentz force equations. For purposes of comparison, we

also numerically solve the complete equations of motion in the absence of a radiation field and Fourier analyze the resultant velocities. The approximate orbit equations are

$$\frac{d}{dz} v_x = \frac{\Omega_w}{\gamma} \cosh\left(\frac{k_w x}{\sqrt{2}}\right) \cos k_w z, \quad (9)$$

$$\frac{d}{dz} v_z = -\frac{\Omega_w}{\gamma} \frac{v_x}{v_z} \cosh\left(\frac{k_w x}{\sqrt{2}}\right) \cos k_w z, \quad (10)$$

where $\Omega_w \equiv eB_w/mc$, $\gamma \equiv (1 - v_0^2/c^2)^{-1/2}$, and the y variations are ignored. A solution can be found of the form

$$\begin{aligned} x &= x_B \cos K_B z - x_w \cos k_w z, \\ v_x &= -x_B K_B v_z \sin K_B z + x_w k_w v_z \sin k_w z, \end{aligned} \quad (11)$$

for which the axial velocity varies as

$$\begin{aligned} v_z &= \sqrt{v_0^2 - (v_B \sin K_B z + v_w \sin k_w z)^2} \\ &\approx v_{||} \left(1 + \frac{v_w^2}{4v_{||}^2} \sin 2k_w z + \frac{v_B v_w}{4v_{||}^2} [\cos(k_w + K_B)z - \cos(k_w - K_B)z] \right), \end{aligned} \quad (12)$$

where

$$\frac{v_{||}^2}{c^2} = 1 - \frac{1}{\gamma^2} \left(1 + \frac{\Omega_w^2}{2k_w^2 c^2} \right).$$

x_w and $v_w (\equiv -x_w k_w v_z)$ describe the amplitude of the fundamental wiggler oscillation, x_B and $v_B (\equiv -x_B K_B v_z)$ describe the amplitude of the modified betatron oscillations, and we have assumed that $v_B < v_w$. Under the assumption that $|k_w x| \ll 1$, substitution of eqs. (11) and (12) into eq. (9) gives

$$K_B^2 = \frac{\Omega_w^2}{4v_z^2} \left(1 + \frac{3}{16} \frac{v_w^2}{v_{||}^2} + \frac{1}{4} k_w^2 x_B^2 \right). \quad (13)$$

The analytic expression also predicts oscillations at $(2k_w \pm K_B)$ and $(k_w \pm 2K_B)$, although at lower amplitude (when $v_B < v_w$). The y gradients, characteristic of the magnet itself, introduce an additional betatron oscillation, which does not couple strongly to the axial velocity.

The single particle equations of motion have been numerically integrated in z assuming the same input taper as for the nonlinear analysis. The resulting velocities are then Fourier-transformed over the uniform wiggler portion of their motion (i.e., $z > N_w \lambda_w$). Figs. 2–4 show the Fourier spectra of the velocity components of a particle starting on axis ($x_0 = 0.0$, $y_0 = 0.0$), a particle starting at $x_0 = 0.0$, $y_0 = 0.3$ cm, and a particle starting at $x_0 = 0.3$, $y_0 = 0.0$ respectively. The different harmonic structure predicted by the analytic theory can be seen in these spectra. Observe that the amplitude of the modified betatron doublet at $(k_w \pm K_B)$ in the axial velocity is relatively independent of the initial y -position. In addition, the amplitude of this doublet increases with increases in the initial x -position (NB, the initial x -position is not identical with x_B). This accounts for the lack of emission near the even harmonics in ref. [9] for which the beam radius was 0.2 cm (in contrast to the case discussed herein for which the beam radius is 1.0 cm). Fig. 5 shows a comparison between the analytic and numerical calculations for K_B as a function of initial x -position with initial $y_0 = 0.0$. As shown in the figure the analytic approximation for K_B [eq. (13)] holds for $x_0 \leq 0.35$ cm, after which it diverges from the numerical solution. The scaling of the magnitude of the betatron oscillations as a function of the initial x -position, obtained from the numerical solutions, is shown in fig. 6.

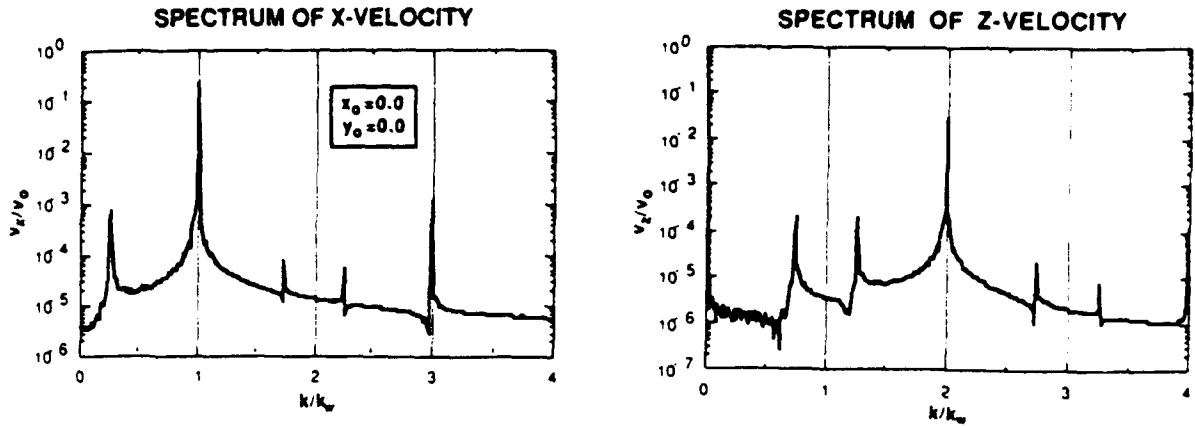


Fig. 2. Fourier decomposition of the electron velocities for a particle injected into the wiggler with $x_0 = 0.0$ and $y_0 = 0.0$.

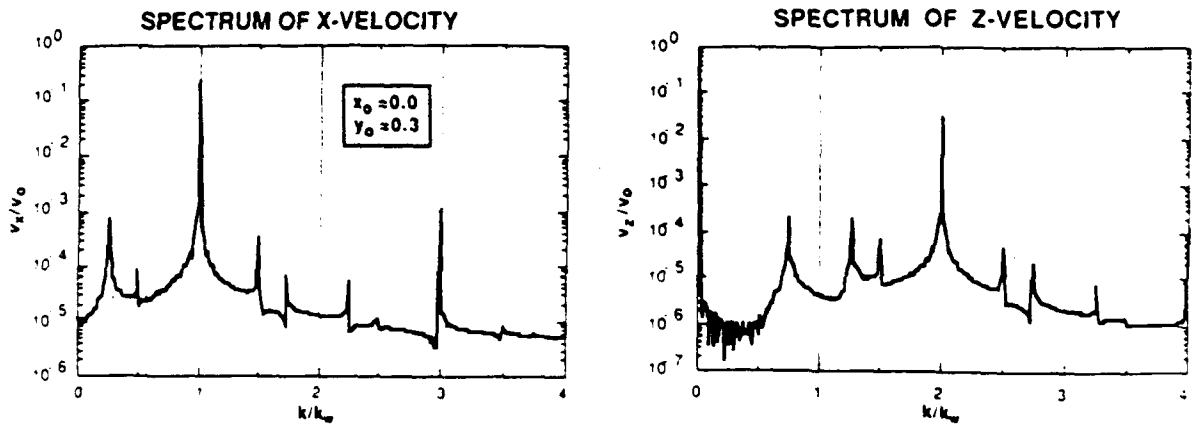


Fig. 3. Fourier decomposition of the electron velocities for a particle injected into the wiggler with $x_0 = 0.0$ and $y_0 = 0.3$.

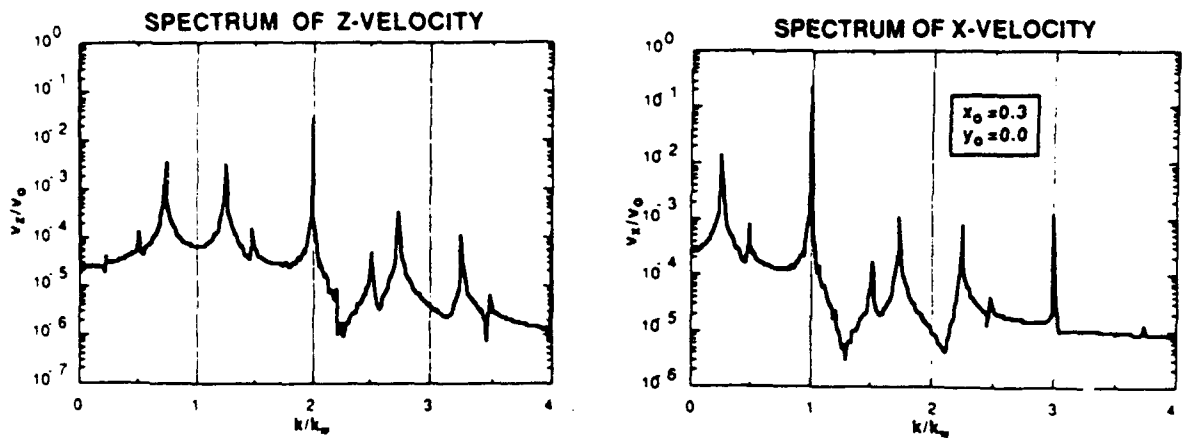


Fig. 4. Fourier decomposition of the electron velocities for a particle injected into the wiggler with $x_0 = 0.3$ and $y_0 = 0.0$.

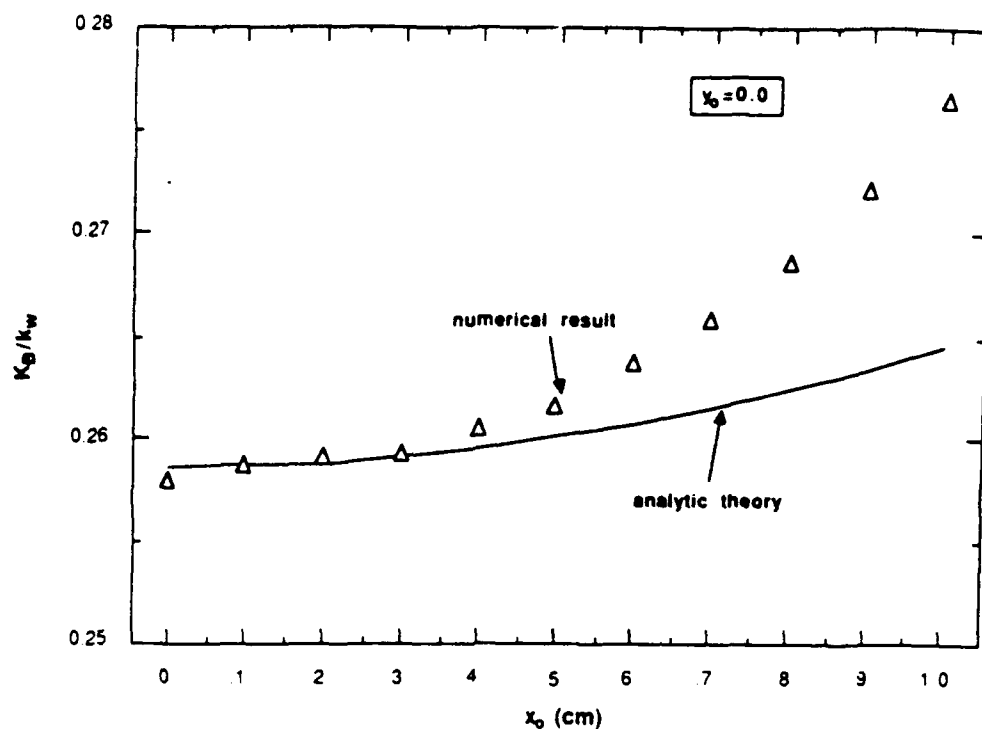


Fig. 5. Scaling of the modified betatron wave number with the initial x -coordinate of the particle.

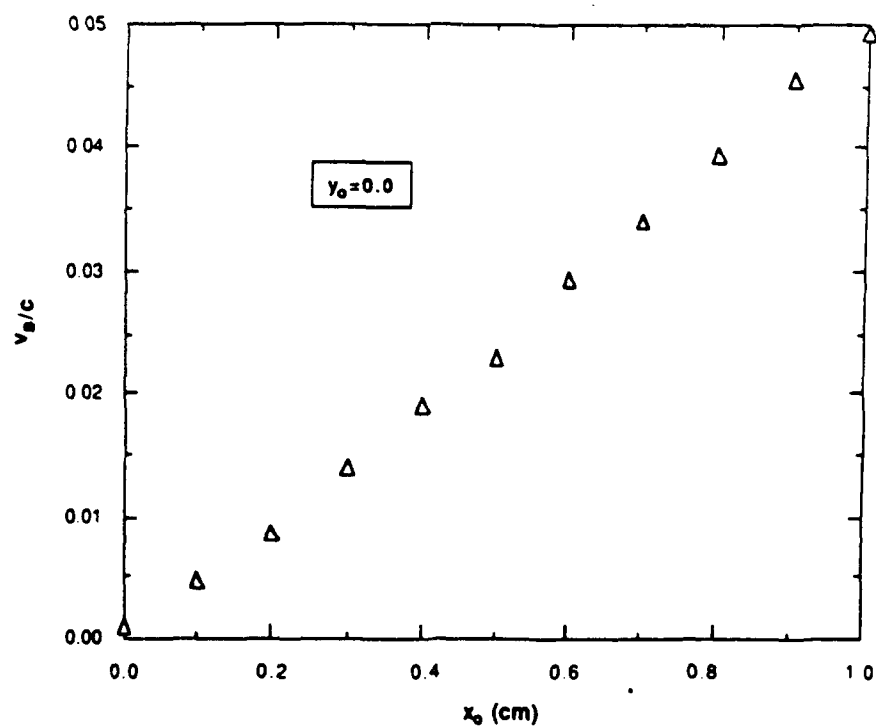


Fig. 6. Scaling of the magnitude of the velocity of the modified betatron oscillation with the initial x -coordinate of the particle.

4. Conclusions

In this paper, we have described the results of a three-dimensional nonlinear simulation of the harmonic radiation from a planar wiggler based FEL amplifier in which wiggler plane focussing is accomplished by means of parabolically shaped pole pieces. The results indicate that the inhomogeneity in the wiggler field in the plane of the bulk wiggler motion can give rise to emission close to the even harmonics in addition to the usual odd harmonic radiation. The source of this additional harmonic radiation is a slow modified betatron oscillation in the wiggler plane which induces oscillation with wave numbers ($k_w \pm K_B$) in the axial velocity. These oscillations in the axial velocity are the source of the even harmonic radiation. The amplitude of the modified betatron oscillations and, hence, the emission near the even harmonics is correlated with the initial displacement of the beam electrons from the axis of symmetry. As a consequence, the additional radiation near the even harmonics can be minimal if the electron beam radius is small [9]. In general, however, the additional harmonic emission will be found with any planar wiggler configuration which exhibits an inhomogeneity in the wiggler plane. Thus, attempts to enhance focussing of the beam in the wiggler plane can also have the effect of producing an enhancement in the harmonic emission.

Acknowledgements

This work has been supported by the Office of Naval Research and the Office of Naval Technology. The authors are grateful to Drs. A.K. Ganguly, R.K. Parker, R.H. Jackson and D. Pershing for helpful discussions.

References

- [1] T.J. Orzechowski, B. Anderson, W.M. Fawley, D. Prosnitz, E.T. Scharlemann, S. Yarema, D. Hopkins, A.C. Paul, A.M. Sessler and J. Wurtele, *Phys. Rev. Lett.* 54 (1985) 889.
- [2] T.J. Orzechowski, B. Anderson, J.C. Clark, W.M. Fawley, A.C. Paul, D. Prosnitz, E.T. Scharlemann, S. Yarema, D.B. Hopkins, A.M. Sessler and J. Wurtele, *Phys. Rev. Lett.* 57 (1986) 2172.
- [3] D.W. Feldman, R.W. Warren, B.E. Carlsen, W.E. Stein, A.H. Lumpkin, S.C. Bender, G. Spalek, J.M. Watson, L.M. Young, J.S. Fraser, J.C. Goldstein, H. Takeda, T.S. Wang, K.C.D. Chan, B.D. McVey, B.E. Newman, R.A. Lohsen, R.B. Feldman, R.K. Cooper, W.J. Johnson, and C.A. Brau, *IEEE J. Quantum Electron.* QE-23 (1987) 1476.
- [4] K.E. Robinson, D.C. Quimby and J.M. Slater, *IEEE J. Quantum Electron.* QE-23 (1987) 1497.
- [5] W.W. Destler, V.L. Granatstein, I.D. Mayergoyz and Z. Segalov, *J. Appl. Phys.* 60 (1986) 521.
- [6] R.M. Phillips, *IRE Trans. Electron Dev.* 7 (1960) 231.
- [7] H.P. Freund, H. Bluem and C.L. Chang, *Phys. Rev. A* 36 (1987) 2182.
- [8] E.T. Scharlemann, *J. Appl. Phys.* 58 (1985) 2154.
- [9] H.P. Freund, C.L. Chang and H. Bluem, *Phys. Rev. A* 36 (1987) 3218.

APPENDIX XII

Nonlinear Theory and Design of a Harmonic Ubitron/Free-Electron Laser

by

H.P. Freund, H. Bluem, and R.H. Jackson

NONLINEAR THEORY AND DESIGN OF A HARMONIC UBITRON / FREE ELECTRON LASER

H.P. FREUND

Science Applications International Corporation, McLean, VA 22102, USA

H. BLUEM

Electrical Engineering Department, University of Maryland, College Park, MD 20742, USA

R.H. JACKSON

Naval Research Laboratory, Washington, DC 20375, USA

A fully three-dimensional nonlinear analysis of the harmonic Ubitron/Free Electron Laser is discussed which is valid for arbitrary harmonic number. The analysis has been performed for a configuration consisting of a beam propagating through a loss-free rectangular waveguide in the presence of a planar wiggler field. The wiggler model includes an adiabatic entry taper to model the injection of the beam into the wiggler, parabolic pole pieces to provide additional focussing in the plane normal to the wiggler, and an amplitude taper downstream from the entry region for efficiency enhancement. The advantage of harmonic operation is that relatively high operating frequencies may be obtained with relatively modest beam energies; however, this occurs at the expense of a greater sensitivity to beam thermal effects. In addition to enhancing the extraction efficiency, a tapered wiggler has been shown to reduce the sensitivity of the interaction to thermal effects. Thus, the tapered wiggler is designed to counter the increased thermal sensitivity of the harmonic interaction. Specific design criteria for a third harmonic experiment operating at 15 GHz with a 55 keV electron beam are discussed.

1. Introduction

The harmonic operation of a Ubitron or Free Electron Laser (FEL) has been described in terms of a linear theory for the gain in a planar wiggler configuration [1] as well as nonlinear analyses of the interaction in both helical [2] and planar [3,4] wiggler devices. These analyses indicate that both the gain and saturation efficiencies of the harmonic interaction are substantial fractions of that found at the fundamental when thermal effects are negligible. However, the harmonic interaction becomes increasingly sensitive to beam thermal effects as the harmonic number increases. In order to compensate for thermal effects, we consider the use of a tapered wiggler to enhance the interaction efficiency. The use of a tapered wiggler for efficiency enhancement has been amply described in the literature [5,6] and demonstrated experimentally [7] for operation at the fundamental. Recently, nonlinear simulations of the fundamental interaction for a planar wiggler [8,9] indicate that a tapered wiggler can reduce the sensitivity of the interaction to thermal effects in addition to enhancing the efficiency. It is our intention in this paper to explore the effects of a tapered wiggler on the harmonic interaction, and to describe the design stages of a third harmonic experiment.

The specific configuration we consider is third harmonic operation in the microwave regime in which the intersection between the beam resonance line and the dispersion relation of the wave is close to grazing near the waveguide cutoff. In this manner, the beam and waveguide parameters may be chosen in such a way as to ensure that: (1) only a single waveguide mode is resonant with the beam, and (2) there is no resonant interaction at the fundamental. Thus, both mode and harmonic competition can be controlled. The specific parameters of interest involve 15 GHz operation with a 55 keV/15 A electron beam. The planned wiggler is a novel modification of a previous electromagnet design [10] using a current sheet to produce a planar wiggler. Field strengths in excess of 1 kG can be achieved at a period of 3 cm. Observe that fundamental operation at this frequency would involve beam energies greater than 200 keV.

The organization of the paper is as follows. The nonlinear formulation is given briefly in section 2. This analysis has been described in detail elsewhere [3,8,9] and is applicable to the treatment of a multiple mode interaction at an arbitrary harmonic (as well as the fundamental). A numerical analysis of the case of interest is presented in section 3 which deals with a third harmonic interaction between the beam and a single

V. NON-LINEAR REGIME THEORY

TE₀₁ mode in a rectangular waveguide. Section 4 deals with the detailed design of an experiment, and a summary and discussion are given in section 5.

2. General formulation

The physical configuration we consider describes an electron beam propagating through a rectangular waveguide in the presence of a planar wiggler field. The planar wiggler field model includes the effect of parabolic tapering of the magnetic pole faces for enhanced focusing of the electron beam [11], and is expressed as

$B_w(x)$

$$= B_w(z) \left\{ \cos(k_w z) \left[\hat{e}_x \sinh\left(\frac{k_w x}{\sqrt{2}}\right) \sinh\left(\frac{k_w y}{\sqrt{2}}\right) + \hat{e}_y \cosh\left(\frac{k_w x}{\sqrt{2}}\right) \cosh\left(\frac{k_w y}{\sqrt{2}}\right) \right] - \sqrt{2} \hat{e}_z \sin(k_w z) \cosh\left(\frac{k_w x}{\sqrt{2}}\right) \sinh\left(\frac{k_w y}{\sqrt{2}}\right) \right\},$$

where B_w denotes the wiggler amplitude, and $k_w (= 2\pi/\lambda_w)$, where λ_w is the wiggler period) is the wiggler wavenumber. In both cases we allow for a tapering of the wiggler field amplitude to model both the injection of the beam into the wiggler, and for efficiency enhancement by a tapered wiggler at some point downstream from the start of the interaction. To this end, we choose

$$B_w(z) = \begin{cases} B_w \sin^2(k_w z/4N_w); & 0 < z < N_w \lambda_w \\ B_w; & N_w \lambda_w < z < z_0 \\ B_w [1 + \epsilon_w k_w (z - z_0)]; & z > z_0, \end{cases}$$

where N_w describes the length of the entry region, and ϵ_w denotes the scale length for variation of the wiggler amplitude relative to the reference point z_0 . Note that since the fringing fields associated with a tapered wiggler have been neglected, it is implicitly assumed that the taper is slow (i.e., N_w is large and $|\epsilon_w| \ll 1$).

The boundary conditions on the radiation fields at the waveguide wall are satisfied by expanding the field in terms of the vacuum waveguide modes. The vector potential of the TE modes in a rectangular waveguide bounded by $-a/2 < x < a/2$ and $-b/2 < y < b/2$ is

$$\delta A(x, y) = \sum_{l,n=0}^{\infty} \delta A_{ln}(z) e_{ln}(x, y) \cos \alpha(z, t),$$

where

$$\alpha(z, t) = \int_0^z dz' k(z') - \omega t,$$

the summation symbol \sum' indicates that both l and n may not be zero.

$$e_{ln}(x, y) = \frac{n\pi}{k_{ln}b} \hat{e}_x \cos\left(\frac{l\pi X}{a}\right) \sin\left(\frac{n\pi Y}{b}\right) - \frac{l\pi}{k_{ln}a} \hat{e}_y \sin\left(\frac{l\pi X}{a}\right) \cos\left(\frac{n\pi Y}{b}\right),$$

where $X = x + a/2$ and $Y = y + b/2$, and the cutoff wavenumber of the mode is given by

$$k_{ln} = \pi \sqrt{\frac{l^2}{a^2} + \frac{n^2}{b^2}}.$$

The equations governing the evolution of the slowly-varying amplitude and phase are found by substitution of these forms for the vector potentials into Maxwell's equations and then averaging over a wave period and orthogonalizing in the transverse dimensions. The result for the TE modes in a rectangular waveguide is of the form

$$\left[\frac{d^2}{dz^2} + \left(\frac{\omega^2}{c^2} - k^2 - k_{ln}^2 \right) \right] \delta a_{ln} = \frac{\omega_b^2}{c^2} F_{ln} \left\langle \frac{\cos \alpha}{|v_z|} e_{ln} \cdot v \right\rangle,$$

$$2k^1 z \frac{d}{dz} (k^{1/2} \delta a_{ln}) = - \frac{\omega_b^2}{c^2} F_{ln} \left\langle \frac{\sin \alpha}{|v_z|} e_{ln} \cdot v \right\rangle,$$

where $\delta a_{ln} = e \delta A_{ln} / mc^2$ is the normalized wave amplitude, and $F_{ln} = 1$ whenever either $l = 0$ or $n = 0$ and 0 otherwise. These equations must be integrated for each mode included in the simulation. Analogous equations may be derived for the TM modes.

The averages indicated in the equations governing the evolution of the amplitude and phase are to be taken over an ensemble of electrons whose trajectories are self-consistently integrated using both the magnetostatic and electromagnetic fields. The average itself is taken over the *initial conditions* of the beam outside the wiggler, and the injection of the beam into the wiggler is modeled by allowing the wiggler amplitude to increase adiabatically from zero to a constant level. This procedure has been adopted because it is difficult to diagnose the beam conditions inside the wiggler. As a consequence, greater accuracy may be obtained by making use of the more reliable knowledge of the beam as it comes off the cathode and subsequently model the injection of the beam into the wiggler. The electron beam in this case will be assumed to be monoenergetic but to have a pitch angle spread in transverse velocity. As a result, we employ an initial momentum space distribution as follows

$$F_0(p_0) = A \exp \left[- (p_{z0} - p_0)^2 / \Delta p_0^2 \right] \times \delta(p_0^2 - p_x^2 - p_y^2) H(p_{z0}),$$

where $H(p_{z0})$ is the Heaviside function, the normalization constant is given by

$$A = \left[\pi \int_0^{\infty} dp_{z0} \exp \left[- (p_{z0} - p_0)^2 / \Delta p_z^2 \right] \right]^{-1}.$$

p_0 describes the total momentum of the beam, and Δp_z describes the axial momentum spread. This axial momentum spread can be related to the cathode or emittance dominated axial energy spread by the relation

$$\frac{\Delta \gamma_z}{\gamma_0} = 1 - \frac{1}{\sqrt{1 + 2(\gamma_0^2 - 1) \frac{\Delta p_z}{p_0}}},$$

where $\gamma_0 = (1 + p_0^2/m^2c^2)^{1/2}$ is the relativistic factor corresponding to the total energy. The averaging operator is defined in terms of this momentum space distribution as

$$\begin{aligned} \langle (\dots) \rangle &= \frac{A}{2\pi A_g} \int_0^{2\pi} d\phi_0 \int_0^{\infty} dp_{z0} \beta_{z0} \\ &\times \exp \left[- (p_{z0} - p_0)^2 / \Delta p_z^2 \right] \\ &\times \iint_{A_g} dx_0 dy_0 \sigma_+(x_0, y_0) \int_0^{2\pi} d\psi_0 \sigma_+(\psi_0) (\dots), \end{aligned}$$

where A_g is the cross-sectional area of the waveguide, $\beta_{z0} = v_{z0}/c$, $\phi_0 = \tan^{-1}(p_{y0}/p_{x0})$ and p_{z0} define the initial momentum space coordinates of the electron, x_0 and y_0 are the initial cross-sectional positions of the electrons, ψ_0 is the initial ponderomotive phase, and σ_+ and σ_- describe the initial electron distributions in cross-section and ponderomotive phase. It should be remarked that the averaging process implicitly describes the overlap between the beam and the radiation field, and no explicit inclusion of a filling-factor is required.

In order to complete the formulation, the electron orbit equations in the presence of the static and fluctuation fields must be specified. It should be emphasized that while the field equations have been averaged over a wave period, no average is performed on the orbit equations. Since the model is intended to describe an amplifier configuration, we choose to integrate in the axial position z and write the Lorentz force equations in the form

$$v_z \frac{d}{dz} \mathbf{p} = -e\delta\mathbf{E} - \frac{e}{c} \mathbf{v} \times (\mathbf{B}_0 + \delta\mathbf{B}),$$

where the electric and magnetic fields

$$\delta\mathbf{E} = -\frac{1}{c} \frac{\partial}{\partial t} \delta\mathbf{A}, \quad \text{and} \quad \delta\mathbf{B} = \nabla \times \delta\mathbf{A}$$

are derivable from the vector potentials and consist in the sum of all the TE and/or TM modes included in any specific simulation. In addition, the axial guide

field must be included in the event of a helical wiggler/axial guide field configuration.

The initial conditions for the electron beam are chosen to describe the injection of a uniform pencil beam centered on the axis of symmetry with a flat-topped density profile and an arbitrary axial momentum spread. The radiation field includes all resonant modes at the frequency of interest. The initial wavenumbers for the modes included in any given case are chosen to correspond to the values of the vacuum modes, and subsequently evolve subject to the dielectric effect of the beam. The growth rates are represented by the first derivatives of the amplitude and are set to zero initially since the wiggler field amplitude vanishes at this point. The wave amplitudes are chosen to represent the injected power level for each mode.

3. Numerical analysis

The particular example under consideration deals with a third harmonic interaction in which the fundamental is below cutoff and in which only the TE₀₁ mode is resonant. The electron beam is characterized by an energy of 55 keV, a current of 15 A, and an initial radius of 0.2 cm. The wiggler has an amplitude of 990 G, a period of 3.0 cm, and an entry taper region which is 5 wiggler periods in length. The waveguide dimensions are $a = 3.2$ cm and $b = 1.58$ cm. We first consider the case of a uniform wiggler and investigate the sensitivity of the interaction to beam thermal effects. The spatial growth of a 3 kW injected signal at a frequency of 15.74 GHz is shown in fig. 1 for the case of a beam with $\Delta \gamma_z = 0$. Saturation occurs with an efficiency of approximately 2.7%. This gives a net gain of 0.12 dB/cm over a total interaction length (i.e., including the entry taper region) of about 70 cm. This frequency corresponds to the central peak of the interaction spectrum. As shown in fig. 2, resonance occurs from approxi-

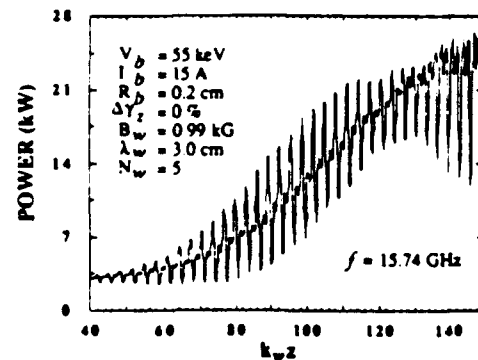


Fig. 1. Graph of the evolution of the power with axial position for an ideal beam in a uniform wiggler.

V. NON-LINEAR REGIME THEORY

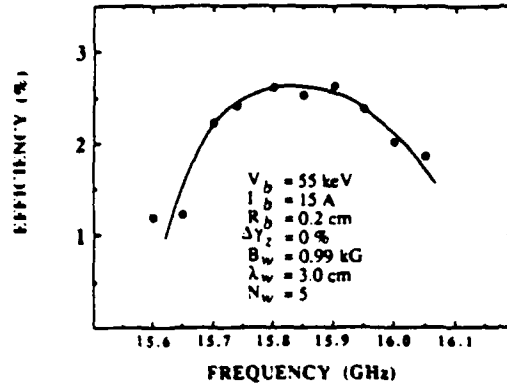


Fig. 2. Spectrum showing the efficiency as a function of frequency for an ideal beam.

mately 15.6 GHz through 16.1 GHz with a peak efficiency of the order of 2.8%.

It is evident from fig. 1 that a substantial modulation is superimposed on the bulk growth of the signal. A Fourier transform of this spatial variation is shown in fig. 3, and the modulation is evident with wavenumbers of $2k_w$, $4k_w$, $6k_w$, $8k_w$, $10k_w$, and etc. In order to explain this we turn to a much simplified model of the interaction. The induced motion in a planar wiggler oscillates at the wiggler period in the plane perpendicular to the field with an amplitude given approximately by $\Omega_w/\gamma_0 k_w$, where $\Omega_w = eB_w/mc$. For the configuration under consideration, therefore, we may write

$$v_z = \frac{\Omega_w}{\gamma_0 k_w} \hat{e}_z \sin k_w z.$$

The interaction will primarily occur with a plane polarized wave of the form

$$\delta E = \delta E_0 \hat{e}_x \sin(kz - \omega t),$$

and depends on the overlap of these quantities through $J \cdot \delta E$, which has the form

$$J \cdot \delta E = -\frac{1}{2} \frac{\Omega_w}{\gamma_0 k_w} \delta E_0 \langle \cos \psi - \cos(\psi - 2k_w z) \rangle.$$

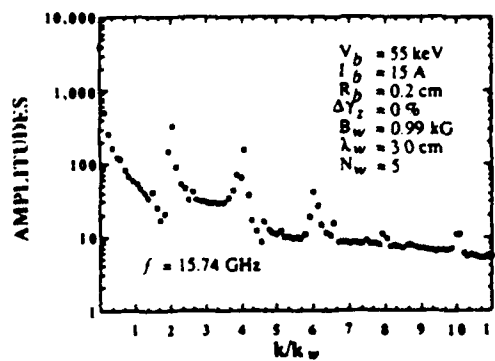


Fig. 3. The Fourier spectrum of the spatial evolution of the power.

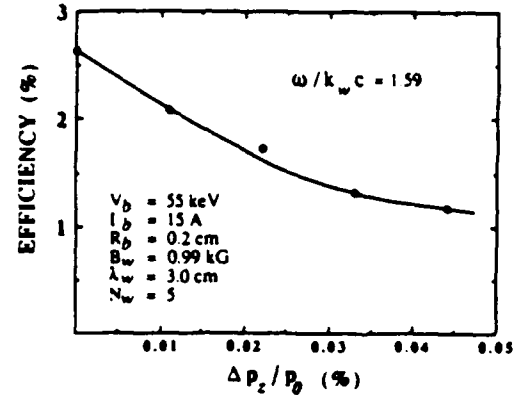


Fig. 4. Graph showing the decrease in efficiency with the increase in thermal spread.

This describes the beating of the wiggler and radiation fields at the fundamental which is the source of the FEL interaction. It is evident that the upper beat wave varies as $\cos \psi$, where ψ is the slowly-varying ponderomotive phase. However, the lower beat wave will oscillate with a wavenumber of $2k_w$ and is the source of the modulation. The interaction is similar at the harmonics, and the modulation at $4k_w$, $6k_w$, etc., derives from higher order oscillations to the wiggler-induced velocity. Observe that such modulation of the signal at the even harmonics of the wiggler period occur, if at all, at a much lower level in the case of a helical wiggler because the symmetry acts to suppress the lower beat wave.

Returning now to the question of the sensitivity of the interaction to thermal effects, we plot the decrease in the efficiency with increasing thermal (in this case through a pitch angle) spread in fig. 4. As shown in the figure, the efficiency decreases by a factor of two as $\Delta p_z/p_0$ increases to a value of about 0.045% corresponding to a value of $\Delta \gamma_z/\gamma_0 = 0.01\%$. This is extremely difficult (if not impossible) to achieve given the

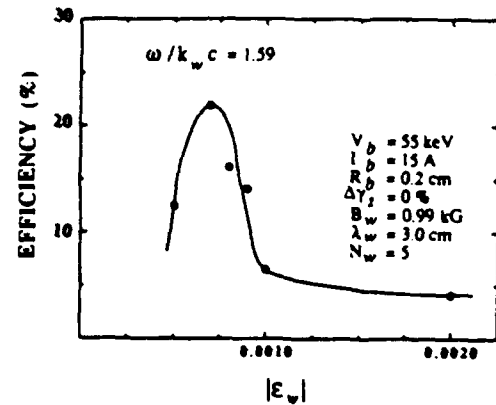


Fig. 5. Graph of the maximum efficiency versus the normalized taper.

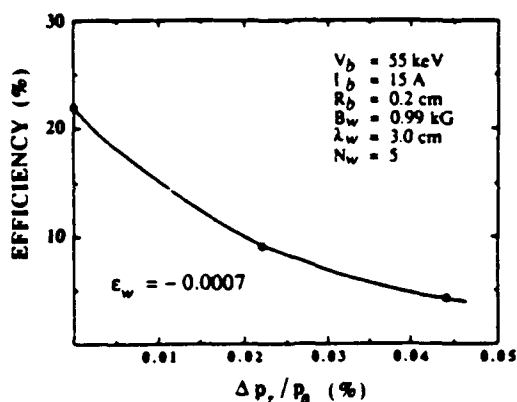


Fig. 6. Variation in the maximum efficiency of a third harmonic tapered wiggler interaction with thermal effects.

current state-of-the-art in electron beam technology, and motivates our study of the effect of wiggler taper on the harmonic interaction.

The effect of a tapered wiggler is shown in fig. 5 in which we plot the maximum efficiency (i.e., if the field is tapered to zero) as a function of the scale length of the taper in the absence of thermal effects. As shown in the figure, the maximum obtainable efficiency is approximately 23% which is almost an order of magnitude greater than that found for the uniform wiggler. In addition, the optimal range for the taper itself is for $0.0005 < |\epsilon_w| < 0.0009$. The optimal range for the taper is governed by the requirements that the taper be rapid enough to maintain the axial beam velocity required for the wave particle resonance but not so rapid that the beam becomes detrapped. By way of comparison $\epsilon_w = -0.0078$ in the experiment at LLNL [7], and simulations of the experiment indicate that the maximum extraction efficiency would occur for [8] $\epsilon_w \approx 0.002$. It appears, therefore, that harmonic experiments require slower tapers than at the fundamental. The reason for this is that the ponderomotive potential is directly proportional to the normalized wiggler amplitude ($\Omega_w/k_w c$) for the fundamental, but varies as the cube of this factor at the third harmonic. As a result, the ponderomotive potential tends to be smaller at the harmonics and the effect of a given wiggler taper is larger. Indeed, the upper bound on the effective taper shown in the figure for $\epsilon_w \approx -0.001$ occurs because the effect of the taper has overwhelmed the ponderomotive force, and the particles have become detrapped (see fig. 5).

4. Experimental design

Harmonic operation of the Ubitron/FEL is an attractive method of overcoming the high voltage nature

of the mechanism. Harmonics can be utilized to reduce the voltage required to achieve gain at a given frequency, or they can be used to access higher frequencies for a set voltage. Operation at harmonics is particularly attractive in the microwave and millimeterwave domain. In this region, the voltage reduction scales as $1/n^2$ (as opposed to $1/\sqrt{n}$ at higher voltages, where n is the harmonic number), and the waveguide properties allow some control over the interaction. The experiment is intended to be a basic proof-of-principle study of harmonics in the Ubitron. As such, the design has not been optimized for harmonic operation; rather, it has been designed to be flexible and to make use of existing equipment as much as possible. The experiment is designed to permit grazing incidence operation with the third harmonic as well as the first harmonic in the same frequency band through voltage tuning. This will allow a direct comparison of the two modes of operation, harmonic versus fundamental. For third harmonic operation, the first harmonic will be cutoff to eliminate any competition between the interactions. The experimental device consists of 6 modular sections: (1) the beam generation region, (2) the rf input coupler, (3) the interaction region, (4) the beam collector, (5) the rf output coupler, and (6) the calorimeter. There are also two resistive current monitors, one before and one after the interaction region.

The electron beam is generated using a 250 kV/250 A SLAC klystron gun which has been modified to reduce the emitted current. Using a series of coils, the beam is compressed and transported through the input coupler and into the interaction region.

The rf input coupler is required in order to inject the signal to be amplified from Ku band guide into an overmoded C band waveguide used in the interaction region. A full investigation of harmonic operation requires several criteria to be met by the input coupler design. The coupler must be efficient over a broadband with some degree of mode control while remaining compact and allowing for beam transmission. The design shown in fig. 7 satisfies these requirements. Two input Ku band guides (WR62) operating in the fundamental TE_{10} mode taper into a C band guide (WR137). If the two input signals are in phase they will combine into a TE_{01} mode. There is little reflection for this mode since the wave impedance does not change. If the two input signals are 180° out of phase, TE_{11}/TM_{11} modes will be launched. To allow beam transmission, a hole is bored in the center of the rf taper piece.

The interaction region consists of standard WR137 waveguide sandwiched between the two halves of a planar wiggler. The wiggler, as shown in fig. 8, is a multiply counterwrapped electromagnet based upon a previous design [10]. In addition to providing current multiplication, the counterwrapping scheme produces a built-in current taper which greatly reduces end effects.

V. NON-LINEAR REGIME THEORY

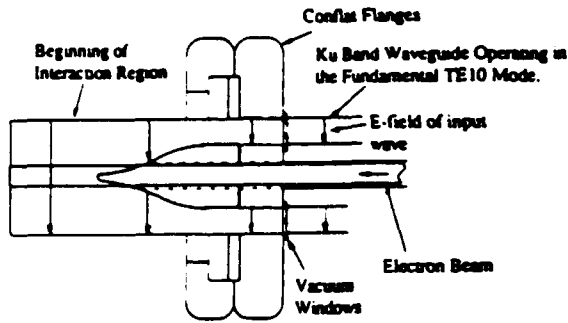


Fig. 7 Input coupler configuration showing the transition from the input signal and beam into the interaction region.

Two other advantages of this wiggler over the original design are that edge asymmetries are reduced and the input and output contacts are on the same side and at the same end. The importance of the latter feature is that the leads from the current supply can be twisted or coaxial, thereby eliminating stray fields from long leads. Wiggle plane focussing is provided by extending the pole pieces down the sides of the waveguide, as can be seen in fig. 8. The magnet shown in the figure is a prototype which has been built and tested. It consists of two wraps while the one to be used in the experiment will have eight wraps on each half. The test wiggler is 10.5 periods long with a 3 cm period. The tests were performed with both pulsed (100 μ s) and AC (60 Hz) currents, and were compared with two-dimensional Poisson calculations. The results of a scan down the axis at the center of the gap shows that end effects are indeed reduced. The measured peak to peak variations, using ac current excitation, are less than 1% for the

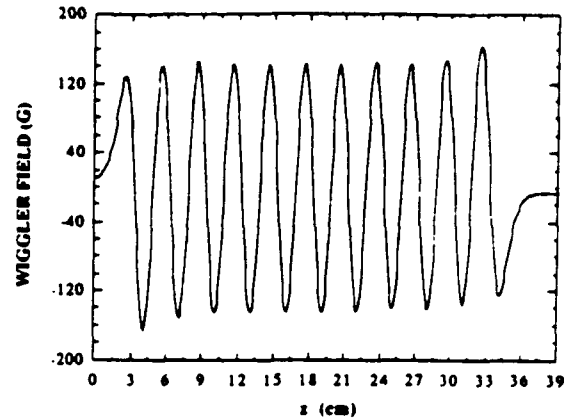


Fig. 9. Graph of the measured axial variation of the prototype wiggler magnet.

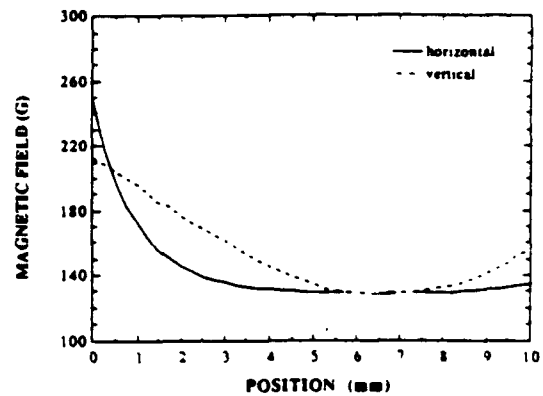


Fig. 10. The horizontal and vertical profiles of the wiggler field in the prototype wiggler magnet.

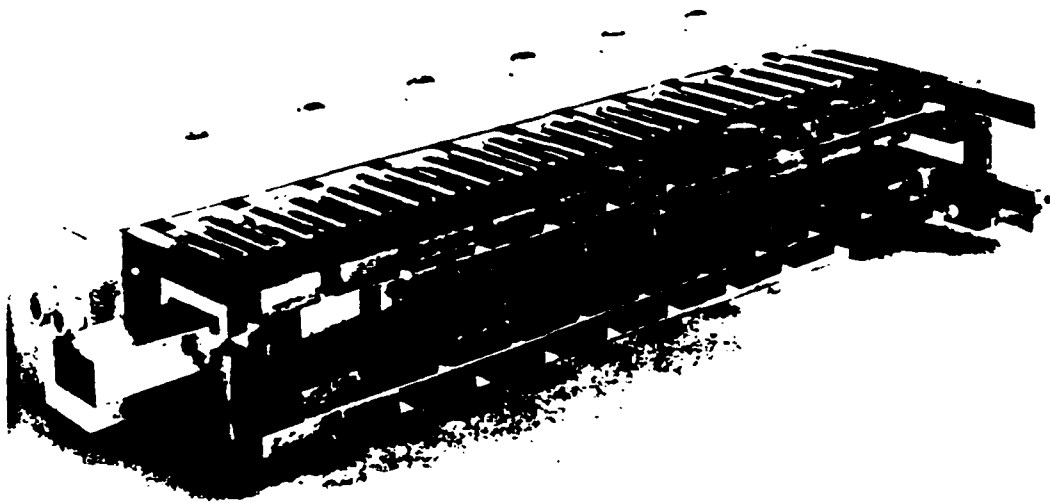


Fig. 8. Photograph of the prototype wiggler.

central six periods. The variations are slightly greater with pulsed current due to excessive noise in the signal, not because of an actual difference in magnet performance. The magnetic field amplitude, however, is lower for pulsed excitation than it is for ac current drive. This is probably due to diffusion effects in the iron. The on-axis scan with ac current is shown in fig. 9. Scans were also taken in the vertical and horizontal directions at fixed points along the axis. A sample result of such a scan is shown in fig. 10. Due to the small excursion distance of the three-axis probe slide, it was not possible to take a complete scan in either direction. As a result, the scans were started at the top or left edge and went for the distance of the slide's micrometer, which was slightly more than half the distance across the gap. The symmetry was checked and found to be good, and the horizontal and vertical gradients in the field will provide focussing for the beam.

The output monitors are mode selective WR137 to WR62 waveguide directional couplers. They will provide waveshape, frequency, mode, and power information. In addition to the TE_{01} mode, the TE_{10} , TE_{20} , TE_{11} , TM_{11} , TE_{21} , TM_{21} , TE_{30} , TE_{31} , TM_{31} , and TE_{40} modes will propagate in the frequency band of interest. The TE_{10} modes can be ignored since they will not be launched and the beam should have no interaction them. To sort out the other modes three different couplers are to be used. One will couple out all of the modes, the second will couple to only the TE_{01} , TE_{11} , and TE_{31} modes, and the third will couple the TE_{01} and TE_{21} modes. The differences between the couplers, along with frequency information, are sufficient to determine the amplified modes.

5. Summary and discussion

In this paper the nonlinear analysis and experimental design for a harmonic Ubitron experiment have been described. The analytical model is appropriate to a rectangular waveguide/planar wiggler configuration and is capable of treating an arbitrary ensemble of waveguide modes. However, the specific parameters employed in the analysis have been chosen to ensure that only the TE_{01} mode is resonant. The results of the

simulation indicate that the harmonic interaction is extremely sensitive to beam thermal effects, which is in accord with previous analyses [1,3]. The use of a tapered wiggler is proposed in order to offset this sensitivity. For the specific parameters of interest, simulation indicates that the extraction efficiency in the limit of an ideal beam can be increased by as much as an order of magnitude through the utilization of a tapered wiggler and that the tapered wiggler offsets, at least in part, beam thermal effects.

Acknowledgements

This research was supported by the Office of Naval Research and the Office of Naval Technology. The authors would like to thank Drs. A.K. Ganguly, R.K. Parker, and D. Pershing for many helpful discussions.

References

- [1] R.C. Davidson, *Phys. Fluids* 29 (1986) 267.
- [2] A.K. Ganguly and H.P. Freund, *Phys. Rev. A* 32 (1985) 2275.
- [3] H.P. Freund, C.L. Chang and H. Bluem, *Phys. Rev. A* 36 (1987) 3218.
- [4] H. Bluem, H.P. Freund and C.L. Chang, *Nucl. Instr. and Meth. A* 272 (1988) 579.
- [5] P. Sprangle, C.M. Tang and W.M. Manheimer, *Phys. Rev. Lett.* 43 (1979) 1932.
- [6] N.M. Kroil, P.L. Morton and M.N. Rosenbluth, in *Physics of Quantum Electronics: Free-Electron Generators of Coherent Radiation*, Vol. 7, eds. S.F. Jacobs, H.S. Plooff, M. Sargent, M.O. Scully and R. Spitzer (Addison-Wesley, Reading, MA, 1980) chaps. 4 and 5, p. 89.
- [7] T.J. Orzechowski, B. Anderson, J.C. Clark, W.M. Fawley, A.C. Paul, D. Prosnitz, E.T. Scharlemann, S. Yarema, D.B. Hopkins, A.M. Sessler and J. Wurtele, *Phys. Rev. Lett.* 57 (1986) 2172.
- [8] H.P. Freund, H. Bluem and C.L. Chang, *Phys. Rev. A* 36 (1987) 2182.
- [9] H.P. Freund, *Phys. Rev. A* 37 (1988) 3371.
- [10] W.W. Destler, V.L. Granatstein, I.D. Mayergoyz and Z. Segalov, *J. Appl. Phys.* 60 (1986) 521.
- [11] E.T. Scharlemann, *J. Appl. Phys.* 58 (1985) 2154.

APPENDIX XIII

Another Technical Memorandum

by

P.M. Phillips

ANOTHER TECHNICAL MEMORANDUM**10/89****Prepared by Purobi M. Phillips**

CURRENT SOTA 3-TERMINAL SOLID STATE DEVICES

In the discussion of the competing capabilities of solid-state devices, we will confine ourselves to High Electron Mobility Transistors (HEMT) since these are the SOTA solid-state 3-terminal devices. They can be divided into 3 distinct categories: conventional HEMT's, Pseudomorphic HEMT's, and Indium Phosphite-based HEMT's. A summary of their various capabilities follows:

- i) **Conventional HEMT's:** These devices provide a good noise figure (NF) over the band 1-60 GHz (for example, 0.4 dB at 8 GHz and 1.8 dB at 60 GHz) and have a high transconductance ($g_m = 400$ mS/mm) which gives a large gain-bandwidth product. However, these devices exhibit larger temperature dependence of gain and noise figure than FET's (good performance at 13°K). The high frequency operation of these devices is limited to a gate-length of $0.25\mu\text{m}$ to no more than about 60 GHz. Operation at 94 GHz requires a gate-length of $0.1\mu\text{m}$; however, operation in this regime displays a high output conductance, poor pinch-off characteristics, and poor rf performance. Following numbers will give some idea about the performance level of HEMT's. A HEMT with $150\mu\text{m}$ gate-width gives 100 mW power at 60 GHz with 3 dB gain at 22% efficiency, and a $900\mu\text{m}$ gate width HEMT gives 0.5 W at 35 GHz.
- ii) **Pseudomorphic HEMT's:** These devices provide a better noise figure than either conventional or Indium Phosphite-based HEMT's for 1-100 GHz. It also provides the best power over 10-100 GHz with f_{max} about 230 GHz. A device with $0.25\mu\text{m}$ gate-length has a high transconductance (600 mS/mm) which in turn results in a high operating frequency. This technology allows a gate-length reduction to $0.1\mu\text{m}$ which sets the upper frequency limit to 94 GHz. A $0.25\mu\text{m}$ gate-length device has the same noise figure as conventional HEMT, but it gives 1-2 dB higher gain. It also provides (1) 14% efficiency and 9 mW power at 94 GHz, (2) a 27% efficiency and 85 mW power at 60 GHz, (3) a 36% efficiency, and 100 mW power at 44 GHz, and (4) a 44% efficiency and 104 mW power at 35 GHz.
- iii) **Indium Phosphite based HEMT's:** This group of devices give the best NF (1-100GHz), but its reliability is very poor, as is the output power. The NF is 1.2 dB at 60 GHz. It has high transconductance (900 mS/mm) and $f_{\text{max}} = 380$ GHz.

There are also Heterojunction Bipolar Transistors (HBT) which are vertical devices. Their transconductance is 10 times better than HEMT's and f_t and f_{max} are about 100-200 GHz. They are, however, difficult to fabricate. Since these are still very much in

developmental stage, power and efficiency data are not available.

SUMMARY

The best solid-state 3-terminal device available today for power and efficiency is the pseudomorphic HEMT. The highest obtainable frequency for these devices is 94 GHz with a maximum output power of 9 mW for a 14% efficiency.

REVIEW OF FIELD-EMISSION TRIODE/TETRODE

Figure 1 (a and b) shows the basic configuration of a field-emission triode/tetrode¹. We will review and recalculate some basic parameters of this proposed device in order to find out its performance limitations compared to the solid-state three terminal devices.

Capacitance calculation for a FE-Triode: A 100 cone square array has 120 μm length. If the height of the dielectric is (see figure 1) 1.5 μm , relative dielectric constant is ϵ , then the parallel-plate capacitance between the gate and the cathode is

$$C_1 = 0.0885 \frac{\epsilon A}{d} \text{ pF}$$

where A is the plate area (in cm^2) and d is the distance between the gate and the cathode (in cm). If $\epsilon = 3.84$ (for SiO_2), then $C_1 = 0.3 \text{ pF}$. This capacity can be reduced by about 2/3 by using selectively applied interconnect metal, which means C_1 becomes about 0.1 pF. Also the spacing between the tips can be reduced to 9 μm and in that case for a 100 cone array, $C_1 = 0.18 \text{ pF}$. Thus, selectively interconnect metals will reduce C_1 to 0.06 pF. If we use $\epsilon = 12$, for pure Si (as used in reference 1) we get $C_1 = 0.3 \text{ pF}$. Figure 2 shows the circuit picture of the FE-Triode. We can consider two different design configurations:

Case I) for a very large Drain (Anode)-Source (Cathode) spacing, $C_1 = 0.3 \text{ pF/mA}$, $C_2 = 0$, $C_3 = 0$ (for detailed calculations please see reference 1).

Case II) for a small D-S spacing (cathode height = 1.5 μm and gate-anode height = 2 μm), $C_1 = 0.3 \text{ pF}$, $C_2 = 0.13 \text{ pF}$, and $C_3 = 0.09 \text{ pF}$.

Transconductance of an FE-Triode: The transconductance is defined by the ratio of change in the plate current to the change in grid voltage, i.e. $g_m = \frac{\partial I_p}{\partial V_g}$. Using C. Spindt's most recent set of data^[3] we get $g_m = 1.0 \text{ mS}$ for 200 cones at 70 V gate voltage and $g_m = 2.0 \text{ mS}$ for 24 cones at 300 V gate voltage with 9 μm spacing between the

tips. Transconductance value is usually used to find the upper frequency limitations for rf devices and we will talk about that in the next section.

Upper frequency limit of a FE-Triode: The frequency at which the *short-circuit current gain* drops to 0 dB is known as f_t and the frequency at which the *power gain* drops to 0 dB is known as f_u or f_{max} . Although f_t is relatively easy to calculate ($f_t = \frac{g_m}{2\pi C_1}$) for each circuit the expression for f_u is not easily obtainable. In addition, there is no simple relationship between the two (f_t and f_u). In reference 1, f_u was found using the programme "COMPACT" which is an amply tested programme in this field. Using the set of data from reference 2 the values of the transconductance obtained were relatively small, e.g. for case I, $g_m = 30 \mu S$ and case II, $g_m = 21 \mu S$ (both for 100 cone array). In order to avoid numerical problems in the computer programme "COMPACT", in reference 1 the value of the transconductances used were 5 times the above value, i.e. for case I, $g_m = 150 \mu S$ and for case II, $g_m = 105 \mu S$. Since the state of the art³ indicates that g_m for 200 cone array is about 1.0 mS at 70 V gate voltage, and 2.0 mS for 24 cone array at 300 V gate voltage, the above values are more than reasonable. For case I, where $f_t = 79.6$ MHz, $f_u = 140$ MHz but for case II where $f_t = 55.7$ MHz, $f_u = 20$ GHz. Thus, it can be seen that for a microwave device f_t and f_u are not necessarily related in a very simple way. In other words, by calculating f_t (which can be calculated easily) we do not necessarily gain any knowledge about the actual *upper usable* frequency.

Using the most recent values of the transconductance (1.0 mS for 40 A/cm² current density for 200 cones and 2.0 mS for 85 A/cm² current density for 24 cones) the upper usable frequency has been calculated. The circuit and the circuit parameters used can be found in reference 1. The programme used to calculate the "S" parameters (and hence the f_u) is "TOUCHSTONE". For $g_m = 0.5$ mS for 100 cones, $f_u = 70$ GHz, for $g_m = 1.5$ mS for 100 cones, $f_u = 130$ GHz and for $g_m = (2 \times 4) = 8$ mS for $(24 \times 4) \approx 100$ cones, $f_u \approx 500$ GHz.

Power and efficiency calculations for FE-Triode: Figure 3 shows a set of current-voltage characteristic curves of a 100 cone array. These sets were derived by using reference 2. For class-A operation, with the drawn load line (which can be taken as a typical case) the output power is

$$P_{out} = \frac{\Delta I_{DS} \Delta V_{DS}}{8}$$

$$= 45 \text{ mW.}$$

And the efficiency can be defined as

$$\eta = 50 \times \frac{V_{max} - V_{min}}{V_{max} + V_{min}} \% \\ = 25\%.$$

Using reference 3, (for 200 cones) another set of characteristic curves were obtained (see figure 4). From this set of curves we get $P_{out} = 3.6$ W and the efficiency is about 30%.

For class-B operation, a push-pull arrangement has to be designed which increases the efficiency and output power, and also reduces the stand-by current to almost zero.

Figure 1b shows the configuration of a FE-Tetrode. It is seen that inclusion of the second grid makes it possible to work as an ordinary vacuum tube. An already existing tube (with thermionic cathode) with dimensions 100 times bigger, works at a frequency of 5 GHz. Therefore, normal scaling rule suggests that our proposed FE-Tetrode should work at hundreds of GHz.

SUMMARY OF THE EXPECTED PERFORMANCE OF FE-TRIODE

With current SOTA FE technology (metal cones, not silicon) we get:

- i) $f_u \approx 130 - 500$ GHz.
- ii) As class-A amplifier $P_{out} \approx 3.5$ W and efficiency is about 30% with gate voltage ≤ 300 V.

Assumptions:

- i) Transconductance ≈ 8.0 mS for 100 cones for 500 GHz operation and $g_m \approx 0.5$ mS for 100 cones for 130 GHz operation.
- ii) Fabrication capability to match the design specification.

Current Status:

Assumption (i) is justified because the current data³ shows that the transconductance is about 2 mS for 24 cone array (at 300 V gate voltage), and is about 1 mS for 200 cone array at about 70 V gate voltage.

These numbers indicate already better performance than that of existing SOTA solid-state 3-terminal devices. Since these numbers were obtained using current equals to $40 \mu\text{A}/\text{tip}$ and $104 \mu\text{A}/\text{tip}$, which are obtainable from Molybdenum cones (Spindt *et al.*) and since the best silicon FE data shows $0.025 \mu\text{A}/\text{tip}$ (Gray *et al.*) there should not be any second thought about using metal cones over silicon cones for rf amplifying devices at this stage of the research.

TECHNICAL ISSUES AND GROWTH POTENTIAL

Because the input resistance strongly affects the highest operating frequency of a triode and because there is uncertainty¹ about its calculation there is only one way to resolve the question – an experiment to model the device accurately. Once the modelling informations are obtained the device can be designed with much more confidence and accuracy for higher frequency operation.

The basic growth potential of vacuum microelectronics is enormous. It has been discussed by many authors in many different occasions. For this particular device research the growth potential lies in the fact if the triodes/tetrodes can be evacuated individually, then it could possibly be integrated with the current MIMIC programme, which is a very significant and strong part of the current solid-state industry. For more details please see reference 4.

FIELD-EMISSION DISTRIBUTED AMPLIFIER

Now we will explain briefly the basic configuration, interaction mechanism and expected performance level of a Field-Emission Distributed Amplifier (FEDA).

In a triode/tetrode vacuum tube, an input signal applied between the gate and the cathode results in an amplified signal in the output (plate/anode) circuit. In the FEDA^{5,6} the emitter, gate and anode are extended in length (but not in width) which forms a double-microstrip parallel-plate transmission line with the field emitter embedded in it over the entire length of the device. It is shown schematically in figure 5. The input signal is applied at one end of the transmission line and the other end is terminated in a non-reflecting resistive load. A "grounded-grid" triode distributed amplifier is not practical because the input signal source must drive the cathode current against the anode current and this results in an excessive load ($1/g_m$) in the input circuit. Therefore a tetrode type of distributed amplifier design has been chosen. The screen-grid is AC grounded to shield the input from capacitively coupling to the output and thus avoid feedback oscillation. The width of the first grid is chosen to be smaller than the screen-grid to minimize the capacitance between this and the cathode base. The applied input signal produces a travelling-wave density-modulated signal that induces a similar amplified density-modulated signal on the output transmission line. The FEDA requires that the phase velocity in the input and the output transmission lines to be identical because the induced output travelling wave must be phase-matched with the input travelling wave. This phase-match was proposed to achieve by dielectrically loading the output line. By extensive modelling⁷ (both experi-

mental and computational) of the output and input lines we have demonstrated that it is possible to control the output phase-velocity by varying different design parameters and dielectric constant of the material in the output line. Thus, both the input and output circuits are wide-bandwidth transmission lines and since the cathode area has been increased the cathode current and the output power increase too.

A small-signal theory⁸ has been developed to find the dependence of the electronic gain on frequency, beam voltage, beam current and the circuit parameters. The electronic gain and the circuit loss increase as the transverse dimension of the circuit is decreased. For optimum net gain, this dimension should lie in the range of 80 – 120 μm . For a single-wedge emitter the maximum gain varies from 2 to 7.0 dB/cm as the gate voltage decreases from 100 to 50 V and the operating frequency range is 45 to 75 GHz for the set of design parameters indicated in figure 6. The gain increases with the current density and so, for a multiple-wedge emitter the gain is expected to be higher whereas the loss is expected to remain the same. The above numbers were obtained using a linear current density of 15 A/cm. Current SOTA FE technology³ can routinely provide 5 A/cm if we assume a wedge to be an assembly of tips 0.2 μm apart. The rapid progress of FE technology suggests the possibility of achieving the higher current density in the near future. The possibility of using multiple wedges also demand less current density from each emitter. To find the parametric dependence of the impedances and losses (of both output and input lines) quasi-static microstrip line theory has been used⁷. Unlike a triode the FEDA-gain occurs in space and hence the length of the device must be a few wavelength long in order to have appreciable gain.

Assuming a wedge to be an assembly of emitter tips 0.2 μm apart and also assuming a current of 4 $\mu\text{A}/\text{tip}$, a simple circuit theory⁵ shows 10's of Watts of output power for about 60 GHz frequency with $\geq 25\%$ efficiency with ≤ 200 V at the gate. Since the state-of-the-art FE technology³ gives 100 $\mu\text{A}/\text{tip}$ the above numbers seem to be quite conservative!

CONCLUSION AND SUMMARY

Because of its interaction mechanism (and, hence, the size) FEDA should not be compared with either the current solid state devices or the FE-Triode. Although it may operate at somewhat lower frequency than the triode it is capable of producing more output power with a broader bandwidth.

GROWTH POTENTIAL

Because of the absence of magnets, heater, or heater power supplies and because of its size and projected performance level it is reasonable to conclude that FEDA has the potential to be a replacement of currently available TWT's.

References

- [1.] Neidert R. E., *Technical Memorandum*, Ser. #6850-34: REN: pi, Feb., 1981.
- [2.] Spindt *et al.*, *J. Appl. Phys*, Dec., 1976.
- [3.] Spindt *et al.*, *Private Communications*, Sept., 1989.
- [4.] Neidert R. E., *Field Emission Array Technology Assessment*, Aug., 1988
- [5.] Gray H. F. and Smith S. T., *Report to L. Fletcher*, , March, 1988.
- [6.] Smith S. T. *Technical Memorandum to J. A. Montgomery*, , Feb., 1988.
- [7.] Phillips P. M., Smith S. T., Gray H. F. *Proceedings of the Second International Conference on Vacuum Microelectronics*.
- [8.] Ganguly *et al.*, manuscript being prepared, 1989.

INTENDED PLAN OF ACTIONS AND REASONS FOR THAT

The primary goal of this project is to build an rf amplifier using the FE technology. The performance of these systems is potentially better than the current solid-state three terminal devices. The distributed amplifier is not a competitor of current solid-state devices for reasons explained above. Of the two configurations discussed, the triode amplifier is *easier* to fabricate than the distributed amplifier. The basic requirements for both amplifiers are high current per tip and high transconductance per capacitance. For microwave transmission line based devices (*e.g.* Distributed Amplifier) the use of silicon (a dielectric) would introduce an unnecessary amount of loss. The silicon tip research (high doping concentration, metal coating etc.) has a long way to go before it can match the performance of metal tips ($\geq 100 \mu\text{A}/\text{tip}$). SRI International has had 20 years of research experience and they have made microtriodes using silicon anodes (because of the easiness of fabrication) and metal coated silicon anodes. Thus, SRI is familiar with the problems associated with microtriode fabrication. Experimentation with microtriodes will give us valuable informations about some intrinsic parameters (*e.g.* transconductance, parasitic resistance, capacitances) that will help us to design a better distributed amplifier. In the process, the goal of building an rf FE-amplifier will be satisfied too. Moreover, the mi-

crotriodes can be cascaded to build a discretely distributed amplifier too. Therefore the plan is to give a contract to SRI for research collaboration and fabrication of an FE-Triode and also for thinking process of a Distributed Amplifier.

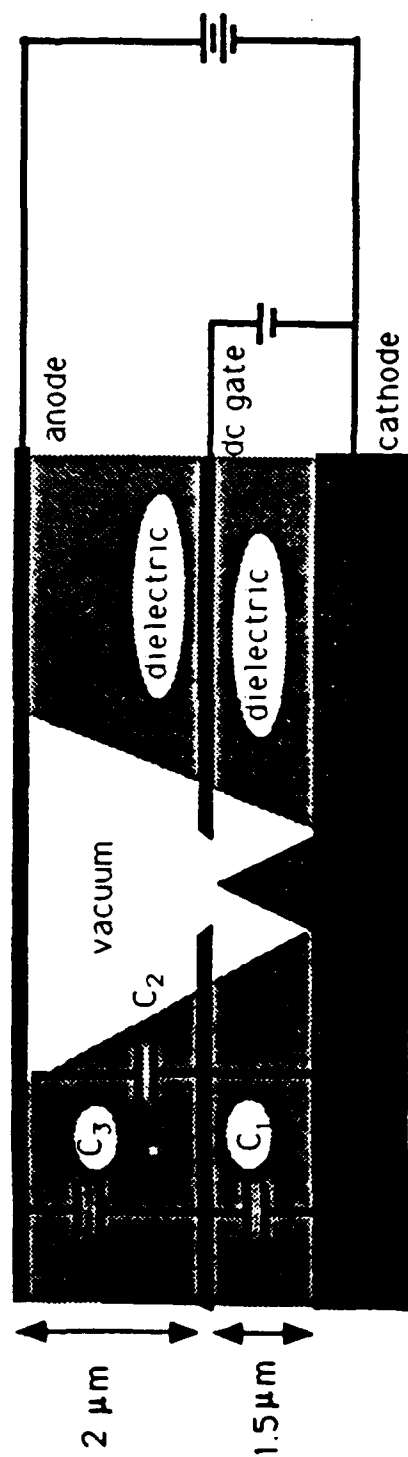


Figure 1(a): FE Triode

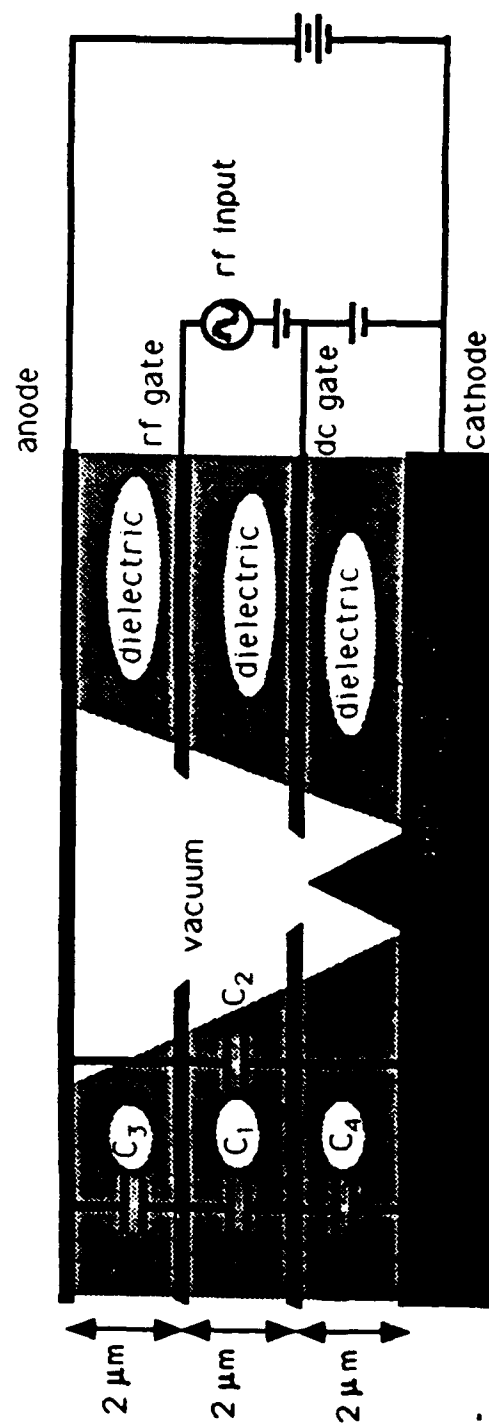


Figure 1(b): FE Tetrode

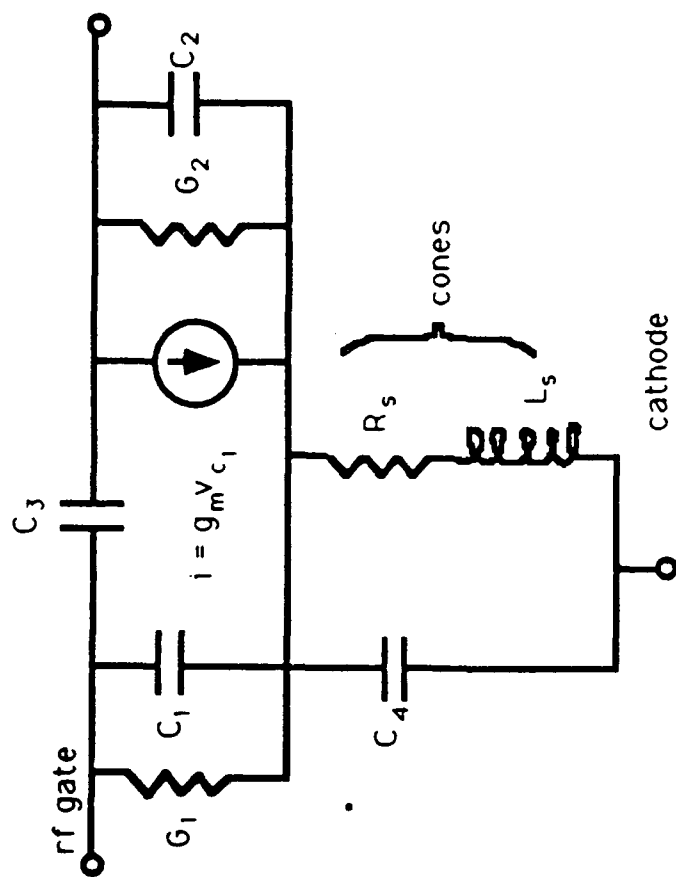


Figure 2. Equivalent Circuit of FE-Triode/Tetrode

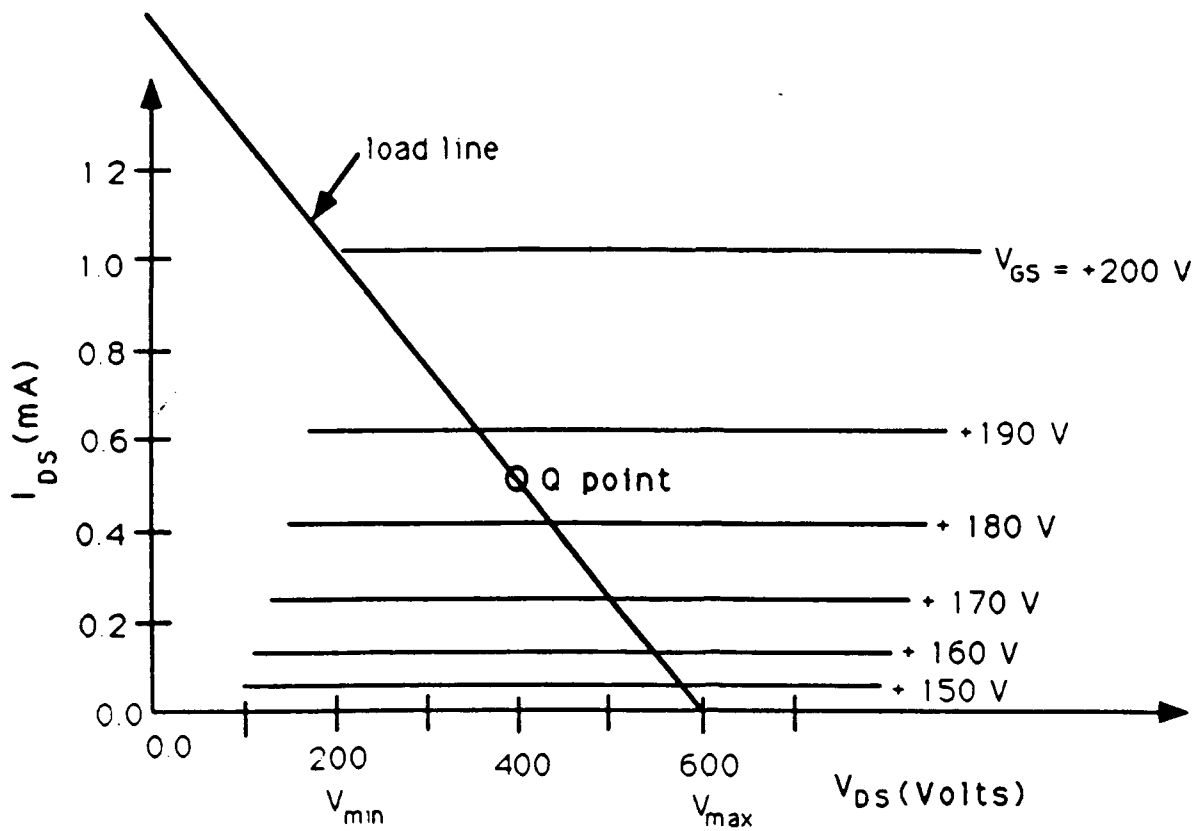


Figure 3. I-V Characteristics for a 100 cone array (Ref. 2)

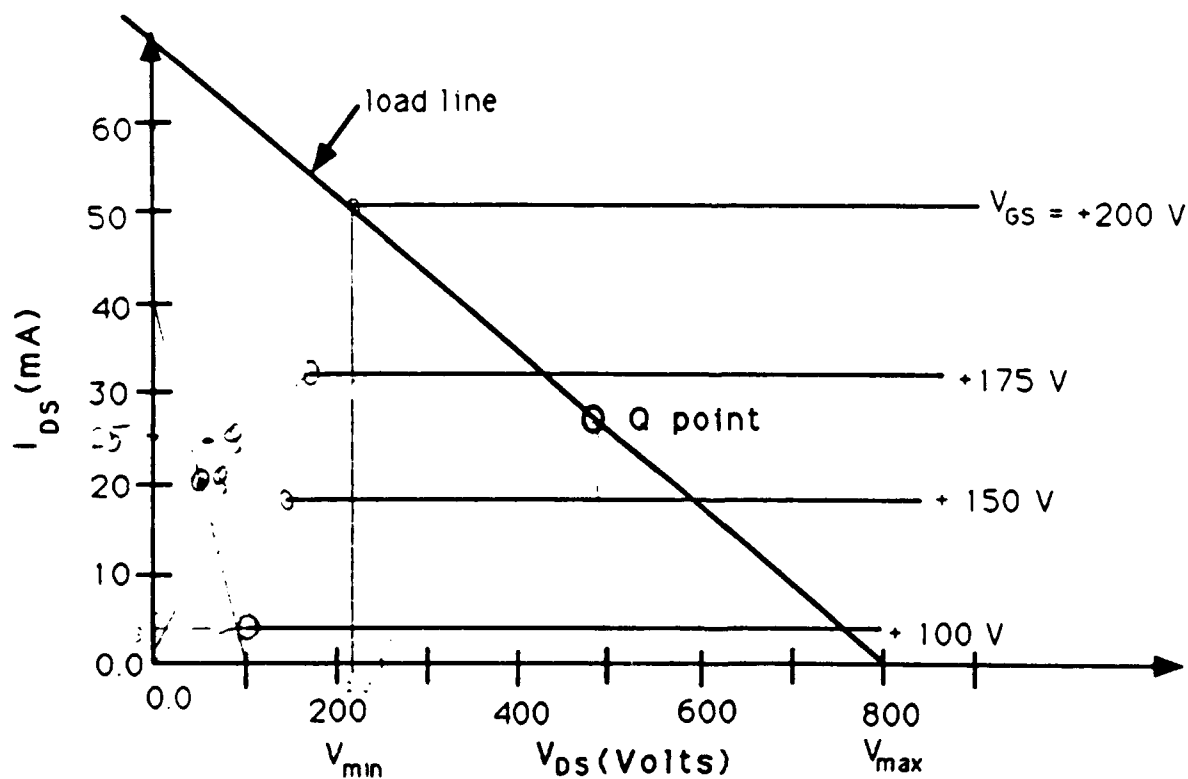


Figure 4. I-V Characteristics for a 200 cone array (Ref. 3)

$$R_g = \frac{V_g}{I_g} = \frac{500}{22 \mu A} = 22.73 K\Omega \quad R_L = \frac{590V}{52mA} = 11.35 K\Omega$$

FIELD EMISSION DISTRIBUTED AMPLIFIER

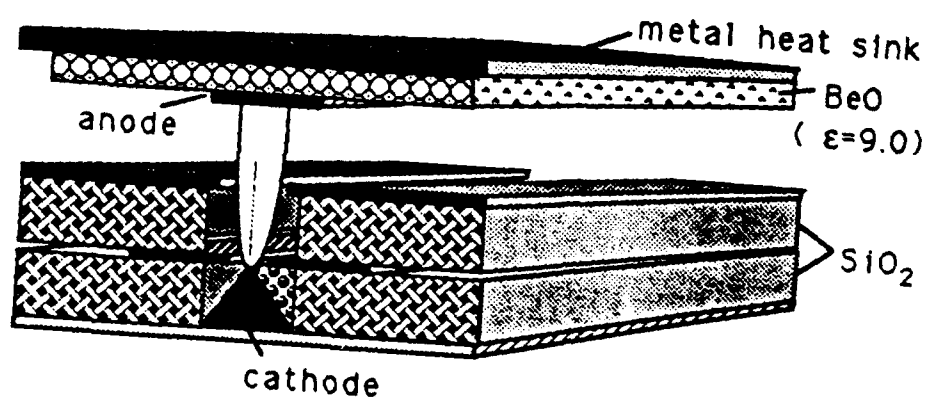


FIGURE 5

FIELD EMITTER DISTRIBUTED AMPLIFIER

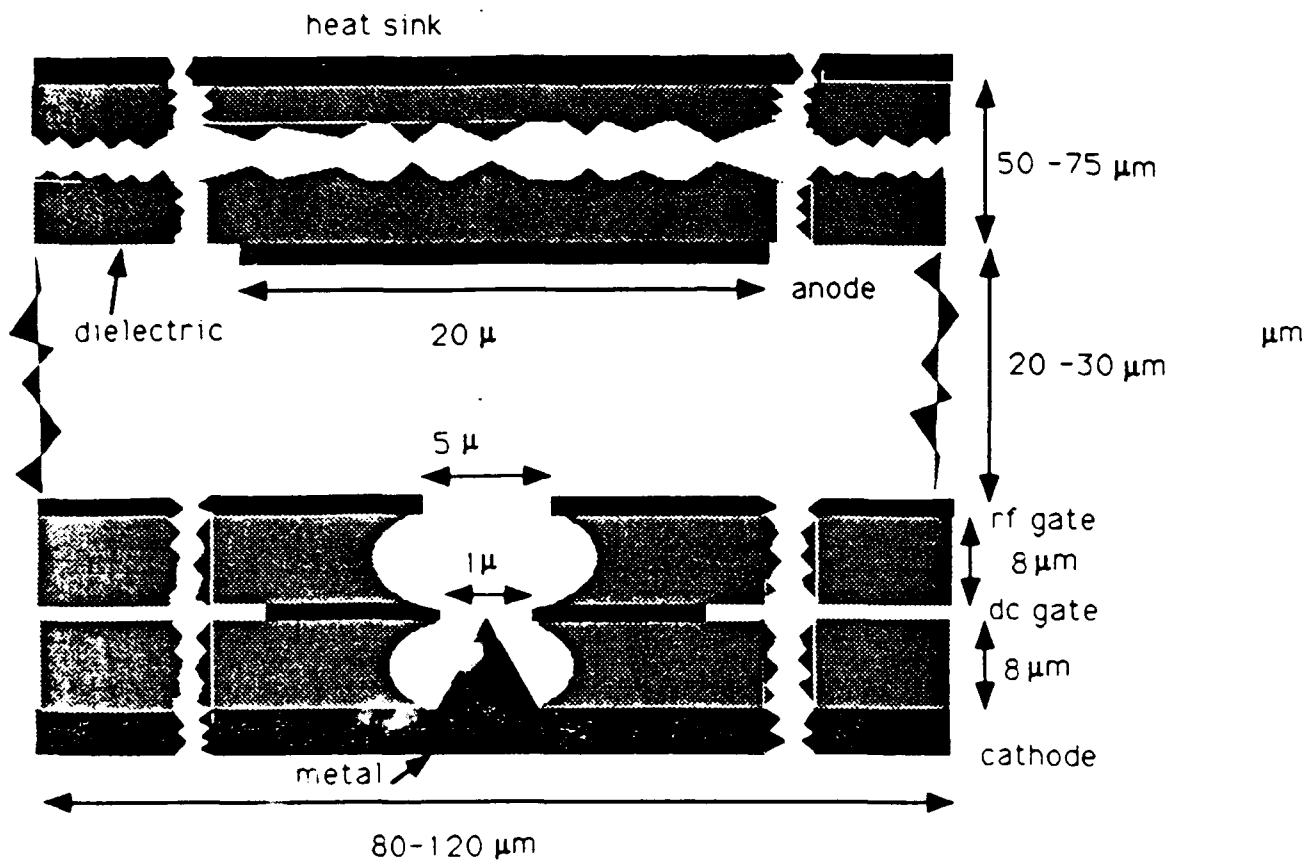


FIGURE 5

APPENDIX XIV

Linear Theory of a Field-Emitter-Array Distributed Amplifier

by

A.K. Ganguly, P.M. Phillips, and H.F. Gray

Linear theory of a field-emitter-array distributed amplifier

A. K. Ganguly, P. M. Phillips,^{*} and H. F. Gray
Naval Research Laboratory, Washington, D.C. 20375

(Received 25 October 1989; accepted 12 for publication February 1990)

A small-signal theory of a field-emission-array distributed amplifier consisting of two microstriplike transmission lines is developed to calculate the premodulation in the input channel and the gain in the output channel. A first-order perturbation analysis is used to treat the beam-wave coupling in this device within the framework of a cold fluid model. The dependence of the linear gain on frequency, beam voltage, beam current, and the circuit parameters is derived to determine the parameter range for operation of the device. It is found that the height of the circuit is restricted to lie between 80 and 120 μm to maintain high electronic gain and low loss arising from the finite conductivity of the metal surfaces. In an output line having a substrate with a relative dielectric constant, $\epsilon_r = 4$, a net gain of 7 dB/cm is calculated with a beam voltage of 60 V and a beam current of 2.14 A/cm in each wedge of a seven-wedge emitter array. As the beam voltage is increased in the range 60–100 V, the net gain decreases from 7.0 to 3.0 dB/cm, while the frequency for maximum gain increases from 50 to 80 GHz with a corresponding increase in the bandwidth. The small-signal instantaneous bandwidth is in excess of 60%.

I. INTRODUCTION

Vacuum microelectronics^{1,2} is an emerging technology in which micrometer-size devices can be fabricated to take advantage of the high-current-density capability and the vacuum ballistic transport properties intrinsic to the field-emitter arrays (FEAs).^{3,4} Because of the high drift velocity in vacuum and the micrometer-scale dimensions available from microelectronics processing techniques, the total transit time (τ) for electrons in vacuum microelectronic devices will be extremely small. It has been suggested⁵ that the FEA-based devices might allow submillimeter-wave amplification at frequencies approaching 1 THz based on the assumption that the upper cutoff frequency (f_u) of a triodelike device is determined by the total transit time, i.e., $f_u \approx 1/(2\pi\tau)$. However, the transit time is not the only factor that limits the upper frequency. One must also consider other factors such as electrode capacitance (C_m), transconductance (g_m), conductor losses on the walls and the electrodes, etc. For example, taking into account the effects of transconductance and capacitance, calculated from experimental FEA data,⁶ an upper-frequency limit of about 3 GHz has been predicted by Anderson⁷ from the relation $f_T = g_m/2\pi C_m$. In the experiment,⁸ the effective area of emission of the electrons is much less than the area of the tip, leading to a low value of g_m . If improved fabrication technique can give uniform emission from the entire tip and if the metal work function can be lowered to 3 eV, f_T can be increased to 250 GHz.

Gray and Greene⁹ proposed a distributed-amplifier configuration to increase g_m following the ideas⁹ originally conceived for vacuum tubes in which the transconductance of the tubes could be added and the capacitances could be used to create an artificial transmission line with large trans-

conductance and small capacitance. Although the circuit has higher f_T , the upper frequency is still limited by the conductor losses in the transmission lines. Kosmahl¹⁰ performed an analytical evaluation of a "discrete" distributed amplifier in which an input transmission line is formed by connecting the gate electrodes of a series of FEA-based triodes (FETRODES) with inductive strips and the output transmission line is similarly formed by connecting the anodes. The device is considered for operation in the frequency range 10–300 GHz. The instantaneous bandwidth of the device is not shown in the paper. Here, we consider a "continuous" distributed amplifier formed from two microstriplike transmission lines with the field-emitter array embedded in the input transmission line. The continuous distributed amplifier is expected to have much broader instantaneous bandwidth than the "discrete" type. The possibility of using the microstrip lines to propagate modulated waves in FEA devices was raised by Brodie and Spindt.¹¹

In this paper, we develop a small-signal theory of a continuously distributed FEA amplifier to calculate the gain as a function of frequency and provide a realistic estimate of the gain and the bandwidth. A description of the continuously-distributed-amplifier configuration is given in Sec. II. Some features of the "cold" circuit such as the field structure, the impedance, and the loss due to the finite conductivity of the metal surfaces are obtained in Sec. II from a full-wave analysis. These quantities are required to develop a small-signal theory for calculating the net gain. The interaction between the beam and the wave is treated in Sec. III on the basis of a cold fluid model. The beam is premodulated in the input channel and the energy extraction from the bunched beam occurs in the output channel. The linear growth rate is calculated from a perturbed dispersion relation. The dependence of the net gain on frequency and the circuit dimensions is shown. The results of the numerical calculation and a discussion of the results are given in Sec. IV and conclusions are shown in Sec. V.

^{*}Permanent address: Science Applications International Corp., McLean, VA 22102.

II. PHYSICAL SYSTEM

The FEA distributed amplifier consists of a multilevel set of metallizations arranged as shown in Fig. 1. The upper section is the output circuit, which is an enclosed microstrip-like transmission line containing the screen electrode and the electron collector. The lower section is a coaxial-like input microstrip transmission line consisting of a wedge-type field-emitter array, a gate electrode, and a screen electrode. The screen electrode is common to both transmission lines and is needed primarily to prevent feedback from the output line to the input line. The input rf signal is applied to the gate electrode. The waves propagate parallel to the wedge. The emitted electrons drift from the cathode to the anode at right angles to the direction of the wave propagation. The aperture in the screen electrode should be small enough so that the rf fields in the two circuits are not directly coupled. The input signal impresses a current modulation on the beam in the input circuit and the modulated current acts as a source for the rf fields in the output circuit. If the phase velocities in the two circuits are identical, all the electrons can experience a decelerating field as they move to the anode and power is extracted from the beam. The two phase velocities can be matched by proper dielectric loading of the circuits. The continuously distributed amplifier is in effect a traveling-wave amplifier where the electrons drift perpendicular to the direction of the wave propagation. The modulated beam excites waves in both the forward and the backward directions. Under the phase-matching condition, the contribution to the amplitude of the wave from each beamlet along the wedge adds in phase in the forward direction while the phase angles vary from 0 to $2\beta L$ in the backward direction (β is the propagation constant and L is the interaction length). As a result, waves grow in the forward direction only, and the ratio of the power in the backward wave to the power in the forward wave is given by $(\sin \beta L / \beta L)^2$. If $\beta L \gg \pi$, the power in the backward wave is negligible. Any signal that travels backward and is not quite canceled by the out-of-phase additions, will have to be absorbed by reverse termination.⁹

In Fig 1, d_1 and d_2 are, respectively, the heights of the dielectric and vacuum regions in the output circuit, $2a$ is the width of the circuit, and $2w$ is the width of the infinitely thin microstrip line. The emitter may consist of a single wedge or an array of N_E wedges separated by a distance Δ with the

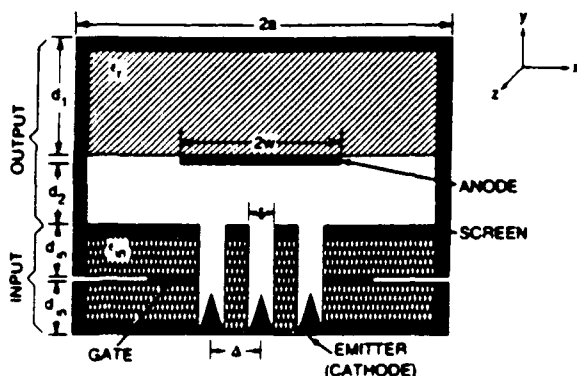


FIG. 1. A cross-sectional view of the distributed amplifier

axes at $x = 0, \pm \Delta, \pm 2\Delta, \dots$. The width of the aperture in the screen electrode over each emitter edge is δ . The apertures in the gate electrode are narrower. The total heights of the output and the input circuits will be denoted by $h_{out} = d_1 + d_2$ and $h_{in} = 2d_{in}$, respectively. ϵ, ϵ_0 and ϵ_n, ϵ_0 denote, respectively, the dielectric constants of the dielectric regions in the output and the input lines. The vacuum dielectric constant is ϵ_0 and the permeability is μ_0 . In the following, we will use a rectangular coordinate system with the z axis parallel to the wedge, the y axis along the height, and the x axis along the width of the transmission lines. The origin of the coordinates is taken at the center of the screen electrode aperture. The set $(\hat{e}_x, \hat{e}_y, \hat{e}_z)$ denotes the unit vectors along (x, y, z) axes.

The output circuit will be modeled as a shielded microstrip transmission line with an infinitely thin strip (anode). A spectral domain analysis was developed by Itoh and Mitra¹² to calculate the dispersion relation of a lossless, shielded microstrip transmission line. We use this theory to obtain explicit expressions for the field components, the power flow, and the impedance in the circuit. The loss due to the finite conductivity is determined from the rf field calculated for perfectly conducting metal surfaces. For the sake of completeness, a brief derivation of the unperturbed dispersion equation is included in the following. The hybrid field components in the microstrip line can be expressed as a superposition of the LSE (TE to y) and LSM (TM to y) modes.¹³ The LSE and the LSM modes are derivable from two scalar potentials ψ^h and ψ^v , respectively. Since we are considering only propagating waves with angular frequency ω and propagation constant β , a solution of the form

$$\psi^{h,v}(x, y, z, t) = \psi^{h,v}(x, y) e^{i(\omega t - \beta z)} \quad (1)$$

will be assumed. The electric and the magnetic fields may be expressed in terms of these potentials as

$$\mathbf{E} = -i\mu\omega\hat{e}_y\psi^v + \frac{1}{i\epsilon\omega}\nabla\left(\frac{\partial\psi^h}{\partial y}\right) - \nabla \times (\hat{e}_y\psi^h), \quad (2)$$

$$\mathbf{H} = -i\epsilon\omega\hat{e}_y\psi^h + \frac{1}{i\mu\omega}\nabla\left(\frac{\partial\psi^v}{\partial y}\right) + \nabla \times (\hat{e}_y\psi^v). \quad (3)$$

From Maxwell's equations, it follows that the functions $\psi^v(x, y)$ and $\psi^h(x, y)$ satisfy the two-dimensional Helmholtz equations

$$\left(\frac{\partial^2}{\partial x^2} + \frac{\partial^2}{\partial y^2} + k_0^2 - \beta_0^2\right)\psi(x, y) = 0, \quad 0 < y < d_2, \quad (4)$$

$$\left(\frac{\partial^2}{\partial x^2} + \frac{\partial^2}{\partial y^2} + \epsilon k_0^2 - \beta_0^2\right)\psi(x, y) = 0, \quad d_2 < y < h_{out} = d_1 + d_2. \quad (5)$$

Here $k_0 = \sqrt{\mu_0\epsilon_0}\omega$ is the free-space propagation constant.

The modes may be divided into even (E_z -even- H_z -odd) and odd (E_z -odd- H_z -even) symmetries with respect to reflection in the yz plane. The even and the odd modes may also be classified as $(\psi^h$ -odd, ψ^v -even) and $(\psi^h$ -even, ψ^v -odd), respectively. Since we are mainly interested in the dominant mode, which is E_z -even- H_z -odd, the equations will be written explicitly for these modes and the changes for

$$\psi(x, y) = \sum_{n=-1}^{\infty} \tilde{\psi}(k_n, y) \sin(k_n x) = \begin{cases} i \sum_{n=-1}^{\infty} A_n^+ \sin(k_n x) \sinh \Gamma_1 (h_{\text{out}} - y), & d_2 < y < h_{\text{out}} \\ i \sum_{n=-1}^{\infty} B_n^+ \sin(k_n x) \sinh \Gamma_2 y, & 0 < y < d_2 \end{cases} \quad (6)$$

and

$$\psi(x, y) = \sum_{n=-1}^{\infty} \tilde{\psi}(k_n, y) \cos(k_n x) = \begin{cases} -i \sum_{n=-1}^{\infty} A_n^- \cos(k_n x) \cosh \Gamma_1 (h_{\text{out}} - y), & d_2 < y < h_{\text{out}} \\ -i \sum_{n=-1}^{\infty} B_n^- \cos(k_n x) \cosh \Gamma_2 y, & 0 < y < d_2 \end{cases} \quad (7)$$

where the tilde represents the Fourier transform and

$$\begin{aligned} k_n &= (2n-1)\pi/2a, \\ \Gamma_1 &= (k_n^2 + \beta^2 - \epsilon_r k_0^2)^{1/2}, \\ \Gamma_2 &= (k_n^2 + \beta^2 - k_0^2)^{1/2}. \end{aligned} \quad (8)$$

$\Gamma_{1,2}$ may be real or imaginary. For imaginary $\Gamma_{1,2}$, the hyperbolic functions in Eqs. (1) and (2) are to be substituted with the corresponding trigonometric functions. In the case of odd symmetry modes, $\cos(k_n x)$, and $\sin(k_n x)$, respectively, should be replaced by $\sin(k_n x)$ and $-\cos(k_n x)$, where $k_n = n\pi/a$ including $n=0$. The Fourier transforms are calculated by taking the inverse transformations

$$\tilde{\psi}(k_n, y) = \frac{1}{a} \int_{-a}^a \psi(x, y) \sin(k_n x) dx, \quad (9)$$

$$\tilde{\psi}(k_n, y) = \frac{1}{a} \int_{-a}^a \psi(x, y) \cos(k_n x) dx. \quad (10)$$

The scalar potentials in Eqs. (6) and (7) are chosen such that the tangential components of \mathbf{E} and the normal components of \mathbf{H} vanish at $y=0$, $y=h_{\text{out}}$, and $x=\pm a$. The coefficients A_n^+ , A_n^- , B_n^+ , and B_n^- are expressed in terms of the unknown current components on the strip by applying the following continuity conditions on the field components at the interface $y=d_2$:

$$E_{z2}(x, d_2) = E_{z1}(x, d_2) \quad (11a)$$

$$E_{x2}(x, d_2) = E_{x1}(x, d_2), \quad (11b)$$

$$H_{z2}(x, d_2) - H_{z1}(x, d_2) = -J_z(x, d_2), \quad (12a)$$

$$H_{x2}(x, d_2) - H_{x1}(x, d_2) = J_x(x, d_2), \quad (12b)$$

where $J_x(x, d_2)$ and $J_z(x, d_2)$ are the components of the surface current density on the microstrip and the subscripts 1 and 2 refer, respectively, to the dielectric ($d_2 < y < h_{\text{out}}$) and the air ($0 < y < d_2$) regions. $J_{xz} = 0$ for $w < |x| < a$ and $J_{xz} \neq 0$ for $0 < |x| < w$. Substituting Eqs. (2), (3), (6), and (7) in Eqs. (11) and (12), we obtain

$$\frac{\Gamma_1 A_n^+}{\epsilon_r \epsilon_0 \omega} = -Z_r \frac{1}{\sinh(\Gamma_1 d_1)} \frac{\beta \tilde{J}_z(k_n) + ik_n \tilde{J}_x(k_n)}{k_n^2 + \beta^2}, \quad (13a)$$

$$\frac{\Gamma_2 B_n^+}{\epsilon_0 \omega} = Z_r \frac{1}{\sinh(\Gamma_2 d_2)} \frac{\beta \tilde{J}_z(k_n) + ik_n \tilde{J}_x(k_n)}{k_n^2 + \beta^2}, \quad (13b)$$

$$A_n^- = Z_r \frac{1}{\sinh(\Gamma_1 d_1)} \frac{k_n \tilde{J}_z(k_n) - i\beta \tilde{J}_x(k_n)}{k_n^2 + \beta^2}, \quad (13c)$$

$$B_n^- = Z_r \frac{1}{\sinh(\Gamma_2 d_2)} \frac{k_n \tilde{J}_z(k_n) - i\beta \tilde{J}_x(k_n)}{k_n^2 + \beta^2}, \quad (13d)$$

where Z_r and Z_h are the impedances defined by

$$Z_r = Z_0 / (\bar{Y}_1^+ + \bar{Y}_1^-), \quad (14a)$$

$$Z_h = Z_0 / (\bar{Y}_1^+ + \bar{Y}_2^+), \quad (14b)$$

$$\bar{Y}_1^+ = \frac{\Gamma_1}{k_0} \coth(\Gamma_1 d_1), \quad \bar{Y}_2^+ = \frac{\Gamma_2}{k_0} \coth(\Gamma_2 d_2), \quad (15a)$$

$$\bar{Y}_1^- = \frac{\epsilon_r k_0}{\Gamma_1} \coth(\Gamma_1 d_1), \quad \bar{Y}_2^- = \frac{k_0}{\Gamma_2} \coth(\Gamma_2 d_2), \quad (15b)$$

$$Z_0 = \sqrt{\mu_0 / \epsilon_0} \quad (\text{vacuum impedance}). \quad (16)$$

In Eqs. (13a)-(13d), $\tilde{J}_z(k_n)$ and $\tilde{J}_x(k_n)$ are the Fourier transforms of $J_z(x, w)$ and $J_x(x, w)$ according to Eqs. (9) and (10), respectively. Finally, two additional boundary conditions are required on the strip:

$$E_{z2}(x, d_2) = 0, \quad |x| < w \quad (17a)$$

$$E_{x2}(x, d_2) = 0, \quad |x| < w. \quad (17b)$$

For $w < |x| < a$, $E_{z2}(x, d_2)$ and $E_{x2}(x, d_2)$ have nonzero values that are yet to be determined. As before, we apply Eqs. (17) in the Fourier-transform domain. On substitution of Eqs. (2), (6), (7), and (13) in Eqs. (16) and (17), we obtain the following two coupled equations relating the four unknown variables, \tilde{J}_z , \tilde{J}_x , \tilde{E}_z , and \tilde{E}_x ,

$$\begin{pmatrix} Z_{zz} & Z_{zx} \\ Z_{xz} & Z_{xx} \end{pmatrix} \begin{pmatrix} \tilde{J}_z \\ \tilde{J}_x \end{pmatrix} = \begin{pmatrix} -i\tilde{E}_z \\ \tilde{E}_x \end{pmatrix}, \quad (18)$$

where $\tilde{E}_z(k_n)$ and $\tilde{E}_x(k_n)$, respectively, are the Fourier transforms of $E_z(x, d_2)$ and $E_x(x, d_2)$ given by Eqs. (9) and (10). The elements $Z_{ij}(k_n)$ are defined by

$$Z_{\pm}(k_n) = \frac{\beta^2 Z_e - k_n^2 Z_h}{k_n^2 + \beta^2}, \quad (19)$$

$$Z_{\pm}(k_n) = \frac{k_n^2 Z_e - \beta^2 Z_h}{k_n^2 + \beta^2}, \quad (20)$$

$$Z_{\pm}(k_n) = Z_{\pm}(k_n) = \frac{\beta k_n (Z_e + Z_h)}{k_n^2 + \beta^2}. \quad (21)$$

It is to be noted that the two pairs of functions $J_z(x, d_2)$, $J_z(x, d_1)$ and $E_z(x, d_2)$, $E_z(x, d_1)$ are nonzero in complementary regions of the domain $-a < x < a$. This special property of the functions is used in the method of moments to eliminate two of the unknown functions, $\{E_z, E_z\}$ by using Galerkin's¹² approach in the Fourier-transform domain. For this purpose we expand $J_z(x, d_2)$ and $J_z(x, d_1)$ in a suitable set of basis functions. For the even modes,

$$J_z(x, d_2) = \begin{cases} \sum_{m=1}^M a_m \xi_{em}(x) & \text{when } 0 < |x| < w \\ 0 & \text{when } w < |x| < a \end{cases} \quad (22)$$

$$J_z(x, d_1) = \begin{cases} \sum_{m=1}^N c_m \eta_{em}(x) & \text{when } 0 < |x| < w \\ 0 & \text{when } w < |x| < a \end{cases} \quad (23)$$

where basis functions¹⁴ chosen are

$$\xi_{em}(x) = \frac{\cos[(m-1)\pi x/w]}{[1 - (x/w)^2]^{1/2}}, \quad (24)$$

$$\eta_{em}(x) = \frac{\sin(m\pi x/w)}{[1 - (x/w)^2]^{1/2}}. \quad (25)$$

Each series expansion in Eqs. (22) and (23) is truncated to a finite number of terms and the integer values of M and N are selected to be large enough to achieve the desired accuracy. From Eqs. (6)-(10), the Fourier transforms $\tilde{\xi}_{em}(k_n)$ and $\tilde{\eta}_{em}(k_n)$ of the basis functions in Eqs. (24) and (25) may be written as

$$\tilde{\xi}_{em}(k_n) = \frac{\pi w}{2a} [J_0(k_n w - (m-1)\pi) + J_0(k_n w + (m-1)\pi)], \quad (26)$$

$$\tilde{\eta}_{em}(k_n) = \frac{\pi w}{2a} [J_0(k_n w - m\pi) - J_0(k_n w + m\pi)]. \quad (27)$$

In Eqs. (26) and (27), $J_0(u)$ is the Bessel function of the first kind and order zero. Substituting Eq. (26) in Eq. (22) and Eq. (27) in Eq. (23), the Fourier transforms of the components of the strip current becomes, for even modes,

$$\begin{aligned} \tilde{J}_z(k_n) &= \sum_{m=1}^M a_m \tilde{\xi}_{em}(k_n), \\ \tilde{J}_z(k_n) &= \sum_{m=1}^N c_m \tilde{\eta}_{em}(k_n). \end{aligned} \quad (28)$$

The corresponding expressions for the odd modes shown in Appendix A. After substituting Eq. (28) in Eq. (18), we take inner products with the basis functions $\tilde{\xi}_{ep}(k_n)$ and $\tilde{\eta}_{ep}(k_n)$ for all p and obtain the matrix equation

$$\sum_{m=1}^M G_{\pm}^{pm} a_m + \sum_{m=1}^N G_{\pm}^{pm} c_m = 0, \quad p = 1, 2, \dots, M \quad (29a)$$

$$\sum_{m=1}^M G_{\pm}^{pm} a_m + \sum_{m=1}^N G_{\pm}^{pm} c_m = 0, \quad p = 1, 2, \dots, N \quad (29b)$$

where the elements G_{\pm} are given by

$$G_{\pm}^{pm} = \sum_{n=-\infty}^{\infty} Z_{\pm}(k_n) \tilde{\xi}_{em}(k_n) \tilde{\xi}_{ep}(k_n), \quad (30a)$$

$$G_{\pm}^{pm} = \sum_{n=-\infty}^{\infty} Z_{\pm}(k_n) \tilde{\eta}_{em}(k_n) \tilde{\xi}_{ep}(k_n), \quad (30b)$$

$$G_{\pm}^{pm} = \sum_{n=-\infty}^{\infty} Z_{\pm}(k_n) \tilde{\xi}_{em}(k_n) \tilde{\eta}_{ep}(k_n), \quad (30c)$$

$$G_{\pm}^{pm} = \sum_{n=-\infty}^{\infty} Z_{\pm}(k_n) \tilde{\eta}_{em}(k_n) \tilde{\eta}_{ep}(k_n). \quad (30d)$$

The set of equations (29) are solved for the propagation constant β by setting its $(M+N) \times (M+N)$ determinant equal to zero. On substituting β in the set of equations (29), all coefficients a_m ($m = 2, \dots, M$) and c_m ($m = 1, \dots, N$) can be determined in terms of a_1 by using $M+N-1$ equations from the set. The only unknown quantity, a_1 , is to be calculated from the power in the transmission line.

It is useful to show explicitly the expressions for E and H in terms of a_1 since the field components will be repeatedly used to calculate various characteristics of the wave propagation such as power flow, conductor losses, and growth due to the interaction with an electron beam. According to Eq. (1), all rf field variables for propagating waves are assumed to be of the form

$$\begin{Bmatrix} E(x, y, z, t) \\ H(x, y, z, t) \end{Bmatrix} = \begin{Bmatrix} E(x, y) \\ H(x, y) \end{Bmatrix} \times e^{i(\omega t - \beta z)}.$$

The equations for $E(x, y)$ and $B(x, y) = \mu H(x, y)$ are derived in Appendix A and are given by

$$\begin{aligned} E_x(x, y) &= \sum_{n=1}^{\infty} Q_{nx}^{(j)} \sin(k_n x) \sinh(\Gamma_j y), \\ B_x(x, y) &= \frac{1}{c} \sum_{n=1}^{\infty} R_{nx}^{(j)} \cos(k_n x) \cosh(\Gamma_j y), \\ E_y(x, y) &= - \sum_{n=1}^{\infty} Q_{ny}^{(j)} \cos(k_n x) \cosh(\Gamma_j y), \\ B_y(x, y) &= \frac{1}{c} \sum_{n=1}^{\infty} R_{ny}^{(j)} \sin(k_n x) \sinh(\Gamma_j y), \\ E_z(x, y) &= -i \sum_{n=1}^{\infty} Q_{nz}^{(j)} \cos(k_n x) \sinh(\Gamma_j y), \\ B_z(x, y) &= \frac{i}{c} \sum_{n=1}^{\infty} R_{nz}^{(j)} \sin(k_n x) \cosh(\Gamma_j y), \end{aligned} \quad (31)$$

where as before the index $j = 1, 2$ is for the dielectric and the air regions, respectively, and the variables y_j are $y_1 = h_{\text{out}} - y$, $y_2 = y$. The coefficients $Q_{np}^{(j)}$ and $R_{np}^{(j)}$ are given by Eqs. (A3)-(A9) in the Appendix.

The average power in the circuit propagating along the z axis can be calculated by using Eq. (31) in the Poynting theorem:

$$r_{\alpha\alpha} = \frac{1}{2} \kappa \epsilon \int_{-a}^a \int_0^w \mathbf{E} \times \mathbf{H}^* \cdot \mathbf{e}_z dx dy = \frac{Z_0 I_w}{4k_0 h} \sum_{n=1}^{\infty} (P_{1n} I_{1n}^2 + P_{2n} I_{2n}^2 + P_{3n} I_{3n}^2), \quad (32)$$

where we have defined a current $I_w = a_1 h$ in amperes and h is a normalizing length, which for convenience may be chosen as $h = h_{out}$. The dimensionless quantities \bar{P}_j 's are

$$\begin{aligned} \bar{P}_{1n} &= \left[\alpha_{ns}^2 \bar{Z}_h^2 \left(\frac{d_1}{h} \psi_1^- + \frac{d_2}{h} \psi_2^- \right) + \alpha_{ns}^2 \bar{Z}_h^2 \left(\frac{\epsilon_r k_0^2}{\Gamma_1^2} \frac{d_1}{h} \psi_1^+ + \frac{k_0^2}{\Gamma_2^2} \frac{d_2}{h} \psi_2^+ \right) - 2\alpha_{ns}^2 \bar{Z}_h \bar{Z}_h \frac{\bar{Y}_2^* + \bar{Y}_1^*/\epsilon_r}{k_0 h} \right], \\ \bar{P}_{2n} &= \left[\alpha_{ns}^2 \bar{Z}_h^2 \left(\frac{d_1}{h} \psi_1^- + \frac{d_2}{h} \psi_2^- \right) + \alpha_{ns}^2 \bar{Z}_h^2 \left(\frac{\epsilon_r k_0^2}{\Gamma_1^2} \frac{d_1}{h} \psi_1^+ + \frac{k_0^2}{\Gamma_2^2} \frac{d_2}{h} \psi_2^+ \right) + 2\alpha_{ns}^2 \bar{Z}_h \bar{Z}_h \frac{\bar{Y}_2^* + \bar{Y}_1^*/\epsilon_r}{k_0 h} \right], \\ \bar{P}_{3n} &= 2\alpha_{ns} \alpha_{ns} \left[-\bar{Z}_h^2 \left(\frac{d_1}{h} \psi_1^- + \frac{d_2}{h} \psi_2^- \right) + \bar{Z}_h^2 \left(\frac{\epsilon_r k_0^2}{\Gamma_1^2} \frac{d_1}{h} \psi_1^+ + \frac{k_0^2}{\Gamma_2^2} \frac{d_2}{h} \psi_2^+ \right) \right] \\ &\quad + 2(\alpha_{ns}^2 - \alpha_{ns}^2) \bar{Z}_h \bar{Z}_h \frac{k_n}{\beta} \frac{\bar{Y}_2^* + \bar{Y}_1^*/\epsilon_r}{k_0 h}, \end{aligned} \quad (33)$$

where

$$\alpha_{ns} = k_n / (k_n^2 + \beta^2)^{1/2}, \quad \alpha_{ns} = \beta / (k_n^2 + \beta^2)^{1/2},$$

the normalized impedance $\bar{Z}_{e,h} = Z_{e,h} / Z_0$ and

$$\psi_j^\pm = \frac{\coth \Gamma_j d_j}{\Gamma_j d_j} \pm \frac{1}{\sinh^2 \Gamma_j d_j} \quad j = 1, 2. \quad (34)$$

The normalized Fourier transforms \bar{I}_{1n} and \bar{I}_{2n} of the strip current distributions are given in the Appendix [Eqs. (A1) and (A2)]. By integration of Eq. (22a) over the width of the strip, the total strip current in the z direction is found to be

$$\begin{aligned} I_z(z, t) &= \left(\int_{-a}^a J_z(x, d_2) dx \right) e^{i(\omega t - \beta z)} \\ &= \pi I_w \frac{w}{h} \left(\sum_{m=1}^M \bar{a}_m J_0(m\pi - \pi) \right) e^{i(\omega t - \beta z)}, \end{aligned}$$

where $\bar{a}_m = a_m / a_1$. The time averaged current I_{Lw}

$$\begin{aligned} I_{Lw}^2 &= \frac{1}{2} \text{Re}(I_z I_z^*) \\ &= \frac{1}{2} \pi^2 I_w^2 \frac{w^2}{h^2} \sum_{m=1}^M \sum_{m'=1}^M \bar{a}_m \bar{a}_{m'} J_0(m\pi - \pi) J_0(m'\pi - \pi). \end{aligned} \quad (35)$$

with

$$\begin{aligned} \bar{P}_{L1} &= \frac{a}{h} \sum_{n=1}^{\infty} \left(\frac{\Gamma_{n2}^2 (|T_{n2}^{(2)}|^2 + |T_{n2}^{(2)*}|^2)}{k_0^2 \sinh^2 \Gamma_{n2} d_2} + \frac{\Gamma_{n1}^2 (|T_{n1}^{(1)}|^2 + |T_{n1}^{(1)*}|^2)}{k_0^2 \sinh^2 \Gamma_{n1} d_1} \right), \\ \bar{P}_{L2} &= \frac{w}{h} \sum_{n=1}^{\infty} \sum_{p=1}^{\infty} \left(\frac{\Gamma_{n2} \Gamma_{p2}}{k_0^2} \coth(\Gamma_{n2} d_2) \coth(\Gamma_{p2} d_2) (T_{n2}^{(2)} T_{p2}^{(2)} + T_{n2}^{(2)*} T_{p2}^{(2)*}) \right. \\ &\quad \left. + \frac{\Gamma_{n1} \Gamma_{p1}}{k_0^2} \coth(\Gamma_{n1} d_1) \coth(\Gamma_{p1} d_1) (T_{n1}^{(1)} T_{p1}^{(1)} + T_{n1}^{(1)*} T_{p1}^{(1)*}) \right) \frac{\sin(k_p - k_n)w}{(k_p - k_n)w}, \end{aligned}$$

The characteristic impedance of the transmission line, Z_w , can be calculated by using Eqs. (31)–(34) in the relation

$$Z_w = P_w / I_{Lw}^2. \quad (36)$$

The attenuation constant for the propagating electromagnetic waves due to the finite conductivity of the metal enclosure and the strip line can be evaluated from $\alpha = P_L / 2P_w$, where P_L is the power loss per unit length along the z direction. P_L can be easily calculated from the standard definition

$$P_L = \int \mathbf{N} \cdot \hat{\mathbf{e}}_n dl, \quad (37)$$

where $\hat{\mathbf{e}}_n$ is a unit vector normal to the surface and \mathbf{N} is the Poynting vector

$$\mathbf{N} = \frac{1}{2} \text{Re}(\mathbf{E}_{tan} \times \mathbf{H}_{tan}^*) = \frac{1}{2\sigma\delta_s} |\mathbf{H}_{tan}|^2 \hat{\mathbf{e}}_n. \quad (38)$$

Here σ is the conductivity and $\delta_s = (2/\mu_0\omega\sigma)^{1/2}$ is the skin depth. After substituting in Eqs. (37) and (38) the appropriate values of \mathbf{H}_{tan} from Eq. (31) for the surfaces at $y = 0, d_2, h_{out}$ and at $x = \pm a$ and performing the line integrals, we get

$$P_L = \frac{Z_0 I_w^2}{4h} \left(\frac{2\epsilon_0\omega}{\sigma} \right)^{1/2} (\bar{P}_{L1} + \bar{P}_{L2} + \bar{P}_{L3} + \bar{P}_{L4} + \bar{P}_{L5}), \quad (39)$$

$$\begin{aligned}\bar{P}_{L3} &= \frac{\omega}{h} \sum_{n=1}^{\infty} \sum_{p=1}^{\infty} \left(\frac{\Gamma_{n2} \Gamma_{p2}}{k_0^2} \coth(\Gamma_{n2} d_2) \coth(\Gamma_{p2} d_2) (T_{n2}^{(2)} T_{p2}^{(2)} - T_{n2}^{(2)} T_{p2}^{(2)}) \right. \\ &\quad \left. + \frac{\Gamma_{n1} \Gamma_{p1}}{k_0^2} \coth(\Gamma_{n1} d_1) \coth(\Gamma_{p1} d_1) (T_{n1}^{(1)} T_{p1}^{(1)} - T_{n1}^{(1)} T_{p1}^{(1)}) \right) \frac{\sin(k_p + k_n) \omega}{(k_p + k_n) \omega}, \\ \bar{P}_{L4} &= \frac{d_2}{h} \sum_{n=1}^{\infty} \sum_{p=1}^{\infty} (-1)^{(n+p)} \left[\left(T_{n2} T_{p2} + \frac{\Gamma_{n2} \Gamma_{p2}}{k_0^2} T_{n2}^{(2)} T_{p2}^{(2)} \right) \left(\frac{\coth(\Gamma_{p2} d_2) + \coth(\Gamma_{n2} d_2)}{(\Gamma_{p2} + \Gamma_{n2}) d_2} \right) \right. \\ &\quad \left. + \left(T_{n2} T_{p2} - \frac{\Gamma_{n2} \Gamma_{p2}}{k_0^2} T_{n2}^{(2)} T_{p2}^{(2)} \right) \left(\frac{\coth(\Gamma_{p2} d_2) - \coth(\Gamma_{n2} d_2)}{(\Gamma_{p2} - \Gamma_{n2}) d_2} \right) \right], \\ \bar{P}_{L5} &= \frac{d_1}{h} \sum_{n=1}^{\infty} \sum_{p=1}^{\infty} (-1)^{(n+p)} \left[\left(T_{n1} T_{p1} + \frac{\Gamma_{n1} \Gamma_{p1}}{k_0^2} T_{n1}^{(1)} T_{p1}^{(1)} \right) \left(\frac{\coth(\Gamma_{p1} d_1) + \coth(\Gamma_{n1} d_1)}{(\Gamma_{p1} + \Gamma_{n1}) d_1} \right) \right. \\ &\quad \left. + \left(T_{n1} T_{p1} - \frac{\Gamma_{n1} \Gamma_{p1}}{k_0^2} T_{n1}^{(1)} T_{p1}^{(1)} \right) \left(\frac{\coth(\Gamma_{p1} d_1) - \coth(\Gamma_{n1} d_1)}{(\Gamma_{p1} - \Gamma_{n1}) d_1} \right) \right].\end{aligned}$$

The dependence of the quantities Γ_1 and Γ_2 on the spectral index n is explicitly shown in the equations above.

We also need the rf field components in the input circuit to calculate the premodulation of the beam. We assume that the input line is a completely symmetric coaxial-like microstrip transmission line. The field components in this case can be obtained from the results derived so far replacing ϵ, ϵ_0 and ϵ_0 by $\epsilon_{in} \epsilon_0$, and d_1 and d_2 by d_{in} in all the equations. For the completely symmetric microstrip line, the lowest-order mode is TEM in character, where $E_z = H_z = 0$ and E_x, E_y, H_x , and H_y are nonzero. Following the notation used for the output line, E_x and E_y for the input line may be written as

$$E_x(x, y) = \sum_{n=1}^{\infty} q_{nx} \sin k_n x \times \begin{cases} \sinh \Gamma y, & -d_{in} < y < 0, \\ \sinh \Gamma(y + 2d_{in}), & -2d_{in} < y < -d_{in}, \end{cases} \quad (40)$$

$$E_y(x, y) = - \sum_{n=1}^{\infty} q_{ny} \cos k_n x \times \begin{cases} \cosh \Gamma y, & -d_{in} < y < 0, \\ \cosh \Gamma(y + 2d_{in}), & -2d_{in} < y < -d_{in}, \end{cases} \quad (41)$$

with similar expressions for B_x and B_y . To satisfy Maxwell's equations, it is required that $\Gamma = k_n$ and $q_{nx} = q_{ny}$. This leads to the dispersion relation $\beta = \sqrt{\epsilon_{in}} k_0$ for the TEM mode propagation in the input line. As in the case of the output line, q_{nx} and q_{ny} are determined by the strip current on the input line.

III. SMALL-SIGNAL THEORY

The dispersion relation derived in the preceding section is modified in the presence of an electron beam. Under the tenuous-beam approximation, we assume that the transverse variations of the fields determined by Γ , remain unchanged but that the propagation constant β can become complex. Within the framework of the linear theory, any quantity $\phi(x, y, z, t)$ is expanded into

$$\phi(x, y, z, t) = \phi_0(x, y, z) + \phi_1(x, y) e^{i(\omega t - \beta z)}, \quad (42)$$

where ϕ_0 is the equilibrium value and ϕ_1 is the small perturbation. The starting point for the development in this section is Maxwell's equation

$$\left(\frac{\partial^2}{\partial x^2} + \frac{\partial^2}{\partial y^2} + \mu_0 \epsilon(y) \omega^2 - \beta^2 \right) E_1(x, y) = i \mu_0 \omega j_1(x, y), \quad (43)$$

where j_1 is the ac current density. Substitute the FTD representation [Eq. (31)] of the field components in Eq. (43), multiply both sides of the equation by $E_1^*(x, y)$, and integrate over the cross section of the output transmission line. Then we obtain

$$\beta_0^2 - \beta^2 = \frac{2i\mu_0\omega}{Z_0^2 I_w^2 N_c} \int_{-\delta/2}^{\delta/2} \int_0^{d_1} j_1 \cdot E_1^* dx dy, \quad (44)$$

where the normalization constant N_c is given by

$$\begin{aligned}N_c &= \frac{2}{Z_0^2 I_w^2} \int_{-\delta}^{\delta} \int_0^{d_{out}} E_1(x, y) \cdot E_1^*(x, y) dx dy \\ &= \sum_{n=1}^{\infty} \left\{ \frac{ad_1}{h^2} \frac{1}{\sinh^2 \Gamma_1 d_1} \left[\frac{k_0^2}{\Gamma_1^2} K_{ny}^2 \left(1 + \frac{\sinh 2\Gamma_1 d_1}{2\Gamma_1 d_1} \right) + (K_{nx}^2 + K_{nz}^2) \left(\frac{\sinh 2\Gamma_1 d_1}{2\Gamma_1 d_1} - 1 \right) \right] \right. \\ &\quad \left. + \frac{ad_2}{h^2} \frac{1}{\sinh^2 \Gamma_2 d_2} \left[\frac{k_0^2}{\Gamma_2^2} K_{ny}^2 \left(1 + \frac{\sinh 2\Gamma_2 d_2}{2\Gamma_2 d_2} \right) + (K_{nx}^2 + K_{nz}^2) \left(\frac{\sinh 2\Gamma_2 d_2}{2\Gamma_2 d_2} - 1 \right) \right] \right\}. \quad (45)\end{aligned}$$

The quantities K_{ax} , K_{ay} , and K_{az} are defined in the Appendix in Eqs. (A9)–(A11). The unperturbed propagation constant is denoted by

$$\beta_0 = (k_0^2 + \Gamma_1^2 - k_a^2)^{1/2} = (\epsilon_r k_0^2 + \Gamma_1^2 - k_a^2)^{1/2}.$$

The small-signal assumption leads to the beam-current density

$$j_1 = -n_1 e v_0 - n_0 e v_1, \quad (46)$$

where $n = n_0 + n_1$ is the electron density and $v = v_0 + v_1$ is the velocity of an electron. The mass and the magnitude of the charge of an electron are denoted by m and e , respectively. It is assumed that the screen electrode and the anode are held at the same dc potential (V) with respect to the cathode (emitter). In the equilibrium state, the electrons drift with a constant velocity $v_0 = v_0 \hat{e}_y$ in the region $0 < y < d_2$. If the electrons are accelerated from zero initial velocity, then $v_0 = (2eV/m)^{1/2}$ in the nonrelativistic limit. The current density j_1 is calculated from a fluid model using the linearized Lorentz equations and the current continuity equation

$$\begin{aligned} \frac{\partial v_{1x}}{\partial y} + i \frac{\omega}{v_0} v_{1x} &= -\frac{e(E_{1x} + v_0 B_{1x})}{m \gamma_0 v_0}, \quad \frac{\partial v_{1x}}{\partial y} + i \frac{\omega}{v_0} v_{1x} = -\frac{e(E_{1x} - v_0 B_{1x})}{m \gamma_0 v_0}, \\ \frac{\partial v_{1y}}{\partial y} + i \frac{\omega}{v_0} v_{1y} &= -\frac{e E_{1y}}{m \gamma_0^2 v_0}, \quad \frac{\partial n_1}{\partial y} + i \frac{\omega}{v_0} n_1 = -\frac{n_0}{v_0} \nabla \cdot v_1, \end{aligned} \quad (47)$$

where $\gamma_0 = (1 - v_0^2/c^2)^{-1/2}$ is the relativistic factor. The ac current density in the output circuit is the sum of two contributions $j_1 = j_1^* + j_1^{\dagger}$, where j_1^* arises from the premodulation of the beam in the input circuit and j_1^{\dagger} is the current modulation produced by the field in the output circuit. In the region $0 < y < d_2$, j_1^{\dagger} is the particular solution of the set of equations (47) obtained with the rf field components given by Eq. (31) and j_1^* is the homogeneous solution that satisfies the boundary condition $j_1^*(y=0)$, which is the premodulation current reaching that point.

The premodulation current in the input line ($-h_m < x < 0$) is obtained by solving equations (47) with the fields [Eqs. (40) and (41)] appropriate for the input line, and the solution should satisfy the Fowler–Nordheim¹⁵ relation at the emitter surface. For a given tip radius and a grid-cathode separation, the grid voltage has to be adjusted to produce the required dc field at the emission surface consistent with the Fowler–Nordheim relation. The dc electric field in the grid-cathode region is very nonuniform. In this region, Eq. (47) is solved approximately by replacing $v_0(z)$ with its average value v_{01} .

The solution of the set of first-order equations (47) is standard and after lengthy algebra, we obtain in the region $0 < y < d_2$ ($x, -\delta/2 < x < x, +\delta/2$, where $x, = 0, \pm \Delta, \pm 2\Delta, \dots$)

$$j_{1x}(x, y) = -\frac{n_0 e^2}{m \gamma_0} \sum_{n=1}^{\infty} \frac{\cos(k_n x)}{\omega^2 + \Gamma_2^2 v_0^2} \left(Q_{ax}^{(2)} (\omega \sinh \Gamma_2 y + i \Gamma_2 v_0 \cosh \Gamma_2 y) + \frac{v_0}{c} R_{ax}^{(2)} (\Gamma_2 v_0 \sinh \Gamma_2 y - i \omega \cosh \Gamma_2 y) \right), \quad (48)$$

$$\begin{aligned} j_{1x}(x, y) &= \frac{n_0 e^2}{m \gamma_0} \sum_{n=1}^{\infty} \frac{\sin(k_n x)}{\omega^2 + \Gamma_2^2 v_0^2} \left(Q_{ax}^{(2)} (\Gamma_2 v_0 \cosh \Gamma_2 y - i \omega \sinh \Gamma_2 y) + \frac{v_0}{c} R_{ax}^{(2)} (\omega \cosh \Gamma_2 y + i \Gamma_2 v_0 \sinh \Gamma_2 y) \right) \\ &+ \frac{n_0 e^2}{m \gamma_0} \sum_{n=1}^{\infty} \frac{\Gamma v_{01}}{\omega^2 + \Gamma^2 v_{01}^2} q_{ax} \sin(k_n x) e^{-\omega y/v_{01}}, \end{aligned} \quad (49)$$

$$\begin{aligned} j_{1y}(x, y) &= -\frac{n_0 e^2}{m \gamma_0} \sum_{n=1}^{\infty} \frac{\cos(k_n x)}{\omega^2 + \Gamma_2^2 v_0^2} Q_{ay}^{(2)} \left[(\Gamma_2 v_0 \sinh \Gamma_2 y - i \omega \cosh \Gamma_2 y) \right. \\ &+ \left. \frac{\beta_0^2 - \beta^2}{k_0^2 + \Gamma_1^2} \left[\left(1 - \frac{2v_0^2}{c^2} \frac{\omega^2 + \Gamma_2^2 v_0^2}{\omega^2 + \Gamma_2^2 v_0^2} \right) \Gamma_2 v_0 \sinh \Gamma_2 y + i \left(\frac{v_0^2}{c^2} + \frac{2\Gamma_2^2 v_0^2}{\omega^2 + \Gamma_2^2 v_0^2} \right) \omega \cosh \Gamma_2 y \right] \right] \\ &+ \sum_{n=1}^{\infty} \left[j_0(0) \left(2 + \frac{\zeta'}{E_0} \right) \frac{q_{ay}}{E_0} e^{-\omega y/v_{01}} + \frac{i n_0 e^2}{m \gamma_0^2} \frac{\omega q_{ay}}{\omega^2 + \Gamma^2 v_{01}^2} \right] \cos(k_n x) e^{-\omega y/v_{01}}, \end{aligned} \quad (50)$$

where $\zeta' = (u - E_0 \partial u / \partial E_0) \zeta$, $\zeta = \{ (2em\Phi^3/\hbar^2) \}^{1/2}$, and $j_0(0) = n_0 e v_0$ is the magnitude of the dc current density at $y = 0$. Here Φ (in volts) is the work function of the emitter, E_0 is the magnitude of the dc electric field at the emitter surface, and \hbar is Planck's constant divided by 2π . If we assume that the beam width increases from δ_e to δ during the transit in the nonuniform field between the emitter and the gate, then $j_0(0)$ is related to the Fowler–Nordheim current¹⁵ j_{FN} by the equation

$$j_0(0) = \frac{\delta_e}{\delta} j_{FN} \approx \frac{\delta_e}{\delta} \frac{e^2 E_0^2}{16\pi^2 \hbar^2 \Phi} e^{-\omega_s/E_0}, \quad (51)$$

where $u \approx 0.95 - eE_0/4\pi\epsilon_0\Phi^2$ and $s \approx 1.1$. For a cylindrically shaped wedge-emitter tip, $\delta_e \approx \pi R_0/2$, where R_0 is the radius of the tip.

The last terms in Eq. (49) and in Eq. (50) show the effect of premodulation of the beam in the input line. The amplification of the waves in the output circuit is caused mainly by these terms in the current density. All other terms in Eqs. (48)–(50)

represent self-modulation effects in the output line, and these terms make a small contribution to the growth of the waves. The factor $j_0(0)(2 + \xi'/E_0)(1/E_0) = \partial j_{0x}/\partial E_0$ appearing in the last term of Eq. (50) is proportional to the transconductance usually defined for a triode element. The output power in a triode is calculated from this term only in the ac current density. E_{1z} is negligible in the dominant mode of the microstrip line, and consequently j_{1z} is very small compared to j_{1y} and j_{1x} . The perturbed dispersion relation may be obtained by substituting Eq. (31) and Eqs. (48)–(50) in Eq. (44). We also set $q_{ny} = Q_{ny}^{(2)}$ assuming that $E_y(x, 0+) = E_y(x, 0-)$ for $x, -\delta/2 < x < x, +\delta/2$. Thus the complex propagation constant is given by

$$\beta_0^2 - \beta^2 = \frac{\nu}{2\gamma_0 h^2 N_{c1}} \sum_{n=1}^{\infty} \sum_{p=1}^{\infty} \left(\frac{\omega^2}{\omega^2 + \Gamma_{n2}^2 v_0^2} (g_{np}^{(1)} G_{np}^+ + g_{np}^{(2)} G_{np}^-) + \frac{\omega^2}{\omega^2 + \Gamma_{p2}^2 v_0^2} (g_{np}^{(3)} g_{np}^+ - g_{np}^{(4)} G_{np}^-) \right), \quad (52)$$

where $\nu = N_E n_0 e^2 d_2 \delta / \epsilon_0 m c^2 = N_0 e^2 / \epsilon_0 m c^2$ ($N_0 = n_0 d_2 \delta$ is the number of electrons per unit length in the axial direction) and

$$\begin{aligned} N_{c1} &= N_c + \frac{\nu}{2\gamma_0} \sum_{n=1}^{\infty} \sum_{p=1}^{\infty} \frac{\omega^2}{\omega^2 + \Gamma_{n2}^2 v_0^2} \frac{k_0^2}{\Gamma_{n2} \Gamma_{p2}} \frac{1}{(k_n^2 + \beta_0^2) h^2} G_{np}^+ K_{ny} K_{py} \\ &\quad \times \left[\left(\frac{v_0^2}{c^2} + \frac{2\Gamma_{n2}^2 v_0^2}{\omega^2 + \Gamma_{n2}^2 v_0^2} \right) \psi_{np}^- - i \frac{v_0 \chi_{np}^+}{\omega d_2} \frac{\omega^2 - \Gamma_{n2}^2 v_0^2 - 2\omega^2 v_0^2 / c^2}{\omega^2 + \Gamma_{n2}^2 v_0^2} \right], \\ g_{np}^{(1)} &= \frac{k_0^2}{\Gamma_{n2} \Gamma_{p2}} \left(\psi_{np}^- + i \frac{v_0 \chi_{np}^+}{\omega d_2} \right) K_{ny} K_{py} + \left(\psi_{np}^- + i \frac{v_0 \chi_{np}^-}{\omega d_2} \right) K_{n2} K_{p2} - \left(\frac{\Gamma_{n2}^2 v_0^2}{\omega^2} \psi_{np}^- - i \frac{v_0 \chi_{np}^-}{\omega d_2} \right) K_{p2} T_{n2}^{(2)}, \\ g_{np}^{(2)} &= \left(\psi_{np}^- + i \frac{v_0 \chi_{np}^+}{\omega d_2} \right) K_{n2} K_{p2} - \left(\frac{\Gamma_{n2}^2 v_0^2}{\omega^2} \psi_{np}^- - i \frac{v_0 \chi_{np}^-}{\omega d_2} \right) T_{n2}^{(2)} K_{p2}, \\ g_{np}^{(3)} &= \left[\frac{\gamma_0 m v_0^2}{e E_0 d_2} \left(2 + \frac{0.95 \xi}{E_0} \right) \cosh \Gamma_{n2} d_{in} \left(\frac{\cosh \Gamma_{p2} d_2 - e^{-\omega d_2 / v_0}}{\sinh \Gamma_{p2} d_2} - i \frac{\Gamma_{p2} v_0}{\omega} \right) e^{-\omega d_{in} / v_0} \right. \\ &\quad \left. + \frac{\omega v_0 / d_2}{\gamma_0^2 (\omega^2 + \Gamma_{n2}^2 v_0^2)} \left(\frac{\Gamma_{p2} v_0}{\omega} + i \coth \Gamma_{p2} d_2 - i \frac{e^{-\omega d_2 / v_0}}{\sinh \Gamma_{p2} d_2} \right) \right] \frac{2k_0^2 K_{ny} K_{py} e^{-\omega d_2 / v_0}}{\Gamma_{n2} \Gamma_{p2} \sinh \Gamma_{n2} d_2}, \\ g_{np}^{(4)} &= \left[\left(1 - i \frac{\Gamma_{p2} v_0}{\omega} \coth \Gamma_{p2} d_2 \right) e^{-\omega d_2 / v_0} + i \frac{\Gamma_{p2} v_0}{\omega} \frac{1}{\sinh \Gamma_{p2} d_2} \right] \frac{2v_0}{\omega d_2} \frac{\omega^2 K_{ny} K_{p2}}{\omega^2 + \Gamma_{n2}^2 v_0^2} \frac{\Gamma_{n2} v_0 / c}{\Gamma_{n2} \sinh \Gamma_{n2} d_2}, \\ G_{np}^{\pm} &= \frac{1}{N_E} \left(\frac{\sin [N_E (k_n - k_p) \Delta / 2]}{\sin [(k_n - k_p) \Delta / 2]} \frac{\sin [(k_n - k_p) \delta / 2]}{(k_n - k_p) \delta / 2} \pm \frac{\sin [N_E (k_n + k_p) \Delta / 2]}{\sin [(k_n + k_p) \Delta / 2]} \frac{\sin [(k_n + k_p) \delta / 2]}{(k_n + k_p) \delta / 2} \right), \\ \psi_{np}^- &= \frac{2}{(\Gamma_{n2}^2 - \Gamma_{p2}^2) d_2^2} (\Gamma_{n2} d_2 \coth \Gamma_{n2} d_2 - \Gamma_{p2} d_2 \coth \Gamma_{p2} d_2), \\ \psi_{np}^+ &= \frac{2}{(\Gamma_{n2}^2 - \Gamma_{p2}^2) d_2^2} (\Gamma_{n2} d_2 \coth \Gamma_{p2} d_2 - \Gamma_{p2} \coth \Gamma_{n2} d_2), \\ \chi_{np}^- &= \frac{2\Gamma_{n2}}{\Gamma_{n2}^2 - \Gamma_{p2}^2} \left(\Gamma_{n2} + \Gamma_{p2} \frac{1 - \cosh \Gamma_{n2} d_2 \cosh \Gamma_{p2} d_2}{\sinh \Gamma_{n2} d_2 \sinh \Gamma_{p2} d_2} \right), \\ \chi_{np}^+ &= \frac{2\Gamma_{n2}}{\Gamma_{p2}^2 - \Gamma_{n2}^2} \left(\Gamma_{p2} + \Gamma_{n2} \frac{1 - \cosh \Gamma_{n2} d_2 \cosh \Gamma_{p2} d_2}{\sinh \Gamma_{n2} d_2 \sinh \Gamma_{p2} d_2} \right). \end{aligned}$$

The quantities K_{np} and $T_{np}^{(2)}$ are given by Eqs. (A9)–(A14) in the Appendix. The dielectric response of the beam to the wave fields modifies the phase velocity of the transmission line modes to $v_{ph} = \omega / \text{Re } \beta$ and the growth (or decay) of the wave in decibels per unit length is $8.686 \text{ Im } \beta$. In our convention, $\text{Im } \beta > 0$ signifies growth and attenuation occurs if $\text{Im } \beta < 0$. The complex propagation constant is numerically calculated from Eq. (52) in the next section. A random-phase approximation may be made in Eq. (52) to

retain only the terms with $n = p$ noting the limiting values of the following geometrical factors:

$$\chi_{nn}^{\pm} = 1, \quad \psi_{nn}^{\pm} = \psi_2^{\pm}$$

[see Eq. (34)], and

$$G_{nn}^{\pm} = 1 \pm \frac{1}{N_E} \frac{\sin(N_E k_n \Delta)}{\sin(k_n \Delta)} \frac{\sin(k_n \delta)}{k_n \delta}.$$

Numerical calculations show that the results from the ran-

dom-phase approximation differ by only 10% from those obtained with Eq. (52).

IV. RESULTS AND DISCUSSION

The numerical calculations are performed by truncating the infinite sum in the spectral decomposition [Eqs. (6) and (7)] to a finite number n_{\max} and the number of basis functions for the expansion of the x and z components of the strip current [Eqs. (22) and (23)] are truncated to N and M , respectively. Calculations show that the choice $n_{\max} = 100$, $M = 3$, and $N = 3$ yields an accuracy of 1 part in 10^4 . The propagation characteristics of a "cold" microstrip transmission line have been widely investigated and an excellent review on this subject can be found in the monograph by Gupta, Garg, and Bahl.¹⁶ A large number of parameters such as d_1 , d_2 , a , w , ϵ , etc., are required to characterize the operation of the circuit. Here we discuss the effects of the variation of a few of these parameters of concern to us. Figure 2 shows the impedance Z_o and the circuit losses (due to the finite conductivity of the metal electrodes and walls) in the output circuit as functions of its total height ($h_{\text{out}} = d_1 + d_2$) for a fixed ratio of d_1/d_2 . For a given h , the electric field in the air region ($0 < y < d_2$) is enhanced as d_1/d_2 is increased. We choose a value $d_1/d_2 = 2.5$ so that the field in the interaction region is high without d_2 being too small. The loss and the impedance are calculated at $f = 20$ GHz for two values of ϵ_r to show the dependence of these quantities on the dielectric constant. Other parameters are listed in the figure. The loss increases very rapidly for $h_{\text{out}} < 50 \mu\text{m}$ and is ~ 1 dB/cm or less for $h_{\text{out}} > 70 \mu\text{m}$. The loss also increases with the increase of ϵ_r . The impedance of the circuit, however, increases with increase in h_{out} and decrease in ϵ_r . For h_{out} in the range of 70 to $100 \mu\text{m}$, the impedance is approximately 55Ω with $\epsilon_r = 4.0$ and 36Ω with $\epsilon_r = 9.0$. The phase velocity, of course, decreases with the

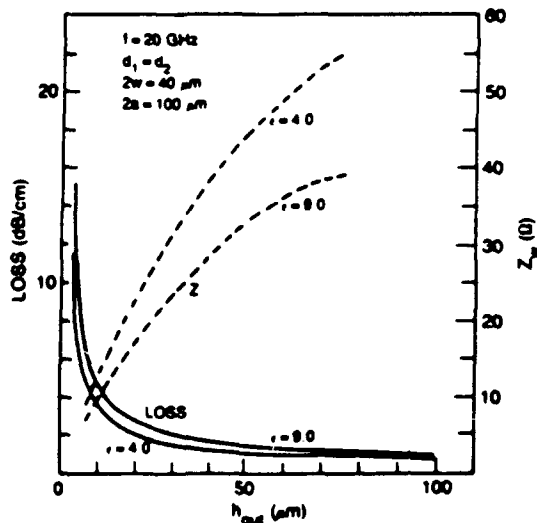


FIG. 2. Loss in the circuit (solid curve) and the characteristic impedance Z_o (dashed curve) of the output transmission line are plotted as functions of $h_{\text{out}} = d_1 + d_2$ for fixed $d_1/d_2 = 2.5$ for two different values of $\epsilon_r = 4.0$ and 9.0 at a frequency $f = 20$ GHz. The other circuit parameters are $2a = 100 \mu\text{m}$, $2w = 40 \mu\text{m}$, $d_1 = 50 \mu\text{m}$, and $d_2 = 20 \mu\text{m}$.

increase in ϵ_r . The two dielectric constants are chosen to cover the range of values of the commonly used insulators such as SiO_2 and Al_2O_3 . The impedance and the circuit loss for the input transmission line are plotted in Fig. 3 as functions of $h_{\text{in}} = 2d_{\text{in}}$ for $\epsilon_{\text{in}} = 2.17$ and 4.13 . A smaller ϵ is required for this circuit to match the phase velocities in the input and the output lines. In the input line, the loss shows a steep rise for $h_{\text{in}} < 12 \mu\text{m}$. It is clear from Figs. 2 and 3 that the transmission lines should be designed with $h_{\text{out}} > 60 \mu\text{m}$ and $d_{\text{in}} > 8 \mu\text{m}$ to maintain low losses and reasonable impedance. As a consequence, the fabrication of a wedge emitter taller than $8 \mu\text{m}$ is necessary.

Since the amplification of the waves depends on a large number of beam and circuit parameters, the calculations will be performed keeping some of the parameters constant. We choose $2w = 40 \mu\text{m}$, $\delta = 4 \mu\text{m}$, $2a = 100 \mu\text{m}$, and $2d_{\text{in}} = 16 \mu\text{m}$. Gain will be calculated for different beam voltage and current, two values of $\epsilon_r = 4.0$ and 9.0 , and two values of $d_1 = 50$ and $75 \mu\text{m}$ with $d_1/d_2 = 2.5$. Hence $d_2 = 20$ and $30 \mu\text{m}$, respectively, for the two cases. The dielectric constant ϵ_{in} is chosen to be equal to the effective dielectric constant of the output line for phase matching. The dispersion characteristics of the output circuit are shown in Fig. 4 where the phase velocity v_{ph} and the impedance Z_o are plotted as functions of frequency for two different values of h . The transmission line is essentially dispersionless in the frequency range 20–100 GHz of interest. The impedance Z_o increases and the phase velocity v_{ph} decreases as the height of the circuit is increased.

The variation of the linear growth rate of the waves with frequency is shown in Fig. 5 for different beam voltages V . As mentioned before, we assume that the screen and the anode are at the same dc potential. In this figure we use $\epsilon_r = 4$, and the total dc beam current from the emitter array consisting of seven wedges ($N_E = 7$) is $I_0 = 15$ A/cm along the wedges. The separation between the wedges is $\Delta = 5 \mu\text{m}$. If the width of the beam at the emitter surface is taken as $\delta_e \approx \pi R_0/2$, the current density at the emitter tip becomes 1.36×10^6 A/cm² for $R_0 = 100 \text{ \AA}$. According to the Fowler–

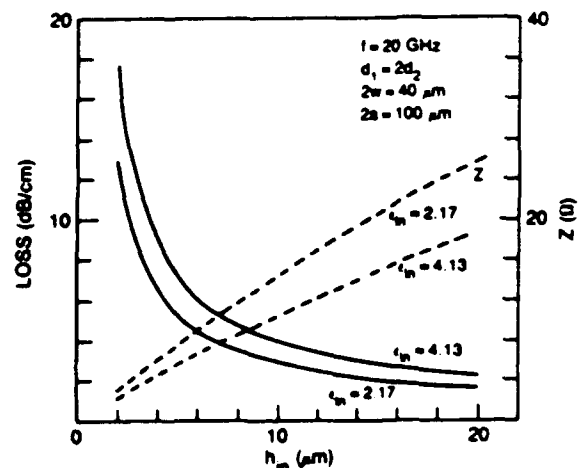


FIG. 3. Loss in the circuit (solid curve) and the impedance (dashed curve) of the input transmission line are shown as functions of $h_{\text{in}} = 2d_{\text{in}}$ at 20 GHz with $\epsilon_{\text{in}} = 2.17$ and 4.13 and $2a = 100 \mu\text{m}$, $2w = 40 \mu\text{m}$.

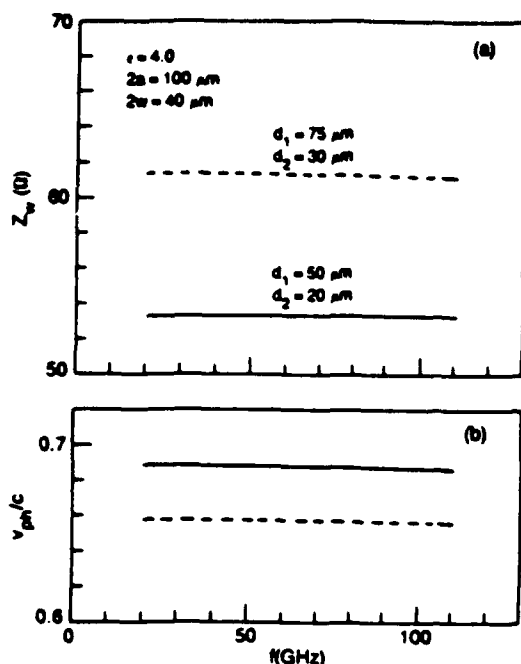


FIG. 4. (a) Impedance and (b) phase velocity v_{ph} of the output circuit as functions of frequency for two values of h_{em} . Solid curves are $d_1 = 50 \mu\text{m}$ and $d_2 = 20 \mu\text{m}$, and dashed curves are $d_1 = 75 \mu\text{m}$ and $d_2 = 30 \mu\text{m}$. Also, $2a = 100 \mu\text{m}$, $2w = 40 \mu\text{m}$, and $\epsilon_r = 4.0$.

Nordheim relation, $E_0 = 5.22 \times 10^7$ V/cm for emission from a metal (e.g., Mo) with work function $\Phi = 4.35$ V while $E_0 = 1.55 \times 10^7$ for $\Phi = 2.0$ V as in LaB_6 . The transit time of the electrons increases as the voltage is lowered and the gain increases with a corresponding decrease in the bandwidth. The maximum electronic gain drops from 8.6 dB/cm at $V = 60$ V to 4.7 dB/cm at $V = 100$ V while the frequency of maximum gain increases from 50 to 80 GHz. The attenuation of the waves due to the finite conductivity is also shown in the figure. A net gain in the range 3–7 dB/cm is expected

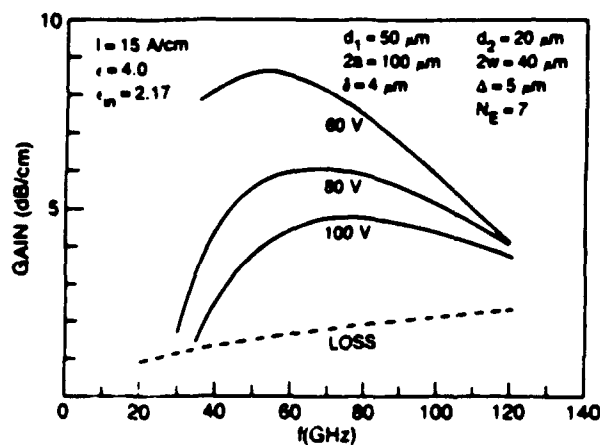


FIG. 5. Electronic gain vs frequency for different beam voltage with total $I_0 = 15 \text{ A/cm}$ in an array with $N_E = 7$, $\epsilon_r = 4.0$, and $\epsilon_{in} = 2.17$. The circuit parameters are $d_1 = 50 \mu\text{m}$, $d_2 = 20 \mu\text{m}$, $2a = 100 \mu\text{m}$, $2w = 40 \mu\text{m}$, $\delta = 5 \mu\text{m}$, $\Delta = 6 \mu\text{m}$, and $h_{em} = 16 \mu\text{m}$. The circuit loss in the output circuit is shown by the dashed curve.

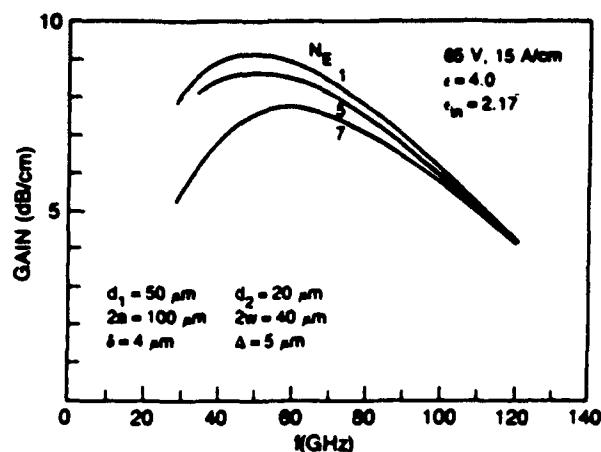


FIG. 6. Electronic gain vs frequency at different values of N_E for a total current $I_0 = 15 \text{ A/cm}$ and $V = 60 \text{ V}$. All other parameters are the same as in Fig. 5.

as V is decreased from 100 to 60 V. The effective dielectric constant, $\epsilon_{eff} = (c/v_{ph})^2$, of the output circuit is approximately 2.17 and this value has to be chosen for ϵ_{in} . The calculations were done with a grid voltage V_g of 50 V. If we assume that the field gradient near the tip is the same as would be obtained from an isolated cylinder, then the distance, R_g , of the grid from the center of curvature of the tip can be estimated from the relation $V_g = E_0 R_0 \ln(R_g/R_0)$. Thus $R_g \approx 0.026 \mu\text{m}$ when $\Phi = 4.35$ V but increases to $R_g \approx 0.28 \mu\text{m}$ with a reduction of the work function to about 2.0 V.

The variation of the growth rate with the number of edges N_E in the emitter array placed along the x axis is shown in Fig. 6. The total emitted current in each case is taken as 15 A/cm along the edge and the separation between the edges is $5 \mu\text{m}$. The growth rate and the bandwidth decrease by a small amount as N_E is increased. The rf field intensity slowly decreases towards the edges of the strip line, and the current density in the high-field region increases as N_E decreases, leading to higher gain. In the following calculations we choose $N_E = 7$, which provides high gain with a reasonable current in each wedge.

We next show the dependence of the gain on other circuit parameters. The gain in a circuit with a higher dielectric constant of $\epsilon_r = 9$ is shown in Fig. 7 where all other parameters are the same as in Fig. 5. The effective dielectric constant of the output line in this case is $\epsilon_{eff} = 4.17$ and ϵ_{in} is adjusted accordingly. The gain decreases with increase in ϵ_r , since the field in the interaction region is weakened. The frequency band of amplification is shifted upwards. The maximum electronic gain at $V = 60 \text{ V}$ is 5.6 dB/cm at a frequency of 60 GHz. The circuit also becomes more lossy at higher values of the dielectric constant. Therefore the net gain in the circuit is much higher at lower values of the dielectric constant.

The variation of the gain with the beam current is displayed in Fig. 8 where the gain is plotted as a function of frequency for different values of the beam current I_0 . The beam voltage is 60 V, $\epsilon_r = 4.0$, $\epsilon_{in} = 2.17$, $d_1 = 50 \mu\text{m}$, and $d_2 = 20 \mu\text{m}$. The maximum electronic gain increases rapidly

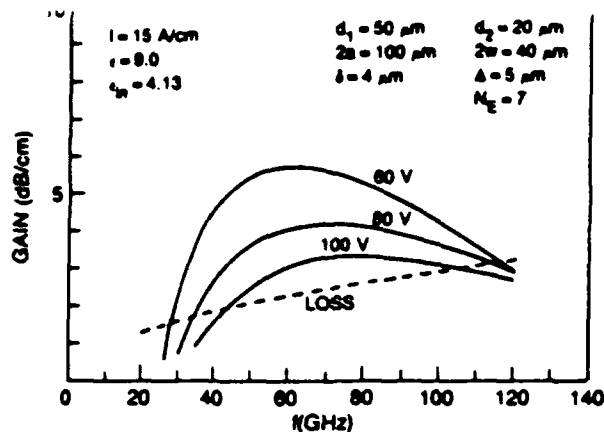


FIG. 7. Electronic gain vs frequency for the same parameters as in Fig. 5 except $\epsilon_r = 9.0$ and $\epsilon_m = 4.13$. The dashed curve shows the circuit loss as a function of frequency.

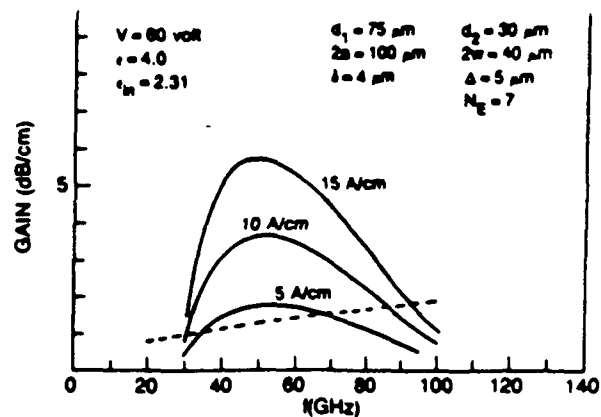


FIG. 9. Electronic gain as a function of frequency with all parameters the same as in Fig. 8 except $d_1 = 75 \mu\text{m}$, $d_2 = 30 \mu\text{m}$, and $\epsilon_m = 2.31$. The dashed curve shows the loss as a function of frequency.

from about 2.5 dB/cm at $I_0 = 5 \text{ A/cm}$ to 8.6 dB/cm at $I_0 = 15 \text{ A/cm}$. The frequency of maximum gain slowly shifts downward from 65 to 55 GHz. The grid voltage changed from 46 to 50 V as the current at each wedge increased from 0.71 to 2.14 A/cm. In Fig. 9, we show the gain for a circuit with increased height. The parameters for this figure are the same as in Fig. 8 except $d_1 = 75 \mu\text{m}$, $d_2 = 30 \mu\text{m}$, and $\epsilon_m = 2.31$ to match ϵ_m of the output circuit. The gain decreases as d_1 and d_2 increases due to the reduction of the field amplitude in the circuit. The loss also decreases slightly with the increase in height of the circuit, but the net gain is lower than that shown in Fig. 9. We have also investigated the variation of the net gain with the width $2a$ of the circuit. For the parameters used in Fig. 9, the optimum gain occurs for $2a \approx 100 \mu\text{m}$.

The theory is developed for the configuration in which the screen and the anode are connected to have equal dc potential and a single microstrip is embedded in the circuit. These are not inherent limitations of the theory. The theory

can be easily be extended to include multiple microstrips in the circuit and a dc potential between the screen electrode and the anode.

V. CONCLUSIONS

A linear theory has been developed to calculate the small-signal gain in a distributed amplifier composed of two microstriplike transmission lines with a wedge-shaped field emitter embedded in the input circuit. The theory will be useful to determine the beam and the circuit parameters required for the successful operation of the device. The calculations show that the height of the circuit should lie in the range 80–120 μm . The loss due to the finite conductivity of the metal walls and the strip line in the circuit is very high if the height is less than 80 μm , whereas the electronic gain is low if the height increases above 120 μm . Similar considerations also show that the relative dielectric constant ϵ_r of the substrate in the output line should be less than 9.0; otherwise, the electronic gain is poor and the circuit loss is high. The calculated gain decreases as the voltage is increased or the current is decreased. A net gain of about 7 dB/cm is predicted with the proper choice of the circuit and the beam parameters. This gain is obtained with a voltage of 60 V and a total current of 15 A/cm in a seven-wedge emitter array. The rapid improvement in the fabrication of FEAs and the performance shown by current Spindt¹⁷ cathodes suggest the possibility of achieving such a high current. The current in each wedge may be further reduced by using multiple sets of a strip-line-emitter array combination instead of a single set. Initial calculations show that the gain decreases only by a small amount in a circuit with multiple strip lines. The frequency for the maximum gain can be varied between 50 and 80 GHz by tuning the anode voltage from 60 to 100 V. The small-signal instantaneous bandwidth at the 3-dB level is approximately 60%. The heating of the anode due to the impact of the electron beam is a problem for this type of device. Improved cooling techniques and the use of a dielectric substrate with high thermal conductivity will be required to alleviate this problem.

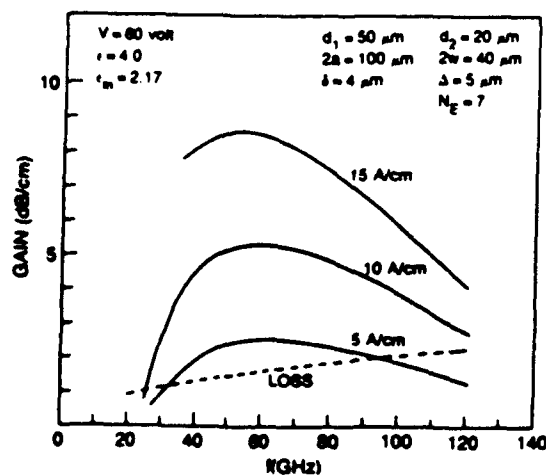


FIG. 8. Electronic gain vs frequency for different beam current at a beam voltage of 60 V. All other parameters are the same as in Fig. 5. The dashed curve is loss as a function of frequency.

ACKNOWLEDGMENTS

This work was supported in part by the Office of Naval Research and in part by the Office of Naval Technology. The authors would like to thank Dr. R. K. Parker, Dr. S. Smith, Dr. S. Ahn, Dr. E. G. Zaidman, and Dr. C. M. Krowne for helpful discussions.

APPENDIX

For convenience, the coefficients $Q_{np}^{(i)}$ and $R_{np}^{(i)}$ in Eq. (31) for the field components in the output transmission line are derived in this appendix. The index $i = 1, 2$ refers to the dielectric and the air regions, respectively. From Eqs. (25) and (27), the Fourier transforms of the strip current for the even modes are found to be

$$\bar{J}_e(k_n) = \frac{I_w}{h} \bar{I}_{ez} = \frac{I_w}{h} \sum_{m=1}^{\infty} \bar{a}_m \frac{\pi w}{2a} [J_0(k_n w - m\pi + \pi) + J_0(k_n w + m\pi - \pi)], \quad (A1)$$

$$i\bar{J}_e(k_n) = \frac{I_w}{h} \bar{I}_{ez} = \frac{I_w}{h} \sum_{m=1}^{\infty} \bar{c}_m \frac{\pi w}{2a} [J_0(k_n w - m\pi) - J_0(k_n w + m\pi)], \quad (A2)$$

where \bar{I}_{ez} and \bar{I}_{ez} are the normalized strip current distributions, $I_w = a_1 h$, $\bar{a}_m = a_m/a_1$, and $\bar{c}_m = c_m/a_1$. As mentioned before in Eq. (32), the normalizing length h may conveniently be taken as $h = h_{out}$. The potentials ψ' and ψ'' may be written in terms of the normalized current distributions from Eqs. (6), (7), (13), (A1), and (A2). On substituting the resulting expressions of ψ' and ψ'' in Eqs. (6) and (7), we get

$$Q_{ez}^{(i)} = \frac{Z_0 I_w}{h} \frac{1}{\sinh \Gamma_i d_i} K_{ez}^{(i)}, \quad (A3)$$

$$Q_{ey}^{(i)} = (-1)^i \frac{Z_0 I_w}{h} \frac{k_0/\Gamma_i}{\sinh \Gamma_i d_i} K_{ey}^{(i)}, \quad (A4)$$

$$Q_{ez}^{(i)} = -\frac{Z_0 I_w}{h} \frac{1}{\sinh \Gamma_i d_i} K_{ez}^{(i)}, \quad (A5)$$

and

$$R_{ez}^{(i)} = (-1)^i \frac{Z_0 I_w}{h} \frac{c\Gamma_i}{\omega \sinh \Gamma_i d_i} T_{ez}^{(i)}, \quad (A6)$$

$$R_{ey}^{(i)} = \frac{Z_0 I_w}{h} \frac{1}{\sinh \Gamma_i d_i} T_{ey}^{(i)}, \quad (A7)$$

$$R_{ez}^{(i)} = (-1)^i \frac{Z_0 I_w}{h} \frac{c\Gamma_i}{\omega \sinh \Gamma_i d_i} T_{ez}^{(i)}, \quad (A8)$$

where

$$K_{ez} = \bar{Z}_{ez}(k_n) \bar{I}_{ez} + \bar{Z}_{ez}(k_n) \bar{I}_{ez}, \quad (A9)$$

$$K_{ey}(k_n) = \frac{\Gamma_i^2 + k_0^2}{k_n^2 + \beta^2} \bar{Z}_e \frac{\beta \bar{I}_{ez} + k_n \bar{I}_{ez}}{k_0}, \quad (A10)$$

$$K_{ez} = \bar{Z}_{ez}(k_n) \bar{I}_{ez} + \bar{Z}_{ez}(k_n) \bar{I}_{ez}, \quad (A11)$$

and

$$T_{ez}^{(i)} = \hat{Z}_{ez}^{(i)}(k_n) \bar{I}_{ez} + \hat{Z}_{ez}^{(i)}(k_n) \bar{I}_{ez}, \quad (A12)$$

$$T_{ey}(k_n) = \frac{\Gamma_i^2 + k_0^2}{k_n^2 + \beta^2} \bar{Z}_e \frac{k_n \bar{I}_{ez} - \beta \bar{I}_{ez}}{k_0}, \quad (A13)$$

$$T_{ez}^{(i)} = \hat{Z}_{ez}^{(i)}(k_n) \bar{I}_{ez} + \hat{Z}_{ez}^{(i)}(k_n) \bar{I}_{ez}. \quad (A14)$$

In Eqs. (A9)–(A14), we define the following normalized impedances: $\bar{Z}_{ez,h} = Z_{ez,h}/Z_0$ where $Z_{ez,h}$ are given in Eqs. (14a) and (14b) and $\bar{Z}_{ey} = Z_{ey}/Z_0$ with Z_{ey} from Eqs. (10)–(21). Also,

$$\hat{Z}_{ez}^{(i)}(k_n) = \left(k_n^2 \frac{k_{0i}^2}{\Gamma_i^2} \bar{Z}_e + \beta^2 \bar{Z}_h \right) / (k_n^2 + \beta^2), \quad (A15)$$

$$\hat{Z}_{ez}^{(i)}(k_n) = \left(\beta^2 \frac{k_{0i}^2}{\Gamma_i^2} \bar{Z}_e + k_n^2 \bar{Z}_h \right) / (k_n^2 + \beta^2), \quad (A16)$$

$$\hat{Z}_{ez}^{(i)}(k_n) = \hat{Z}_{ez}^{(i)}(k_n) = \beta k_n \left(\frac{k_{0i}^2}{\Gamma_i^2} \bar{Z}_e - \bar{Z}_h \right) / (k_n^2 + \beta^2), \quad (A17)$$

where $k_{01} = \sqrt{\epsilon_r} k_0$ and $k_{02} = k_0$. Similar expressions hold for the odd modes except \bar{I}_{ez} and \bar{I}_{ez} are calculated from the following basis functions chosen for this symmetry:

$$\xi_{om}(x) = \frac{\sin[(m - \frac{1}{2})\pi x/w]}{[1 - (x/w)^2]^{1/2}}, \quad (A18)$$

$$\eta_{om}(x) = \frac{\cos[(m - \frac{1}{2})\pi x/w]}{[1 - (x/w)^2]^{1/2}}. \quad (A19)$$

The Fourier transforms of these functions are

$$\bar{\xi}_{om}(k_n) = \frac{\pi w}{2a} [J_0(k_n w - (m - \frac{1}{2})\pi) - J_0(k_n w + (m - \frac{1}{2})\pi)], \quad (A20)$$

$$\bar{\eta}_{om}(k_n) = \frac{\pi w}{2a} [J_0(k_n w - (m - \frac{1}{2})\pi) + J_0(k_n w + (m - \frac{1}{2})\pi)]. \quad (A21)$$

Thus for odd modes

$$\bar{I}_{ez} = \sum_{m=1}^{\infty} \bar{c}_m \bar{\eta}_{om}(k_n), \quad \bar{I}_{ez} = \sum_{m=1}^{\infty} \bar{a}_m \bar{\xi}_{om}(k_n). \quad (A22)$$

As mentioned before, $k_n = n\pi/a$ for the odd modes, and the field components are obtained from Eq. (30) replacing $\cos(k_n x)$ with $\sin(k_n x)$ and $\sin(k_n x)$ with $-\cos(k_n x)$.

¹ K. Shoulder, *Advances in Computer*, edited by F. L. Alt (Academic, New York, 1961), pp. 135–293.

² R. F. Green, H. F. Gray, and G. J. Campisi, *IEDM Tech. Dig.* 1985, 172.

³ H. F. Gray, G. J. Campisi, and R. F. Green, *IEDM Tech. Dig.* 1986, 776.

⁴ C. A. Spindt, I. Brodie, L. Humphrey, and E. R. Westerberg, *J. Appl. Phys.* 47, 5248 (1976).

⁵ H. F. Gray, in *Proceedings of the IEEE MTT Symposium on Engineering Microwave Technology*, 1989, edited by J. Pierro, p. 22.

⁶ C. A. Spindt, C. Holland, and R. D. Stowell, *Appl. Surf. Sci.* 16, 268 (1983).

⁷ W. A. Anderson, in *Proceedings of the 2nd International Conference on Vacuum Microelectronics*, edited by R. Turner (IOP, Bristol, U. K., 1989), pp. 217–221.

⁸ H. F. Gray and R. F. Greene, Navy Case No. 70.437, March 1987 (Patent submitted).

- ⁹E. L. Ginzton, W. R. Hewlett, J. H. Jasberg, and J. D. Noe, *Proc. IRE* **36**, 956 (1948)
- ¹⁰H. G. Kosmahl, *IEEE Trans. Electron Devices* **ED-36**, 2728 (1989)
- ¹¹I. Brodie and C. A. Spindt, *Appl. Surf. Sci.* **2**, 179 (1979)
- ¹²T. Itoh and R. Mitra, *IEEE Trans. Microwave Theory Tech.* **MTT-22**, 896 (1974)
- ¹³R. Harrington, *Time Harmonic Electromagnetic Fields* (McGraw-Hill, New York, 1961), pp. 158-163.
- ¹⁴C. M. Krowne, A. A. Mostafa, and K. A. Zaki, *IEEE Trans. Microwave Theory Tech.* **MTT-36**, 1850 (1988)
- ¹⁵R. H. Fowler and L. W. Nordheim, *Proc. R. Soc. London Ser. A* **119**, 173 (1928)
- ¹⁶K. C. Gupta, R. Garg, and J. J. Bahl, *Microstrip Lines and Slotlines* (Artech, Norwood, MA, 1979), pp. 41-101
- ¹⁷C. A. Spindt (private communication).

APPENDIX XV

Electromagnetic Properties of a Field Emission Distributed Amplifier

by

P.M. Phillips, S.T. Smith, and H.F. Gray

Electromagnetic properties of a field emission distributed amplifier

Purobi M. Phillips*, Sidney T. Smith and Henry F. Gray.

Naval Research Laboratory, Washington D.C., U.S.A. * Science Applications International Corporation, McLean, Va, U.S.A.

ABSTRACT: The basic idea and the design parameters of a fully Distributed Field Emitter Amplifier are described.

1. INTRODUCTION

The performance of many microwave and millimeter-wave devices can be improved significantly by using field-emitting arrays. The high-current density and low transit time of field emitter arrays make possible high-frequency, high-power triodes, better density-modulated klystrones, small and wide-band TWT's and wide-band, high-frequency, high-power, compact (magnet-less), radiation-hard distributed amplifiers. The idea of Distributed Amplification was first proposed by W. S. Percival in 1936¹ and the name "Distributed Amplifier" was due to Ginzton *et al.*² The present paper describes a continuously distributed amplifier using field emitters.

2. CONFIGURATION AND BASIC MECHANISM

The FEDA (Field Emission Distributed Amplifier) consists of two physically bonded, but electrically independent, parallel microstrip-like transmission lines, one lying parallel to and directly over, the other (figure 1).

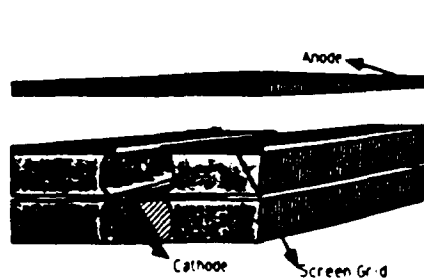


Figure 1. Field Emitter Distributed Amplifier

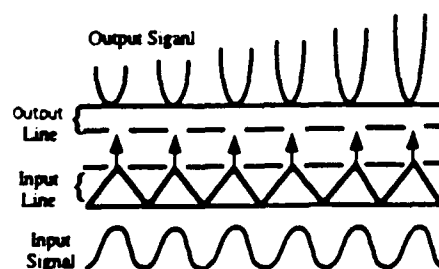


Figure 2. Basic Mechanism of a FEDA

The input line contains the wedge-like field emitters. A "grounded-grid" or "grounded-gate" triode distributed amplifier is not practical because the input signal must drive the cathode against the anode current, and this results in an excessive load ($1/g_m$) in the input circuit, where g_m is the transconductance. Therefore, a tetrode type of distributed amplifier design has been chosen. The screen-grid is AC grounded to shield the input from capacitively coupling to the output and thus avoid feedback oscillation. The width of the first grid is chosen to be smaller than the screen grid to minimize the capacitance between this and the cathode base.

The applied input signal produces a travelling-wave density-modulated signal that induces a similar amplified density-modulated signal on the output transmission line. Figure 2 demonstrates this mechanism in an exaggerated form. The input signal is applied at one end of the input transmission line, and the other end is terminated in a non-reflecting resistive load. The output transmission line serves as the electron collector and/or anode. This type of FEDA requires that the phase velocity in the input and the output transmission lines to be identical because the induced output travelling wave must be phase-matched with the input travelling wave. This phase-match is proposed to achieve by dielectrically loading the output line. Thus, the output line contains the anode, a layer of dielectric and a grounded heat sink. The output and input transmission lines were modelled macroscopically to determine the degree of match. The next section contains the results of these modellings as well as other design parameters.

3. CIRCUIT DESIGN

Four different output line structures were tested. Figure 3 shows the different dimensions of these structures. The dielectric used was styCAST with a dielectric constant of 9 to simulate BeO or Al_2O_3 .

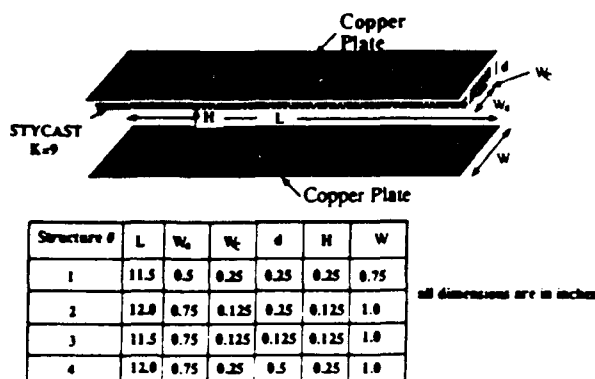


Figure 3. Modelling of Output Line.

Figure 4 (a, b, c, and d) shows the results of these preliminary tests along with theoretical values. The theoretical points were obtained from a 2-dimensional code for microstrip line that uses the full-wave analysis. It is to be noted that in a microstrip line the lowest order mode is the TM_0 which has a zero frequency cutoff. The next higher order mode is a TE mode with a divergence frequency f_c , below which it cannot exist (figure 5³). This divergence frequency f_{cTE} is calculated for all four structures tested and it can be seen that the agreement between the experimental points and the theory is quite good below this frequency as the theory does not include this TE mode. It is concluded from these tests that it is possible to slow the phase velocity in the output line sufficiently by dielectric loading to match the phase velocity of the dielectrically-loaded input line.

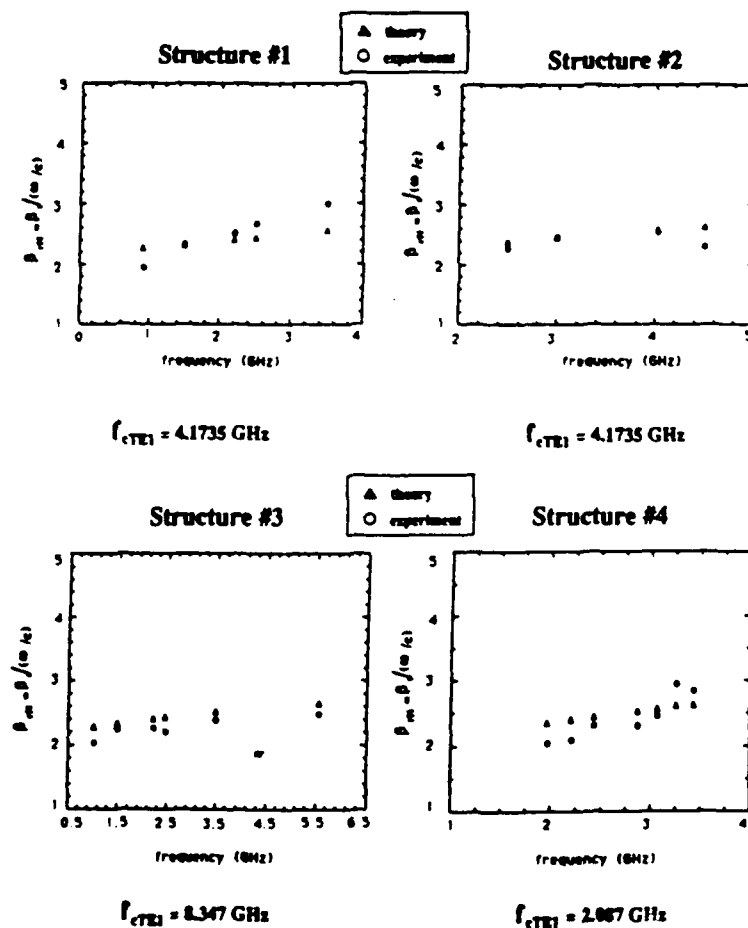


Figure 4. Dispersion in Output Line.

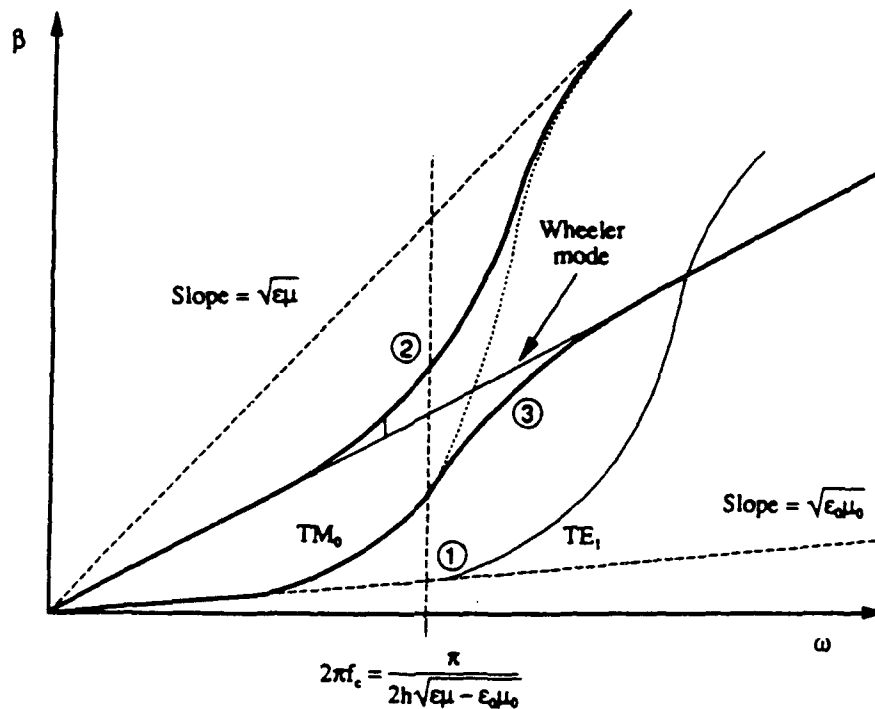


Figure 5. $\beta - \omega$ Diagram for Microstrip
and Surface Wave Modes.

To find the parametric dependence of output-line-impedance and the phase velocity, the simple, quasi-static microstrip line theory was used. Figure 6 shows the results. The critical parameter for the loss in the output line appears to be the air(vacuum) gap. The loss increases as the gap decreases, so the loss was calculated for a small value of this gap ($5\mu\text{m}$) as a function of frequency by again treating the output line as a microstrip line (Figure 7).

The input line was modelled (Figure 8a) to find the dispersion characteristics. Figure 8b shows the result. In order to find the loss in the input line it was treated as a covered stripline, and Figure 9 shows that for high frequency operation (50 GHz) and with all other parameters fixed, the cathode has to be tall ($8\mu\text{m}$).

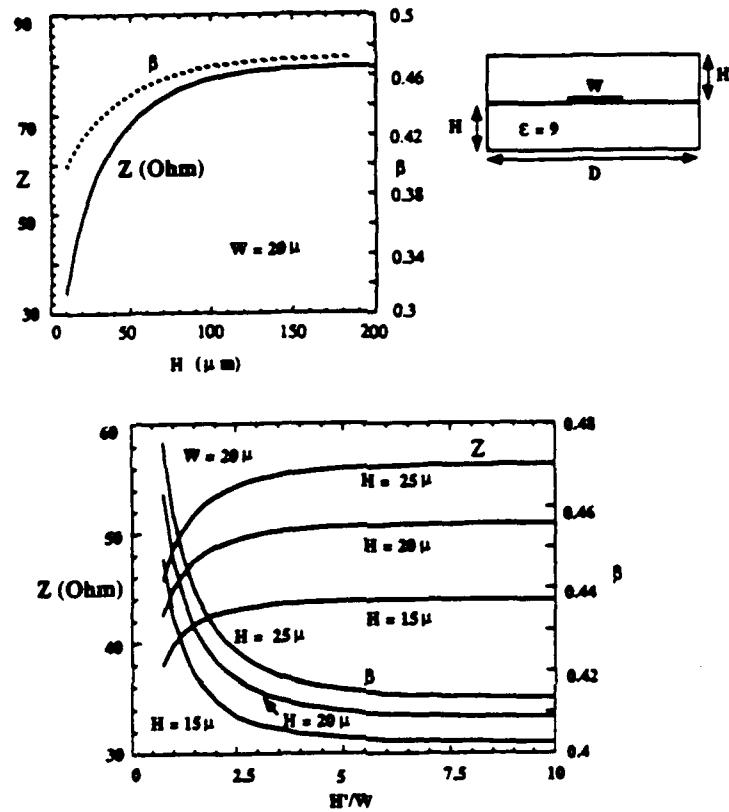


Figure 6. Scaling of Output Line.

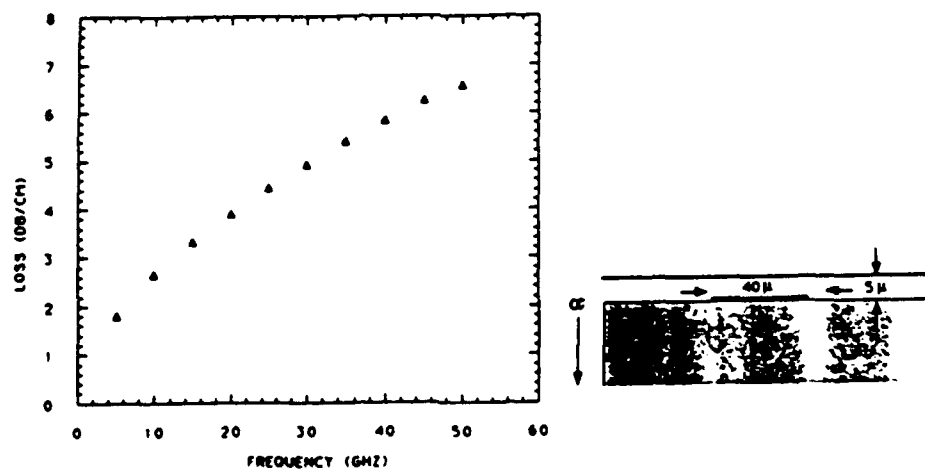


Figure 7. Output Line Loss.

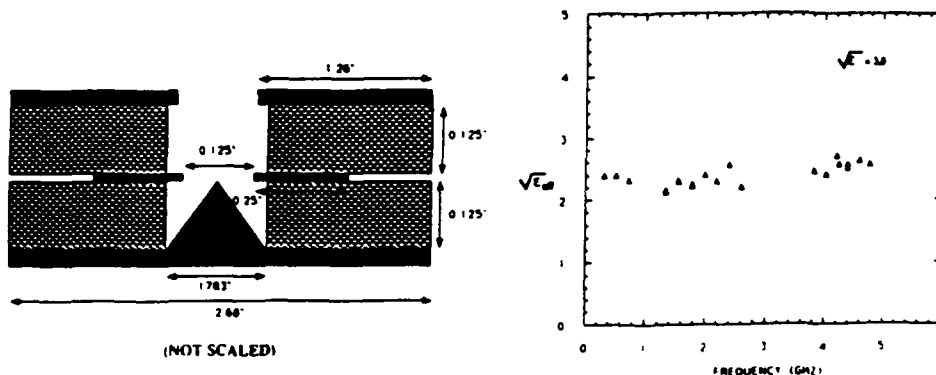


Figure 8. Modelling of Input Line.

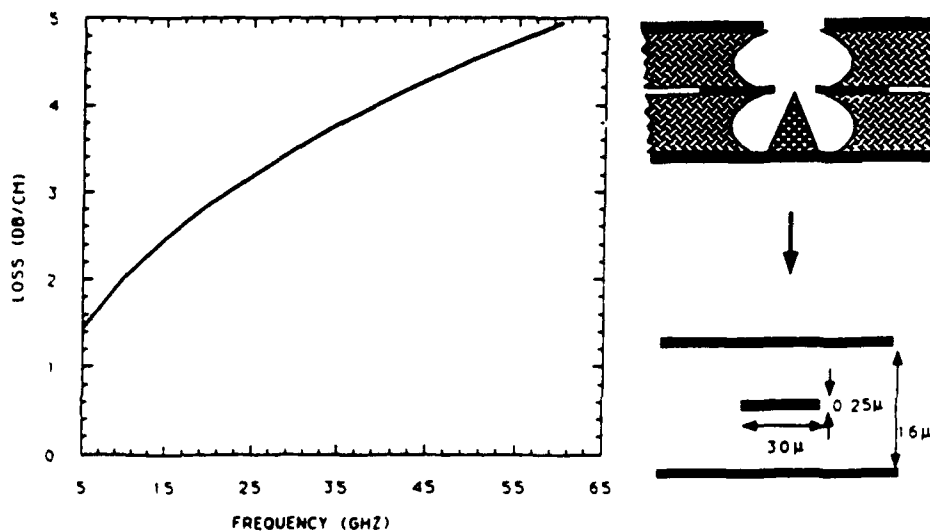


Figure 9. Input Line Loss.

4. ACKNOWLEDGEMENT

The authors gratefully acknowledge constant helpful discussions and stimulating interactions with their co-workers Robert E. Neidert and Achintya K. Ganguly.

5. REFERENCES

1. W. S. Percival, *British Patent Specification* No. 460, 562, July, 1936.
2. E. L. Ginzton *et al.* *Proceedings of the I. R. E.*, pp. 956-969, August, 1948.
3. C. P. Hartwig *et al.* *G-MTT Int. Microwave Symp. Digest, Detroit, Michigan*, pp. 110-116, 1968.

APPENDIX XVI

Field Emission Triodes

by

R.E. Neidert, P.M. Phillips, S.T. Smith, and C.A. Spindt

Field Emission Triodes

Robert E. Neidert, *Member, IEEE*, Purobi M. Phillips, Sidney T. Smith, and Charles A. Spindt

Abstract—Triode RF amplifier structures using field emission cathodes have been investigated from both the theoretical and experimental viewpoint. This paper describes the physically large experimental structure which has been used and the theoretical calculations on that structure. The agreement between theory and experiment for both dc and ac measurements is shown to be very good. The theoretical circuit modeling has produced information which will be useful in future work for higher frequency operation. RF voltage gain of about 11 dB has been measured at low frequencies, dropping to 0 dB at 200 kHz, with a cathode which had only $38\text{-}\mu\text{S}$ transconductance. Model calculations on the large structure used show operation to about 2 MHz with more typical transconductance of $380\text{-}\mu\text{S}$ for a 1000-cone field emission cathode.

I. INTRODUCTION

THREE-terminal amplifying devices have had only two landmark improvements since early vacuum tubes—the mid 1950's when germanium and silicon bipolar transistors were developed, creating an order of magnitude of high-frequency extension and the mid 1970's when gallium arsenide FET's were developed creating another order of magnitude of high-frequency extension to 50 GHz, and leading into the current era of planar monolithic microwave and millimeter-wave circuits on gallium arsenide. Currently, new material systems and shorter gates have pushed FET technology upward by another factor of two in frequency. It is not expected, however, that much further extension with useful power and gain will be achieved, e.g., the best solid-state three-terminal device available today for power and efficiency is the pseudomorphic HEMT [1]. The approximate simultaneous upper limits for these devices include frequency of 94 GHz, output power of 50 mW, and efficiency of 20%, with 3 dB of power gain.

Two major technology areas contribute now to the prospect of another order of magnitude of high-frequency extension for three-terminal amplifying devices. These two areas are submicrometer fabrication capability and the field-emission array fabrication demonstrated by several different groups of researchers including SRI International [2]. The advantages of a field-emitter-based three-terminal device also include radiation hardness and small transit time. The intrinsic high-frequency limit of any multiterminal device depends on several different factors including transit time, interelectrode capacitances, transconductance, and input and output resistances. By innovative device design the solid-state community has been able to approach the transit-time limit for both bipolar and field-effect transistors. That is, they have been able to create extremely small and in-

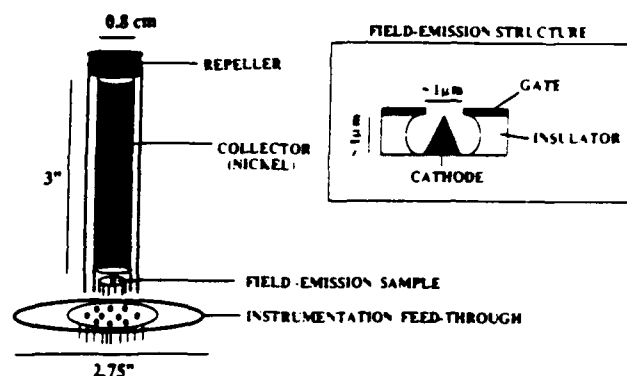


Fig. 1. Test arrangement of NRL field-emission triode using SRI cathode

genious structures which prevent the other parameters from setting the upper frequency limit. These improvements came slowly in bipolar transistors, taking about ten years to get from the audio range to the lower microwave range; they came faster for FET's. Assuming that such structures can also be found for field-emission-based microtriodes, it is fair at this time to use transit time as the eventual frequency limitation for them. As mentioned before, for a field-emission-based microtriode, the transit-time-limited frequency is quite high. For an accelerating voltage (V) of 300 V, if the electron traveling distance (L) is $20\text{ }\mu\text{m}$, and if the initial velocity is assumed to be zero then the transit time (where the transit angle is 2π) $\tau = 2L / (5.93 \times 10^5 \sqrt{V})$ seconds and the transit-time-limited frequency, given by $f = 1/\tau$, is around 260 GHz. Therefore, there is no need to be concerned about transit-time effects until performance to at least a tenth of the transit-time-limited frequency, 26 GHz or so, is reached. At this high-frequency range, an optimization has to be found between the device size and its power dissipation capability.

In this paper we discuss the results from testing a number of NRL-constructed field-emitter-based triodes using SRI-made cathodes. The results include $I-V$ characteristics, transconductance, and voltage gain as a function of frequency. A circuit-type model is also developed using the measured values of intrinsic and parasitic elements, that agrees very well with the experimental results.

II. NRL FIELD EMISSION TRIODE STRUCTURES

Fig. 1 shows the basic structure of the current experimental form of the NRL field emission triode using SRI cathodes. The field emission cathode, made at SRI (so far we have used only 1000-cone arrays) is $250\text{ }\mu\text{m}$ in diameter and sits on top of a standard TO5 header. The header is spot-welded to a 10-pin Varian instrumentation feedthrough, along with a cylindrical nickel anode of 0.8 cm in diameter, 3 in in length, above the anode is a metallic repeller. The anode is cleaned by vacuum firing at 10^{-7} T pressure and it is about 3 to 4 mm away from

Manuscript received July 26, 1990; revised October 1, 1990. This work was partially funded by the Office of Naval Technology. The review of this paper was arranged by Associate Editor I. Brodie.

R. E. Neidert and S. T. Smith are with the Naval Research Laboratory, Washington, DC 20375-5000.

P. M. Phillips is with Science Applications International Corporation, McLean, VA 22102.

C. A. Spindt is with SRI International, Menlo Park, CA 94025.

IEEE Log Number 9041422.

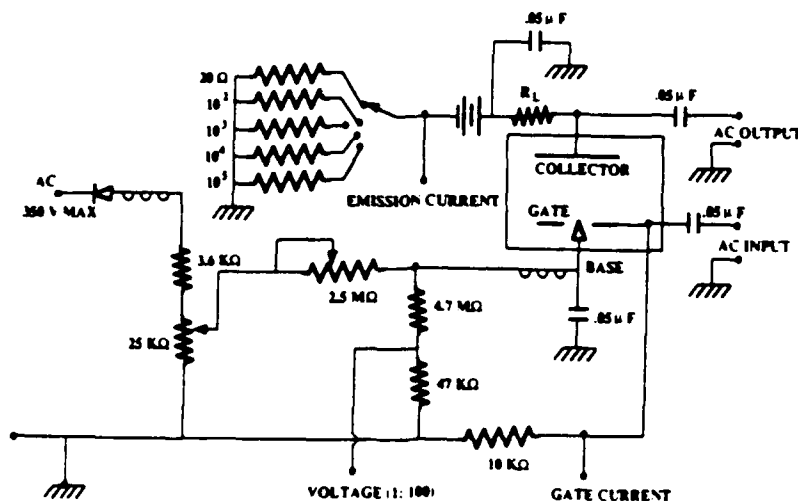


Fig. 2. Schematic of the test circuit.

the SRI cathode-gate structure. The cathode-gate assembly is a standard SRI sample made out of molybdenum pyramidal tips, about $1 \mu\text{m}$ high. The gate radius is about $0.55 \mu\text{m}$ and the tips are $6 \mu\text{m}$ apart. The whole assembly is put into a vacuum chamber and baked at about 450°C and the ultimate pressure that we routinely achieve is about $1-2 \times 10^{-9}$ T. Fig. 2 gives the circuit assembly used to test this structure. This circuit is a slightly modified form of the one used at SRI.

III. CURRENT-VOLTAGE CHARACTERISTICS

Fig. 3(a) and (b) shows the characteristics of collector current as a function of collector voltage for a number of gate voltages, commonly known as plate or anode characteristics. Fig. 4 shows the mutual or transfer characteristics which give the variation of collector current as a function of gate voltage with collector voltage as a parameter. The data for these figures were obtained from a sample designated as 405A. The name is given by SRI which indicates the process number and the dimensions of the arrays. All these graphs show strong resemblance to pentode characteristics, which we believe is due to the remoteness of the anode (4 mm away from the gate-cathode assembly). Data for Fig. 3(b) were obtained for two relatively low voltages to ensure that the total current does not exceed $10 \mu\text{A}$, so that when collector current approaches zero, the gate can absorb the total emission current without damage. This figure indicates that the anode has to be about 15 V above the gate (in our circuit, the gate is at zero potential) in order to collect all the emitted electrons. Fig. 5 shows the current-voltage characteristics of the sample 392A. Both 405A and 392A consist of 1000 cones, $6 \mu\text{m}$ apart, but 392A, after one day's operation, started to show an appreciable amount of gate current. In Fig. 5 we plotted this gate current as well as collector current as functions of gate voltage. The three sets of data points were taken on three different days. The circles correspond to the first day, the stars and the triangles correspond to the second and the third days, respectively. This figure indicates how the performance deteriorated with time. It also shows the mostly linear nature of gate current which indicates that it is probably leakage current. Although one of the points in the first day's set of data points suggests some kind of field emission (Fowler-Nordheim) characteristics of the gate current, we think that this isolated data point probably is not reliable enough to draw any conclusion, since the other two sets of data points do not show this trend at

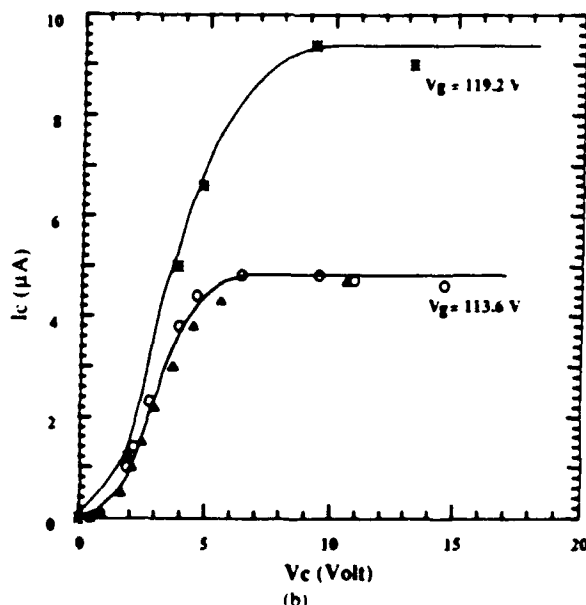
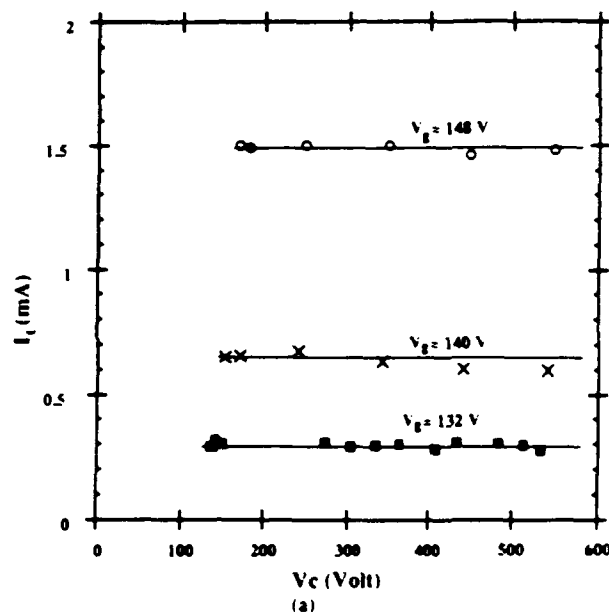


Fig. 3. (a) Plate characteristics of the sample 405A. (b) Plate characteristics of the sample 405A.

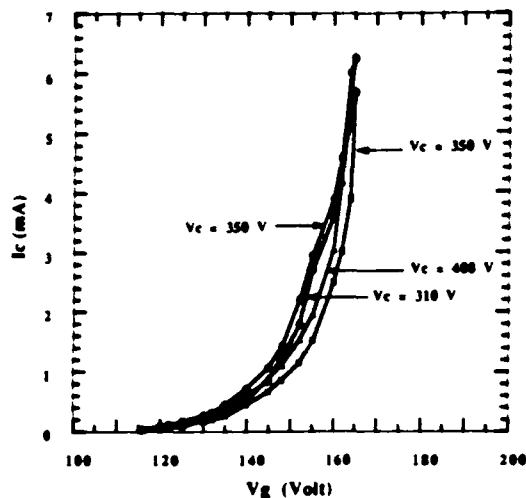
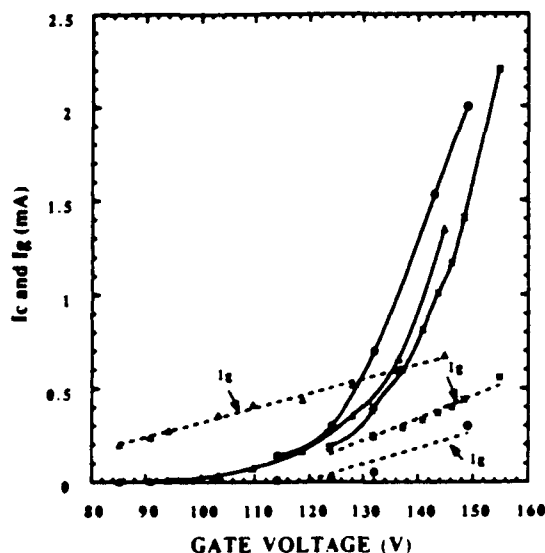


Fig. 4. Transfer characteristics of the sample 405A.

Fig. 5. I - V characteristics of the sample 392A for $V_c = 300$ V

all. From Figs. 3 and 4 we can also conclude that the output resistance (or plate resistance) of the device

$$R_p = \left. \frac{\partial V_r}{\partial I_r} \right|_{I_c}$$

is nearly infinite.

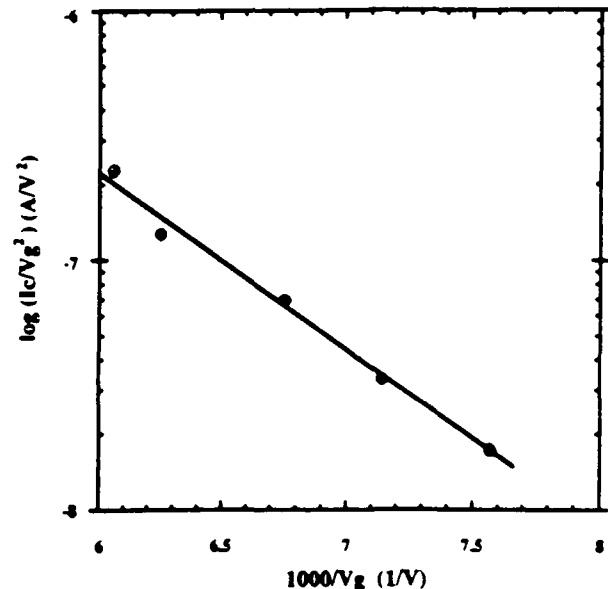
Fig. 6(a) and (b) presents Fowler-Nordheim plots for the two samples cited above. For the sample 392A, the three lines again correspond to data taken on three different days. The circles are first day's data, the stars and the triangles are second and third days', respectively. Using the Fowler-Nordheim equation

$$I_c = aV_g^2 e^{b10^4/V_g}$$

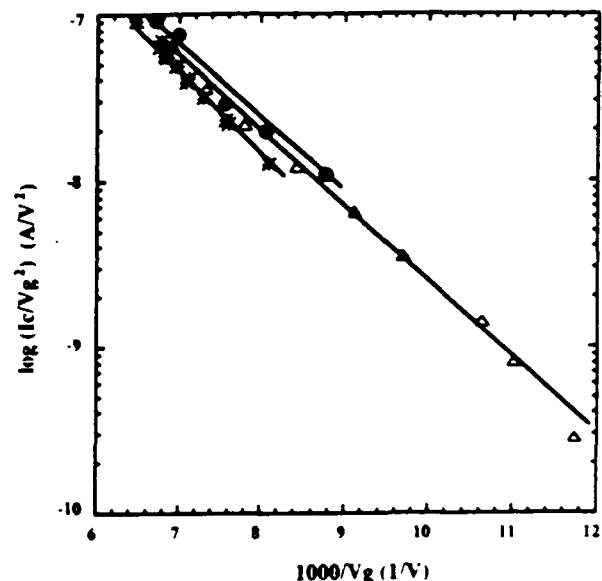
the two constants a and b can be found from these graphs and hence the transconductance

$$g_m = \left. \frac{\partial I_c}{\partial V_g} \right|_{V_c} = ae^{b10^4/V_g} (2V_g - 10^4 b)$$

can be obtained too. Transconductance can also be measured by



(a)



(b)

Fig. 6. (a) Fowler-Nordheim plot of the sample 405A (b) Fowler-Nordheim plot of the sample 392A

using the discrete data points of I_c and V_g . Fig. 7 is a plot of transconductance of the sample 405A. The solid curves are least square error fit to the measured data points. The data for $V_c = 162.5$ V (triangles) were taken after two voltage dips in the power line. At the same time the capacitor of the ion pump started to fail. As a result of these disturbances the cathode started to die too. We believe these are the reasons for the scattered data points on the top part of the graph. Although we presented these scattered data along with other more uniform sets, the scattered data do not represent the normal behavior of the cathodes.

IV. VOLTAGE GAIN VERSUS FREQUENCY

Voltage gain of an amplifier can be defined as the ratio of output voltage across a load resistor to the voltage across the input terminals. Fig. 2 shows the schematic of the test circuit

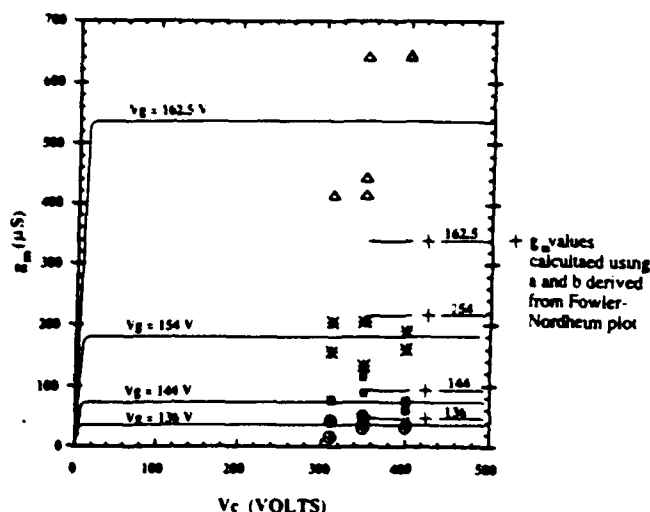


Fig. 7. Measured transconductance of the sample 405A using $g_m = \Delta I_c / \Delta V_g$.

The signal to be amplified was applied to the gate and the amplified signal was measured across a 100-k Ω resistor R_L at the output. A few 0.05- μ F capacitors were used for the purpose of dc blocking and ac bypassing. The interelectrode capacitances were measured before and after the sample was installed in the chamber to establish which capacitances were truly "interelectrode" and which ones were directly to ground. Fig. 8 shows the circuit used in the program Touchstone to find a theoretical model for the measured voltage gain for the sample 392A. The resistance and the inductance of a single cone, made of molybdenum, and having the approximate shape shown in Fig. 1, were calculated to be 1 Ω and 0.1 pH, in series with each other. For the 1000-cone array the cones are all in parallel and the resistance and the inductance values are then of the order of 0.001 Ω and 0.0001 pH, respectively. These values of resistance and inductance from cathode to ground are not significant at low frequencies such as a few megahertz; they are shown here for completeness. For this particular sample the voltage gain dropped to 0 dB at 220 kHz, but this is the sample where the gate-leakage current was appreciable and the collector current was unusually low. Hence the transconductance at $V_g = 140$ V was only 38 μ S. Fig. 9 shows the experimental points of voltage gain as a function of frequency along with the theoretical curve obtained from Touchstone. Fig. 9 also shows a dashed curve which was obtained from Touchstone using the same interelectrode capacitances and the same infinite output resistance R_p but the transconductance used was 380 μ S which is more typical of a good working cathode. For the dashed curve, the frequency at which the voltage gain dropped to 0 dB is about 2 MHz.

The frequency at which the voltage gain is 3 dB less than the low-frequency plateau gain can be related to the R and C values of a single RC network as follows: $|V_G(f)| = 0.707 = -3$ dB = magnitude of the voltage gain at frequency f , where $f = 1/(2\pi RC)$, provided the rolloff is being caused predominantly by a single RC network. Frequency f is in hertz, R is in ohms, and C is in farads. In the case presented here, because the input (the gate) was driven with a low-impedance source (50 Ω), the input capacitance to ground is not important and does not contribute at all to the gain rolloff. Therefore, for this case, the so-called figure of merit $f_T = g_m/(2\pi C_{\text{gate-cathode}})$ has no importance whatsoever. The frequency at which short-circuit current gain drops to unity [3] is called f_T , but power gain can exist to much higher frequency [4]. Reference [4] shows how f_{max} , the fre-

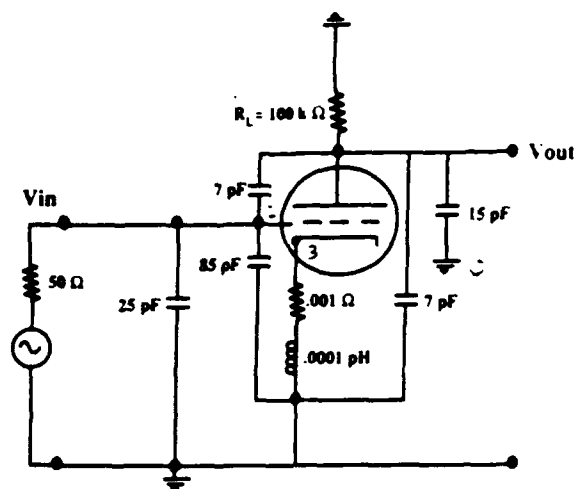


Fig. 8. Model used in Touchstone to find voltage gain versus frequency

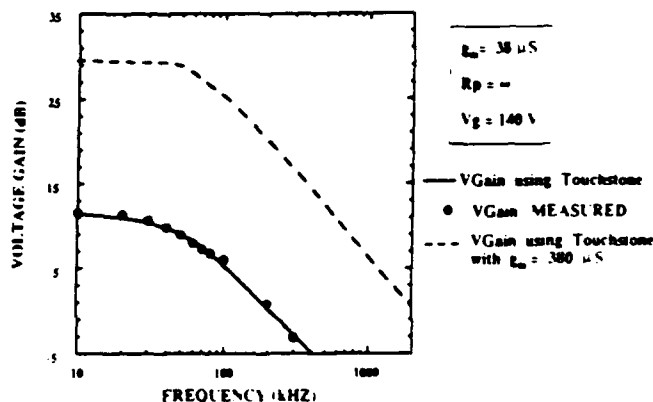


Fig. 9. Voltage gain versus frequency

quency at which the power gain drops to unity, is related to all of the equivalent circuit parameters in a more complicated manner. In our experiment, the voltage gain rolloff is being caused by the output network, consisting of the infinite output resistance of the tube driving the load resistance shunted by the total capacitance from anode to ground, where the near infinite ac output resistance is equal to the reciprocal of the near-zero slope of the I_c - V_c curve at the bias point (see Fig. 3). Indeed, for the example of Fig. 8, for $R_L = 100$ k Ω , and $C_{\text{anode-}g_{nd}} = 29$ pF, $|V_G(f)| = 0.707 = -3$ dB when $f = 1/(2\pi \times 100 \times 10^3 \Omega \times 29 \times 10^{-12} \text{ F}) = 55$ kHz. This agrees almost perfectly with the measured results (dots) given in Fig. 9. The 7 pF from anode to gate is included in the 29 pF because the much larger 110 pF from gate to ground effectively grounds it. The output rolloff frequency would be higher if the triode output resistance could be reduced. Notice also that the input rolloff frequency would be, for $R = 50$ Ω and $C = 110$ pF, $f_{in} = 1/(2\pi \times 50 \Omega \times 110 \times 10^{-12} \text{ F}) = 29$ MHz. From this it is obvious that the input circuit is not controlling the performance of the amplifier described here, but it also shows that the input circuit would limit at fairly low frequency even if the output circuit limitations were corrected.

V. DISCUSSION

The feasibility of an RF triode using an SRI field-emission cathode has been shown and both dc and ac measurements have

been made. The major significance of the work to date is in the development of the circuit model for a field-emission triode, which is not the same as that for a triode using space-charge-limited operation. The work presented here shows that all the significant circuit model parameters can be readily calculated or measured, and that the measured ac gain agrees well with that calculated from the circuit model. This means that if a microwave structure can be formulated whose circuit can be fairly accurately modeled, the modeled results can be trusted. This is the basis of our future work.

Preliminary calculations on future structures indicate that orders of magnitude increase in transconductance (more cones and/or more current per tip) can be used so long as the largest lateral dimension of the cathode does not exceed a quarter of a wavelength at the desired operating frequency, thereby preventing nonuniform RF field across the structure. At 10 GHz, for instance, a quarter wavelength in a material with dielectric constant 3.84 (SiO_2), such as might be used in part of the structure, is about 4000 μm . A square cathode about 3000 μm on a side could be used at 10 GHz and if cone spacing is 6 μm , then 250 000 cones could theoretically be used. The gate-to-cathode capacitance needs to be reduced; selective interconnect metallization to small metal circles above each cone, rather than full metal coverage of the gate, is one improvement fairly easy to make. All unnecessary metal and dielectric can be eliminated in future designs integrating device and circuit.

Reducing the triode output resistance increases the output rolloff frequency dramatically. Just changing it from near infinity down to 100 k Ω doubles the rolloff frequency for the circuit of Fig. 8; reducing it to 1 k Ω increases the rolloff frequency a thousand times. Placing the anode close enough to the cathode can create noninfinite output resistance by making the anode voltage have some effect on the anode current, remembering that the ac output resistance is the reciprocal of the anode I - V curve slope. This procedure will increase the capacitance between the anode and the gate but an optimum distance in this regard can be reached.

Further improvements might come from the addition of a separate RF input grid between anode and the one now used to dc bias the cones to field emission. With a separate RF grid, additional degrees of design freedom can be created, but more importantly, space-charge-limited operation may be possible. Triodes of this kind in space-charge-limited operation already operate to at least 3 GHz [5], and microtriodes could probably go to much higher frequency. It is not possible to extrapolate with certainty to millimeter-wave frequency operation, but there are reasonable steps to be taken now to reach the microwave range, and there will be new ideas to come.

REFERENCES

- [1] P. M. Smith *et al.*, "Microwave and mm-wave power amplification using pseudomorphic HEMTs," *Microwave J.*, pp. 71-86, May 1990.
- [2] C. A. Spindt *et al.*, "Physical properties of thin-film emission cathodes with molybdenum cones," *J. Appl. Phys.*, pp. 5248-5263, Dec 1976.
- [3] J. Millman and C. C. Halkias, *Electronic Devices and Circuits*. New York: McGraw-Hill, 1967, pp. 369-462.
- [4] C. M. Crowne and R. E. Neidert, "Examination of millimeter-wave frequency-gain behaviour of GaAs MESFETs," *Int. J. Electron.*, vol. 58, pp. 407-412, 1985.
- [5] A. S. Gilmour, *Microwave Tubes*. Dedham, MA: Artech House, 1986, p. 192.



Robert E. Neidert (S'56-M'70) received the B.E. (E.E.) degree in 1959 from Vanderbilt University, Nashville, TN, and has done graduate work at the University of Florida, St. Petersburg.

From 1959 to 1962 he was with the Sperry Microwave Electronics Company, Clearwater, FL, where he was engaged in the development of microwave components for radar systems. From 1962 to 1969 he served as senior design engineer and project leader at the General Electric Company, Communications Products Department, Lynchburg, VA, in the design and development of microwave components and solid-state sources for TV and multiplex telephone radio relay equipment. From 1969 to 1972 he was a principal engineer at Radiation Systems, Inc., McLean, VA, where his work was in antenna and antenna feed network design. Since 1972 he has been involved in research on microwave and millimeter-wave devices and circuits at the Naval Research Laboratory, Washington, DC. He has authored numerous papers in the fields of communications systems components, microwave integrated circuits, computer-aided microwave circuit design, bipolar and FET amplifier design, FET modeling, and millimeter-wave circuits.

Mr. Neidert is a member of Tau Beta Pi.



Purobi M. Phillips was born in India on April 19, 1961. She received the B.Sc. degree in physics from Presidency College, Calcutta, India, in 1983, and the A.M. and Ph.D. degrees in physics from Dartmouth College, Hanover, NH, in 1985 and 1987, respectively.

Since 1987 she has been a Research Scientist with Science Applications International Corporation's Plasma Physics division where she is assigned to work in the Electronics Science and Technology Division of the Naval Research Laboratory. Her current research area is vacuum microelectronics.

Sidney T. Smith, photograph and biography not available at the time of publication.



Charles A. Spindt received the B.S. degree in electrical engineering from California State University at San Jose and the Ph.D. degree in engineering physics from the Eurotechnical Research University.

He joined SRI International, Menlo Park, CA, in 1961 where he is now Director of the Vacuum Microelectronics Program and is currently involved in the development of vacuum microelectronics devices. He has conducted research in vacuum deposition systems, thin-film deposition techniques, ultrahigh vacuum deposition systems, thin-film high-density information storage devices, fabrication of dense arrays of microchannel electron multipliers, micrometer-size field-emission tube techniques, thin-film field-emission cathodes, x-y addressable thin panel displays based on field emitter arrays, and field ionization sources for mass spectrometry. He has authored or co-authored over 50 papers and articles and holds 9 U.S. patents.

Dr. Spindt is a member of Sigma Xi and the American Vacuum Society.